RARE-EARTH-DOPED TeO_2 DISTRIBUTED BRAGG REFLECTOR LASERS

RARE-EARTH-DOPED TELLURITE DISTRIBUTED BRAGG REFLECTOR ON-CHIP LASERS

By BRUNO LUÍS SEGAT FRARE, B. Eng., B. Sc.

A thesis submitted to the School of Graduate Studies in partial fulfillment of the requirements for the degree Doctor of Philosophy.

McMaster University
Department of Engineering Physics
Doctor of Philosophy (2024)
Hamilton, Ontario - Canada

TITLE: Rare-earth-doped tellurite distributed Bragg reflector on-chip lasers

AUTHOR: Bruno Luís Segat Frare, B. Eng., B.Sc.

SUPERVISOR: Dr. Jonathan D. B. Bradley

NUMBER OF PAGES: xx, 154

Lay Abstract

Integrated photonics is an emerging technology that revolves around tiny circuits on chips, similar to electronics, but using light instead of electricity. Photonic integrated circuits can help achieve faster and more power-efficient devices for a wide range of applications. In this work, we explore the potential of tellurite glass, a material that has promising optical properties, to achieve on-chip lasers. Lasers are one of the fundamental components in these light-driven circuits but are challenging to be realized on a chip-scale. We achieved compact lasers, which are more than ten times thinner than a strand of hair, a couple of centimeters long, and emit invisible (infrared) eye-safe light. These devices are compatible with volume production and there is much room for optimizing them. The lasers investigated here are highly promising for applications including imaging systems (LiDAR) for autonomous vehicles, augmented and virtual reality, data communications, and chemical and physical sensors.

Abstract

Tellurite glass is a material with advantageous optical properties, such as high transparency from visible to mid-infrared wavelengths, high nonlinearity, and high solubility of light-emitting rare earth dopants. Although tellurite has been investigated in fibers and in some waveguide studies, there is still much to explore about it in integrated photonics. Here, we use a hybrid platform that monolithically combines tellurite with commercially available silicon nitride chips. The platform leverages silicon nitride's many advantages, including its low propagation losses, mature fabrication techniques with small feature sizes, and low cost for mass production, to enable the development of new on-chip tellurite glass light sources. This thesis aims to study the optical properties of distributed Bragg reflector cavities and explore their potential for lasing when the tellurite is doped with different rare earths, namely erbium and thulium. Chapter 1 provides an overview of the context of this work, introducing the materials and cavity used here. Chapter 2 introduces the basic theory behind waveguides and Bragg gratings, as well as rare earth rate equation gain models, coupled mode theory, and a laser model based on the shooting method. Chapter 3 discusses the design, fabrication, and characterization of passive properties of distributed Bragg reflector cavities using undoped tellurite. Chapters 4 and 5 present proof-of-concept laser demonstrations, by using tellurite doped with erbium and thulium, respectively. These lasers constitute the first demonstrations of distributed Bragg reflector lasers in this hybrid tellurite-silicon nitride platform. Chapter 6 combines the laser model introduced in Chapter 2 with the designs and results from Chapters 3–5 to investigate different routes to optimize the laser performances by studying how their efficiencies vary with different parameters, such as background loss, cavity and grating lengths, and rare earth concentration. Chapter 7 summarizes this work and provides insights into future research work.

Acknowledgements

First, I would like to thank my supervisor, Dr. Jonathan D. B. Bradley, for trusting in me and giving me the opportunity to contribute to this project. I would not have made it this far without his support, guidance, and helpful discussions. I will always be grateful for life-changing opportunities, such as attending the Siegman School and Photonics West. Thank you for listening to my complaints, frustration, and self-depreciative humor. I have always been reluctant to address you without your full title, but after so many years, I will make an exception: do not worry *Jon*, I will not try to reinvent the wheel… BUT, even if I do, I will not spend too much time on it.

I would like to express my gratitude to my committee members, Dr. Andrew P. Knights and Dr. Chang Qing Xu, for their valuable suggestions and feedback on my work. I would like to extend these thanks to Dr. Harold Haugen, who was initially part of my committee before he retired. Many of our discussions from our committee meetings are present in this thesis, directly or indirectly.

Most certainly, I would not have made it to the end if it were not for the amazing members of Bradley Research Group. Thanks to the first generation of BRG students, namely Dr. Henry C. Frankis, Dr. Dawson Bonneville, Dr. Khadijeh Miarabbas Kiani, Dr. Hamidu M. Mbonde, and Dr. Jeremy Miller, who have not only welcomed and trained me, but also established the lab and groundwork that made this project possible. If I have seen a little further, it was only because I stood on your shoulders! While they paved the way for me, I would not be able to continue without the new – and now senior – students who have joined the group after me. Thank you, Batoul Hashemi, for joining me in my crazy deposition plans including the infamous midnight run and all the help with the measurements (and, of course, for all the gossip). Thank you, Pooya Torab Ahmadi, for working with me on the intense and frustrating alumina depositions, and for the hundreds of Metricon measurements. Thank you, Niloofar Majidian Taleghani, for your kindness and tremendous help measuring hundreds of gratings. Thank you, Cameron Naraine, for helping me so much in my first years, for the unwavering comradery, and fruitful discussions. Thank you, Arthur Mendez-Rosales, not only for all the help with the setups, but also for the great times outside the lab, in random *rolês*. Thank you all for listening to me complaining about life all the time, working so well as a team, and, of course, for joining me for pump and pray experiments. I would also like to thank our summer undergraduate and high school students for their assistance, in particular Anoop Dhillon, Dennis Yankovsky, Evan Jonker, and Joy Justing. It was a pleasure – I mean, it was *cool cool* – to work with you.

Thank you to the CEDT staff, namely Doris Stevanovic and Dr. Nebile Isik Goktas, for all the efforts in maintaining our research facilities and for the tremendous help in fixing our beloved sputtering system. The hundreds of hours spent working in the cleanroom would not have been pleasant without you.

I am grateful for all the training and help that Dr. Zhilin Peng provided with SEM imaging, always with a smile on his face – even when I booked sessions with short notice.

Thank you to the Engineering Physics department staff, Robert, Samantha, Linda, Emma, and Nicole for all the help with administrative work, and Reza and Catherine for your support. Every time I needed something (and it was not a few), you have always gone the extra mile to help.

A special thanks to Ryan Warriner and all the MODEL team, for helping me improve my English skills and prepare for presentations.

This work would not be possible without the support of CMC, ITF Technologies, and LioniX, which also provided tools and services that were pivotal to this project.

Last, but not least, I would like to thank my parents and my brother for supporting me from a (long) distance and believing that I could do this.

Table of Contents

List of Figures

List of Tables

List of Abbreviations

ASE	Amplified stimulated emission
CEDT	Centre for emerging device technologies
CMOS	Complementary metal–oxide–semiconductor
CMT	Coupled-mode theory
CW	Continuous-wave
DBR	Distributed Bragg reflector
DFB	Distributed feedback
DUV	Deep ultraviolet
EDFA	Erbium-doped fiber amplifier
ESA	Excited-state absorption
ETU	Energy transfer upconversion
EYDFA	Erbium-ytterbium-co-doped fiber amplifier
FBG	Fiber Bragg grating
FEM	Finite element method
FP	Fabry-Pérot
FSR	Free spectral range
FWHM	Full width at half maximum
LiDAR	Light detection and ranging
LPCVD	Low-pressure chemical vapour deposition
OSA	Optical spectrum analyzer
PIC	Photonic integrated circuit
RAM	Random-access memory
RE	Rare earth
RETU	Reverse energy transfer upconversion
RF	Radio frequency
SEM	Scanning electron microscope
SiN	Silicon nitride
SOI	Silicon-on-insulator
SSD	Sold-state drive
TE	Transverse electric
TM	Transverse magnetic
TMM	Transfer matrix method
VECSEL	Vertical external-cavity surface-emitting laser
WDM	Wavelength division multiplexer

Declaration of Academic Achievement

I, Bruno Luís Segat Frare, declare that the thesis "*Rare-earth-doped tellurite distributed Bragg reflector on-chip lasers*" was written by and presents research work led by myself. The silicon nitride chips were fabricated at the LioniX foundry and CMC provided access to RSoft. Dr. Dawson B. Bonneville helped with the Bragg grating designs (Chapters 3–5) and Dr. Hamidu M. Mbonde led the overall silicon nitride layout, which included these and other designs and coordinated the layout submission with the foundry (Chapters 3–5).

Additional contributions made by others to this work include:

Chapter 3:

- Batoul Hashemi and Niloofar Majidian Taleghani assisted with applying the Cytop polymer cladding, as well as the tellurite film and waveguide background loss measurements.
- Niloofar Majidian Taleghani, Batoul Hashemi, Evan Jonker, Anoop Dhillon, and Joy Justin worked with me to test the samples after the post-processing and acquiring parts of the passive transmission data.
- Dr. Zhilin Peng assisted with scanning electron microscopy imaging.
- Doris Stevanovic and Dr. Nebile Isik Goktas assisted with sputtering system repairs.

Chapter 4:

- Pooya Torab Ahmadi helped with the fabrication and characterization of tellurite films.
- Batoul Hashemi assisted with the characterization of the tellurite film and waveguide background loss, as well as the erbium concentration.
- Dr. Henry C. Frankis provided training and guidance throughout this work.
- Arthur Mendez-Rosales helped with preparing the optical setup.
- Dennis Yankovsky assisted with lifetime measurements.
- Anoop Dhillon helped with loss characterization.
- Dr. Zhilin Peng assisted with scanning electron microscopy imaging.

Chapter 5:

- Batoul Hashemi helped with thin film depositions and cutback measurements.
- Pooya Torab Ahmadi and Niloofar Majidian Taleghani helped with RBS measurements and data analysis.
- Doris Stevanovic and Dr. Nebile Isik Goktas assisted with sputtering system repairs.

Chapter 6:

- Arthur Mendez-Rosales suggested the use of normalized populations to solve thulium's rate equations, which made the Matlab code possible.

Nothing in science has any value to society
if it is not communicated.

- Anne Roe

Preface

July 2024
McMaster University
Hamilton, ON

Dear reader,

Welcome to my Ph.D. thesis, what a journey this has been! It began when I moved from Brazil to Canada in May 2019 as a master's student. Little did I know that my stay would extend for five years, after transferring to the PhD program. Soon after this change, we were hit by the COVID-19 pandemic, which now feels like a collective nightmare and is still mind-boggling that it really happened.

Before the pandemic, I was the newest member of our research group. When in-person activities resumed over a year later, I found myself as a senior student, as most of my senior colleagues had graduated. This had a tremendous impact on my learning curve, since I missed the natural knowledge transfer that occurs in daily lab interactions. Consequently, I quickly assumed new responsibilities and it was challenging to suddenly become the person to whom new students would come for guidance. I became in charge of leading all thin film depositions in the group, after a few weeks of training. However, due to limited use and preventive maintenance during the pandemic, the sputtering system had to be shut down for major corrective maintenance. The repair process, which was led by me, consumed another year, leaving me in my third year with minimal experimental progress – a tremendous setback for an experiment-based project.

Despite these challenges, this thesis represents a fraction of the work undertaken over the past five years. However, especially if you are a graduate student, please know that there was plenty of frustration, failure, and imposter syndrome involved until the story told in this thesis started to take shape. The majority of the results presented here were obtained in the final months before my defense, with much of the data analysis and modeling occurring concurrently with the writing process. What you will find here is not a chronological depiction of facts, but rather a story that took tremendous effort to be told in a (hopefully) cohesive and logical manner.

My primary goal in writing this thesis was to make it informative, accessible, and enjoyable to read. I aimed to balance formal scientific rigor with engaging and approachable language, including details that, while now obvious to me, required significant commitment to comprehend initially. Whether I have succeeded in this endeavor is for you to judge. I hope you find the reading both enlightening and enjoyable!

Bruno Luís Segat Frare

1. Introduction

This chapter starts with a brief introduction to fibers and integrated photonics, followed by an overview of silicon- and tellurite glass-based photonic integrated circuit platforms. Then, a summary of types of integrated laser cavities is presented, as well as demonstrations of on-chip rare-earth-based distributed Bragg reflector lasers and some of their applications.

1.1. FIBER OPTICS AND PHOTONICS

In his book *Sapiens: a Brief Story of Humankind*, the historian Yuval Harari argues that gossip is one of the key evolutional features behind the success of our species. We have thrived in an adverse world as large and (mostly) cohesive groups, whereas our ancestors failed to do so [1]. With the Cognitive Revolution (30,000 to 70,000 years ago), communication gained unparalleled levels of complexity through the development of language. From primitive forms of visual and sound communication to the advent of speech and, later, writing, social bonding enabled societies as we know today to take shape. Tens of thousands of years after the Cognitive Revolution, the Industrial Revolution in the 19th century promoted technological breakthroughs that have evolved at an incredible pace across 150 years [2]: telegraph, telephone, radio, television, satellite communications, personal computers, cellphones, and the Internet, of course. With the launch of the World Wide Web in 1993, the Internet became one of the pillars of globalization and redefined society at every level, from personal behavior and relationships to the economy and geopolitics.

When the Internet first became available to the public, providers leveraged the existing telephone (dial-up connection) and later cable television (broadband internet) transmission lines [3] to deliver services to residences. Even though broadband internet was a significant improvement over dial-up connectivity, they both relied on copper wire transmission lines. With the tremendous growth of internet usage in the 1990s and 2000s, data transmission through optical fibers became widely adopted due to their capacity to overcome limitations of coaxial wires, such as signal attenuation, bandwidth, speed, weight, and electromagnetic interference [4,5], enabling the current data-driven society. Fibers are capable of confining and guiding light beams, similar to how copper wires can guide electric current. They were developed across the 20th century and, in 1970, the first low-loss fiber was achieved at Corning, enabling long-haul networks [5]. In parallel, other key components for optical communications were invented, such as the semiconductor laser, the lithium niobate modulator, and the erbium-doped fiber amplifier (EDFA) [5].

The success of fibers goes beyond telecommunications. They are also widely used in medical, sensing, defense, aerospace, and industrial applications [6]. Fiber lasers are known for their high efficiency, beam quality, stability, high power, and narrow linewidth, with applications in material processing and manufacturing, surgical procedures, sensing, and light detection and ranging (LiDAR) systems [7–11]. The field that studies light (which is made of photons), light-based devices such as fibers and lasers, and optical systems is called photonics. It encompasses light generation, propagation, amplification, detection, modulation, spectroscopy and all their applications.

1.2. Integrated Photonics

With the ubiquitous presence of optical fiber systems in the 21st century, the miniaturization of such technology is a natural next step, similar to how the evolution of electronics led to integrated circuits. The arrangement of light-driven components onto chips is known as photonic integrated circuits (PICs), which enable the assemble of multiple photonic components to form tiny optical systems. The development of PICs lies in the realm of integrated photonics, a field that aims to bring the advantages of optics to a chip-scale. Just as light revolutionized telecommunications, it carries a tremendous potential to open the door to the realization of compact devices with enhanced performance and new applications [12].

The concept of integrated photonics emerged about a decade after the first demonstration of a laser in 1960 [13,14]. The fundamental building block of such technology is known as a waveguide, a structure that can confine and guide light on a chip scale, similar to what fibers do on a larger scale (we will discuss waveguide theory in Chapter 2). Throughout the 1970s, light guiding in thin films was reported, and the first steps were taken toward fabricating compact devices on a substrate [15,16]. Since then, in the past 50 years, many platforms using different materials have been investigated for their use in integrated photonics, with various levels of success and challenges associated.

Ideally, a PIC platform should offer features such as low propagation and coupling losses, broadband transparency, small footprint and waveguide bend radii, compatibility with standard foundry fabrication techniques for scalable production at low cost, as well as the ability to integrate all circuit building blocks including light sources, optical switches, modulators, and detectors [17]. These components can be categorized into active and passive components. Active components such as lasers, detectors, and modulators require an external power source to operate. On the other hand, waveguides, filters, and splitters do not need a power supply to function.

So far, many materials have been investigated as potential candidates to realize reliable PICs. As we will see in the next section, silicon is an important and mature material used as both a substrate and waveguiding material in PICs. Glasses are also widely used in photonics due to their excellent optical properties including high transparency, ease of fabrication, and compatibility with many substrates [18]. These include silica, alumina [19,20], chalcogenide [18,21] and phosphate [18,22–24] glasses. In addition to those glasses, many other materials have been explored for applications in integrated photonics, such as silicon carbide [25], tantalum pentoxide [26], polymers [27], III-nitride [28], aluminium nitride [29], lithium niobate [30–34], and silicon nitride [35–38].

The remarkable success of laser diodes makes III-V semiconductor materials of interest in photonic integrated circuits. However, the growth of III-V layers involves expensive and complex steps that are not compatible with standard silicon-based complementary metal-oxide semiconductor (CMOS) processing. Currently, it is challenging to monolithically grow these materials on a silicon substrate, due to their large lattice mismatch and polarity difference [39,40]. One way to overcome this limitation is to use a different substrate, such as indium phosphide (InP) [41–44]. The main advantages of using III-V materials include their excellent laser and amplifier performances and ability to be electrically pumped [44]. The main disadvantages of these platforms are their cost, fabrication complexity, and difficulty in being mass-produced [41]. Another way to leverage the performance of active III-V devices revolves around the hybrid integration of III-V components on chips based on a different platform, such as Si [39,45], Si_3N_4 [46,47], or $LiNbO_3$ [48,49]. Again, cost, fabrication, and scalability are the main challenges associated with this approach [39].

1.3. Silicon-based Photonics

Given the extreme maturity of silica-based optical fibers, **silicon dioxide** (SiO_2) would be a natural material candidate to produce waveguides on a chip. Although low-loss silica waveguides have been demonstrated [50], their low refractive index translates into large bend radii (several mm) [51], which are prohibitive to achieve compact devices. However, SiO_2 is still widely used as a bottom and top cladding around a waveguiding core material [52–55]. In general, its low refractive index can maintain appropriate index contrasts with typical waveguide materials, which is a necessary condition to confine light within a core – this will be discussed in more detail in Chapter 2. This, in addition to silica's low loss, makes it an excellent kind of optical *insulator* that reduces the mode leakage from the waveguiding core and passivates it, like how it is employed in electronics.

One of the most mature subfields of integrated photonics is **silicon** (Si) photonics [56]. The main advantage of developing PICs based on Si is the opportunity to leverage the well-established, multi-billion-dollar CMOS foundries used in electronics. Silicon has a high refractive index, which enables compact waveguides and tight bend radii on the order of a few micrometers [57]. The Si waveguides can be fabricated on a thermally oxidized silicon substrate [58], which gives this platform the name silicon-on-insulator (SOI). It typically offers moderate propagation losses and a wide range of active and passive components have been demonstrated in this platform, including switches, modulators, photodetectors, directional couplers, grating couplers, and resonators [59,60]. However, due to its indirect bandgap, silicon cannot efficiently emit light, which makes the realization of reliable optical amplifiers and lasers a key challenge in this platform [45]. Additionally, Si is not suitable for visible light applications, because it is highly absorbing at wavelengths below 1.1 μm [61].

In the past decades, **silicon nitride** (Si_3N_4) has emerged as an excellent PIC platform that maintains CMOS-compatibility, while complementing the advantages and overcoming some of the challenges associated with Si [35–37,62,63]. Silicon nitride's ultra-low losses are one of its main advantages, as well as small feature sizes available in mass production at low cost, and wide transparency range, from visible to mid-infrared [38,53]. Even though its refractive index is significantly lower than silicon's, Si_3N_4 still offers a moderate refractive index contrast to SiO_2 claddings, enabling compact devices with bend radii in the order of a few hundred micrometers [38]. In 2022, a Si_3N_4 waveguide amplifier was achieved by directly doping the waveguide with erbium via ion implantation, yielding results comparable to state-of-the-art erbium-doped fiber amplifiers [64], and narrowing the performance gap between fiber and PIC.

1.3.1. Hybrid Monolithic Integration of Light-emitting Materials on Silicon

Some approaches aim to achieve the monolithic integration of gain materials into commercially available platforms, such as silicon or silicon nitride waveguides, in which active functionalities are not readily available in all foundry platforms. In this case, the material layers can be engineered to form a hybrid waveguide[1] structure that allows sufficient mode interaction with the active gain medium to achieve light emission in CMOS-compatible platforms. The driving force behind these approaches is to add functionalities to commercially available platforms by using simple, low-cost, and scalable fabrication processes. For example, alumina has been used in combination with silicon waveguides to achieve signal enhancement [65]. It has also been successfully combined with silicon nitride chips to achieve compact lasers [66–68].

1.3.2. Tellurite Glass Hybrid Integrated Photonics

Of glass materials proposed for integrated photonics, tellurite glass has a wide range of attractive properties. It has a relatively high refractive index (~ 2.1 at 1550 nm) and is highly transparent from visible to mid-infrared wavelengths [69]. It has strong acousto-optic effects [70,71], high nonlinearity [72], and high chemical stability [69], in addition to its excellent rare-earth solubility and large emission cross sections that make it a promising candidate for an active gain medium in PICs [73–75]. Moreover, it can be processed at low temperatures (< 200 °C) using straightforward wafer-scale techniques, which are attractive features for effective post-processing fabrication on PIC platforms [76,77].

Although tellurium dioxide has been extensively investigated in fiber-based applications [78–83], it is challenging to fabricate high-quality tellurite waveguides [69]. Fabrication of low-loss tellurite thin films via reactive sputtering has been demonstrated [72] and one successful method to etch low-loss TeO_2 waveguides is the use of reactive ion etching in a hydrogen-methane-argon atmosphere [69]. However, when this technique was applied on erbium-doped tellurite thin films, erbium hydride compounds were re-deposited on the waveguide surface, making it extremely rough (lossy) due to the formation of granular features [73,84]. Therefore, further efforts are required to develop suitable etch

[1] The terminology here can be confusing. Hybrid integration of III-V materials often refers to the integration of a III-V chip to a CMOS-compatible chip, using complex techniques such as transfer printing and wafer bonding. In this thesis, the expressions "hybrid platform" and "hybrid waveguide" refer to the formation of a composite waveguiding layer through the monolithic integration of a material on a CMOS-compatible chip using a simple processing step.

processes for rare-earth-doped tellurite films. In addition, processing at a wafer-scale of tellurite and other non-standard materials is difficult to incorporate into PICs which use standard foundry processes. Nonetheless, high-gain tellurite waveguide amplifiers and lasing off chip facets have been demonstrated, showing the excellent promise of the material [73].

One way to avoid the challenges associated with fabricating on-chip tellurite devices is to combine it with mature platforms. For instance, the hybrid structure formed when tellurite glass is added on top of thin silicon nitride waveguides combines the aforementioned advantages of both materials. Tellurium dioxide's slightly higher refractive index than Si_3N_4 causes an expansion of the propagating optical mode into the tellurite layer. By engineering the thickness of each layer, it is possible to achieve more than 50% of light traveling in the tellurite glass, which can act as a gain medium when doped with rare earths. As a result, active devices can be realized in commercially available silicon nitride chips, with the potential for seamless integration with passive and nonlinear components on the same chip. Our research group has demonstrated low losses on this platform [85,86], as well as net gain in erbium-doped tellurium dioxide [87], in addition to optical amplifiers and microring lasers using thulium-doped TeO_2 [88,89]. Figure 1.1 shows a concept art of the lasers we will investigate in this work using this hybrid platform.

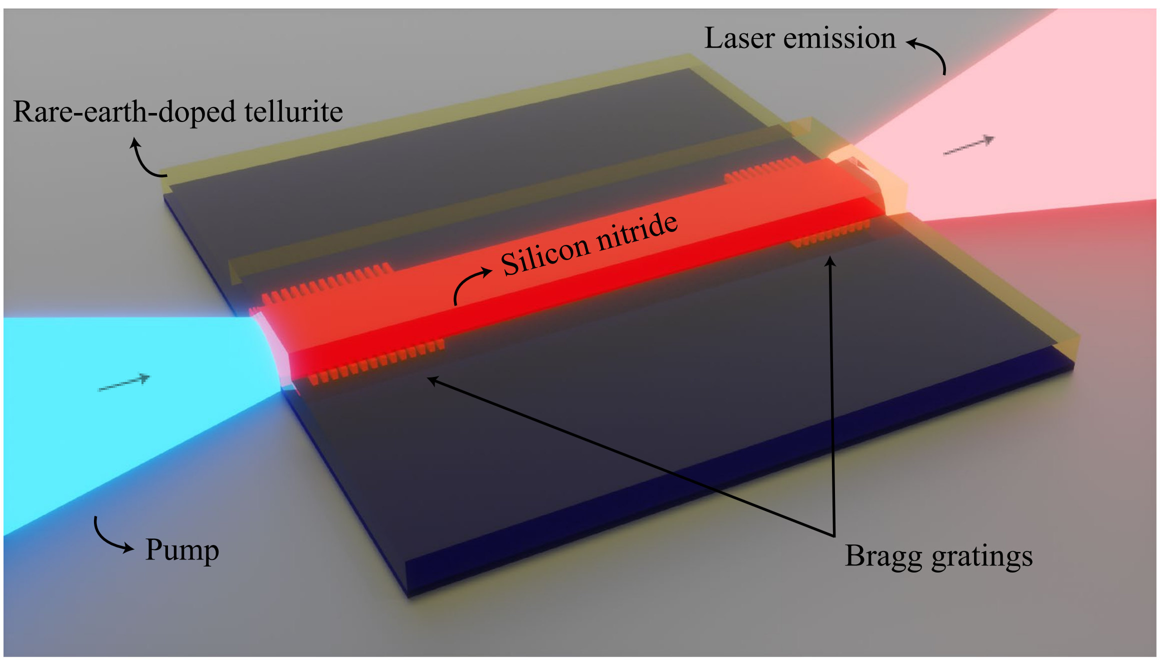

Figure 1.1. Concept art highlighting features of the platform and type of laser cavity used in this work.

A similar approach can be used on silicon-on-insulator chips. However, three main issues arise when the silicon nitride waveguides are replaced by silicon. First, silicon's high refractive index, combined with the standard 220-nm thickness that has been adopted by foundries, causes the optical mode to be highly confined in the Si layer. As a result, significantly lower mode overlaps (and consequently gain) can be achieved with the TeO_2 layer (< 20%). Second, silicon waveguides typically have higher losses than silicon nitride, which means that a higher gain coefficient is needed to overcome propagation losses and promote optical amplification or lasing. Third, silicon has high absorption at many rare earth pump wavelengths (< 1.1 μm). These three aspects combined make it challenging for this platform to achieve the same level of performance as the silicon nitride-tellurite combination. Still, our group has demonstrated lasing applying thulium-doped-tellurite on Si microdisks [90], which also shows the promise of hybrid integration on silicon.

1.4. ON-CHIP LASERS

In a technology that revolves around light, it comes as no surprise that on-chip light sources are a crucial component in photonic integrated circuits[2]. Laser sources are pivotal for applications in areas such as telecommunications [91,92], optical and quantum computing [93–95], augmented and virtual reality [96–98], LiDAR systems [99–101], lab-on-a-chip medical devices [102–105], and sensing [102,106–110]. Nevertheless, achieving reliable lasers on a chip scale that meet the performance requirements for such applications while being economically viable for mass production is a challenging task [109].

The emission wavelength of a laser is one of its key parameters, and different applications require sources that operate in different ranges of the electromagnetic spectrum. On-chip lasers emitting in the ultraviolet and visible spectrum have been increasingly investigated in recent years [111–117]. However, lasers that operate in the near-infrared around 1310 or 1550 nm wavelengths are of particular interest, due to their potential to be straightforwardly combined with conventional fiber technology [109]. Additionally, an ideal on-chip laser source would have the following attributes [109]:

- **High output power**, to deliver the required signal to the application it was designed for.
- **Narrow linewidth**, to maintain the spatial and temporal coherence needed in most applications.
- **Continuous-wave emission**, for stable operation.
- **Electrical pumping**, to achieve compact circuits that can be integrated with existing microelectronic technology.
- **Chemical, mechanical, and temperature stability**, to withstand a wide range of operating conditions with an appropriate lifespan.
- **Compatibility with CMOS-processing**, to be mass-produced at a low cost.

The approach that comes closest to meeting all of these requirements is the hybrid integration of III-V laser materials on silicon. However, as mentioned earlier, it is challenging to mass produce them at low cost using CMOS foundries. Many alternatives that partially fulfil the aforementioned characteristics have been explored, including

[2] Although off-chip lasers can be coupled to chips, we ideally want to achieve fully on-chip solution for simplicity and compactness.

quantum cascade [118–121], plasmonic [122–124], quantum dot [125–129], nanowire [130–133], perovskite [134–137], and rare-earth lasers [20,33,138].

1.4.1. Rare-earth-based Lasers

The rare earths (REs) are a group of metals that mostly belong in the lanthanide series in the periodic table. Despite the name, they are not scarce materials[3] and the largest rare earth deposits are located in China, Vietnam, Brazil, and Russia [139]. Their electronic structure consists of a partially filled 4f orbital that is shielded from external fields by outer electron shells. Such a unique configuration gives them chemical stability and fascinating magnetic, catalytic, and optical properties that are minimally affected by their surroundings [140]. Rare earths have been commercially explored after World War II, driven by separation techniques developed during the Manhattan Project that enabled improved ore processing and high purities [141]. They have found applications in a wide range of fields, including permanent magnets, petroleum refining, chemical synthesis processes, green energy, biomedicine, and defense [142–144]. However, it is in photonics that REs shine…literally, due to their luminescence properties.

Rare earths can be used as dopants, usually in the trivalent ion form (RE^{3+}), in various host materials, e.g. polymers, semiconductors, crystals, and glasses [145]. In photonic applications, rare-earth-doped materials can be optically pumped to excite the RE ions and generate light at specific wavelengths that depend on the population dynamics of their energy levels. This will be discussed in more detail in Chapter 2, but, for now, keep in mind that such processes can establish an active gain medium that will serve as a basis to achieve optical amplification and lasing. Some rare-earth ions that are commonly used in amplifiers and lasers include Praseodymium (Pr), Neodymium (Nd), Holmium (Ho), Erbium (Er), Thulium (Tm), and Ytterbium (Yb).

Optical fibers can be doped with rare-earth ions, a combination that proved to be fundamental to the success of fiber networks, by enabling optical amplifiers (EDFAs) to support long-haul transmission, as well as laser sources. Rare-earth lasers are versatile in the sense that they can be designed to operate at fixed or tunable wavelengths from visible to infrared within a RE’s emission spectrum [8,9,146]. They are stable, can have high quantum efficiencies and deliver narrow linewidths and high output powers [8,147]. Erbium and holmium lasers are used in high-precision, minimally invasive surgeries in urology, dermatology, and ophthalmology [148–152]. Neodymium-doped yttrium aluminum garnet (Nd:YAG) lasers are pivotal to industrial applications such as laser cutting and welding [153–155]. Thulium lasers have applications in dentistry treatments, as well as in telecommunications [156–158].

In integrated photonics, REs have been explored to achieve compact gain media in PICs. Optical gain and lasing have been demonstrated in rare-earth-doped materials such as lithium niobate [33], phosphate glass [24], alumina [159,160], silicon nitride [64], and tellurite [87–89]. The RE ions can be incorporated into the host materials through post-

[3] If you are curious, the name “rare earth” comes from the fact that they are not usually found in pure form and processing of large quantities of ore is required to achieve sufficient purity.

processing techniques such as ion implantation, or simultaneously via chemical or physical vapour deposition, for example.

1.4.2. On-chip laser cavities

So far, we have focused on the material aspects of PICs and introduced the key ingredient (rare-earth-doped tellurite glass) that was used for the realization of active gain media in this work. Now, another pivotal element in building a laser will be introduced: optical cavities. This section introduces some of the main types of integrated optical cavities, with a focus on distributed Bragg reflector cavities, which are the subject of study of this thesis.

On its website, RP Photonics provides the following definition [161]:

> *An optical resonator (or resonant optical cavity) is an arrangement of optical components which allows a beam of light to circulate in a closed path.*

In other words, it is a structure in which light can be trapped into a fixed path, in a way that the electromagnetic field spatial distribution is stable over time forming optical modes. Commonly used cavities can be categorized into two groups: standing (also known as linear or longitudinal) and travelling wave resonators (also called ring resonators) [161]. In **standing wave resonators**, the light beam bounces between two mirrors, while in **travelling wave resonators**, light circulates within a closed loop. When the cavity contains a gain medium capable of generating sufficient light to overcome the roundtrip losses (which include propagation losses and light leaking out of the cavity), a stimulated emission chain reaction can promote lasing.

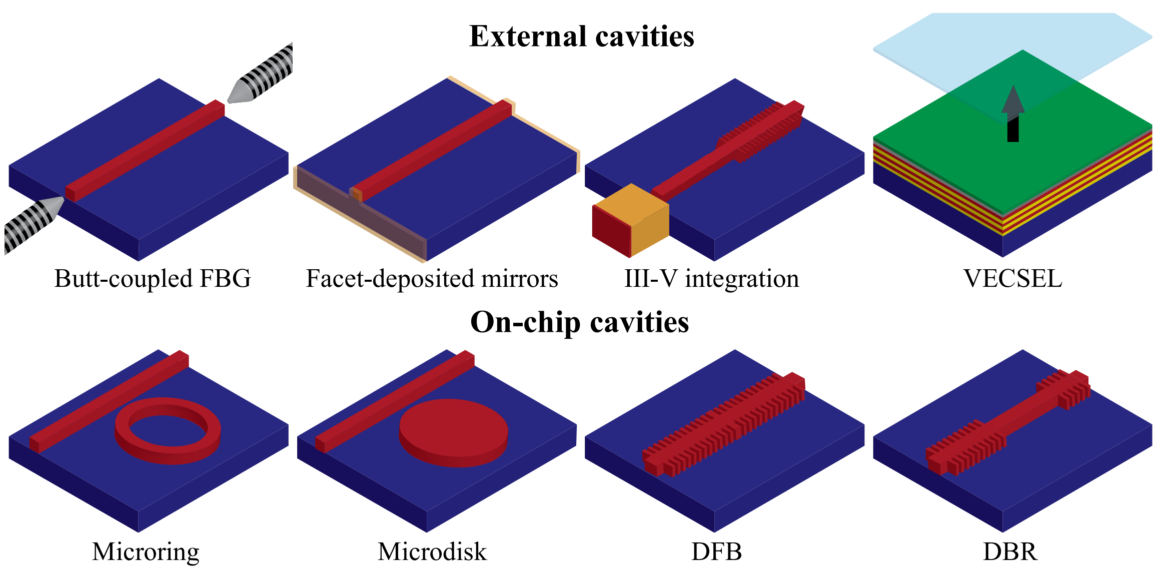

Figure 1.2. Basic integrated photonic laser cavities.

Figure 1.2 highlights some types of basic laser cavities that have been investigated in integrated photonics. **External cavity** lasers include off-chip elements and take advantage of easily available components, even though they require precise optical alignment and often cannot be straightforwardly integrated with other PIC components. Examples include standing wave resonators like butt-coupled fiber Bragg gratings (FBG) [162,163], facet-deposited mirrors [164,165], integration of III-V semiconductor optical amplifiers butt-coupled to a chip [166–168], and vertical external-cavity surface-emitting lasers (VECSELs) [169,170]. **On-chip cavity** lasers, on the other hand, use exclusively on-chip elements and the laser output can be easily integrated with other PIC components. They are robust in the sense that all elements are fixed onto the chip and no optical alignment is required. Microring and microdisk resonators, as well as Sagnac loop reflectors, can be fabricated in a single processing step [171–178] Bragg-reflector-based structures such as distributed feedback (DFB) and distributed Bragg reflector (DBR) cavities provide excellent operation stability and can be designed to achieve single mode emission and narrow linewidths, but require an extra fabrication step to pattern the reflectors [24,159,179–182].

1.4.3. DISTRIBUTED BRAGG REFLECTOR LASERS

Distributed Bragg reflector lasers are based on cavities defined between two Bragg grating regions, as we will see in detail in Chapter 2. They have been demonstrated using many approaches such as hybrid integrated III-V materials [183]. However, DBR cavities are particularly interesting for rare-earth waveguide lasers, because they allow for precise control over the operation wavelength within the rare earth emission bands. They are robust and offer stable operation, while can be tailored to optimize the balance between gain and loss, which is a challenge in the chip-scale. They are also relatively simple to design and implement, which is beneficial for proof-of-concept demonstrations in less mature laser materials, such as the rare-earth-doped tellurite glass explored in this thesis. The working principle, optical behavior, and design aspects of DBR cavities will be formally introduced in Chapter 2. Some of their advantages include:

- **Versatility:** the design of each set of Bragg reflectors can be precisely tailored to control the cavity optical response, reflecting specific wavelengths while transmitting others.
- **Compactness:** the reflectors can be patterned directly on the waveguide sidewalls or surroundings (laterally or on the top cladding).
- **Simplicity:** DBR cavities are similar to Fabry-Pérot cavities (arguably the most straightforward type of cavity, consisting of two mirrors facing each other).
- **Manufacturability:** they can be monolithically integrated in PICs, using CMOS-compatible processing steps, such as stepper lithography.
- **Performance:** they can deliver high powers and narrow linewidths, while operating with good stability.

Challenges associated with DBR lasers are often related to their fabrication. They typically require high-resolution fabrication techniques to pattern the gratings, which often require feature sizes down to tens of nanometers. Moreover, one of the drawbacks of this type of cavity is that they are usually multimode, as we well see in Chapter 2, which can be overcome by careful cavity design.

Here, we will focus on DBR lasers based on erbium and thulium, operating near 1.5 and 1.9 µm, respectively. These two wavelengths can be transmitted with low propagation losses in the materials that constitute the platform used here. Additionally, the Bragg grating features needed to reflect them are feasible with current patterning methods and their resolution limits. Erbium-based lasers naturally attract significant interest, due to their maturity in fiber technology, as well as compatibility with telecommunication networks, and their ability to efficiently emit eye-safe light in the C-band (1530–1565 nm) [138]. They can also be used in applications including LiDAR systems and sensing.

With the rapidly increasing data traffic worldwide, the extension of communication network operation to around 2 µm wavelength has been explored for having the capability to offer high bandwidth transmission, while maintaining eye-safety [158,184]. In this context, lasers based on thulium are of interest, due to its ultrabroad emission ranging from 1.6 to 2.2 µm and potential to achieve high power lasers. Thulium lasers are also of interest for LiDAR systems, medical diagnostics, and sensing. Even though thulium-doped lasers have been realized in PICs [89,90,185–188], and record high continuous wave and pulsed powers were demonstrated in [185,189], Bragg-grating-based thulium lasers have not been extensively investigated. In addition, prior to this work erbium and thulium on-chip DBR-based tellurite lasers were not reported. Table 1.1 summaries some of the erbium- and thulium-based DBR lasers that have been demonstrated in various platforms.

Table 1.1. Rare-earth-based distributed Bragg reflector waveguide lasers.

Lasing wavelength (nm)	Platform	Gain medium	Pump wavelength (nm)	Threshold (mW)	Efficiency (%)	Max. power (mW)	Ref.
1546[a]	Phosphosilicate glass	Er-doped phosphosilicate	976	60	N/A	0.34	[180]
1553[a]	Al-doped germanosilicate	Er/Al-doped germanosilicate	979	21	N/A	0.4	[182]
1561.1[a]	Ti:$LiNbO_3$	Er-doped $LiNbO_3$	1480	70	2	1.1	[181]
1561[b]	Ti:$LiNbO_3$	Er-doped $LiNbO_3$	1480	54.8	0.69	0.65	[190]
1536[b]	Phosphate glass	Er/Yb-codoped phosphate glass	977	50	26	80	[164]
1540[b]	Phosphate glass	Er-doped phosphate glass	980	60	13	11	[191]
1536[a]	SiN-Al_2O_3	Al_2O_3:Er	978	44	2.6	5.1	[68]
1561				N/A	N/A	2.5	
1596				N/A	N/A	0.5	
1533.3–1564.5[a]	SiN-TeO_2	TeO_2:Er	1470	13–26	0.06–0.36	0.35	This work
1881[a]	SiN-Al_2O_3	Al_2O_3:Tm	1612	65	23	387	[185]
1875.1[a]	SiN-TeO_2	TeO_2:Tm	1610	20	5	4.47	This work

[a]Fully integrated DBR cavity, [b]DBR/facet-deposited mirror cavity.

1.5. Thesis Objectives

The main goal of this thesis is to develop novel lasers in tellurite glass for silicon-based PICs. This is carried out by designing and fabricating silicon nitride photonic chips using a commercial foundry and monolithically applying rare-earth-doped tellurite on the chips via a simple, low temperature post-processing reactive sputtering step. To achieve this goal, a series of DBR cavity variations were designed, fabricated, and characterized. By analyzing their passive properties, it was possible to better understand how different Bragg grating designs perform on this platform. A laser model was also developed to explore different routes toward performance optimization of erbium- and thulium-based tellurite lasers. In summary, this thesis aims to show for the first time fully integrated on-chip DBR tellurite lasers and provide the foundations for the realization of optimized lasers in the future.

1.6. Statement of Thesis Work

This thesis contains 7 chapters that discuss the design, fabrication, and passive characterization of DBR cavities in tellurite-covered silicon nitride waveguides, as well as demonstrations of lasing around 1.5 and 1.9 μm wavelengths by doping the tellurite layer with erbium and thulium, respectively.

In Chapter 1, a brief overview of current research areas within integrated photonics is presented, including a description of and the motivation for the hybrid tellurite-silicon nitride platform used in this work. Moreover, common types of integrated laser cavities are highlighted, with a focus on the advantages of using DBR cavities to achieve on-chip rare earth lasers.

Chapter 2 provides the theoretical background upon which this work is built. The fundamentals of waveguiding in dielectric media and Bragg gratings are introduced, as well as much of the terminology used throughout the thesis. Erbium and thulium laser models based on the shooting method combined with coupled mode theory and rare-earth rate equation gain models are also discussed.

Chapter 3 addresses the design and fabrication of DBR cavities for operation around 1310 and 1550 nm wavelengths. As we will see, operation at these two wavelengths can be achieved with the same grating design, by adjusting the tellurite and silicon nitride thicknesses. This facilitates the design and fabrication process and the detailed understanding of these cavities can be extended to the thulium window. Then, it focuses on the passive characterization of these cavities and on a comprehensive study of the grating properties to understand their performance in laser designs.

Chapter 4 presents a published manuscript on the characterization of erbium-doped tellurite DBR lasers based on the designs investigated in Chapter 3. Several lasers were demonstrated with different sidewall grating and waveguide widths, operating at wavelengths within the erbium emission band.

Chapter 5 is a manuscript currently under preparation for submission to a peer-reviewed journal on thulium-doped tellurite DBR lasers. A proof-of-concept laser is demonstrated with high output directionality and operation near the peak emission wavelength of thulium. It also investigates the thermal sensitivity of these cavities, to explore their potential use as tunable lasers and temperature sensors.

Chapter 6 combines the laser model built in Chapter 2 with the designs and experimental results discussed in Chapters 3–5, to study the influence of several parameters in the laser performance, such as cavity design and background loss. The simulation results provide us with guidelines on how to optimize erbium and thulium-doped tellurite DBR lasers and generally rare-earth-doped tellurite lasers in the future.

Chapter 7 summarizes the work presented in this thesis. It also provides suggestions and insights for future research on rare-earth-doped tellurite glass and Bragg-grating-based lasers in CMOS-compatible PIC platforms.

1.7. Publications

The following is a list of publications by the author that include the results presented in this thesis:

- **B. L. Segat Frare**, B. Hashemi, N. Majidian Taleghani, P. Torab Ahmadi, D. B. Bonneville, H. M. Mbonde, H. C. Frankis, P. Mascher, P. Ravi Selvaganapathy, and J. D. B. Bradley, "A thulium-doped tellurite distributed Bragg reflector waveguide laser on a silicon nitride chip" [Working title, manuscript under preparation].
- **B. L. Segat Frare**, P. Torab Ahmadi, B. Hashemi, D. B. Bonneville, H. M. Mbonde, H. C. Frankis, A. P. Knights, P. Mascher, J. D. B. Bradley, "On-chip hybrid erbium-doped tellurium oxide–silicon nitride distributed Bragg reflector lasers," *Applied Physics B* 129, 158 (2023).

Additionally, the author has contributed to the following conference presentations and proceedings:

- **B. L. Segat Frare**, P. T. Ahmadi, B. Hashemi, H. C. Frankis, P. Mascher and J. D. B. Bradley, "Integrated distributed Bragg reflector lasers in silicon nitride waveguides coated with erbium-doped tellurite," presented at *Photonics North,* Montreal, Canada (2023).
- **B. L. Segat Frare**, D. B. Bonneville, H. M. Mbonde, P. T. Ahmadi, B. Hashemi, H. C. Frankis, P. Mascher, J. D. B. Bradley, "Erbium-doped tellurium oxide distributed Bragg reflector lasers on silicon nitride chips," *Proc. SPIE* 12424, Integrated Optics: Devices, Materials, and Technologies XXVII, 124240E (2023).
- **B. L. Segat Frare**, B. Hashemi, D. Bonneville, H. Mbonde, J. D. B. Bradley, "Distributed Bragg reflector cavities on tellurium oxide-coated silicon nitride waveguides," invited talk at *Photonics North*, Niagara Falls, Canada (2022).

The author has also contributed as a co-author to the following works that are not part of this thesis, including journal publications, conference presentations, and proceedings:

- H. M. Mbonde, N. Singh, **B. L. Segat Frare**, M. Sinobad, P. T. Ahmadi, B. Hashemi, D. B. Bonneville, P. Mascher, F. X. Kaertner, J. D. B. Bradley, “Octave-spanning supercontinuum generation in a CMOS-compatible thin Si_3N_4 waveguide coated with highly nonlinear TeO_2,” *Optics Letters*, 49, 10 (2024).
- J. D. B. Bradley, **B. L. Segat Frare**, B. Hashemi, P. T. Ahmadi, M. A. Méndez-Rosales, N. Majidian Taleghani, C. M. Naraine, K. Miarabbas Kiani, H. C. Frankis, D. B. Bonneville, J. H. Schmid, P. Cheben, P. R. Selvaganapathy, P. Mascher, A. P. Knights, "Prospects and design considerations for hybrid glass-silicon waveguides," *Proc. SPIE* PC12891, Silicon Photonics XIX, PC1289107 (2024).
- R. Botter, Y. Klaver, R. te Morsche, **B. L. Segat Frare**, B. Hashemi, K. Ye, A. Mishra, R. B.G. Braamhaar, J. D. B. Bradley and D. A. I. Marpaung, “Stimulated Brillouin scattering in tellurite-covered silicon nitride waveguides,” [Preprint] (2023).
- H. M. Mbonde, **B. L. Segat Frare**, T. Wildi, P. T. Ahmadi, B. Hashemi, D. B. Bonneville, T. Herr, J. D. B. Bradley, "Measured anomalous dispersion, Kerr comb, and lasing in hybrid TeO_2-coated Si_3N_4 waveguides," 23rd *International Conference on Transparent Optical Networks,* Bucharest, Romania (2023).
- D. B. Bonneville, M. Albert, R. Arbi, M. Munir, **B. L. Segat Frare**, K. Miarabbas Kiani, H. C. Frankis, A. P. Knights, A. Turak, K. N. Sask, and J. D. B. Bradley, "Hybrid silicon-tellurium-dioxide DBR resonators coated in PMMA for biological sensing," *Biomedical Optics Express* 14, 1545–1561 (2023).
- C. Horvath, J. N. Westwood-Bachman, K. Setzer, A. McKinlay, C. M. Naraine, H. M. Mbonde, **B. L. Segat Frare**, P. T. Ahmadi, P. Mascher, J. D. B. Bradley, M. Aktary, "Prototyping of silicon nitride photonic integrated circuits for visible and near-infrared applications," *Proc. SPIE* 12424, Integrated Optics: Devices, Materials, and Technologies XXVII, 1242404 (2023).
- B. Hashemi, **B. L. Segat Frare**, P. T. Ahmadi, H. C. Frankis, H. M. Mbonde, P. Mascher, and J. D. B. Bradley, “Spiral integrated optical amplifiers on silicon nitride waveguides coated with erbium-doped tellurium dioxide,” presented at *Photonics North*, Montreal, Canada (2023).
- P. T. Ahmadi, Y. Gao, **B. L. Segat Frare**, B. Hashemi, K. Miarabbas Kiani, H. C. Frankis, A. P. Knights, P. Mascher, and J. D. B. Bradley, “Investigation of varying microdisk cavity design for hybrid rare-earth-doped TeO_2-coated Si on-chip lasers,”, poster presented at *Photonics North,* Montreal, Canada (2023).
- H. M. Mbonde, N. Singh, **B. L. Segat Frare**, M. Sinobad, P. T. Ahmadi, B. Hashemi, D. B. Bonneville, F. X. Kärtner, and J. D. B. Bradley, "Octave-spanning supercontinuum generation in a thin Si_3N_4 waveguide coated with highly nonlinear TeO_2," in *Frontiers in Optics + Laser Science* (FIO, LS), paper FW7E.3 (2022).
- J. D. B. Bradley, K. M. Kiani, H. Mbonde, C. Naraine, D. Bonneville, **B. L. Segat Frare**, H. Frankis, A. Knights, "Tellurium oxide active and nonlinear optical devices

integrated on silicon photonics platforms," invited talk at *Photonics North*, Niagara Falls, Canada (2022).

- C. Horvath, J. Westwood-Bachman, K. Setzer, C. Naraine. H. Mbonde, **B. L. Segat Frare**, J. D. B. Bradley, M. Aktary, "Prototyping of silicon nitride photonic integrated circuits using electron beam lithography," invited talk at *Photonics North*, Niagara Falls, Canada (2022).
- N. Singh, M. V. **B. L. Segat Frare**, J. D. B. Bradley, and F. Kaertner, "Large mode area waveguide for silicon photonics and modelocked lasers," poster presented at *CLEO* in San Jose, California, USA (2022).

2. Theoretical Background

This chapter discusses the fundamental theory relevant to this work and is divided into four sections. The first is an introduction to waveguide theory and hybrid waveguides. The second focuses on Bragg grating theory, including uniform gratings and distributed Bragg reflector cavities. Then, the population dynamics of erbium and thulium ions and their gain coefficients are formulated. Lastly, erbium- and thulium-doped-tellurite distributed Bragg reflector laser models are built using the shooting method combined with coupled-mode theory equations.

Electromagnetism is a powerful, fascinating, and beautifully formulated theory of Physics. In a simple set of four equations, Maxwell-Heaviside consolidated an extremely successful mathematical formulation that synthesizes centuries of human knowledge and can help us understand a tremendous variety of natural phenomena. These equations show us: electric charges affect their surroundings through electric fields, there are no magnetic monopoles, electricity and magnetism are connected and how they interact with different materials, an electric field can be generated by a magnetic field varying in time, and electric current or an oscillating electric field can generate magnetic fields. Furthermore, they enable electric power generation and distribution, motors, electronics, data storage, medical imaging, and navigation instruments. And, if all that was not enough, they astonishingly show us that light is an electromagnetic wave, how it propagates, and how it interacts with matter. Finally, they reveal to us that the speed of light is a consequence of the electric permittivity and magnetic permeability of the propagating medium, as well as how light reflects and refracts at interfaces. Therefore, we start this chapter with an ode to the famous Maxwell's Equations:

$$\boldsymbol{\nabla} \cdot \mathbf{E} = \frac{\rho}{\varepsilon}, \tag{2.1}$$

$$\boldsymbol{\nabla} \cdot \mathbf{B} = 0, \tag{2.2}$$

$$\nabla \times \mathbf{E} = -\frac{\partial \mathbf{B}}{\partial t}, \tag{2.3}$$

$$\nabla \times \mathbf{B} = \mu \mathbf{J} + \mu\varepsilon \frac{\partial \mathbf{E}}{\partial t}, \tag{2.4}$$

where ∇ is the nabla operator ("$\boldsymbol{\nabla} \cdot$" and "$\nabla \times$" are the divergent and curl operators, respectively), $\mathbf{E}$ is the electric field, ρ is the electric charge density, ε is the medium electric permittivity ($\varepsilon = \varepsilon_0$ in vacuum), $\mathbf{B}$ is the magnetic flux density (which we will call magnetic field for simplicity), $\frac{\partial}{\partial t}$ is the partial derivative with respect to time, μ is the magnetic permeability of the medium ($\mu = \mu_0$ in vacuum), and $\mathbf{J}$ is the current density.

Equations 2.3 and 2.4 are coupled, first-order, partial differential equations that can be decoupled if we apply the curl operator to them and use the vector calculus identity

$\nabla \times (\nabla \times \mathbf{A}) = \nabla(\nabla \cdot \mathbf{A}) - \nabla^2\mathbf{A}$ of a vector $\mathbf{A}$. A detailed derivation can be found in references [61] and [192]. This set of operations results in the following equations, where ∇^2 is the Laplacian:

$$\nabla^2\mathbf{E} = \mu\varepsilon\frac{\partial^2\mathbf{E}}{\partial t^2}, \tag{2.5}$$

$$\nabla^2\mathbf{B} = \mu\varepsilon\frac{\partial^2\mathbf{B}}{\partial t^2}. \tag{2.6}$$

Equations 2.5 and 2.6 have the format of a three-dimensional wave equation, $\nabla^2\mathbf{A} = \frac{1}{v^2}\frac{\partial^2\mathbf{A}}{\partial t^2}$, in which $v = \frac{1}{\sqrt{\mu\varepsilon}}$ is the velocity with which the wave propagates. In vacuum, the conclusion is amazingly shocking:

$$v = v_0 = \frac{1}{\sqrt{\mu_0\varepsilon_0}} \equiv c, \tag{2.7}$$

the velocity of propagation of an electromagnetic wave is c, the Speed of Light (!). And here is where Electricity, Magnetism, and Optics meet.

Fundamentally, the study of propagation of electromagnetic waves – light – consists of solving these wave equations, either in free space or dielectric media. In the next section, we will briefly explore how we can use equations 2.5 and 2.6 in the context of waveguides and what we can learn from their solutions.

2.1. Integrated Waveguides

A waveguide is a structure capable of confining and routing light, similar to how a copper wire transmits electric current. However, the intrinsic wave-nature of light introduces fundamental differences that prohibit us from going much further in this analogy. As we will see in this section, the necessary condition to confine light is having a medium with a higher refractive index than its surroundings. In the propagation direction, we can make use of ray optics to gain an intuition of how waveguiding can be achieved through total internal reflection. In the transverse direction, looking at the waveguide cross section, we can introduce the concept of optical modes by returning to the wave equations.

2.1.1. Fundamentals

To approach this problem, we will first consider a beam propagating in the z direction within a material stack known as a planar waveguide. By analyzing the beam trajectory using the ray optics approach, we sacrifice some of the mathematical formality, but gain valuable qualitative intuition of how light can propagate in a waveguide. Keep in mind, though, that the same conclusions can be drawn by solving Maxwell's Equations, to which we will soon return when we look at the waveguide cross section in section 2.1.1.2.

2.1.1.1. Total Internal Reflection

Consider the planar (or slab) waveguide structure shown in Figure 2.1. This is the simplest type of waveguide and light is confined in only one dimension, y, while propagating in the z-direction (we assume that the structure is infinite in both the x and z dimensions). Each material layer has a different refractive index, n_i $(i = 1, 2, 3)$, and we wish to confine light in the middle layer, which has a refractive index of $n_1 > n_2, n_3$. Let us first consider cases I and III shown in the picture. When a light beam propagating in the high refractive index layer reaches the interface with the adjacent material at an angle (θ_{12} or θ_{13}), it can be partially reflected with the angle of incidence and partially refracted at a different angle (θ_2 or θ_3). The refracted beam can be described by the Snell-Descartes Law (which can also be derived directly from the wave equation [192]):

$$n_a \sin \varphi_a = n_b \sin \varphi_b, \tag{2.8}$$

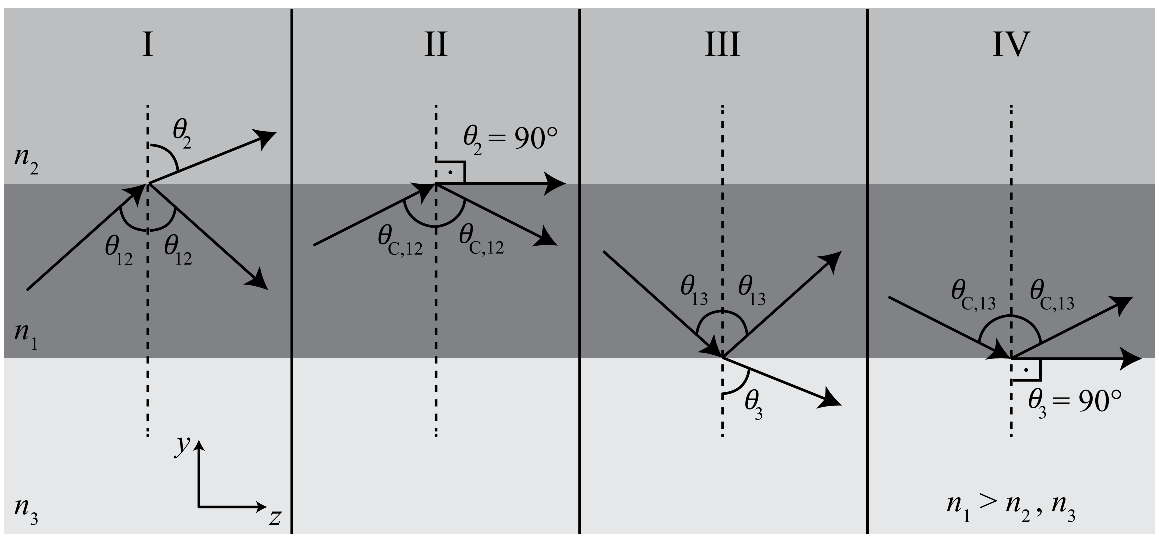

Figure 2.1. Incident beam on a planar waveguide, considering different interface and angle conditions.

where $\varphi_a = 0° < \theta_{12}, \theta_{13} < 90°$ is the angle of incidence of a beam propagating in the medium with high refractive index $n_a = n_1$, and $\varphi_b = 0° < \theta_2, \theta_3 < 90°$ is the angle of refraction in the medium with a lower refractive index $n_b = n_2, n_3$. Since in our example $n_a > n_b$, there is a critical angle $\varphi_C = \theta_{C,12}, \theta_{C,13}$ at which $n_a \sin \varphi_a = n_b$, reaching the maximum value possible on the right-hand side of the equation. At this point, the equation can only be satisfied if $\varphi_b = 90°$ (cases II and IV of Figure 2.1) and any further increase in φ_a will result in an equation that cannot be satisfied. Therefore, for angles $\varphi_C < \varphi_a < 90°$ there cannot be refraction, and the incident beam is completely reflected. Moreover, if the angle of incidence is greater than the critical angles at both interfaces simultaneously ($\theta_{12} > \theta_{C,12}$ and $\theta_{13} > \theta_{C,13}$), the beam propagating in the high index medium will be confined to that layer, forming a waveguide. This phenomenon is called total internal reflection. Note that if $n_1 < n_2, n_3$ there would not exist a critical angle, and it would not be possible to confine the light beam in the middle layer. Consequently, to form a waveguide, it is necessary to build a structure surrounded by lower refractive index media[4]. There are exceptions to this rule such as hollow core fibers, but they are beyond the scope of this thesis.

2.1.1.2. Optical Modes and Effective Index

Now that we have gained valuable intuition from a simple ray optics analysis, we can return to the wave equations and understand what happens in the xy plane, perpendicular to the direction of propagation (z direction). We will focus on the electric field, but the same process can be done for the magnetic field (they are perpendicular). Consider the asymmetric planar waveguide shown in Figure 2.2, with $n_1 = 2$, $n_2 = 1.6$, and $n_3 = 1.4$. The wave equation can be solved analytically through separation of variables, dividing the problem into three regions, each corresponding to a different layer, and using the appropriate electric field boundary conditions. A formal derivation can be found in references [61] and [193]. Here, we will avoid a step-by-step solution and focus on the results, summarized in Figure 2.2. The first thing to note is that we have a group of solutions, indicated by $m = 0, 1, 2, \dots$, which are called optical modes. Next, we see that the mode shapes (electric field amplitude) vary only along the *y*-direction, which is the only finite direction and where we have the varying refractive indices that constitute the waveguide (see left-hand side of Figure 2.2). Along the *x*-direction, the solution is constant, as shown in the cross-sectional mode profile representations on the right-hand side of the figure – this is what you would see if you were to project the waveguide output onto a screen. These mode profiles were simulated considering a 1-µm-thick waveguiding layer and a 1-µm wavelength beam using the finite element method, which we will introduce in section 2.1.1.4.

The shapes of these optical modes resemble solutions to other well-known problems in physics, such as standing waves in a string or a particle in a finite quantum well. This is no coincidence: modes occur when waves – not only electromagnetic, but any kind of wave, including mechanical and *probability* waves – are confined in space establishing a stable spatial distribution that is constant in time.

When propagating in a homogenous medium, the speed of light (phase velocity) is lower than in vacuum and given by c divided by the medium refractive index. In the context of waveguides, an analogous effective refractive index (n_{eff}) can be defined. It depends on the waveguide geometry and refractive indices of the materials used, but also on the optical mode, meaning that different modes will have different phase velocities [194]. The effective index of a mode gives us useful information on how it propagates in the waveguide as if it were propagating in an equivalent homogenous medium [61]. The effective wavelength λ of light propagating in a waveguide can then be written in terms if the wavelength in vacuum (λ_0), $\lambda = \frac{\lambda_0}{n_{\text{eff}}}$. Similarly, an effective group index (n_{g}) can be defined for the group velocity (v_{g}), $v_{\text{g}} = \frac{c}{n_{\text{g}}}$, which is the speed at which information travels in the waveguide [194,195].

[4] The same conclusion can be reached via Maxwell's Equations, but the process is arguably less intuitive.

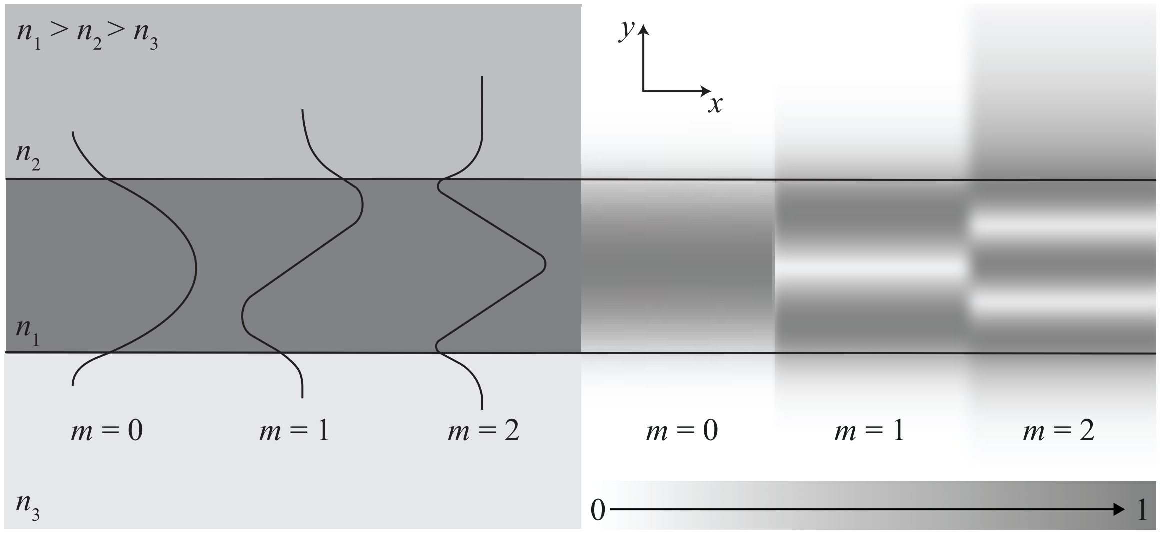

Figure 2.2. Optical modes in an asymmetrical planar waveguide. On the left, a vertical cut shows the electric field profile along the *y*-axis for the first three solutions. On the right, their cross-sectional profiles are shown.

2.1.1.3. Evanescent Field and Confinement Factor

Figure 2.2 also shows us that the optical modes are not completely confined to the waveguiding material: while most of the electric field is inside the middle layer in an oscillatory configuration, part of it penetrates in the adjacent layer following an exponential decay. This lingering component is the **evanescent field**, which can enable light interaction with grating features and coupling between adjacent waveguides running in parallel [193]. It is also used in sensing applications due to the interaction of light with the waveguide surroundings, which can affect the behavior of optical devices [196].

We can then define **confinement factor** Γ as the percentage of power travelling in a layer or feature of a waveguide. Mathematically, it can be defined as [61]:

$$\Gamma = \frac{\iint_{\text{feature}} |\mathbf{E}|^2 dA}{\iint_{\text{all space}} |\mathbf{E}|^2 \, dA}\,, \tag{2.9}$$

where dA is the area element, $dA = dxdy$ in cartesian coordinates.

2.1.1.4. Finite Element Method

So far, we have analyzed a simple planar waveguide, which can be analytically solved using the wave equation. However, when studying more complex geometries such an approach quickly becomes infeasible. As an alternative, numerical methods are powerful and convenient tools to tackle these problems. In this context, mode solvers based on the finite element method (FEM) are popular and are implemented in commercially available software. This method is not limited to optical systems and is widely used to solve multiphysics problems [197].

The basic idea of the FEM is to discretize a complex geometry into a *mesh* formed by small subdomains, that are usually rectangular or triangular in two-dimensional problems. These subdomains (finite elements) can have the same size (uniform mesh) or varying sizes (non-uniform mesh). In general, the finer the mesh, the more accurate the solution, but the higher the computational cost. Figure 2.3 illustrates a rib waveguide structure with three different materials divided into a uniform mesh. Then, the equations that govern the phenomena (Maxwell's equations in this case) of interest are approximated by interpolation functions, often through variational approaches [198]. These functions are solved at each mesh element, maintaining appropriate boundary conditions, to guarantee that the solutions are single-valued (continuous) at the finite element interfaces [199]. The solutions from each element are then combined to output the solution for the entire domain. A typical result obtained using a FEM mode solver is shown in the inset of Figure 2.3.

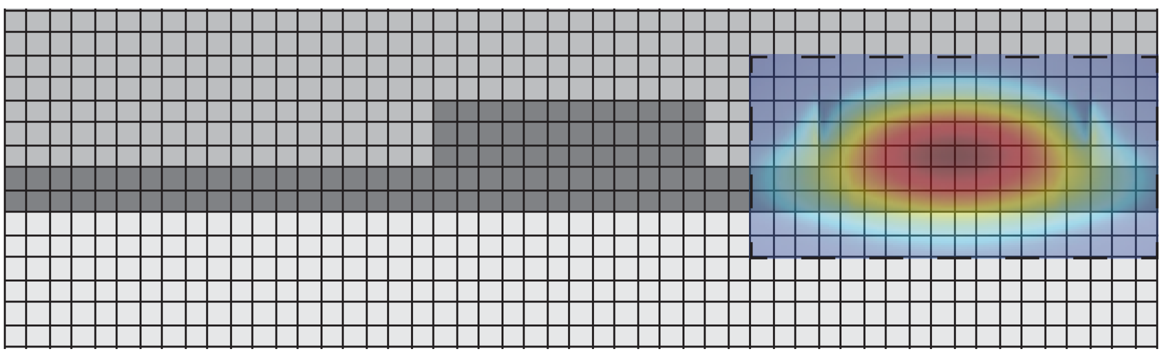

Figure 2.3. Visual representation of a uniform mesh. Inset: example of a fundamental transverse electric field mode profile found using a finite element method solver.

In this thesis, a commercially available FEM mode solver, Synopsys RSoft, was used in the design process to obtain key parameters (electric field mode profile, effective index, and confinement factor) to feed the laser model that will be introduced in Section 2.4.

2.1.2. SILICON-BASED WAVEGUIDES

Several types of waveguide geometries have been explored for different applications [200], and Figure 2.4 illustrates a few examples. A waveguide can be tailored to achieve a certain mode distribution, minimize propagation losses due to mode overlap with rough sidewalls, explore non-linear or acousto-optic phenomena, or even to avoid overlap with the silica underlayer to enable the use of wavelengths beyond its transmission window [200]. Here, we will focus on strip and rib CMOS-compatible waveguides made of silicon or silicon nitride. Strip waveguides consist of a rectangular waveguiding layer, which provides mode confinement in two dimensions. Such an arrangement enables compact waveguides with highly confined modes, tight bend radii, and dense photonic circuits [200]. However, they are sensitive to fabrication variation along the direction of propagation, as well as sidewall roughness, which contributes to an increase in propagation loss [200]. Rib waveguides are similar to strip waveguides, formed by a strip structure on top of a planar (slab) waveguiding layer. They can have reduced mode interaction with the sidewalls, thus typically lower propagation losses [201], and are also advantageous for electro-optic applications, because they have more room for electrical connections to be made directly to the waveguide [195]. A disadvantage of this type of waveguide, is that they usually require larger bend radii, resulting in larger circuit footprints [200].

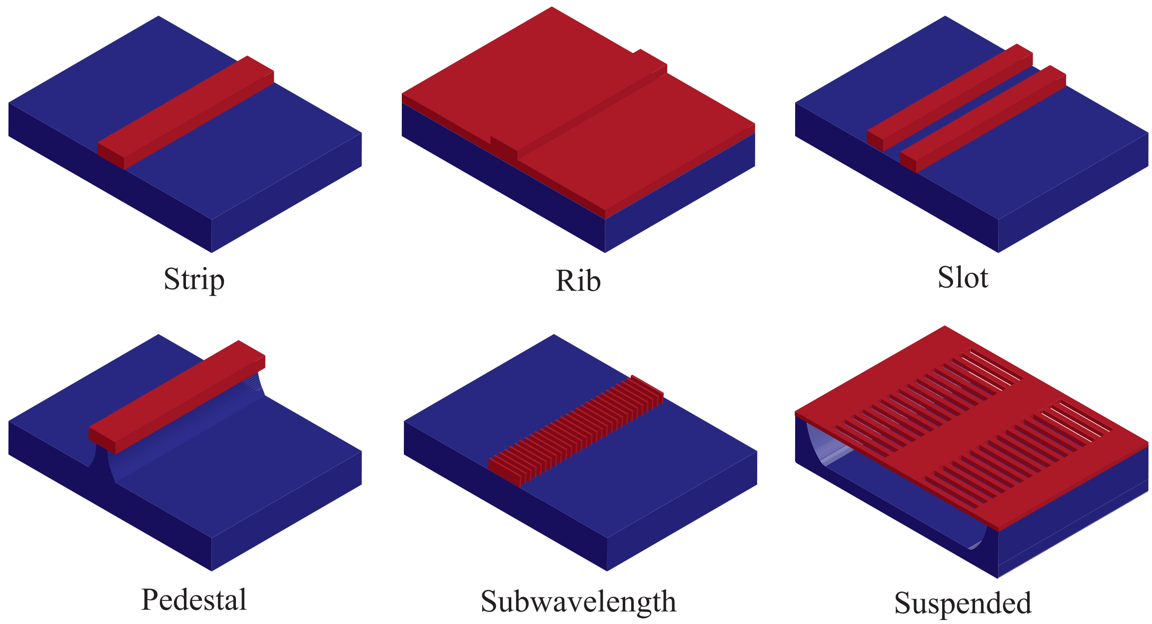

Figure 2.4. Examples of different types of waveguides.

2.1.2.1. Silicon

Silicon's high refractive index ($n_{\mathrm{Si}} = 3.47$ at 1550 nm) provides a large refractive index contrast when surrounded by silica ($n_{\mathrm{SiO_2}} = 1.44$ at 1550 nm), enabling compact and high-confinement ridge waveguides. The typical geometry of an Si waveguide is a 220-nm-thick, 500-nm-wide ridge structure, optimized to guarantee simultaneous single-mode transverse electric (TE) and transverse magnetic (TM) operation [195]. However, the high index contrast also makes these waveguides particularly sensitive to sidewall roughness, especially for narrow waveguides, in which there is high modal overlap with the sidewalls [17,202]. Usually, such waveguides have losses on the order of 1–3 dB/cm, which can drastically increase to more than 30 dB/cm for sidewall root-mean-square roughness of 10 nm [202]. The propagation losses can be reduced to < 0.3 dB/cm by increasing the waveguide width to ~ 2 μm, at the cost of having multimode operation [202].

2.1.2.2. Silicon Nitride

Unlike the silicon-on-insulator platform, the silicon nitride waveguide geometries adopted by foundries and research groups are less standardized. Some commercially available approaches include single- and double-stripe waveguides such as the TriPleX platform [53] and buried waveguides achieved by the Damascene process [203]. On these and other platforms, the waveguide geometry design space has been extensively explored by researchers [37]. In this work, our base-geometry will be a strip waveguide. Strip thicknesses greater than 400 nm typically provide a high mode confinement (≫ 50%) at wavelengths in the C-band, while in thinner silicon nitride layers (< 200 nm) there is low confinement (≲ 50%). The moderate refractive index of Si_3N_4 ($n_{Si_3N_4}$ = 1.99 at 1550 nm) results in bend radii on the order of hundreds of micrometers, which is two orders of magnitude greater than that of the aforementioned Si waveguides. However, ultralow losses (< 0.5 dB/m) have been demonstrated in silicon nitride, and it enables the use of wavelengths below silicon's transparency window in the visible and near-infrared [37].

2.1.3. Hybrid Waveguides

Hybrid waveguides are structures made of two or more materials that form a composite waveguide in which a significant portion of the modes propagates in each material. In this work, hybrid geometries are achieved by monolithically integrating a tellurite layer onto silicon nitride strip structures. Figure 2.5 shows schematics of hybrid silicon and silicon nitride strip waveguides with a 300-nm-thick tellurite coating layer. On one hand, the 220-nm-thick, 500-nm-wide Si waveguide maintains a high mode confinement even though some of the mode (< 15%) overlaps with the tellurite glass. On the other hand, due to the similar refractive index of Si_3N_4 and TeO_2 (n_{TeO_2} = 2.1 at 1550 nm), the mode expands significantly into the tellurite, with which the mode has more than 50% overlap, considering a 200-nm-thick, 1200-nm-wide nitride ridge in this case. Because of the similar indices, it resembles a rib waveguide made purely of TeO_2, but here the Si_3N_4 strip acts as a perturbation to form the thicker core region in the otherwise planar TeO_2 film. These hybrid waveguides allow for us to combine the interesting optical properties of tellurite glass, including nonlinear [204], acousto-optic [70], and active functionalities, to CMOS-compatible platforms [87–90]. Here, we will leverage the excellent rare-earth solubility of TeO_2 to introduce active gain media in low-loss silicon nitride chips. This approach allows for more interaction of light with the gain medium, thus having the potential to achieve higher gain per unit length than in a standard Si platform.

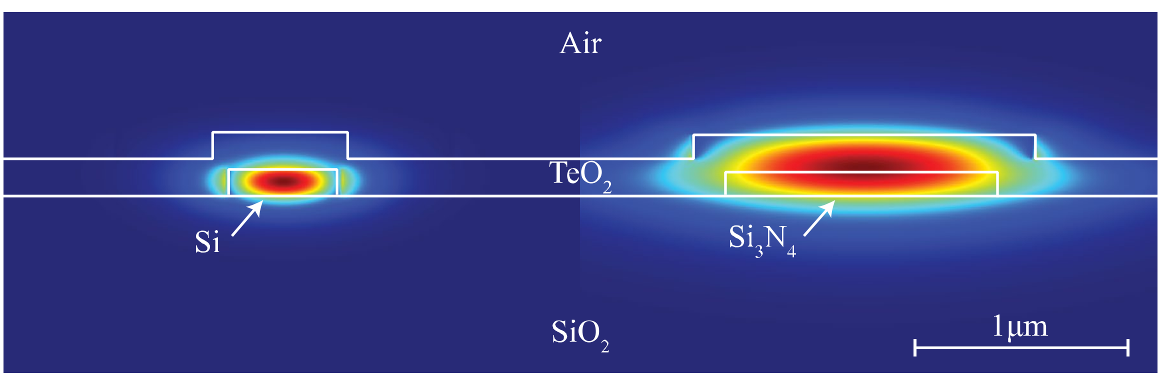

Figure 2.5. Fundamental TE mode profile in hybrid silicon- and silicon nitride-tellurite waveguides at 1550 nm wavelength.

2.2. Waveguide Bragg Gratings

In the previous section, we overviewed fundamental aspects of waveguiding in dielectric media. Now, we take a step further by introducing Bragg gratings, the type of reflectors that will be used to build the optical cavities investigated here. Bragg gratings are periodic perturbations in refractive index along the direction of propagation of light, which act as a one-dimensional diffraction grade that couples light between forward and backward propagating modes. In other words, they are mirrors that reflect specific wavelengths when the grating period Λ satisfies the Bragg condition [193],

$$\Lambda = \frac{m\lambda}{2n_{\mathrm{eff}}}, \tag{2.10}$$

where $m \in \mathbb{N}^*$, λ is the free-space wavelength, and n_{eff} is the effective index of the mode of interest, considering an unperturbed waveguide. The wavelength that satisfies this condition is known as the Bragg wavelength, λ_{B}. In this work, we will focus on first-order gratings ($m = 1$) designed to reflect the fundamental transverse electric (TE) mode.

Figure 2.6 shows the top view of a ridge waveguide with sidewall corrugations as an example of Bragg gratings. The periodic change in refractive index can be produced in several ways, such as by exposing a photosensitive material to an interference pattern using ultraviolet light [205], direct writing using femtosecond laser [206] or physically corrugating the waveguide [207–211]. The latter include corrugations made at a top cladding surface, waveguide sidewall, or through pillars running parallel to the waveguide (which we will refer to as multipiece gratings). In this work, we will investigate the last two types, with a focus on sidewall gratings.

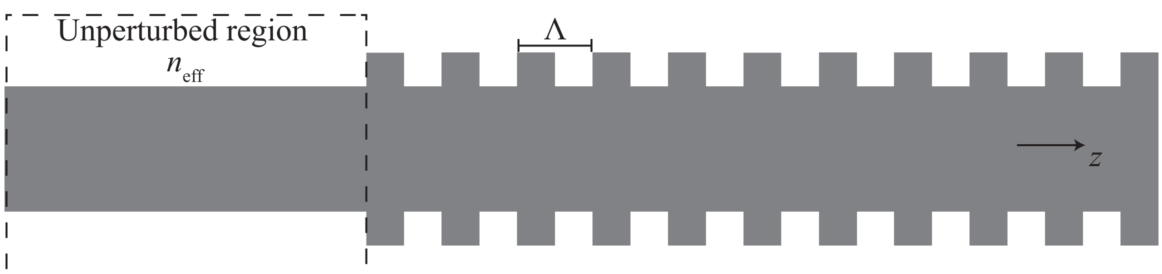

Figure 2.6. Top view of a sidewall-corrugated ridge waveguide.

Each time light passes through a grating feature, it experiences a change in the effective index, which is similar to the normal incidence at an interface between materials with different refractive indices discussed in Section 2.1.1.1. However, the difference in effective index between Bragg grating features is typically very small (which is why they are defined as periodic *perturbations* in refractive index). As a result, only a tiny fraction of light is reflected within one grating period and, as we increase the grating length, we can control how much light is reflected in total. And that is the beauty of it: we can engineer the grating geometry and length to produce mirrors with specific reflectivity at a specific wavelength, while transmitting the other wavelengths. Another reason to *brag* about this type of reflector is that they can be compact and monolithically integrated directly in waveguides, with little impact on the footprint. Since the reflections occur along the grating length (and not at a single plane in space), Bragg mirrors are known as *distributed reflectors*.

We can model and analyze the optical response of Bragg gratings using approaches such as coupled-mode theory and the transfer matrix method. Here, we will first focus on the former because it is intuitive, relatively simple, and can easily be combined with a gain model – which will be carried out in Section 2.4 to build a laser model. In the next section, we will introduce and apply coupled-mode theory to Bragg reflectors. Then we will use coupled-mode theory results to build transfer matrices that describe uniform gratings and distributed Bragg reflector cavities.

2.2.1. Coupled-mode Theory

Coupled-mode theory (CMT) is a useful tool widely used for modeling the behavior of electromagnetic waves [212]. The basic idea of applying it in the context of a Bragg reflector goes back to the concept of treating it as a one-dimensional diffraction grating. Instead of considering light reflection at each grating feature, we will model the grating as an entity that couples light between two contradirectional modes. Let us define two quantities, $A(z)$ and $B(z)$ that are related to the electric field of the forward- and backward-propagating modes, a and b respectively, in a (convenient) way such that the power carried by each mode is given by $|A(z)|^2$ and $|B(z)|^2$. For now, we will consider a lossless and gainless scenario. The theoretical study of Bragg gratings through coupled-mode theory has been performed in detail by Yariv [213–216]. Here, we overview it by highlighting some of the key steps and results.

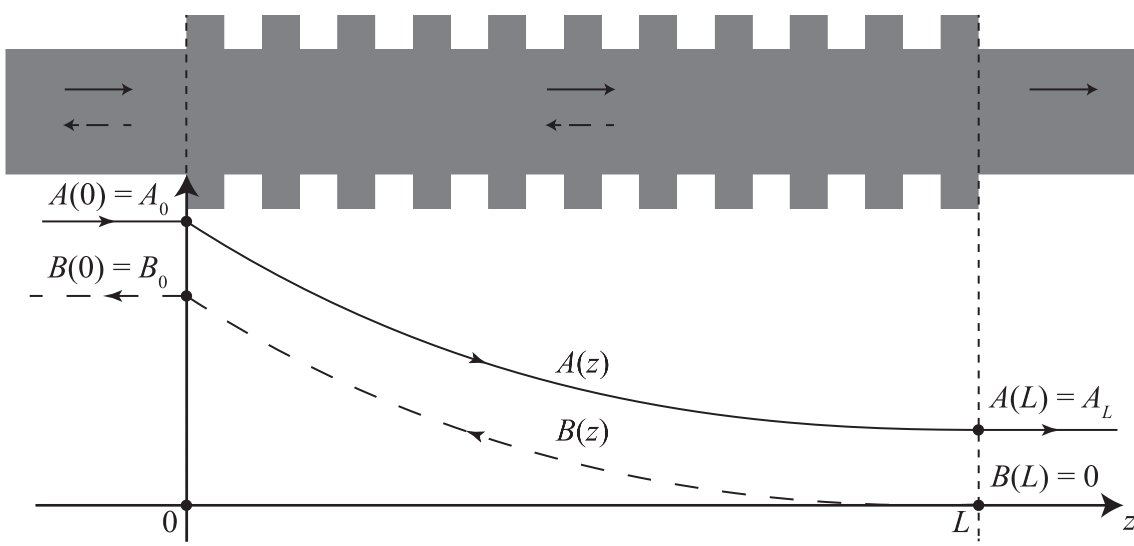

Figure 2.7. Forward- and backward-propagating modes in a lossless sidewall-corrugated waveguide.

Figure 2.7 illustrates the problem we must solve: the incident mode a with magnitude $A(z=0)=A_0$ (where the grating starts) is partially coupled into a backward propagating mode b, reaching the end of the grating with magnitude $A(z=L)=A_L$. The backward-propagating mode is generated solely by the grating response, therefore $B(z=L)=0$, and when it reaches the point $z=0$, it is represented by $B(z=0)=B_0$. Mathematically, we can describe how they vary along the propagation direction through [213]

$$\frac{dA}{dz}=-i\kappa Be^{i2\Delta\beta z}, \tag{2.11}$$

$$\frac{dB}{dz}=i\kappa Ae^{-i2\Delta\beta z}, \tag{2.12}$$

where κ is a coupling coefficient that represents how much power from one mode is transferred to the other in units of m^{-1}, and $\Delta\beta$ is a phase-mismatch constant that represents the deviation from the Bragg condition (β_B) (i.e. how far from the Bragg wavelength a given wavelength is):

$$\Delta\beta\ =\beta-\beta_B=\frac{2\pi n_{\mathrm{eff}}}{\lambda}-\frac{\pi}{\Lambda}. \tag{2.13}$$

For a rectangular surface-corrugated grating, κ can be expressed as [217]:

$$\kappa\ =\frac{\Gamma(n_{\mathrm{h}}^2-n_{\mathrm{l}}^2)}{\lambda_{\mathrm{B}}n_{\mathrm{eff}}}\sin(\pi D), \tag{2.14}$$

where Γ is the confinement factor in the grating features, as defined in Section 2.1.1.3, n_{h} and n_{l} are the higher and lower refractive indices of the alternating materials that make up the grating teeth, and $0<D<1$ is the grating duty cycle, that represents the fraction of the grating period filled with the higher index material. Here, we will use this equation to design both sidewall and multipiece gratings, given their designed rectangular shape, as we will see in more detail in Chapter 3.

The solutions to Equations 2.11 and 2.12 are [213]

$$A(z)=A_0e^{i\Delta\beta z}\frac{\{\Delta\beta\sinh[\xi(z-L)]+i\xi\cosh[\xi(z-L)]\}}{-\Delta\beta\sinh(\xi L)+i\xi\cosh(\xi L)}, \tag{2.15}$$

$$B(z)=i\kappa A_0e^{-i\Delta\beta z}\frac{\sinh[\xi(z-L)]}{-\Delta\beta\sinh(\xi L)+i\xi\cosh(\xi L)}, \tag{2.16}$$

where $\xi\equiv\sqrt{\kappa^2-(\Delta\beta)^2}$. We can now calculate the grating reflectivity (R) and transmissivity (T) from the reflection (r) and transmission (t) coefficients [213,217,218]:

$$R = |r|^2 \equiv \frac{B_0}{A_0} = \left|\frac{-i\kappa\tanh(\xi L)}{-\Delta\beta\tanh(\xi L)+i\xi}\right|^2 = \frac{\kappa^2\tanh^2(\xi L)}{(\Delta\beta)^2\tanh^2(\xi L)+\xi^2}, \tag{2.17}$$

$$T = |t|^2 \equiv \frac{A_L}{A_0} = \left|e^{i\Delta\beta L}\frac{i\xi\,\mathrm{sech}(\xi L)}{-\Delta\beta\tanh(\xi L)+i\xi}\right|^2 = \frac{\xi^2\,\mathrm{sech}^2(\xi L)}{(\Delta\beta)^2\tanh^2(\xi L)+\xi^2}. \tag{2.18}$$

Now, we will analyze how these solutions are affected when we introduce loss and gain components to the grating region. Figure 2.8 illustrates the qualitative behavior of the two modes in this case. For now, we will use an internal net gain factor γ that combines all these contributions, such that $\gamma < 0$ when the sources of loss overcome the gain and $\gamma > 0$ otherwise. Equations 2.11 and 2.12 become [213]

$$\frac{dA}{dz} = -i\kappa B e^{i2\Delta\beta z} + \gamma A, \tag{2.19}$$

$$\frac{dB}{dz} = i\kappa A e^{-i2\Delta\beta z} - \gamma B. \tag{2.20}$$

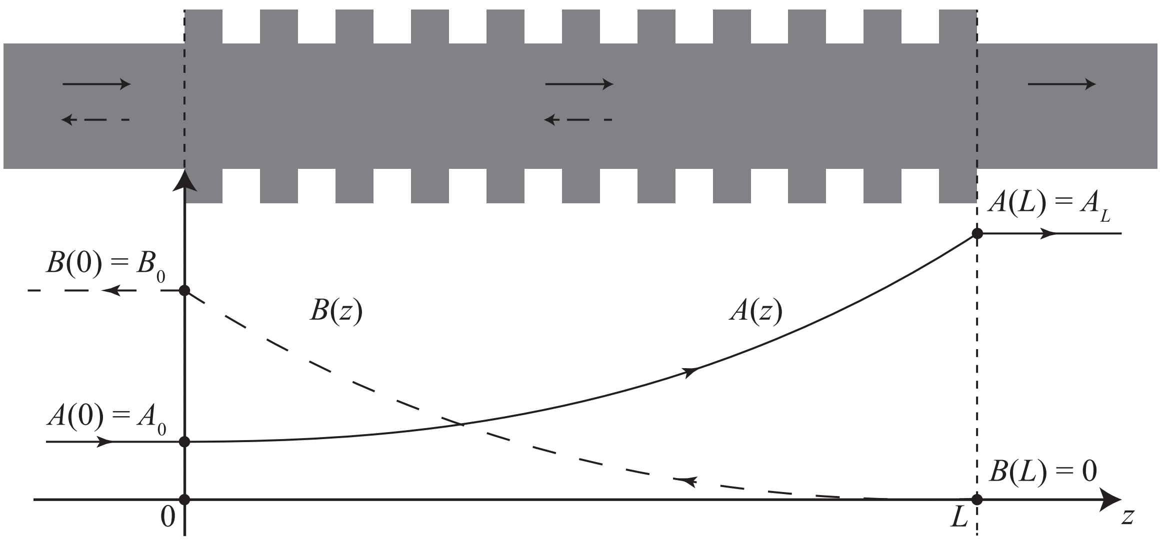

Figure 2.8. Forward- and backward-propagating modes in a sidewall-corrugated waveguide with gain.

In this case, if we remove the grating response by making $\kappa = 0$, then the solutions are simply exponential curves that respectively increase along the $+z$ (A) or $-z$ (B) direction, which is the expected behavior for an unperturbed waveguide. If we make the change of variables [213]

$$A(z) = A'(z)e^{\gamma z}, \tag{2.21}$$

$$B(z) = B'(z)e^{-\gamma z}, \tag{2.22}$$

such that $A(0) = A'(0) = A_0$, Equations 2.19 and 2.20 become

$$\frac{dA'}{dz} = -i\kappa B' e^{i2(\Delta\beta + i\gamma)z}, \tag{2.23}$$

$$\frac{dB'}{dz} = i\kappa A' e^{-i2(\Delta\beta + i\gamma)z}. \tag{2.24}$$

If we now define $\Delta\beta' = \Delta\beta + i\gamma$ and $\xi' = \sqrt{\kappa^2 - (\Delta\beta')^2}$, Equations 2.23 and 2.24 turn out to be equivalent to Equations 2.11 and 2.12 from the lossless case. Therefore, the solutions in terms of the original fields $A(z)$ and $B(z)$ are given by

$$A(z) = A'(z)e^{\gamma z} = A_0 e^{i\Delta\beta z} \frac{\{\Delta\beta' \sinh[\xi'(z-L)] + i\xi' \cosh[\xi'(z-L)]\}}{-\Delta\beta' \sinh(\xi' L) + i\xi' \cosh(\xi' L)}, \tag{2.25}$$

$$B(z) = B'(z)e^{-\gamma z} = i\kappa A_0 e^{-i\Delta\beta z} \frac{\sinh[\xi'(z-L)]}{-\Delta\beta' \sinh(\xi' L) + i\xi' \cosh(\xi' L)}. \tag{2.26}$$

Similarly, the reflectivity and transmissivity are given by

$$R = |r|^2 \equiv \left|\frac{B_0}{A_0}\right|^2 = \left|\frac{-i\kappa \tanh(\xi' L)}{-\Delta\beta' \tanh(\xi' L) + i\xi'}\right|^2 = \frac{\kappa^2 \tanh^2(\xi' L)}{(\Delta\beta')^2 \tanh^2(\xi' L) + {\xi'}^2}, \tag{2.27}$$

$$T = |t|^2 \equiv \left|\frac{A_L}{A_0}\right|^2 = \left|e^{i\Delta\beta L} \frac{i\xi' \operatorname{sech}(\xi' L)}{-\Delta\beta' \tanh(\xi' L) + i\xi'}\right|^2 = \frac{{\xi'}^2 \operatorname{sech}^2(\xi' L)}{(\Delta\beta')^2 \tanh^2(\xi' L) + {\xi'}^2}. \tag{2.28}$$

Of course, if $\gamma = 0$, then $\Delta\beta' = \Delta\beta$ and $\xi' = \xi$, and all these results become the same as the lossless case.

So far, we have considered γ to be constant, i.e., not varying along z. In most real situations this assumption does not hold, i.e. $\gamma = \gamma(z)$, which makes an analytical solution far from trivial. So, we will come back to this in Sections 2.3 and 2.4, where we will discuss laser dynamics and build an iterative method to solve the CMT equations for $\gamma = \gamma(z)$.

2.2.2. The Transfer Matrix Method

The Transfer Matrix Method (TMM) is an important tool in Optics that allows us to study the propagation of light through multiple optical elements by breaking down the contribution of each feature as a linear transformation that can be expressed in a matrix form [219]. This is valid because wave equations such as Equations 2.5 and 2.6 are linear, meaning that any linear combinations of their solutions are also solutions. Please note we will keep using the same symbols defined in the previous section. Consider the forward- and backward-propagating fields $A(z)$ and $B(z)$: we can write linear operators in a matrix form that follows the general expression

$$\begin{bmatrix} A(z) \\ B(z) \end{bmatrix} = \begin{bmatrix} T_{11} & T_{12} \\ T_{21} & T_{22} \end{bmatrix} \begin{bmatrix} A(0) \\ B(0) \end{bmatrix}, \tag{2.29}$$

where the matrix $\boldsymbol{T}$ is called a transfer matrix. For a straight unperturbed waveguide subject to gain and losses, the transfer matrix is given by [217]

$$\boldsymbol{T}_{\mathbf{straight}} = \begin{bmatrix} e^{(-i\beta+\gamma)z} & 0 \\ 0 & e^{(i\beta-\gamma)z} \end{bmatrix}. \tag{2.30}$$

As expected, if we apply $\boldsymbol{T}_{\mathbf{straight}}$ to equation 2.29, we find that $A(z) = A(0)e^{(-i\beta+\gamma)z}$, where the $-i\beta z$ term tells us that it is a forward-propagating wave and γz accounts for the net gain. A similar expression is obtained for $B(z)$. Now, we can use the CMT solutions to build a transfer matrix for a Bragg grating section ($\boldsymbol{T}_{\mathbf{Bragg}}$) [217]

$$\boldsymbol{T}_{\mathbf{Bragg}} = \begin{bmatrix} \cosh(\xi' L) - i\frac{\Delta\beta'}{\xi'}\sinh(\xi' L) & i\frac{\kappa}{\xi'}\sinh(\xi' L) \\ -i\frac{\kappa}{\xi'}\sinh(\xi' L) & \cosh(\xi' L) + i\frac{\Delta\beta'}{\xi'}\sinh(\xi' L) \end{bmatrix}. \tag{2.31}$$

Note that the determinant of both transfer matrices is equal to 1, which means that they are invertible and, consequently we can calculate A and B at any point as long as we know their values in one point in space (not necessarily $z = 0$). If we substitute $\boldsymbol{T}_{\mathbf{Bragg}}$ in Equation 2.29 and use the boundary condition $B(L) = 0$, we get

$$A(L) = T_{11}A(0) + T_{12}B(0), \tag{2.32}$$

$$\cancelto{0}{B(L)} = T_{21}A(0) + T_{22}B(0) \;\Rightarrow\; B(0) = -\frac{T_{21}}{T_{22}}A(0). \tag{2.33}$$

Now, if we calculate the grating reflectivity and transmissivity, we find that

$$R = \left|\frac{B_0}{A_0}\right|^2 = \left|-\frac{T_{21}}{T_{22}}\right|^2 = \frac{\kappa^2\tanh^2(\xi' L)}{(\Delta\beta')^2\tanh^2(\xi' L)+\xi'^2}, \tag{2.34}$$

$$T = \left|\frac{A_L}{A_0}\right|^2 = \left|\frac{T_{11}T_{22}-T_{12}T_{21}}{T_{22}}\right|^2 = \left|\frac{\det(\boldsymbol{T}_{\mathbf{Bragg}})}{T_{22}}\right|^2 = \left|\frac{1}{T_{22}}\right|^2 = \frac{\xi'^2\operatorname{sech}^2(\xi' L)}{(\Delta\beta')^2\tanh^2(\xi' L)+\xi'^2}. \tag{2.35}$$

As expected, these are equivalent to the results we found in 2.27 and 2.28.

Now that we have built transfer matrices for straight waveguides and Bragg gratings, we have a powerful tool that allows for us to calculate the optical behavior of an arbitrary combination of straight and grating sections. We will use it to study the spectral response of distributed Bragg reflector cavities in Section 2.2.4.

2.2.3. Uniform Gratings

The structures we have described in the previous section – Bragg gratings with fixed geometry and length – are known as uniform gratings. Now that we have a robust mathematical formalism to describe them, we can use it to qualitatively analyze the gratings' optical response. To simplify our discussion, we will return to the lossless and gainless scenario, so we can focus solely on the passive response of the distributed Bragg reflectors.

2.2.3.1. Spectral Response

The lossless uniform grating reflection and transmission are given by Equations 2.17 and 2.18. The wavelength dependence is given by the phase-mismatch parameter, $\Delta\beta$, defined by Equation 2.13. Figure 2.9 shows the typical Bragg grating response around the Bragg wavelength. It was generated using the Matlab code available in Appendix I, considering a 5-mm-long uniform grating with Λ = 387 nm, λ_{B} = 1550 nm, n_{eff} = 2, and κ = 643.5 m^{-1}.

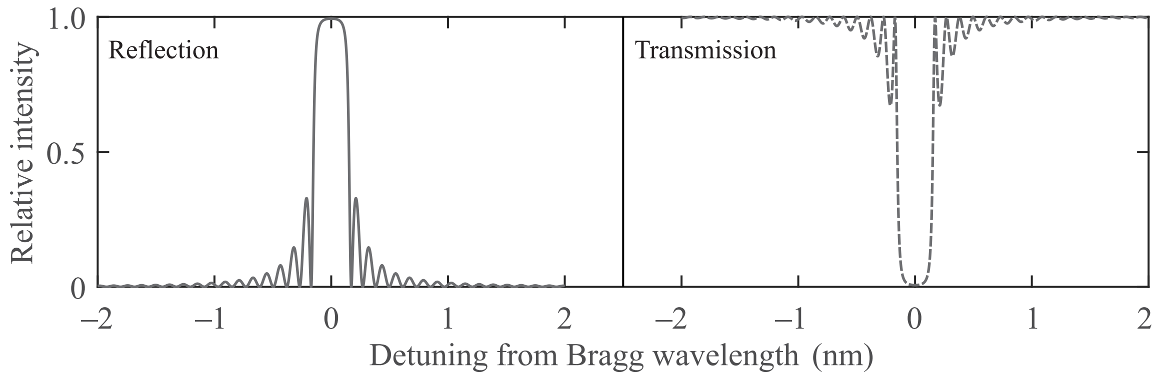

Figure 2.9. Reflection and transmission spectra of a uniform Bragg grating around the Bragg wavelength.

The grating has a strong response at the Bragg wavelength, which quickly decays into sidelobes with decreasing magnitudes on both sides after which it becomes essentially transparent. Being a one-dimensional diffraction grating, the Bragg grating spectral behavior resembles the patterns we see in slit-diffraction experiments [220]. Moreover, since this is a lossless scenario, energy is conserved and $R + T = 1$.

2.2.3.2. Grating Strength and Stopband

Now, let us take a closer look at what happens at the Bragg wavelength, at which the reflection is maximum. Here, the phase-mismatch $\Delta\beta$ is zero and $\xi = \kappa$, meaning that the reflectivity and transmissivity from Equations 2.17 and 2.18 can be rewritten as

$$R(\lambda = \lambda_{\mathrm{B}}) = \tanh^2(\kappa L), \tag{2.36}$$

$$T(\lambda = \lambda_{\mathrm{B}}) = \mathrm{sech}^2(\kappa L). \tag{2.37}$$

From now on in this thesis, the expression grating reflectivity will refer to the definition from Equation 2.36, i.e., the peak value. This value is a function of the coupling coefficient and the grating length. However, keep in mind that $\kappa = \kappa(\Gamma, n_{\mathrm{h}}, n_{\mathrm{l}}, \lambda_{\mathrm{B}}, n_{\mathrm{eff}}, D)$ as per the definition from Equation 2.14. We can then define the **grating strength** as the product κL. Figure 2.10a shows the spectral response of gratings with fixed coupling coefficient and increasing lengths, generated using the same code from Appendix I. The width of the central peak is known as the grating stopband ($\Delta\lambda_{\text{stopband}}$) and, for strong gratings and considering that the effective index is constant around the Bragg wavelength, it is given by [217,218]

$$\Delta\lambda_{\text{stopband}} = \frac{\kappa\lambda_B^2}{\pi n_{\text{eff}}}. \tag{2.38}$$

Its dependence on κ (but not L) explains why, in Figure 2.10a, the stronger gratings have similar stopbands: for a fixed κ, increasing the length primarily affects the grating peak reflectivity, but not its bandwidth. Note how in Figure 2.10b, where the grating length is kept constant and the coupling coefficient is varied, the grating stopband follows the trend given by Equation 2.38, even though the peak reflectivity is still determined by the grating strength, κL.

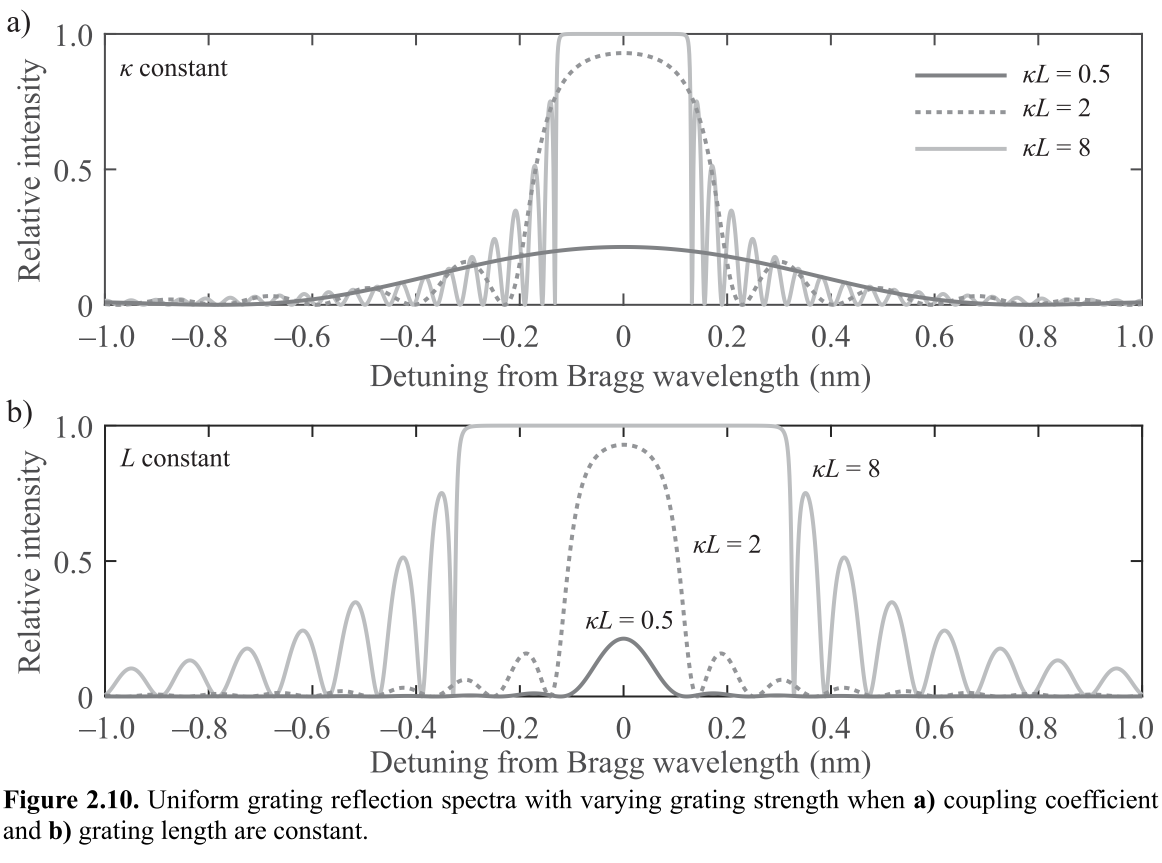

Figure 2.10. Uniform grating reflection spectra with varying grating strength when **a)** coupling coefficient and **b)** grating length are constant.

2.2.4. DISTRIBUTED BRAGG REFLECTOR CAVITIES

We can combine two sets of Bragg gratings to make a distributed Bragg reflector (DBR) cavity, much like a Fabry-Pérot cavity consisting of two mirrors facing each other. Figure 2.11 depicts a DBR cavity formed by input and output sets of gratings separated by a gap, with lengths L_{in}, L_{out}, and L_{gap}, respectively. The effect of each of these sections on light propagating across the cavity is given by their respective transfer matrices, as indicated in Figure 2.11.

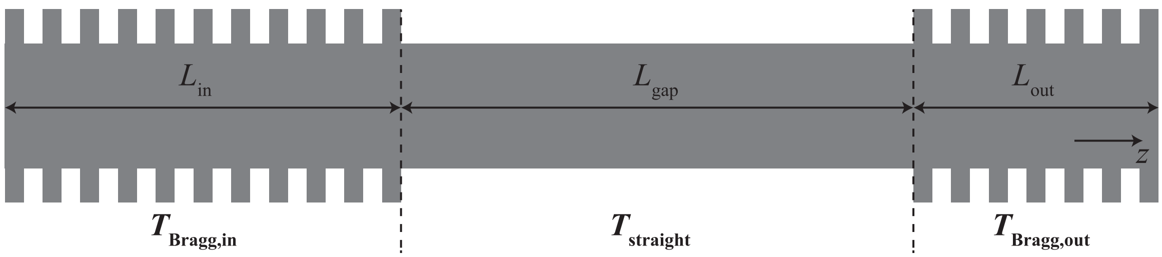

Figure 2.11. A distributed Bragg reflector cavity and the transfer matrices that describe each of its sections.

In principle, each grating can have a different design and the formalism we have built so far is robust enough to account for this. In this work, we investigate cavities formed by two sets of gratings with identical geometry, but we allow them to have different lengths. That is the premise we will follow to analyze their optical properties. According to the transfer matrix method, the optical response of a DBR cavity ($\boldsymbol{T}_{\textbf{DBR}}$) is given by the product of each section's matrix, in the reverse order that they occur (successive linear transformations to the original beam):

$$\begin{bmatrix} A(z) \\ B(z) \end{bmatrix} = \boldsymbol{T}_{\textbf{Bragg,out}} \boldsymbol{T}_{\textbf{straight}} \boldsymbol{T}_{\textbf{Bragg,in}} \begin{bmatrix} A(0) \\ B(0) \end{bmatrix} \equiv \boldsymbol{T}_{\textbf{DBR}} \begin{bmatrix} A(0) \\ B(0) \end{bmatrix}, \tag{2.39}$$

where $\boldsymbol{T}_{\textbf{straight}}$ and $\boldsymbol{T}_{\textbf{Bragg}}$ are the transfer matrices given by Equations 2.30 and 2.31, respectively. To calculate the product $\boldsymbol{T}_{\textbf{Bragg,out}} \boldsymbol{T}_{\textbf{straight}} \boldsymbol{T}_{\textbf{Bragg,in}}$ by hand is obviously a tedious process and the result does not hold an aesthetic appeal. Thankfully, this can be calculated numerically, and I provide, in Appendix I, a Matlab code that performs these calculations (feel free to use it!).

2.2.4.1. Spectral Response

Figure 2.12 shows the optical transmission of several (lossless) DBR cavities, with fixed L_{gap} = 3 mm and κ = 321.8 m^{-1}, but different combinations of input and output grating lengths. When both sets of gratings are identical, we have symmetric cavities (see Figure 2.12 a, b, c). When they have different strengths, we have asymmetric cavities (see Figure 2.12 d, e, f).

In Chapter 3, we will focus on studying the passive behavior of symmetric cavities because, as we will see, they can help us extract useful empirical data regarding the grating performance. However, in Chapters 4 and 5, we will shift our attention to asymmetric cavities, since, in the context of lasers, they can promote directionality in the laser output (through the weaker set of gratings), a desired feature in most cases to efficiently harvest the laser emission.

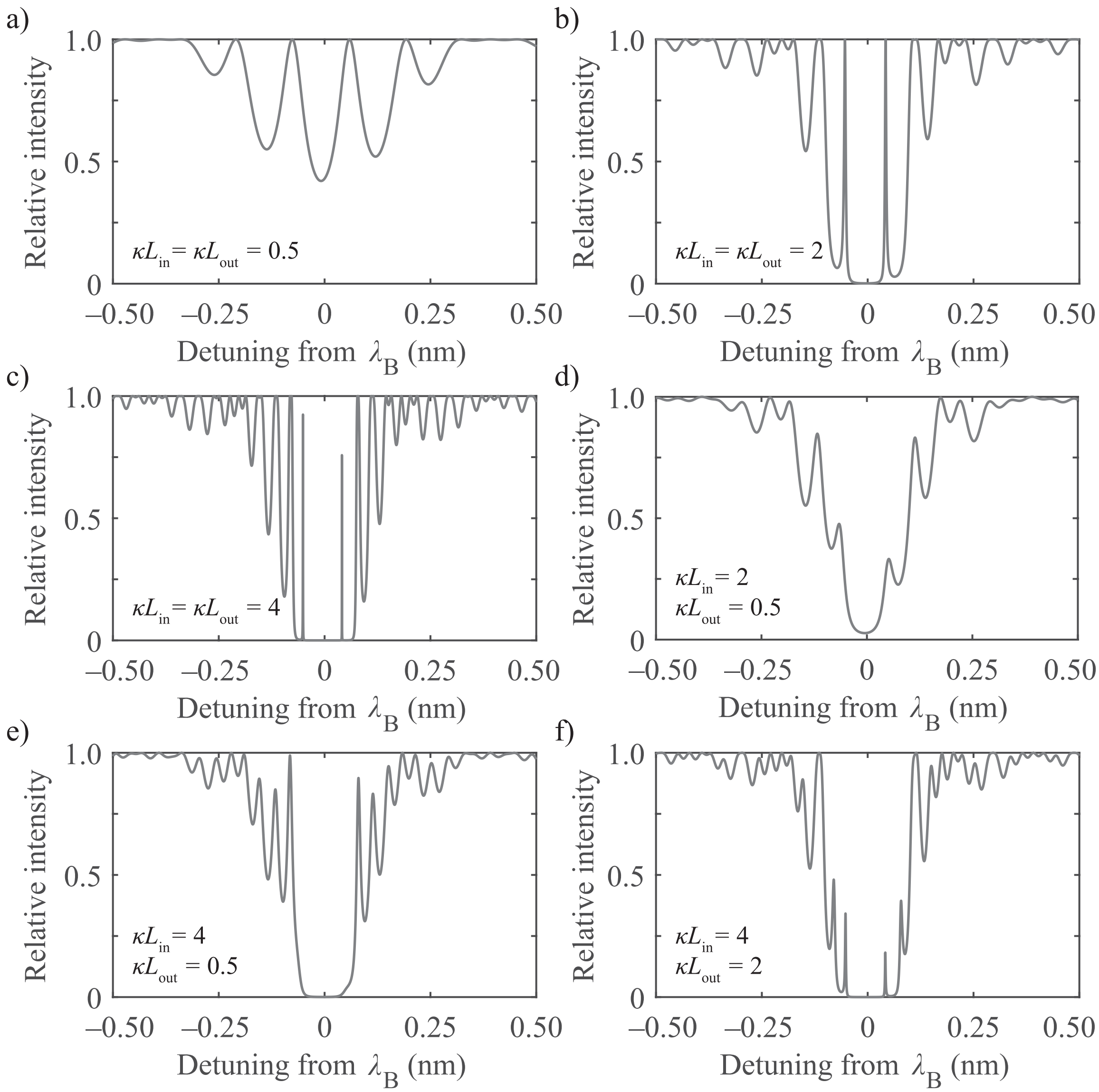

Figure 2.12. a, b, c) Symmetric and **d, e, f)** asymmetric DBR cavity transmission spectra for various grating strength combinations.

2.2.4.2. Penetration and Effective Length

I have mentioned earlier that a DBR cavity resembles a Fabry-Pérot cavity. Consider again Figure 2.11: if we were the replace the two sets of gratings with dielectric mirrors at the dotted lines, then the cavity length would be simply L_{gap}. However, given the distributed reflection nature of Bragg gratings, light trapped in the cavity *penetrates* a non-negligible length into the grating regions. When the refractive index contrast between the two alternating materials that make up the gratings is low, this penetration length L_{pen} can be expressed in terms of the grating length (L_{grating}) as [218,221]

$$L_{\text{pen}} = \frac{\tanh(\kappa L_{\text{grating}})}{2\kappa}, \tag{2.40}$$

and we can define an effective cavity length L_{eff}

$$L_{\text{eff}} = L_{\text{gap}} + L_{\text{pen,in}} + L_{\text{pen,out}}, \tag{2.41}$$

where $L_{\text{pen,in}}$ and $L_{\text{pen,out}}$ are the penetration lengths of the input and output gratings, respectively. Naturally, for a symmetric DBR cavity, $L_{\text{pen,in}} = L_{\text{pen,out}}$ and the expression becomes $L_{\text{eff}} = L_{\text{gap}} + 2L_{\text{pen}}$. As an example, the penetration lengths for the three symmetric cavities shown in Figure 2.12 (a, b, c) are approximately 0.72, 1.5, and 1.55 mm, respectively. These are on the same order of magnitude as our fixed L_{gap} = 3 mm.

2.2.4.3. Free Spectral Range, Finesse, and Quality Factor

Consider the symmetric cavity shown in Figure 2.12b, where $\kappa L = 2$ and L_{gap} = 3 mm. In that case, there are two resonances within the grating stopband, which are due to different longitudinal modes across the cavity. Figure 2.13 illustrates how the cavity spectrum is affected as we vary L_{gap}. There is only one resonance (single longitudinal mode) when L_{gap} = 1 mm, while multiple periodic resonances (multiple longitudinal modes) are observed for L_{gap} = 20 mm. The distance between each resonance ($\Delta\lambda_{\text{FSR}}$) is defined as the cavity's free spectral range (FSR), which is given by [218,222]

$$\Delta\lambda_{\text{FSR}} \equiv \frac{2\pi}{L_{\text{roundtrip}}} \left| \left(\frac{\partial \beta}{\partial \lambda}\right)^{-1} \right| = \frac{\lambda_B^2}{2 n_{\text{eff}} L_{\text{eff}}}, \tag{2.42}$$

where $L_{\text{roundtrip}}$ is the cavity roundtrip length and β is the propagation constant defined in Equation 2.13. Single longitudinal mode operation can then be achieved when the FSR is greater than the grating stopband ($\Delta\lambda_{\text{FSR}} > \Delta\lambda_{\text{stopband}}$), which happens when

$$L_{\text{gap}} < \frac{\pi}{2\kappa} - L_{\text{pen,in}} - L_{\text{pen,out}} = \frac{\pi - \tanh(\kappa L_{\text{in}}) - \tanh(\kappa L_{\text{out}})}{2\kappa}. \tag{2.43}$$

In many laser applications, it is desired to have single mode operation. However, this requires extremely short DBR cavities, which are usually not sufficient to achieve enough gain in the context of rare-earth lasers. To overcome this, distributed feedback cavities (DFB) are often used to realize single mode lasers [218].

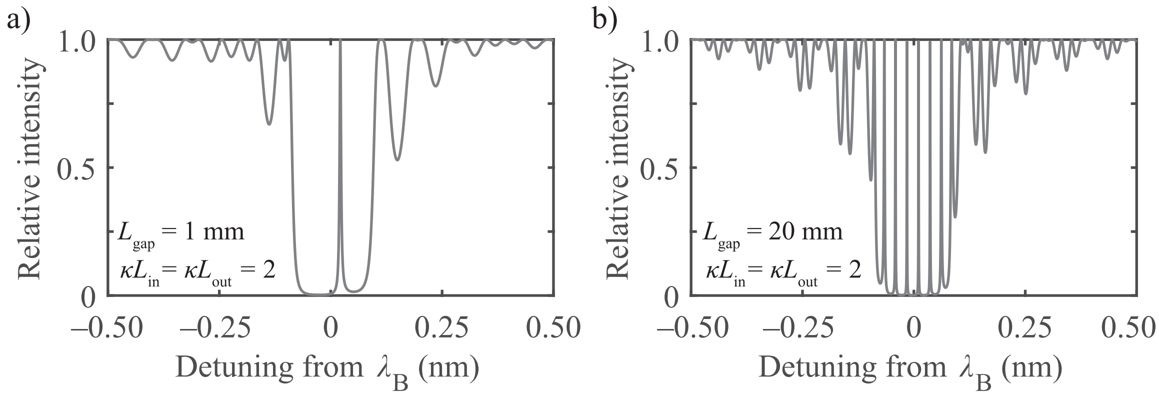

Figure 2.13. DBR cavity response for different cavity lengths, exhibiting **a)** one or **b)** multiple longitudinal modes, when the free spectral range is larger or smaller than the grating stopband, respectively.

We can define finesse (F) to express how sharp the longitudinal mode resonances are in relation to the FSR:

$$F \equiv \frac{\Delta\lambda_{\mathrm{FSR}}}{\Delta\lambda_{\mathrm{FWHM}}}, \tag{2.44}$$

with $\Delta\lambda_{\mathrm{FWHM}}$ being the resonance's full width at half maximum (FWHM), which we will consider to be the –3 dB width. For a symmetric DBR cavity, we can also approximate it as the finesse of a symmetric Fabry-Pérot cavity, in terms of the cavity effective length, total propagation loss coefficient (α_{T}), and mirrors/gratings reflectivity [218,223]:

$$F = \frac{\pi e^{-\frac{\rho L_{\mathrm{eff}}}{2}}}{1-e^{-\rho L_{\mathrm{eff}}}}, \tag{2.45}$$

where $\rho = \alpha_{\mathrm{T}} - \frac{1}{L_{\mathrm{eff}}}\ln(R)$.

Similarly to how the finesse expresses resonance sharpness in relation to the FSR, we can define the quality factor (Q), which serves as a measure of how sharp the longitudinal mode resonances are in relation to the peak wavelength (λ_{peak})

$$Q \equiv \frac{\lambda_{\mathrm{peak}}}{\Delta\lambda_{\mathrm{FWHM}}} = \frac{\lambda_{\mathrm{peak}}F}{\Delta\lambda_{\mathrm{FSR}}}. \tag{2.46}$$

The Q-factor is related to the losses within the cavity (propagation losses, reflectors' transmission) and, for high-Q cavities, it also represents the amount of energy stored inside them [218].

2.2.4.4. Grating-induced Losses

In Section 2.1.2, we briefly discussed how the waveguide propagation losses can be significantly impacted by sidewall roughness. Since Bragg gratings are essentially perturbations in the waveguide cross section along the direction of propagation, it comes as no surprise that they can introduce additional losses in relation to an unperturbed waveguide. In the previous section, we introduced the total propagation loss coefficient, α_{T}, which accounts for all the sources of losses within the cavity. For a passive cavity, i.e., with no rare-earth absorption, we can break down the total losses into two main contributions: the waveguide background loss α_{BG}, which is the unperturbed waveguide propagation loss, and the grating-induced loss, $\alpha_{\mathrm{grating}}$. Therefore, we can express the loss contributions within a symmetric cavity as

$$L_{\mathrm{eff}}\alpha_{\mathrm{T}} = L_{\mathrm{eff}}\alpha_{\mathrm{BG}} + 2L_{\mathrm{pen}}\alpha_{\mathrm{grating}}. \tag{2.47}$$

The grating losses are then given by

$$\alpha_{\mathrm{grating}} = \frac{L_{\mathrm{eff}}}{2L_{\mathrm{pen}}}(\alpha_{\mathrm{T}} - \alpha_{\mathrm{BG}}). \tag{2.48}$$

Using, again, the analogy with a symmetric Fabry-Pérot cavity, we can find a relationship between losses, reflectivity, and finesse [218,224]

$$\ln\left(\frac{\cos\left(\frac{\pi}{F}\right)}{1-\sin\left(\frac{\pi}{F}\right)}\right) = L_{\mathrm{eff}}\alpha_{\mathrm{T}} - \ln(R). \tag{2.49}$$

This relationship gives us a method to calculate grating losses and reflectivity: if we measure symmetric cavities with the exact same sets of gratings, but varying gap lengths, we can measure finesse as a function of effective length (calculated using Equation 2.42). Then a simple linear fit can give us α_{T} (slope) and the grating reflectivity (y-intercept). The unperturbed waveguide background loss can usually be extracted from cutback or microring resonator Q-factor measurements [225,226], making it easy to obtain the grating losses from α_{T}. Once we calculate $\alpha_{\mathrm{grating}}$ for a given grating design, we can use Equation 2.49 to calculate their reflectivity as a function of grating length by measuring the finesse of symmetric cavities with varying grating lengths. This is the key idea behind the method used in Chapter 3 to investigate grating properties.

2.3. LASER DYNAMICS

So far, we have focused on waveguide and distributed Bragg reflector cavity theory. Now, we will discuss the last component required to achieve a laser: the gain medium. In particular, we will dive into light-matter interaction phenomena and analyze different light absorption and emission processes that contribute to enabling a rare-earth active gain medium. In other words, to quantify light emission we must understand the electron population dynamics in the active medium, which is determined by its allowed energy levels and pump and emitted light characteristics.

An incident pump photon with energy equal to the gap between two energy levels, E_1 and E_2, can excite an electron from the lower to the higher energy state, as indicated in

Figure 2.14. This process is known as **absorption** and the rate at which it occurs depends on three parameters: the number of incident photons per unit time, the probability of a photon being absorbed, promoting an electron to an excited state, and the electron population in the lower energy level. The former can be calculated by dividing the incident power (P_{in}, in units of W = J·s^{-1}) by the energy of a single photon (given by $E_{\text{photon}} = h\nu_{\text{photon}}$, where $h \sim 6.626 \cdot 10^{-34}$ J·s is the Planck constant and ν_{photon} is the photon frequency in units of s^{-1}). The probability of a photon being absorbed is given by the material's absorption cross section at the incident photon wavelength, $\sigma_{\text{abs,in}}$ (in units of m^2), while the electron population of each energy level is given by $N_i, i \in \mathbb{N}$. In this case, the rate at which the population of each level varies over time can be expressed as

$$\frac{dN_2}{dt} = \frac{P_{\text{in}}}{h\nu_{\text{photon,in}},}\sigma_{\text{abs,in}}N_1 = -\frac{dN_1}{dt}. \tag{2.50}$$

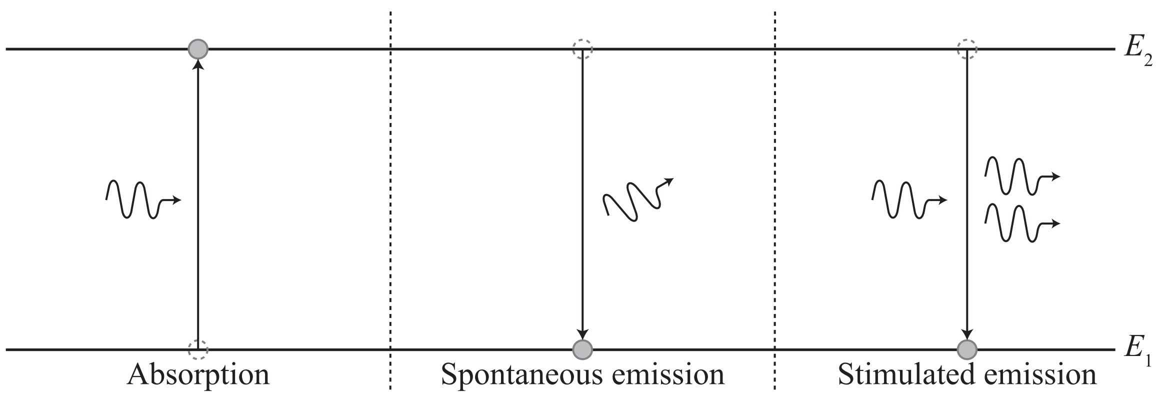

Figure 2.14. Diagram illustrating absorption, spontaneous emission, and stimulated emission transitions in a two-level system.

Usually, the excited state is metastable, meaning that, if we wait long enough, an excited electron will tend to decay back to its original energy state, emitting a photon with the same energy as the energy difference between the two levels, in a process called **spontaneous emission**. Here, the photon has random polarization, phase, and direction. We define the **lifetime** of an energy level i, τ_i, as a time constant of an exponential decay proportional to e^{-t/τ_i}, such that at the time $t = \tau_i$ the excited-state population decayed to an e^{-1} ratio to the starting population. Mathematically, we can describe this process as

$$\frac{dN_2}{dt} = -\frac{1}{\tau_2}N_2 = -\frac{dN_1}{dt}. \tag{2.51}$$

However, if an electron in an excited state (for example, after absorbing a photon but before spontaneously decaying) interacts with a new incident photon, **stimulated emission** can happen. In this case, the excited electron will also decay to the lower energy level, but will emit a photon identical to the incident photon (same energy, polarization, phase, and direction) [227]. Mathematically, it can be described similarly to absorption, but using an emission cross section $\sigma_{\mathrm{em,in}}$ instead

$$\frac{dN_2}{dt} = -\frac{P_{\mathrm{in}}}{h\nu_{\mathrm{photon,in}}}, \sigma_{\mathrm{em,in}} N_2 = -\frac{dN_1}{dt}. \tag{2.52}$$

These three processes form the basis for the study of population dynamics. However, as we will soon discuss, these are not the only phenomena involved in real scenarios. To enable continuous-wave (CW) lasers, we need to make stimulated emission more likely to happen than spontaneous emission when the system reaches a steady-state equilibrium $\left(\frac{dN_1}{dt} = \frac{dN_2}{dt} = 0\right)$, promoting a chain reaction. This is attained when we achieve **population inversion**, meaning that there are more electrons in the excited state than in the lower-energy state. An intuitive way to think about it is to consider the case where all the electrons are initially at the energy level E_1. When incident photons interact with them, absorption is the most likely process to occur. This will happen until $N_2 = N_1$ and, at that point, each photon will have a 50% chance of being absorbed or decay through stimulated emission (if τ_2 is long enough and there are sufficient incident photons) and the populations N_1 and N_2 will remain effectively constant and no significant light emission will be observed. This means we cannot achieve population inversion with two-level systems. In fact, materials usually exhibit intricate, multi-level energy structures and additional radiative and non-radiative processes play important roles in the population dynamics. Usually, lasers are modeled using simplified three- or four-level systems. Before we proceed, let us introduce a few other processes, shown in Figure 2.15, that can happen in a multi-level system and that will be relevant when we analyze the population dynamics of Er^{3+} and Tm^{3+} ions.

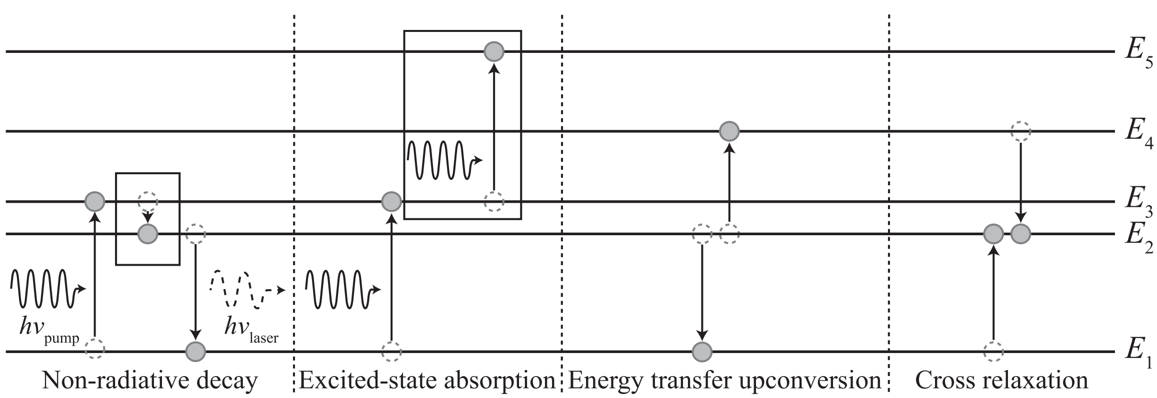

Figure 2.15. Diagram of some transitions that can occur in a multi-level system. Note that in the non-radiative decay example, a later radiative transition can occur, emitting a photon that has lower energy (and thus longer wavelength) than the incident photon.

Electrons in an excited state can decay to a lower energy level through **non-radiative** decay, i.e., without emitting a photon, such as in the case where a phonon is emitted instead. These processes are usually fast compared to the lifetime of the transition of interest for light emission (radiative lifetime), so we can often consider that the population of the higher energy level is constantly equal to zero and that the electrons are effectively transferred directly to the level with longer lifetime (in Figure 2.15, that means that the transition $E_1 \rightarrow E_3$ is effectively $E_1 \rightarrow E_2$). Note that in this three-level scenario it is possible to achieve population inversion: an incident pump photon with energy $h\nu_{\text{pump}} = E_3 - E_1$ has always a higher probability of being absorbed rather than promoting emission (E_3 is always "empty", while E_1 is populated), so the pump photon can always contribute to increasing the population of E_2; at the same time, if there are enough pump photons and the lifetime τ_2 is long enough, it is possible to have $N_2 > N_1$, which means that an emitted photon with energy $h\nu_{\text{laser}} = E_2 - E_1$ can have a higher probability of stimulating the $E_2 \rightarrow E_1$emission than the $E_1 \rightarrow E_2$ absorption in a neighbour active medium ion. This can trigger a chain reaction that generates highly coherent Light Amplification by Stimulated Emission of Radiation – LASER – across the gain medium, since photons emitted by stimulated emission are identical.

An excited ion can also undergo an **excited-state absorption** (ESA) transition, when an excited electron absorbs a photon, shifting to a higher energy level, as illustrated by Figure 2.15. Moreover, two neighbouring excited ions can exchange energy, resulting in one of them transitioning to a higher energy level, while the other decays to a lower energy level. This non-radiative transition is called **energy transfer upconversion** (ETU) and is highly dependent on the distance between the ions [228]. It is particularly relevant in applications where high rare-earth concentrations are used, such as in this work. Since this process requires two interacting ions, the rate at which it occurs is proportional to N_i^2, the population of the energy level E_i that originates the transition. Using the diagram of Figure 2.15, we can express the ETU contribution to the population dynamics as

$$\frac{dN_1}{dt} = -W_{\text{ETU}} N_2^2 = \frac{dN_4}{dt}, \tag{2.53}$$

$$\frac{dN_2}{dt} = -2W_{\text{ETU}} N_2^2, \tag{2.54}$$

where W_{ETU} is a parameter dependent on the host material and rare-earth concentration, which is expressed in units of $\text{m}^{-3}\text{s}^{-1}$ and represents the probability of upconversion to happen [218,228]. Note that, in each transition, the starting energy level loses two electrons, while the other two levels gain one each. Similarly, a reverse energy transfer upconversion (RETU) transition, also known as **cross relaxation** mechanism, can take place, in which energy is non-radiatively transferred between electrons in different energy levels that transition to an intermediary energy level. This process is particularly relevant in thulium-doped systems, where it is possible to pump electrons with 793-nm light from the ground state to a high energy level that then undergo RETU and produce two electrons in an energy level of interest for light emission. In this case, a single pump photon can promote two electrons to the energy level relevant to lasing, yielding a quantum efficiency of 200% [229]. Using the diagram from Figure 2.15, we can express RETU as

$$\frac{dN_1}{dt} = -W_{\text{RETU}} N_1 N_4 = \frac{dN_4}{dt}, \tag{2.55}$$

$$\frac{dN_2}{dt} = 2W_{\mathrm{RETU}}N_1N_4, \tag{2.56}$$

where W_{RETU} is also a material-dependent RETU parameter. When both ETU and RETU are relevant to the population dynamics, we can define a cross relaxation coefficient $C_{\mathrm{R}} = W_{\mathrm{RETU}}N_1N_4 - W_{\mathrm{ETU}}N_2^2$ that combines their effects [229].

Now that we introduced some of the processes that can contribute to the population dynamics and how they can be expressed mathematically, we can write *rate equations* that take into account the most relevant transitions for a given rare-earth-ion and allow us to understand the laser dynamics. We will apply these concepts to Er^{3+} and Tm^{3+} ions in Sections 2.3.1 and 2.3.2.

I briefly mentioned earlier that, for continuous-wave lasers, we are usually interested in the system's *steady-state* equilibrium. After we build the appropriate rate equations for a gain medium, we can solve them when $\frac{dN_i}{dt} = 0$ and using the fact that the total number of ions (N_{T}) should be conserved, $N_{\mathrm{T}} = \sum_i N_i$. For now, let us consider that we are interested in making a laser out of a transition $E_2 \rightarrow E_1$ (it can be, for instance, the three-level system used to explain non-radiative decay). Assume that we solved the rate equations and found an expression that represents the steady-state solutions N_1 and N_2. We can then define the gain (g) and absorption (α) coefficients, in units of m^{-1}, as follows [218]:

$$g = \sigma_{\mathrm{em,laser}}N_2 - \sigma_{\mathrm{abs,laser}}N_1 - \alpha_{\mathrm{BG,laser}}, \tag{2.57}$$

$$\alpha = \sigma_{\mathrm{em,pump}}N_2 - \sigma_{\mathrm{abs,pump}}N_1 - \alpha_{\mathrm{BG,pump}}, \tag{2.58}$$

where $\sigma_{\mathrm{em,laser}}$, $\sigma_{\mathrm{em,pump}}$ and $\sigma_{\mathrm{abs,laser}}$, $\sigma_{\mathrm{abs,pump}}$ are the emission and absorption cross sections at the laser emission and pump wavelengths, and $\alpha_{\mathrm{BG,laser}}$, $\alpha_{\mathrm{BG,pump}}$ are the background loss at each wavelength. Similarly to how we introduced coupled-mode theory in Section 2.2.1, we are assuming that N_1 and N_2 and, therefore, g and α, are constant. However, Equations 2.50 and 2.52 make it clear that both photon absorption and stimulated emission depend on the incident pump/laser powers, which, in reality, vary greatly as they propagate in a waveguide. As a result, $N_{\mathrm{i}} = N_i(z)$, $g = g(z)$, and $\alpha = \alpha(z)$, meaning that, in a realistic scenario, these quantities should be calculated at each point across the direction of propagation z. This will be addressed in Section 2.4, where we build an iterative model to solve the coupled-mode theory equations.

2.3.1. POPULATION DYNAMICS OF ER^{3+} IONS

Erbium ions have a relatively complicated energy diagram, with many transitions available, including ESA and ETU effects. For emission at wavelengths around 1550 nm, erbium-doped gain media can be pumped at wavelengths around either 980 or 1480 nm. Here, we will focus on the laser dynamics under 1480-nm pumping, but the same process can be used to derive the equations that describe population dynamics for 980-nm pumping [218].

2.3.1.1. Er^{3+} Energy Level Diagram

Figure 2.16 shows a simplified energy level diagram of Er^{3+} ions and the main transitions of interest for our purposes [218,230,231]. It also indicates photon wavelengths that can excite a ground state electron to the energy levels involved in each transition.

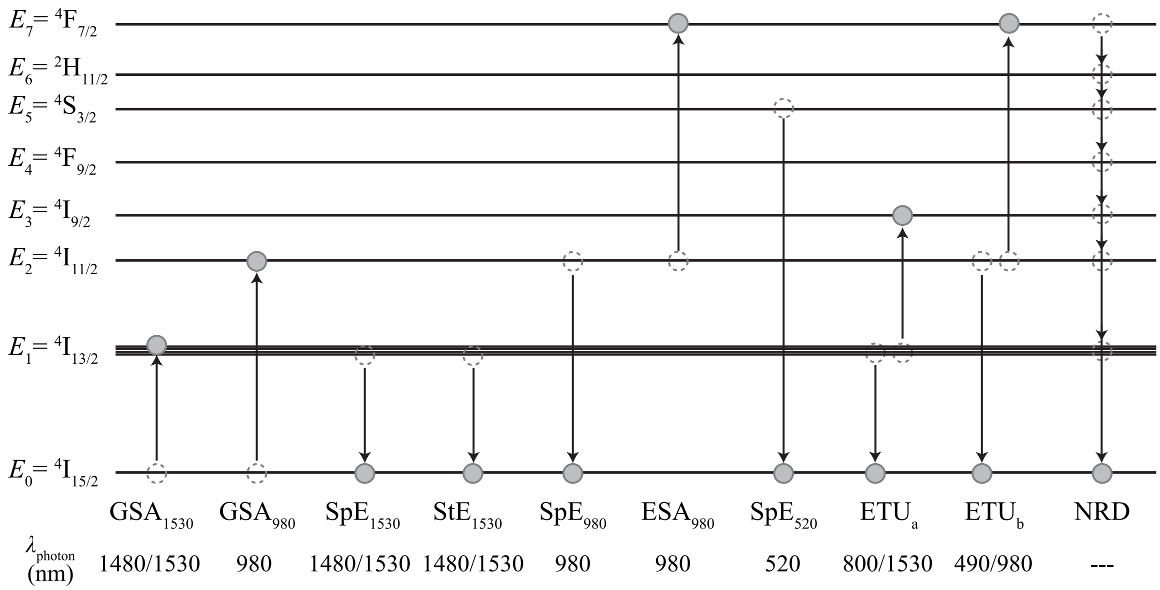

Figure 2.16. Simplified energy diagram of Er^{3+} ions showing transitions of interest, as well as the equivalent peak photon wavelength involved in each transition. The shorter wavelengths in the ETU examples represent the required photon energy to excite an electron from the ground state to the highest energy level.

Energy levels shown in this type of diagram are usually an amalgamation of manifolds, as indicated in the state ${}^4I_{13/2}$, which is composed of several Stark levels [218]. It follows a brief description of each transition highlighted in Figure 2.16:

GSA_{1530}: Ground-state absorption around 1530 nm to the manifold state ${}^4I_{13/2}$. At 1480-nm pump operation, the pump and signal are absorbed to upper and lower Stark levels, respectively.

GSA_{980}: Ground-state absorption around 980 nm to the manifold state ${}^4I_{11/2}$.

SpE_{1530}: Spontaneous emission around 1530 nm from the manifold state ${}^4I_{13/2}$ to the ground state.

StE_{1530}: Stimulated emission around 1530 nm.

SpE_{980}: Spontaneous emission around 980 nm.

ESA_{980}: Excited-state absorption around 980 nm from ${}^4I_{11/2}$ to ${}^4F_{7/2}$.

SpE_{520}: Spontaneous emission around 520 nm. Energy levels ${}^4S_{3/2}$ and ${}^2H_{11/2}$ are very close and can both contribute to this transition, which emits a characteristic secondary erbium green light when pumped.

ETU_a and **ETU_b**: Energy transfer upconversion between ions in the ${}^4I_{13/2}$ and ${}^4I_{11/2}$ levels, respectively.

NRD: Non-radiative decays. These transitions usually have very short lifetimes in comparison with the excited state transition of interest for lasing.

2.3.1.2. Er^{3+} Absorption and Emission Cross Sections

When many ions are brought together, their energy manifolds overlap and become bands of available states [232]. In amorphous materials, there are slight variations in both the local host medium structure surrounding each ion and their corresponding energy manifolds, which leads to inhomogeneous broadening. As a result, the emission and absorption spectra of rare-earth-doped glass media exhibit a continuous response across a wavelength range. As an example, Figure 2.17 shows the normalized cross sections of the transitions associated with the $^4I_{13/2}$ level and $^4I_{15/2}$ ground state in an erbium-doped silica fiber [233].

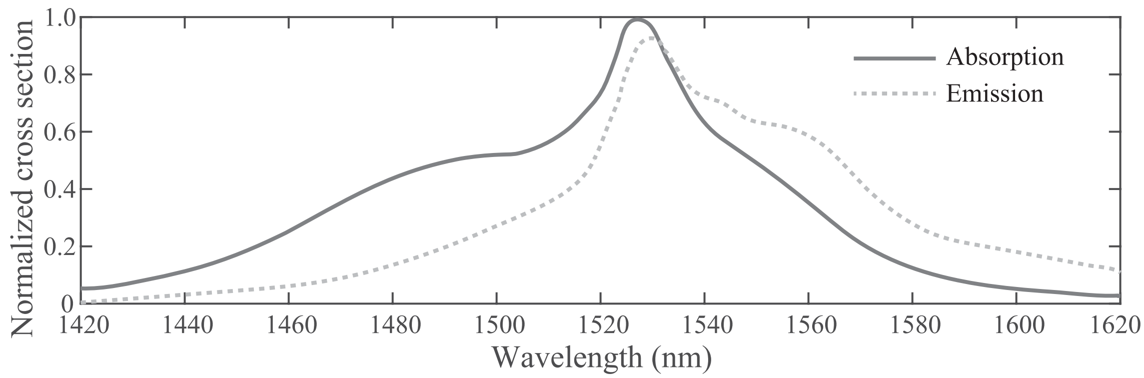

Figure 2.17. Normalized absorption and emission cross sections of an erbium-doped silica fiber [233].

As mentioned in Section 1.4.1, these optical transitions of interest are shielded by outer electronic shells in rare earths. However, even though the overall shapes of the curves shown in Figure 2.17 remain similar across different hosts, the exact cross sections must be determined for each host material. Note that, in Figure 2.17, the emission cross section is greater than the absorption cross section at wavelengths above ~1530 nm, which makes it easier to achieve population inversion, illustrating why erbium is a great dopant to achieve lasers in the C-band. This is due to the thermal distribution of the population at each level.

2.3.1.3. Er^{3+} Rate Equations

We can now use the energy diagram of Figure 2.16 to write the rate equations that describe the population dynamics of an erbium-doped laser. We will maintain our definition that N_i is the population of the energy level E_i, with E_i representing the states indicated in Figure 2.16. Moreover, we will make a three-level approximation considering the energy states E_0, E_1, and E_2. To do so, we will assume that the lifetime of level E_3 is much lower than that of E_2 ($\tau_3 \ll \tau_2 \ll \tau_1$) such that $N_{i>2} = 0$ (refer to [231] for lifetime estimates for each energy level in erbium-doped alumina thin films, which show that this approximation is valid). In TeO_2 films, τ_2 can be relatively long (up to ~ 0.2 ms) due to tellurite's low phonon energy [84]. This has a more significant impact when pumping at 980 nm, since the level E_2 ($^4I_{11/2}$) is directly excited. Although further spectroscopy work is needed to determine it for our films, we expect τ_2 to be at least a third of the τ_1 values observed in this work (~ 0.62 ms), as we will see in Chapter 4. We must then determine N_0, N_1, and N_2 considering the contributions of GSA_{1530}, SpE_{1530}, StE_{1530} (at both pump and signal wavelengths), as well as ETU_a.

First, let us define R_{mn} as the total rates of the transition $E_m \rightarrow E_n$, including absorption, spontaneous emission, and stimulated emission contributions (but not upconversion yet). They can be written as

$$R_{01} = \frac{P_{\text{pump}}}{h\nu_{\text{pump}},}\sigma_{\text{abs,pump}} + \frac{P_{\text{laser}}}{h\nu_{\text{laser}},}\sigma_{\text{abs,laser}}, \tag{2.59}$$

$$R_{10} = \frac{P_{\text{pump}}}{h\nu_{\text{pump}},}\sigma_{\text{em,pump}} + \frac{P_{\text{laser}}}{h\nu_{\text{laser}},}\sigma_{\text{em,laser}} + \frac{1}{\tau_1}, \tag{2.60}$$

$$R_{21} = \frac{1}{\tau_2}. \tag{2.61}$$

Then, the rate equations can be written as (including upconversion)

$$\frac{dN_1}{dt} = R_{01}N_0 - R_{10}N_1 + R_{21}N_2 - 2W_{\text{ETU}_\text{a}}N_1^2, \tag{2.62}$$

$$\frac{dN_2}{dt} = -R_{21}N_2 + W_{\text{ETU}_\text{a}}N_1^2. \tag{2.63}$$

Using the conservation of total number of electrons discussed earlier, $N_\text{T} = \sum_i N_i$, we can express N_0 in terms of N_1 and N_2

$$N_0 = N_\text{T} - N_1 - N_2. \tag{2.64}$$

The solutions to Equations 2.62 and 2.63 for the steady-state condition are

$$N_1 = \frac{\sqrt{(R_{01}+R_{10})^2 + 4W_{\text{ETU}_\text{a}}\left(1+\frac{R_{01}}{R_{21}}\right)R_{01}N_T} - (R_{01}+R_{10})}{2W_{\text{ETU}_\text{a}}\left(1+\frac{R_{01}}{R_{21}}\right)}, \tag{2.65}$$

$$N_2 = \frac{W_{\text{ETU}_a}N_1^2}{R_{21}}. \tag{2.66}$$

2.3.1.4. Er^{3+} Ion Quenching

Thus far, we have considered that all erbium ions equally contribute to light emission and amplification. In reality, a significant fraction of these ions can be part of localized erbium clusters across the host material or close to impurities, especially those belonging to the hydroxyl (OH^-) group [230]. Such arrangements are susceptible to favor non-radiative processes that quickly bring the Er^{3+} ion back to the ground state after absorbing a photon. These fast-quenched ions do not contribute to light emission (even though they still "consume" a pump photon that could have been absorbed by an active, unquenched ion).

While the first excited state lifetime τ_1 can be on the order of milliseconds and, τ_2, tens of microseconds, quenched ions may decay after tens of nanoseconds or up to a few microseconds [230,231].

We can revisit our rate equations to account for quenched ions. To do so, we will divide our erbium ion population into active ($N_{\mathrm{T,a}}$) and quenched ($N_{\mathrm{T,q}}$) ions such that

$$N_{\mathrm{T,a}} = N_{\mathrm{T}}\left(1 - f_{\mathrm{q}}\right), \tag{2.67}$$

$$N_{\mathrm{T,q}} = N_{\mathrm{T}} f_{\mathrm{q}}, \tag{2.68}$$

where $0 < f_{\mathrm{q}} < 1$ is the fraction of quenched ions. We can then write two sets of rate equations, one for each type of ion. For the active ions, we simply replace N_{T} with $N_{\mathrm{T,a}}$ in Equation 2.64. For the quenched ions, we follow the same procedure using $N_{\mathrm{T,q}}$, but we also update the excited state lifetimes τ_1 and τ_2 in Equations 2.60 and 2.61 to reflect the fast-quenching process. Here, we will use quenched ion lifetimes of 1 µs for all excited states [230,231].

2.3.1.5. Er^{3+} Absorption and Gain Coefficients

We can now write the absorption and gain coefficients of our erbium gain medium using Equations 2.57 and 2.58

$$g = \sigma_{\mathrm{em,laser}}(N_{2,\mathrm{a}} + N_{2,\mathrm{q}}) - \sigma_{\mathrm{abs,laser}}(N_{1,\mathrm{a}} + N_{1,\mathrm{q}}) - \alpha_{\mathrm{BG,laser}}, \tag{2.69}$$

$$\alpha = \sigma_{\mathrm{em,pump}}(N_{2,\mathrm{a}} + N_{2,\mathrm{q}}) - \sigma_{\mathrm{abs,pump}}(N_{1,\mathrm{a}} + N_{1,\mathrm{q}}) - \alpha_{\mathrm{BG,pump}}, \tag{2.70}$$

where $N_{i,\mathrm{a}}$ and $N_{i,\mathrm{q}}$ are the active and quenched ion population of the energy level E_i, respectively, such that $N_{\mathrm{T,a}} = N_{1,\mathrm{a}} + N_{2,\mathrm{a}}$, $N_{\mathrm{T,q}} = N_{1,\mathrm{q}} + N_{2,\mathrm{q}}$, and $N_{\mathrm{T}} = N_{\mathrm{T,a}} + N_{\mathrm{T,q}}$.

2.3.2. Population Dynamics of Tm^{3+} Ions

Thulium has a slightly simpler energy diagram compared to erbium. For emission around 2000 nm wavelengths, thulium-doped gain media are usually pumped around 780 or 1600 nm. In both cases, cross relaxation mechanisms play a significant role in the population dynamics and cannot be ignored, even though they are less pronounced under 1600-nm pumping [234]. Here, we will focus on the population dynamics when thulium ions are in-band pumped by light around 1600 nm, but similar equations can be derived for indirect pumping via wavelengths around 780 nm [234,235]. In tellurite glass, for Tm^{3+} concentrations below roughly 10^{21} ions/cm^3, ion quenching is not as detrimental as for erbium [236,237], and its main effects can be incorporated into our rate equations by adjusting the lifetime of the $^3F_4$ energy level, as well as the cross relaxation parameters [236,237]. Therefore, we will not explicitly consider a fraction of quenched thulium ions as we did for erbium, but, instead, we will assume a single lifetime value for all the Tm^{3+} ions in the simulations carried out in Chapter 6.

2.3.2.1. Tm^{3+} Energy Levels and Lifetimes

Figure 2.18 shows a simplified energy level diagram of Tm^{3+} ions and the main transitions of interest for emission around 2000 nm [234,235]. It also indicates photon wavelengths that can excite a ground state electron to the energy levels involved in each transition.

Here is a brief description of each transition highlighted in Figure 2.18:

GSA_{1600}: Ground-state absorption in the 1500–2000 nm range to the manifold state $^3F_4$. At 1600-nm pump operation, the pump and signal are absorbed to upper and lower Stark levels, respectively.

GSA_{780}: Ground-state absorption near 800 nm (typically 780 or 793 nm) to the $^3H_4$ level.

SpE_{1900}: Spontaneous emission in the 1600–2200 nm range from the manifold state $^3F_4$ to the ground state.

StE_{1900}: Stimulated emission between 1600–2200 nm.

CR: Cross relaxation between the energy levels $^3H_4$ and $^3F_4$.

ETU: Energy transfer upconversion between ions in $^3F_4$ level.

NRD: Non-radiative decays. These transitions usually have very short lifetimes in comparison with the excited state transition of interest for lasing.

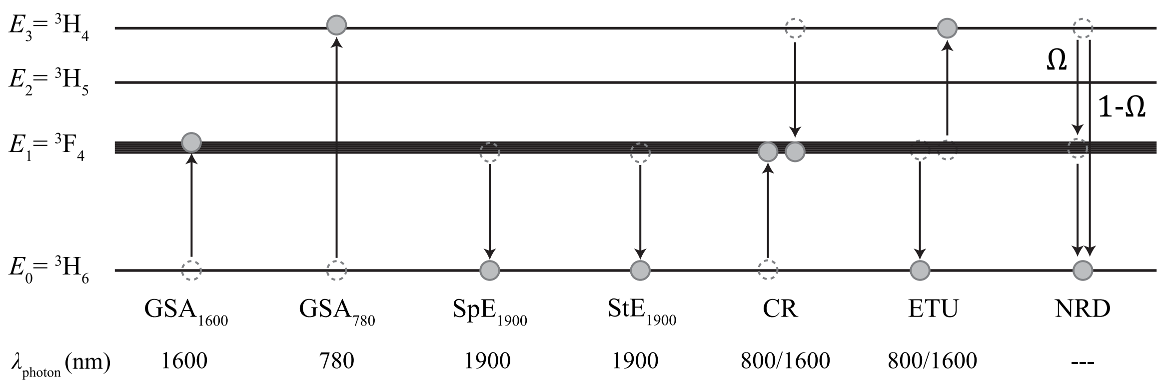

Figure 2.18. Simplified energy diagram of Tm^{3+} ions showing transitions of interest, as well as the equivalent peak photon wavelength involved in each transition. The shorter wavelengths in the CR and ETU examples represent the required photon energy to excite an electron from the ground state to the highest energy level.

Here, we will also consider that electrons excited to the $^3H_4$ level can either decay to the $^3F_4$ level or directly to the ground state $^3H_6$ via non radiative decay. To account for that, we define the branching ratio $0 < \Omega < 1$ which represents the probability of the transition $^3H_4 \rightarrow {}^3F_4$ to happen[5]. Then, $1 - \Omega$ is the probability of $^3H_4 \rightarrow {}^3H_6$ occurring. We will assume $\Omega = 0.082$, based on alkali-barium-bismuth-tellurite glass works [229,238],

[5] The branching ratio is usually represented by β, but here we use Ω to avoid confusion with the propagation constant.

because further spectroscopy measurements are needed to determine the exact value of Ω for the films used in this work.

2.3.2.2. Tm^{3+} Absorption and Emission Cross Sections

The normalized absorption and emission cross sections of a thulium-doped silica fiber are shown in Figure 2.19 [239]. One of the advantages of thulium is its extremely wide emission band that spans over hundreds of nanometers. The absorption cross section is also wide but, more importantly, it has low overlap with the emission cross section at wavelengths below 1700 nm, unlike erbium. This helps with achieving population inversion and a high gain coefficient.

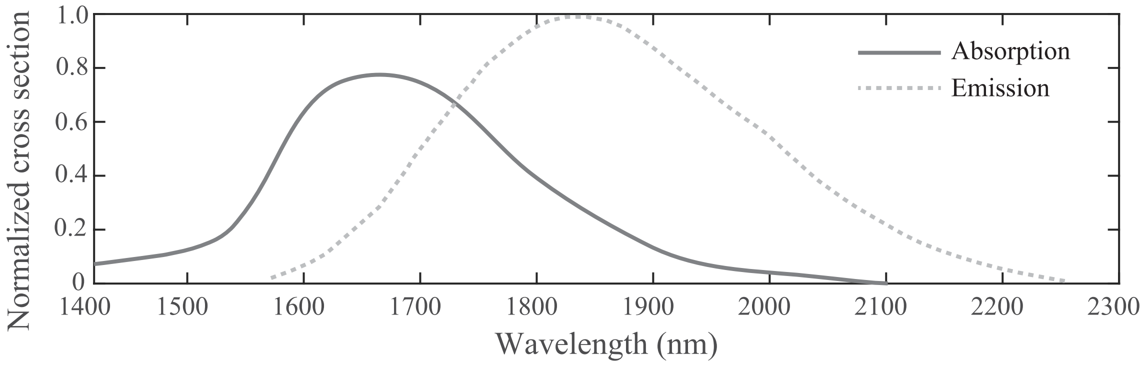

Figure 2.19. Normalized absorption and emission cross sections of a thulium-doped silica fiber [239].

2.3.2.3. Tm^{3+} Rate Equations

Following the same procedure we used for erbium and using the diagram from Figure 2.18, we can write the rate equations for thulium under 1600 nm pumping. We consider that any electrons that populate the energy level $^3H_5$ quickly decay to the $^3F_4$ level, so we can ignore its population (N_2 = 0) [229]. Moreover, we now return to the E_i nomenclature to refer to the energy levels as shown in Figure 2.18. The transition rates without the cross relaxation terms are given by

$$R_{01} = \frac{P_{\text{pump}}}{h\nu_{\text{pump}}}\sigma_{\text{abs,pump}} + \frac{P_{\text{laser}}}{h\nu_{\text{laser}}}\sigma_{\text{abs,laser}}, \tag{2.71}$$

$$R_{10} = \frac{P_{\text{pump}}}{h\nu_{\text{pump}}}\sigma_{\text{em,pump}} + \frac{P_{\text{laser}}}{h\nu_{\text{laser}}}\sigma_{\text{em,laser}} + \frac{1}{\tau_1}, \tag{2.72}$$

$$R_{32} = \frac{\Omega}{\tau_3}. \tag{2.73}$$

$$R_{31} = \frac{1-\Omega}{\tau_3}. \tag{2.74}$$

Including the cross relaxation terms, the rate equations can then be written as

$$\frac{dN_1}{dt} = R_{01}N_0 - R_{10}N_1 + R_{31}N_3 + 2C_{\text{R}}, \tag{2.75}$$

$$\frac{dN_3}{dt} = -(R_{31} + R_{32})N_3 - C_{\mathrm{R}} = -\frac{1}{\tau_3}N_3 - C_{\mathrm{R}}\,, \tag{2.76}$$

with $C_{\mathrm{R}} = W_{\mathrm{RETU}}N_0N_3 - W_{\mathrm{ETU}}N_1^2$, as introduced just before Section 2.3.1. We use again the conservation of total electrons to express $N_0 = N_{\mathrm{T}} - N_1 - N_3$. However, this system of equations is now nonlinear, due to the introduction of the cross relaxation term, which is proportional to N_0N_3, a product of two variables. Therefore, we move away from an analytical solution and must use numerical methods to solve them instead. They can be solved using the Matlab function *fsolve* [229,234,235], as shown in the code available in Appendix II.

2.3.2.4. Tm^{3+} Absorption and Gain Coefficients

For now, let us assume that we know the solutions N_0, N_1, and N_3. The gain and absorption coefficients can be directly calculated using Equations 2.57 and 2.58, which give us

$$g = \sigma_{\mathrm{em,laser}}N_1 - \sigma_{\mathrm{abs,laser}}N_0 - \alpha_{\mathrm{BG,laser}}, \tag{2.77}$$

$$\alpha = \sigma_{\mathrm{em,pump}}N_1 - \sigma_{\mathrm{abs,pump}}N_0 - \alpha_{\mathrm{BG,pump}}. \tag{2.78}$$

2.4. Laser Modeling

We have now introduced all the ingredients we need to make waveguide lasers: a waveguide platform, an optical cavity, a pump source, and a gain medium. In section 2.2.4, when we discussed the coupled-mode theory equations that describe a DBR cavity in the presence of a gain medium, we considered the forward and backward fields to be $A = A(z)$ and $B = B(z)$, and the net gain coefficient γ to be constant. In reality, all these parameters vary across the waveguide cross section, because the mode profile – and, therefore, intensity – follows a distribution in the xy plane, as we have seen in Figure 2.5. This means that the mode not only partially overlaps with the gain medium, but with varying intensity. Moreover, as we have seen in the previous section, the gain and absorption coefficients are given by the population dynamics, which are a function of the pump and laser powers, also dependent on x, y, and z. To accurately model a laser, we must then solve the CMT equations considering $A = A(x,y,z)$, $B = B(x,y,z)$, and $\gamma = \gamma(x,y,z)$. We will also take into account a more general case where the device can be double-sided pumped. Under these considerations, the CMT equations cannot be solved analytically, and we must make use of numerical methods to do so. Here, we opt to use an iterative technique known as the shooting method, which has been widely used to model rare-earth lasers and amplifiers [240–245]. As you can imagine, there are several things to consider here, and it is a far-from-trivial problem to solve. Therefore, I will make an extra effort to make this section accessible and not omit relevant details. We will start with a brief introduction to the shooting method, followed by a detailed statement of the problem to be solved and the necessary parameters involved, as well as a step-by-step description of how to implement an algorithm to find the solutions using Matlab.

2.4.1. THE SHOOTING METHOD

The shooting method is an iterative technique to solve differential equations subject to boundary conditions [246–250]. It consists of converting a boundary condition problem into an initial condition one, requiring that we know the solution at two points (usually the boundary conditions). Then, we will guess a solution (we will talk more about the guess later), iteratively solve the differential equations, and compare our solution to the known boundary condition. If the difference (error) between them is larger than a tolerance that we set, we update our initial guess and restart solving the equation. We repeat this guess-solve-compare procedure until the solution converges (i.e. the error is within the chosen tolerance). This is where the method's name comes from: we shoot at a target (boundary condition) and after analyzing how far from it we landed (error), we keep adjusting our shoot (guess) until we hit the target. Let us analyze how this applies to the problem we are trying to solve.

Figure 2.20 illustrates the problem to be solved. In a double-side pumping configuration, we must account for forward- and backward-propagating pump ($P_{\mathrm{P,fwd}}$, $P_{\mathrm{P,bwd}}$) and signal/laser ($P_{\mathrm{L,fwd}}$, $P_{\mathrm{L,bwd}}$) powers. For simplicity, when I refer to a quantity at position z, I mean its total value, obtained by adding all the contributions throughout the cross section at the point, for example: $P_{\mathrm{L,fwd}}(L) = \sum_{x,y} P_{\mathrm{L,fwd}}(x, y, L)$. These are ultimately the quantities that matter for our final results. We will ignore the regions $z < 0$ and $z > L$, isolating the DBR response. As a result, we will consider that $P_{\mathrm{P,fwd}}(0)$ and $P_{\mathrm{P,bwd}}(L)$ are the launched forward and backward pump powers, respectively (known values). In the lasers investigated in this work, the cavities have an offset of 250 μm from the chip facets, much shorter than the device length (1~2 cm), which makes this approximation valid. The pump modes are not reflected by the gratings, so they are simply absorbed across the cavity in their direction of propagation, determined by the absorption coefficient (which is not constant). Moreover, we have the following boundary conditions for the laser powers: $P_{\mathrm{L,fwd}}(0) = P_{\mathrm{L,bwd}}(L) = 0$ (no forward signal at $z < 0$ or backward signal at $z > L$, since all the laser power is generated inside the cavity). The fields A and B that we introduced in Section 2.2.1 are related to the laser powers such that $P_{\mathrm{L,fwd}}(z) = |A(z)|^2$ and $P_{\mathrm{L,bwd}}(z) = |B(z)|^2$.

Our goal is to calculate the laser output powers in the forward and backward directions, $P_{\mathrm{L,fwd}}(L)$ and $P_{\mathrm{L,bwd}}(0)$. We will divide the z-direction into a uniform mesh with discrete length increments Δz and use the shooting method to guess an initial value $P_{\mathrm{L,bwd}}(0) = G_1^2 \Rightarrow B(0) = G_1$. We will also define a tolerance or maximum acceptable error, err. Next, we will use the pump powers at $z = 0$ to calculate the steady-state populations in each energy level at each (x, y) point in the cross section (we still do not know $P_{\mathrm{P,bwd}}(0)$, but we will return to it soon). Then, we can calculate the gain and absorption coefficients at the initial point. Next, we start to propagate the pump and laser powers: at the point $z = n\Delta z$ ($n \in \mathbb{N}^*$), we use the gain and absorption coefficients calculated in the previous point, $z = (n - 1)\Delta z$, to update the laser and pump powers and calculate the new set of gain and absorption coefficients to be used in the step $n + 1$. Of course, only the part of the mode that interacts with the gain medium (in our case, Er^{3+}- or Tm^{3+}-doped TeO_2) contribute to laser emission and pump absorption – all the other points in the cross section only contribute to background loss. Moreover, we need to solve slightly different equations in each region: near the edges we have the grating effect, whereas in the gap region we only have gain and absorption effects. After we propagate all our entities across the entire device, we check if the backward laser emission at $z = L$ is within the tolerance (it should be zero, according to the boundary conditions): $|B(L)| = \left|\sqrt{P_{\mathrm{L,bwd}}(L)}\right| < \mathrm{err}$. If it satisfies this condition, we have found the solution. Otherwise, we will try another guess, and repeat this process until the algorithm converges to a solution. We will also define a maximum number of iterations acceptable to stop the calculations if no solution is found by then – this will be necessary if the algorithm does not converge, which usually happens due to one of these three reasons: unsuitable initial guess, unsuitable method to update guess, or the device cannot lase, for instance when the pump power is below the lasing threshold or the losses overcome the gain in a roundtrip inside the cavity.

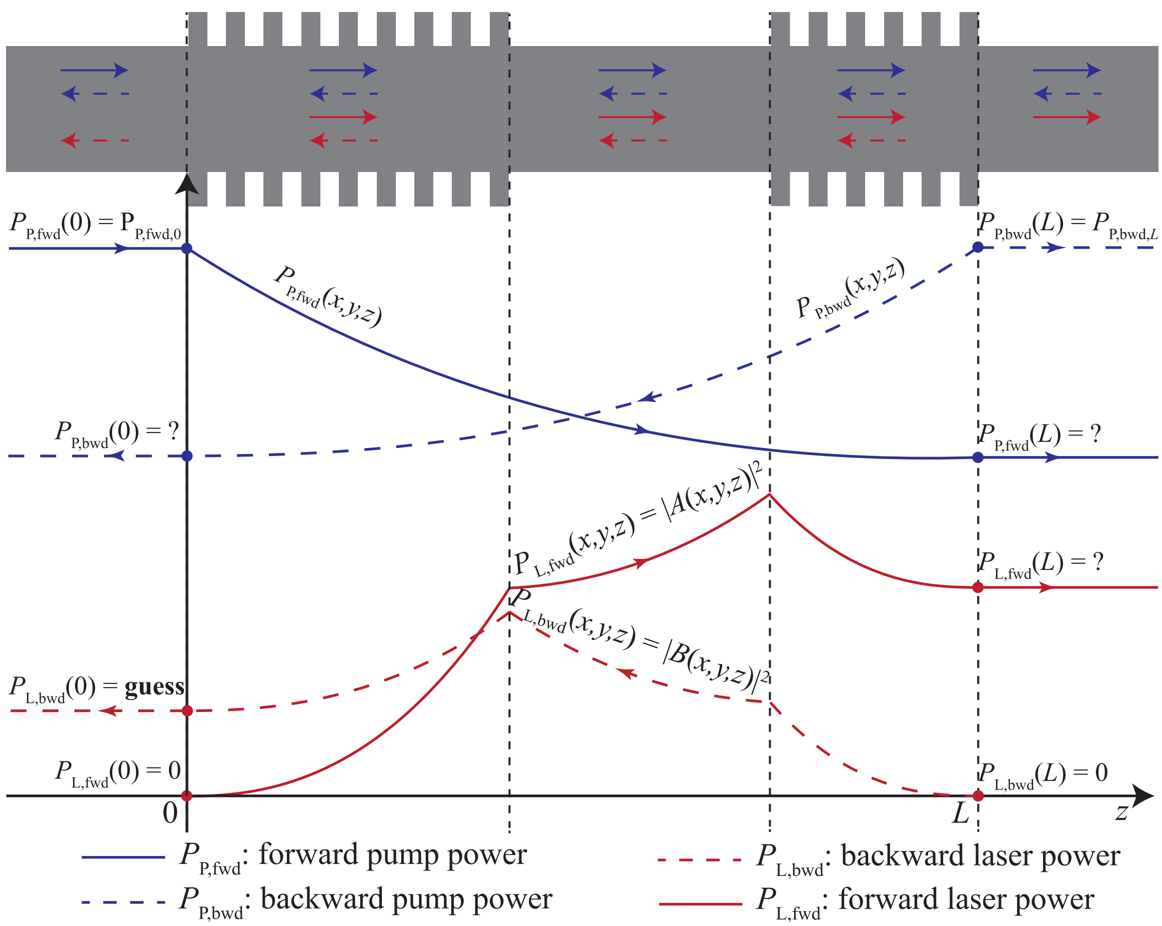

Figure 2.20. Diagram of the problem to be solved using the shooting method, showing forward and backward pump and laser powers, boundary conditions, parameter to be guessed, and unknown quantities which we will find by solving the problem.

Several questions remain:

- How to calculate $P_{\mathrm{P,bwd}}(0)$?
- How to choose our initial guess G_1?
- How to update our guess for the next iterations?
- How to account for the cross-sectional power distribution?
- How to write and solve iterative coupled-mode theory equations?

We will address the first three in this section, and the last two in the following.

With the exception of the backward pump, we know the value of all other parameters at $z = 0$ and we will propagate them along the z direction. Our approach starts by initializing the backward pump as zero in all points along z, except at $z = L$, where $P_{\mathrm{P,bwd}}(L) = P_{\mathrm{P,bwd},L}$. Then, as we propagate all the powers considering their values (and the gain/absorption coefficients) at $z = (n-1)\Delta z$, we will update the backward pump using the parameters at $z = (n+1)\Delta z$, which essentially means that we are propagating it in the backward direction. This means that in the first iteration only $P_{\mathrm{P,bwd}}(L)$ is different than zero, in the second iteration the $P_{\mathrm{P,bwd}}(L)$ and $P_{\mathrm{P,bwd}}(L-\Delta z)$ are different than zero, and so on, as shown in Figure 2.21. If our mesh along z has $N = 1 + \frac{L}{\Delta z}$ points, it will take N iterations to propagate the backward pump across the device. However, at each iteration all the non-zero $P_{\mathrm{P,bwd}}(z)$ points affect the laser and forward pump powers and are corrected in the following iteration using the absorption coefficients calculated in the previous iteration. In this way, all the parameters are constantly correcting each other at each iteration.

0	0	0	⋯ Iterations ↓	0	0	$P_{\mathrm{P,bwd},L}$
0	0	0	⋯	0	$P_{\mathrm{P,bwd}}(L\text{-}\Delta z)$	$P_{\mathrm{P,bwd},L}$
0	0	0	⋯	$P_{\mathrm{P,bwd}}(L\text{-}2\Delta z)$	$P_{\mathrm{P,bwd}}(L\text{-}\Delta z)$	$P_{\mathrm{P,bwd},L}$
⋮	⋮	⋮	⋯	⋮	⋮	⋮
0	$P_{\mathrm{P,bwd}}(\Delta z)$	$P_{\mathrm{P,bwd}}(2\Delta z)$	⋯	$P_{\mathrm{P,bwd}}(L\text{-}2\Delta z)$	$P_{\mathrm{P,bwd}}(L\text{-}\Delta z)$	$P_{\mathrm{P,bwd},L}$
$P_{\mathrm{P,bwd}}(0)$	$P_{\mathrm{P,bwd}}(\Delta z)$	$P_{\mathrm{P,bwd}}(2\Delta z)$	⋯	$P_{\mathrm{P,bwd}}(L\text{-}2\Delta z)$	$P_{\mathrm{P,bwd}}(L\text{-}\Delta z)$	$P_{\mathrm{P,bwd},L}$

Figure 2.21. Backward pump propagation across iterations.

2.4.1.1. Initial Guess and Iterative Corrections

Choosing both an appropriate initial guess and an adequate method to update it is key to achieving an efficient model [240,245], and it might require some trial and error for each problem to be solved. Here, we will follow a simple, intuitive approach, to the detriment of higher computational cost and lower algorithm efficiency. This is certainly one aspect that can be optimized in future iterations of this model.

Here, we choose an initial guess that is close to zero and lower than the real backward laser emission. In Chapters 4 and 5, we will use experimental data to support our choices. The general approach here is to start with an initial guess G_1, as shown in Figure 2.22. Since this value is lower than the "real" $B(0)$, $B(z)$ becomes negative in some part of the device, as indicated in the figure. Since $B(z)$ represents an electric field, it cannot assume negative values. We can then update our guess using a fixed small increment ΔG, such that $G_m = G_1 + (m-1)\Delta G, m \in \mathbb{N}^*$, and the solution to $B(z)$ will be offset to higher values at each iteration, until $|B(L)| = \left|\sqrt{P_{\mathrm{L,bwd}}(L)}\right| < \mathrm{err}$. When that happens, we consider the algorithm to have converged and the final guess G_s is the solution to $B(0)$, and the laser's backward emission is simply $P_{\mathrm{L,bwd}}(0) = B^2(0)$.

Since we chose to use fixed increments ΔG to update the initial guess, it is important to test a few combinations of G_0, ΔG, and err, to make sure that the algorithm converges in an acceptable amount of time. In general, we will consider $\mathrm{err} = 10^{-3}$, because it translates to a tolerance of 10^{-6} W in the output power, which is below the 0.01 mW (10^{-5} W) precision in the measurements performed in this work.

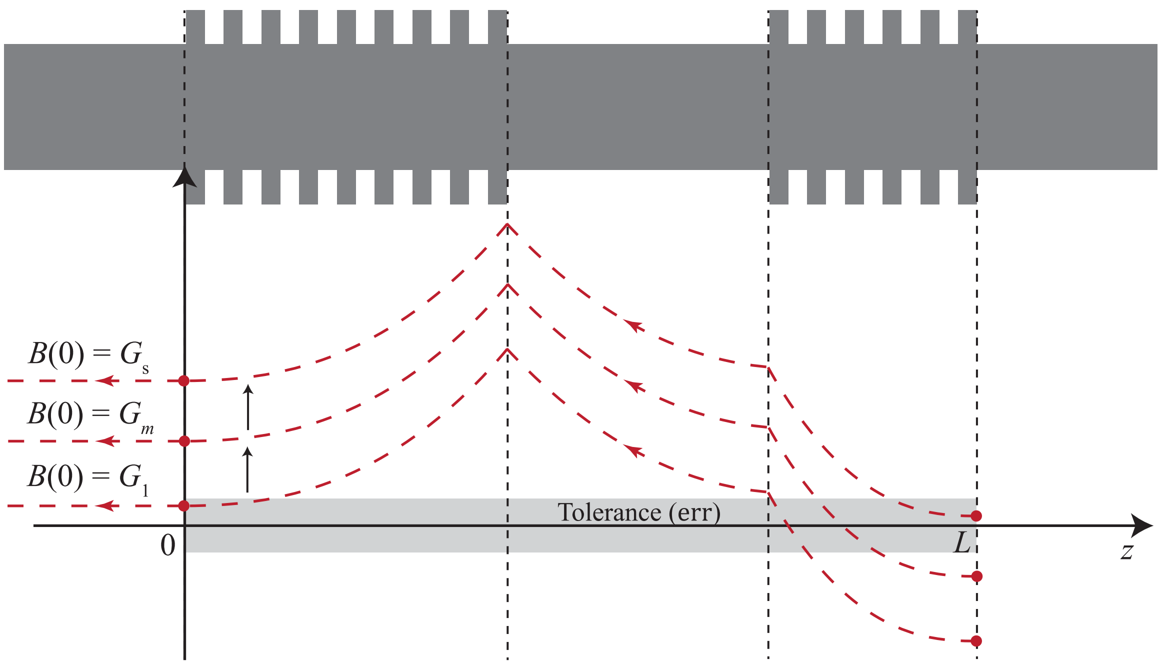

Figure 2.22. Backward laser emission ($B(z)$ field) guesses and corrections. The algorithm is considered to have converged when $B(L)$ is within the chosen tolerance.

2.4.2. ALGORITHM

Let us see what the shooting method algorithm looks like when applied to the coupled-mode theory equations we introduced in Section 2.2.1. We will now be able to take into account the cross-sectional power distribution, as well as absorption and gain coefficients that vary along the direction of propagation. First, we will use simulated mode profiles to account for the field distribution in the plane perpendicular to the direction of propagation. Then, we will write an iterative version of the differential equations we want to solve.

2.4.2.1. Normal Power Distribution

When we use a finite element method solver to generate mode profiles as the ones shown in Figure 2.5, we usually obtain a file containing an array with $i \times j$ elements, with i and j being the number of mesh elements along the y and x directions. These elements are typically the normalized electric field or power, in the sense that the element with the largest magnitude has a value of 1. This means that they are not normalized in space, i.e., the sum of all elements is not equal to 1. Here, we use electric field distribution arrays, obtained through RSoft finite element method mode solver at the pump and signal wavelengths. Moreover, we use a uniform mesh for simplicity (all the elements have the same area). However, it is possible to implement non-uniform meshes, which can significantly reduce the algorithm's computational cost. If $E_{\mathrm{P}}(x,y)$ and $E_{\mathrm{L}}(x,y)$ are the simulated electric field distribution for the fundamental TE mode at the pump and laser wavelengths, respectively, their spatially normalized distributions $\phi_{\mathrm{P}}(x,y)$ and $\phi_{\mathrm{L}}(x,y)$ can be expressed as

$$\phi_{\mathrm{P}}(x,y) = \frac{E_{\mathrm{P}}(x,y)}{\sum_{\mathrm{all}} E_{\mathrm{P}}(x,y)}, \tag{2.79}$$

$$\phi_{\mathrm{L}}(x,y) = \frac{E_{\mathrm{L}}(x,y)}{\sum_{\mathrm{all}} E_{\mathrm{L}}(x,y)}, \tag{2.80}$$

which are now normalized in space, satisfying $\sum_{\mathrm{all}} \phi_{\mathrm{P}}(x,y) = \sum_{\mathrm{all}} \phi_{\mathrm{L}}(x,y) = 1$. Similarly, we can write the normalized pump and laser intensity distributions $\Phi_{\mathrm{P}}(x,y)$ and $\Phi_{\mathrm{L}}(x,y)$ as

$$\Phi_{\mathrm{P}}(x,y) = \frac{E_{\mathrm{P}}^2(x,y)}{\sum_{\mathrm{all}} E_{\mathrm{P}}^2(x,y)}, \tag{2.81}$$

$$\Phi_{\mathrm{L}}(x,y) = \frac{E_{\mathrm{L}}^2(x,y)}{\sum_{\mathrm{all}} E_{\mathrm{L}}^2(x,y)}. \tag{2.82}$$

Since we use uniform meshes to solve for $E_{\mathrm{P}}(x,y)$ and $E_{\mathrm{L}}(x,y)$, $\Phi_{\mathrm{P}}(x,y)$ and $\Phi_{\mathrm{L}}(x,y)$ describe both normalized intensity distributions and normalized power distributions (Intensity = Power/Area), because all the mesh elements have the same area. With these definitions we can rewrite the pump and laser powers as follows:

$$P_{\mathrm{P},d}(x,y,z) = \Phi_{\mathrm{P}}(x,y) P_{\mathrm{P},d}(z), \tag{2.83}$$

$$P_{\mathrm{L},d}(x,y,z) = \Phi_{\mathrm{L}}(x,y) P_{\mathrm{L},d}(z), \tag{2.84}$$

with $d = \mathrm{fwd}, \mathrm{bwd}$. Additionally, the auxiliary fields $A(x,y,z)$ and $B(x,y,z)$ can be expressed as $A(x,y,z) = \phi_{\mathrm{L}}(x,y)A(z)$ and $B(x,y,z) = \phi_{\mathrm{L}}(x,y)B(z)$. The quantities $P_{\mathrm{P},d}(z), P_{\mathrm{L},d}(z), A(z), B(z)$ represent their total magnitude at the point z, as defined in the previous section.

We can then update the coupled-mode theory and rate equations by substituting these quantities with their new definitions. We must consider one more thing: only the rare-earth TeO_2 layer contributes to light emission. So, we must properly represent the steady-state populations at each point in the xy plane. RSoft also outputs a file that contains the refractive index cross section distribution $n(x, y)$ using the same mesh as the mode solver. We can simply use it to create a total population distribution $N_T(x, y, z)$

$$N_T(x, y, z) = \begin{cases} N_T, & if\, n(x, y) = n_{\mathrm{TeO_2:RE}} \\ 0 & \text{otherwise} \end{cases}, \tag{2.85}$$

where $n_{\mathrm{TeO_2:RE}}$ is the refractive index of the gain medium used in the RSoft simulations. The populations of each energy level can all be initialized as $N_i(x, y, z) = 0$, since their values will be updated using the steady state solutions.

The gain and absorption coefficients, $g(x, y, z)$ and $\alpha(x, y, z)$, can be calculated as we propagate the powers and solve the rate equations along the direction of propagation, using equations 2.57 and 2.58 and replacing $N_i \to N_i(x, y, z)$. In the cross section points in which there is no active material, $N_i(x, y, z) = 0$ and the coefficients are reduced to the background losses $g(x, y, z) = -\alpha_{\mathrm{BG,laser}}$ and $\alpha(x, y, z) = -\alpha_{\mathrm{BG,pump}}$.

2.4.2.2. Iterative Coupled-mode Theory Equations

Now, we can (finally) write the iterative coupled-mode theory equations. To do so, we are going to use the Euler method, which is the simplest, most basic, first-order Runge-Kutta method to solve differential equations [251]. Essentially, we return to the definition of the derivative of a function f

$$\frac{df(z)}{dz} = \lim_{dz \to 0}\left(\frac{f(z+dz) - f(z)}{dz}\right), \tag{2.86}$$

making the approximation

$$\frac{df(z)}{dz} \approx \frac{f(z+\Delta z) - f(z)}{\Delta z} \to \frac{f_n - f_{n-1}}{\Delta z}, \tag{2.87}$$

where Δz is the step size along the direction of propagation and $n \in \mathbb{N}$, such that $z_n = n\Delta z$, is the position at the step n. We can then rewrite the coupled-mode equations 2.19 and 2.20 in iterative form (and implement the spatial distribution terms) as

$$A_n = \phi_{\mathrm{L}} A_{n-1} + \Delta z\left[-i\kappa\phi_{\mathrm{L}} B_{n-1} e^{i2\Delta\beta\Delta z} + \; g_{n-1}\phi_{\mathrm{L}} A_{n-1}\right], \tag{2.88}$$

$$B_n = \phi_{\mathrm{L}} B_{n-1} + \Delta z\left[i\kappa\phi_{\mathrm{L}} A_{n-1} e^{-i2\Delta\beta\Delta z} - \; g_{n-1}\phi_{\mathrm{L}} B_{n-1}\right], \tag{2.89}$$

with $A_0 = 0$ (boundary condition), $B_0 = G$ (guess). These equations are used in the grating regions, and, in the gap region between the two reflectors, the grating term is omitted ($\kappa = 0$). The pump powers are only absorbed in all regions and can be expressed as

$$P_{\mathrm{P,fwd},n} = \Phi_{\mathrm{P}} P_{\mathrm{P,fwd},n-1} + \alpha_{n-1} \Phi_{\mathrm{P}} P_{\mathrm{P,fwd},n-1} \Delta z, \tag{2.90}$$
$$P_{\mathrm{P,bwd},n} = \Phi_{\mathrm{P}} P_{\mathrm{P,bwd},n+1} + \alpha_{n+1} \Phi_{\mathrm{P}} P_{\mathrm{P,bwd},n+1} \Delta z. \tag{2.91}$$

Equation 2.91 represents the backward pump propagation, as shown in Figure 2.21.

Even though we implement the general equations, we will solve them at the Bragg wavelength, since our focus is to investigate the peak laser output power and efficiency. This will provide us with an upper limit for the laser efficiency, since DBR lasers are typically multimode and mode competition can occur, promoting lasing at several wavelengths simultaneously. The strong gratings used in this work often make lasing at the edge of the grating stopband more favourable (as we will see in Chapters 4 and 5). However, when we optimize the cavities in Chapter 6, we will see that the best slope efficiencies are achieved with weaker output gratings, which makes the emission at the Bragg wavelength approximation valid. While it is possible, in principle, to solve them for a given wavelength range, the computational cost can be prohibitive and it does not necessarily provide us significant further insights regarding the cavity behavior, which we can more easily investigate through its passive properties.

2.4.2.3. Material Property Input Parameters

As we have seen throughout this chapter, many input parameters are required to solve the differential equations that describe a DBR laser. Tables 2.1 and 2.2 summarize the spectroscopic parameters used in the erbium- and thulium-based laser models used in this work. Not all of them are known for our rare-earth-doped tellurite thin films and further spectroscopy studies must be carried out to determine all the parameters accurately. As a result, some parameters are assumed to be the same as published values from other types of tellurite glass or other materials, as indicated in the tables. The remaining parameters, such as err, G_1, ΔG, Δz, etc., can be found in the Matlab codes available in Appendices III and IV.

Table 2.1. Spectroscopic parameters for Er^{3+}-based DBR laser model.

Parameter	Description	Value	Unit	Source
$\sigma_{\mathrm{abs,pump}}^{1470}$	Pump absorption cross section at 1470 nm	$2.98 \cdot 10^{-25}$	m²	[230]
$\sigma_{\mathrm{em,pump}}^{1470}$	Pump emission cross section at 1470 nm	$4.1 \cdot 10^{-26}$	m²	
$\sigma_{\mathrm{abs,laser}}^{1530}$	Laser absorption cross section at 1530 nm	$7.16 \cdot 10^{-25}$	m²	
$\sigma_{\mathrm{em,laser}}^{1530}$	Laser emission cross section at 1530 nm	$6.99 \cdot 10^{-25}$	m²	
$\sigma_{\mathrm{abs,laser}}^{1550}$	Laser absorption cross section at 1550 nm	$3.69 \cdot 10^{-25}$	m²	
$\sigma_{\mathrm{em,laser}}^{1550}$	Laser emission cross section at 1550 nm	$4.42 \cdot 10^{-25}$	m²	
$\sigma_{\mathrm{abs,laser}}^{1560}$	Laser absorption cross section at 1560 nm	$2.76 \cdot 10^{-25}$	m²	
$\sigma_{\mathrm{em,laser}}^{1560}$	Laser emission cross section at 1560 nm	$3.91 \cdot 10^{-25}$	m²	
$W_{\mathrm{ETU_a}}$	Upconversion parameter	$2.8 \cdot 10^{-24}$	m^3s^{-1}	
τ_1	Lifetime of excited state $^4I_{13/2}$	$620 \cdot 10^{-6}$	s	Measured [Chapter 4]
τ_2	Lifetime of excited state $^4I_{11/2}$	10^{-6}	s	Assumed

Table 2.2. Spectroscopic parameters for Tm^{3+}-based DBR laser model.

Parameter	Description	Value	Unit	Source
$\sigma_{\mathrm{abs,pump}}^{1610}$	Pump absorption cross section at 1610 nm	$1.9\cdot10^{-25}$	m²	Tellurite fiber [252]
$\sigma_{\mathrm{em,pump}}^{1610}$	Pump emission cross section at 1610 nm	$1.5\cdot10^{-26}$	m²	
$\sigma_{\mathrm{abs,laser}}^{1875}$	Laser absorption cross section at 1875 nm	$9.6\cdot10^{-26}$	m²	
$\sigma_{\mathrm{em,laser}}^{1875}$	Laser emission cross section at 1875 nm	$6.6\cdot10^{-25}$	m²	
τ_1	Lifetime of excited state $^3F_4$	$\sim300\cdot10^{-6}$	s	[253]
τ_3	Lifetime of excited state $^3H_4$	$345\cdot10^{-6}$	s	Tellurite glass [238]
Ω	Branching ratio	0.082	–	
W_{ETU}	Upconversion parameter	$\sim5\cdot10^{-24}$	m^3s^{-1}	YAG:Tm^{3+} [229]
W_{RETU}	Cross relaxation parameter	$\sim1.8\cdot10^{-22}$	m^3s^{-1}	

2.4.2.4. Calculation Steps

Figure 2.23 shows a flowchart summarizing the laser calculation algorithm. After entering the input parameters and setting a tolerance, we choose the initial guess. Next, we use the known values at $z = 0$ to solve the rate equations and calculate the gain and absorption coefficients at the origin. Then, we propagate all the parameters along z using their values at the adjacent position. When we reach the point $z = L$, we check if the backward-propagating auxiliary field satisfies $B(L) < \mathrm{err}$. If it does, we have found the solution. Otherwise, we update the initial guess and propagate the parameters again, until the solution is found. We set a maximum number of iterations allowed, after which, if no solution was found, we consider that the algorithm did not converge and/or the device did not lase.

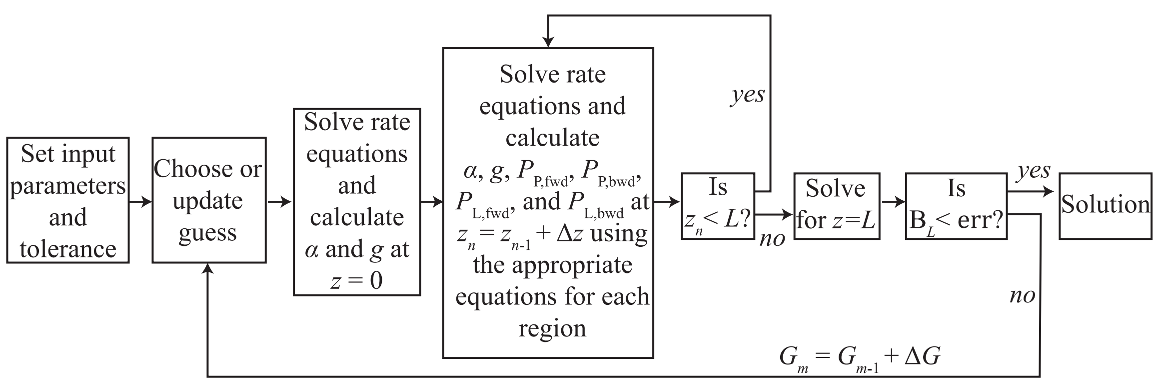

Figure 2.23. Flowchart illustrating the shooting method algorithm used to model rare-earth-based DBR lasers.

The complete Matlab implementation of the erbium and thulium laser models are available in Appendices III and IV. The original files used here are also available as open-source tools in my GitHub repository [254].

2.4.2.5. Results and Design Optimization

Once the algorithm converges and we achieve a solution, we can extract many details of the simulated device: forward and backward laser emission power, as well as the distribution along the direction of propagation of pump and laser powers, gain and absorption coefficients, and average population of each energy level. By solving the problem for different pump powers, we can also calculate the laser slope efficiency and threshold by linearly fitting the output laser power in each direction.

We can then use the model to gain insight into optimized laser designs. By varying different parameters, we obtain trends such as laser slope efficiency as a function of grating length/strength, cavity length, emission wavelength, pump wavelength, background loss, and rare earth ion concentration.

2.5. Summary

In this chapter, we covered the fundamental theory behind the work reported in this thesis. We started with an introduction to waveguide theory. Then, we explored waveguide Bragg grating theory using coupled-mode theory and the transfer matrix method, with and without a gain medium. We used the theoretical formalism to describe distributed Bragg reflector cavities and their properties, such as transmission spectrum, penetration and effective length, free spectral range, finesse, and grating-induced losses. Next, we described the population dynamics of erbium- and thulium-doped gain media, which were used to implement laser models based on the shooting method applied to the coupled-mode theory equations.

As we progress through this thesis, we will often refer to the formalism and equations presented here, avoiding unnecessary repetitions. In particular, the design and data analysis presented in Chapter 3 are based on the content of Section 2.2, which not only introduced the Bragg grating theory, but also provided us with a method to empirically extract grating properties by investigating symmetric DBR cavities. The laser modeling method presented in Section 2.4 will be validated in Chapter 6 against experimental data and used to propose optimized erbium- and thulium-based DBR laser cavity designs.

3. Design, Fabrication, and Passive Characterization

This chapter discusses the design, fabrication, and characterization of distributed Bragg reflector cavities in a hybrid platform that combines CMOS-compatible silicon nitride chips with tellurite glass, operating in the O- and C-bands. It is organized in three main sections. The first one revolves around the approach used to design sidewall and multipiece waveguide Bragg gratings. The second focuses on the fabrication and post-processing steps followed to achieve working devices. Then, the last section reports on the passive properties of uniform gratings and distributed Bragg reflector cavities, obtained through analysis of measured optical transmission spectral data. As we will see, several fabrication aspects make it challenging to reliably achieve the small features necessary for Bragg gratings, which are extremely sensitive to fabrication variations. The main results obtained include cavity Q factors on the order of (0.7–11)·10^5 and finesses between 3.0 and 72 with grating coupling coefficients between 1110 and 2860 m^{-1}. The grating-induced losses were found to be within the measurement resolution, indicating an upper-limit loss of < 0.8 dB/cm for 100-nm-wide sidewall gratings operating in the C-band.

3.1. INTRODUCTION

In Chapter 1, I mentioned that two wavelength ranges are of particular interest in integrated photonics, namely the O- and C-band, which stand for the original (1260–1360 nm) and conventional (1530–1565 nm) band, respectively. Both bands are important, due to their excellent transmission characteristics that made them ubiquitous in optical fiber-based telecommunications. In fact, the development of integrated photonics components operating in these wavelength ranges is crucial for improving the capabilities of optical communications systems. By developing active and passive on-chip components within these bands, we can leverage the established fiber technology and promote seamless integration with existing networks, while enabling new functionalities with reduced power consumption and cost.

Bragg gratings are periodic structures that can reflect specific wavelengths of light in a distributed manner. They are compact and versatile mirrors that can be tailored to achieve fully customized optical properties such as reflection bandwidth and strength. Fiber Bragg gratings (FBG) have found remarkable success over the last decades in applications including filters [255], and temperature and strain sensors [256]. They have been extensively used to make optical cavities, such as distributed Bragg reflector (DBR) and distributed feedback (DFB) cavities. In these configurations, Bragg-grating-based lasers have been achieved yielding high power, high efficiency, and narrow linewidths [11]. Such lasers have been widely used in applications including medicine, defense, and industry [11].

In integrated photonics, waveguide Bragg gratings have been extensively studied in various platforms, including silicon-on-insulator [209,257], silicon nitride [258], lithium niobate [259], phosphate glasses [205], alumina [211], and hybrid alumina-silicon nitride [66]. These examples include sidewall and multipiece gratings as the ones discussed in this work, as well as surface corrugated gratings. Several methods for patterning gratings have been explored, such as direct writing [206], laser interference lithography [211], and UV exposure [205]. In particular, Bernhardi has studied surface-corrugated Bragg gratings in alumina waveguides coated with silica as a top layer in which the gratings were patterned via laser interference lithography followed by a reactive-ion etch step [218]. The study proposed here follows a similar approach as in his previous work, applying analogous methods to sidewall and multipiece gratings in a hybrid platform instead.

In this chapter, we investigate the design, fabrication, and experimental aspects of passive Bragg grating-based devices operating in the O- and C-band using a hybrid tellurite-silicon nitride platform. Here, we consider undoped tellurium dioxide to first understand the optical behavior of distributed Bragg reflector cavities with different grating designs before we investigate their potential for lasing in the next chapters. The small feature sizes required and high sensitivity of the gratings make them challenging to fabricate. This is the first time Bragg gratings are investigated in this platform and this work aims to demonstrate their feasibility and lay the groundwork for the development of enhanced devices in the future. By fully understanding these cavities, we can gain insight into optimizing them to build efficient lasers. The cavities operating around 1310 nm can pave the way to achieve praseodymium- or neodymium-doped tellurite lasers, which require further research and are yet to be demonstrated in this platform. On the other hand, cavities operating around 1550 nm can be used to achieve erbium-based lasers as we will see in Chapter 4.

3.2. Design

The starting point in designing integrated photonic devices is to choose the basic waveguide geometry for the intended application, in this case hybrid TeO_2-Si_3N_4 distributed Bragg reflector lasers. For this project, LioniX foundry provided us with the option to fabricate 0.2- and 0.1-µm-thick silicon nitride chips using the same lithography mask. Leveraging these two silicon nitride thicknesses, we can engineer the hybrid waveguide's effective index to operate at different wavelengths using a single grating period. My approach here was to design devices that could operate within either the O- or C-band depending on the silicon nitride and tellurite thicknesses. This strategy allows the use of a single lithography mask to produce both sets of devices, significantly reducing the design efforts and fabrication costs.

The main goal of this work was to achieve erbium-based DBR lasers, which led me to first design the devices for 1550 nm operation using 0.2-µm-thick silicon nitride waveguides. Then, the same waveguide widths were considered for 0.1-µm-thick SiN to engineer the effective index for operation near 1310 nm by adjusting the thickness of the tellurite layer, which is added in a post-processing step at McMaster University.

As we discuss the design steps, you will notice that I frequently refer to fabrication aspects, even though fabrication will formally be discussed in Section 3.3. This is due to the small feature sizes intrinsic to Bragg gratings, which often require working on the edge of what is feasible using current nanopatterning technology, especially for first-order Bragg gratings such as the ones investigated in this work. Consequently, fabrication feasibility is an important consideration that cannot be ignored throughout the design process.

3.2.1. Hybrid TeO_2-Si_3N_4 Waveguide Geometry

For 1550 nm operation, the SiN thickness (t_{SiN}) was chosen to be 0.2 μm to allow for sufficient overlap with the active medium [86]. The designed TeO_2 thickness ($t_{\mathrm{TeO_2}}$) was selected as 0.35 μm to account for fabrication variability, so that the Bragg condition can be matched within the optimal tellurite thickness range of 0.25 μm < $t_{\mathrm{TeO_2}}$ < 0.45 μm that enables lateral mode confinement and integration with tight bend radii (< 300 μm), as previously studied by Frankis et al. [86]. The total device length, L_{total} = 10 mm, is the length of the chip, defined by the lithography reticle size, and is such that the device is long enough to fit several combinations of grating lengths. Moreover, the waveguides include an offset of 0.5 mm from each chip facet before the grating region starts, meaning that the DBR cavities have a maximum length of 9 mm from the beginning of the input grating until the end of the output reflectors. The waveguide width (w_{SiN}) was chosen as 1.2 μm, which is close to the single mode cutoff [86]. Single-mode operation is desirable to maximize the power coupled into the fundamental mode because the Bragg response is sensitive to the mode effective index and other modes are not reflected. Figure 3.1a illustrates the chosen waveguide geometry, in which an additional 0.5-μm-thick silica cladding was considered, because in most applications a passivation layer is desired to protect and insulate the devices. Figure 3.1b summarizes RSoft simulation results indicating that this structure has an effective index of ~1.83 at 1550 nm, using undoped tellurite's typical refractive index of $n_{\mathrm{TeO_2}} = 2.08$[6]. The mode overlap with the tellurite layer is 62.6%. If we calculate the Bragg condition (Equation 2.10) using the simulated effective index, we find that a grating period of around 420 nm is required to reflect light in the C-band.

Now, if we consider the same SiN waveguide width of 1.2 μm, but with a thickness of 0.1 μm, it is possible to find the appropriate tellurite thickness needed to reflect wavelengths in the O-band with the same grating period of 420 nm. Using the Bragg condition again, an effective index of 1.56 is needed to reflect 1310 nm wavelength, which can be achieved with a ~0.07-μm-thick tellurite layer, as shown in Figure 3.1c and Figure 3.1d. In this case, 16.9% mode overlap with TeO_2 can be attained. However, there is room to increase the tellurite thickness (and overlap) if we do not use a silica cladding or replace it with a lower refractive index material, as we will see throughout this chapter.

[6] The undoped tellurite refractive index can be slightly lower depending on the film stoichiometry. We have observed values as low as 1.99 when it is doped, as it tends to decrease with increasing dopant concentration.

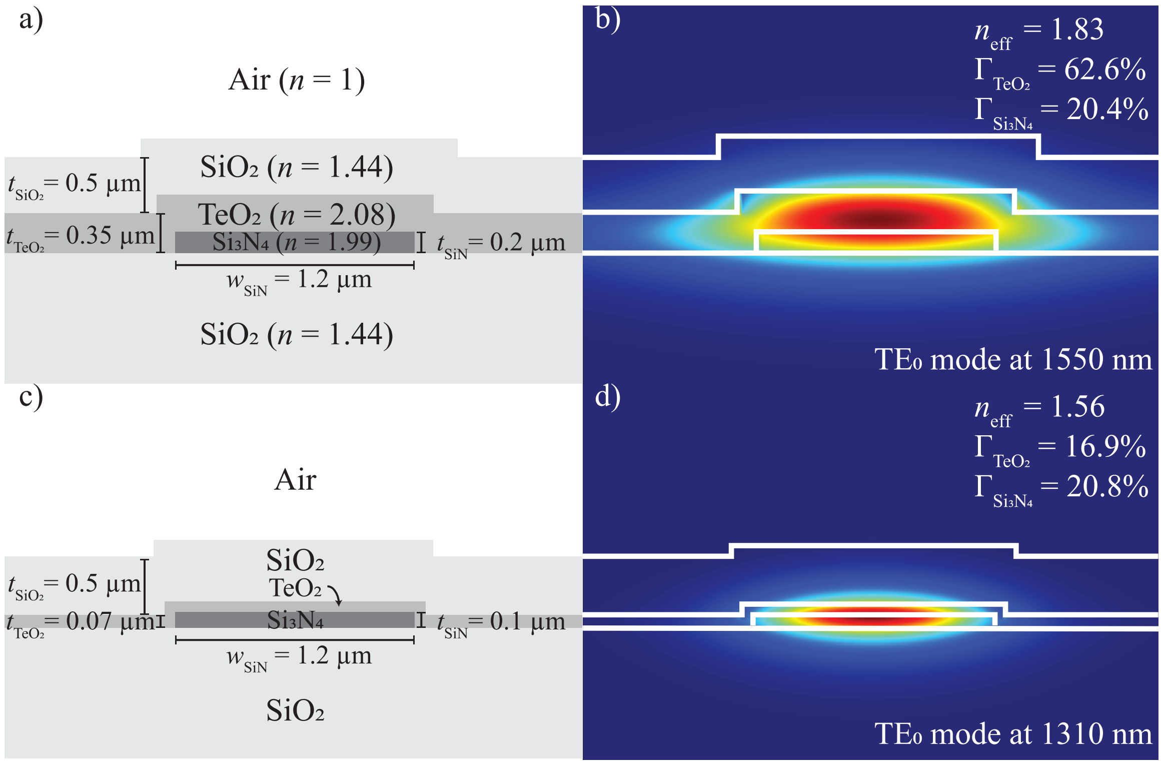

Figure 3.1. a, b) C-band and **c, d)** O-band waveguide cross section and fundamental TE mode profile, respectively.

3.2.2. Grating Geometry and Reflectivity

Now that we have chosen the waveguide structures, we can use them as baselines to define the grating designs and estimate their response for different geometries. As we designed the waveguide cross section, it was impossible to dissociate it from the grating design, since we had to engineer its effective index to guarantee operation at the desired wavelength ranges. As a result, we have fixed the grating period as 420 nm. Now, we will focus our efforts on designing the grating shape and size. In this LioniX fabrication run, we allocated 2.4 × 10 mm² of footprint to study the gratings. Moreover, we decided to prepare four device blocks with different cavity configurations and grating designs. Two of those blocks were chosen to be dedicated to the study of sidewall gratings, while the other two would be focused on multipiece, pillar gratings. In this section we will discuss the grating design process used, not only to justify my design choices, but also to hopefully provide guidelines for future Bragg grating-based work in this platform.

The general workflow to design the Bragg gratings involves the following steps:

- Simulate the unperturbed waveguide fundamental TE mode profile, and use its effective index to determine the grating period for the desired operating wavelength;

- Repeat the mode simulation, but now considering the waveguide cross section in the presence of gratings and extracting the confinement factor in the grating features. In RSoft, this is done by using the partial power monitor;
- Use Equation 2.14 to estimate the grating coupling coefficient κ;
- Use Equation 2.36 to calculate the peak reflectivity for different grating lengths L_{grating};
- Iterate this process until suitable combinations of κ and L_{grating} are found to achieve the desired reflectivity. Keep in mind that increasing κ will also increase the transmission stopband, as discussed in Chapter 2.

In this work, κ was designed to enable reflectivities greater than 90% for grating lengths of ~ 3 mm. With this choice, we can achieve a wide reflectivity range for grating lengths between 0.5 and 3 mm, while allowing to fit several gap variations between two sets of 3-mm-long grating within the maximum length available of 9 mm.

3.2.2.1. Sidewall gratings

This project was the first time that our research group designed Bragg grating-based devices for the LioniX platform. As a result, there were two main concerns about how the fabricated gratings would deviate from the designed geometry. The first revolved around an expected rounding of the grating features, which is intrinsic to the lithography process used to pattern them [260], rather than the well-defined rectangular gratings obtained from electron-beam writing [261]. This effect arises from the fact that the grating width is typically in the order of tens of nanometers, well below the minimum feature size of 300 nm recommended by the foundry (which is double the 150 nm resolution of the stepper used). The grating rounding can have a direct impact on the estimated grating coupling coefficient potentially making them weaker due to a smooth width variation, as opposed to the rectangular, step function-like shape used to derive the theoretical formalism discussed in Chapter 2. The second concern arouse from the fact that a grating period of 420 nm means that each feature has a length of 210 nm in a 50% duty cycle, which was the preferred duty cycle for simplicity. This length is below the recommended minimum feature size available and could result in significant wavelength shifts in the grating response (if the period is off) or in the grating not being patterned altogether. It was important to discuss all these considerations with the foundry during the design process to make sure that the devices could be fabricated. From these discussions, it was determined that the proposed period was feasible, and the rounding would be the main deviation from the designed geometry. This means the operation wavelength of the fabricated devices would be close to the expected, but there would be some uncertainty on how strong the gratings would be. Therefore, we opted for relatively wide gratings in case they turned out weaker than expected and to ensure they would be properly patterned.

Figure 3.2 illustrates the sidewall grating design. In the unperturbed region, the silicon nitride waveguide width is $w_{\text{SiN}} = 1.2$ µm. Within the grating region, its width is modulated between minimum (w_{min}) and maximum (w_{max}) widths as defined in Figure

3.2, such that the effective index modulation is centered at that of the unperturbed region, matching the indices of both sections (see transition highlighted by the dashed circle). This symmetrical modulation around the unperturbed waveguide effective index helps maintain the Bragg wavelength roughly constant with varying sidewall widths [257].

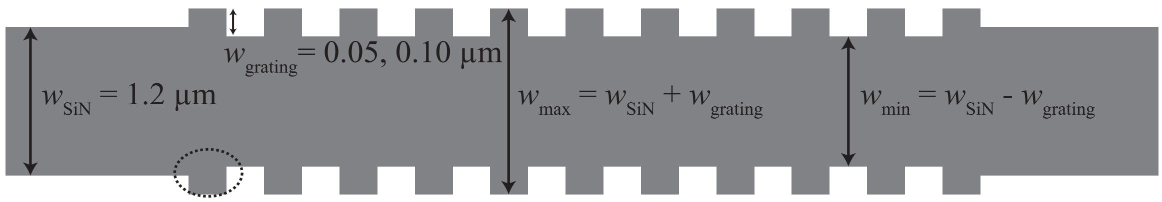

Figure 3.2. Sidewall grating design.

By implementing the waveguide cross section when $w_{\mathrm{SiN}} = w_{\mathrm{max}}$ in RSoft, and drawing the grating features as separate shapes, we can define partial power monitors that output the mode overlap (confinement factor) with each grating tooth. The total grating confinement factor was obtained by adding both contributions (or simply multiplying the overlap with a single tooth by 2 due to symmetry). Figure 3.3a shows how the grating's coupling coefficient κ varies with its width, calculated using Equation 2.14. Despite the difference in electric field distribution shown in Figure 3.1b and 3.1d, the chosen sidewall design allows for similar grating strength in both O- and C-band for their respective designs described in Figure 3.1a and Figure 3.1c. Considering the fabrication aspects and the desired reflectivity-length balance discussed earlier, the sidewall grating widths were chosen to be 50 and 100 nm. The simulation results show that 0.34% (0.74%) and 0.55% (1.07%) of light overlaps with each 50 nm (100 nm) grating tooth for the O- and C-band design, respectively.

Figure 3.3b shows the theoretical grating reflectivity as a function of grating length for all the sidewall designs used in this work. Additionally, Table 3.1 shows the theoretical reflectivity for the grating lengths that will be used in Section 3.2.4 to build symmetrical DBR cavities.

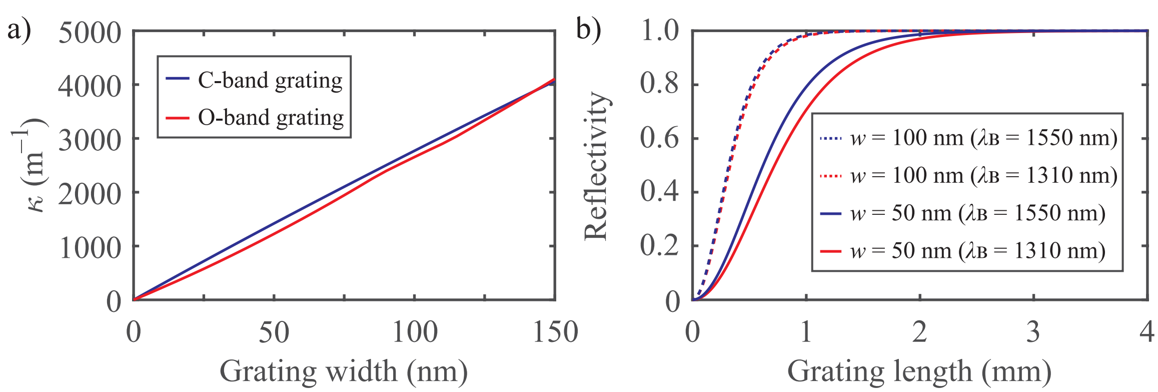

Figure 3.3. a) Grating coupling coefficient as a function of sidewall grating width and **b)** peak reflectivity as a function of grating length for the chosen grating designs.

Table 3.1. Designed sidewall grating lengths and their respective reflectivity.

Grating width (μm)	Bragg wavelength (nm)	$\Gamma_{\mathrm{grating}}$ (%)	κ (m^{-1})	L_{grating} (mm)	R (%)
0.05	1310	0.68	1222.4	0.50	29.7
				0.75	52.5
				1.00	70.6
				1.25	82.8
				1.50	90.3
				2.00	97
				2.50	99.1
				3.00	99.7
				4.00	99.9
	1550	1.1	1420.8	0.50	37.3
				0.75	62.1
				1.00	79.2
				1.25	89.2
				1.50	94.5
				2.00	98.6
				2.50	99.7
				3.00	99.9
				4.00	99.99
0.1	1310	1.49	2662.4	0.50	75.6
				0.75	92.9
				1.00	98
				1.25	99.5
				1.50	99.8
				2.00	99.99
				2.50	99.999
				3.00	100
				4.00	
	1550	2.14	2769.7	0.50	77.8
				0.75	93.9
				1.00	98.4
				1.25	99.6
				1.50	99.9
				2.00	99.99
				2.50	99.999
				3.00	100
				4.00	

3.2.2.2. Multipiece Gratings

A similar procedure was followed to design the multipiece gratings. Here, we chose the grating width to be 300 nm, the recommended minimum feature size by the foundry. Then, the grating coupling coefficient was designed by adjusting the gap between the grating and the waveguide. The design is shown in Figure 3.4 and here, unlike the sidewall gratings, the waveguide width is constant throughout the entire device. However, there are linearly tapered regions with length $L_{\mathrm{taper}} = 50$ μm in addition to the nominal grating length to smoothly transition in and out of the perturbed region. Figure 3.5a shows how the grating coupling coefficient varies with gap size (g), exhibiting orders of magnitude of variation over a 1.5-μm range. This behavior is significantly different from that of the varying sidewall grating width due to the evanescent field behavior of the electric field distribution as we move away from the waveguide sidewalls. As a result, the taper was designed in a way that the widest gap, g_{max}, was around 1.4 μm, meaning that within the taper region the gap varies by ~ 0.01 μm after each grating period.

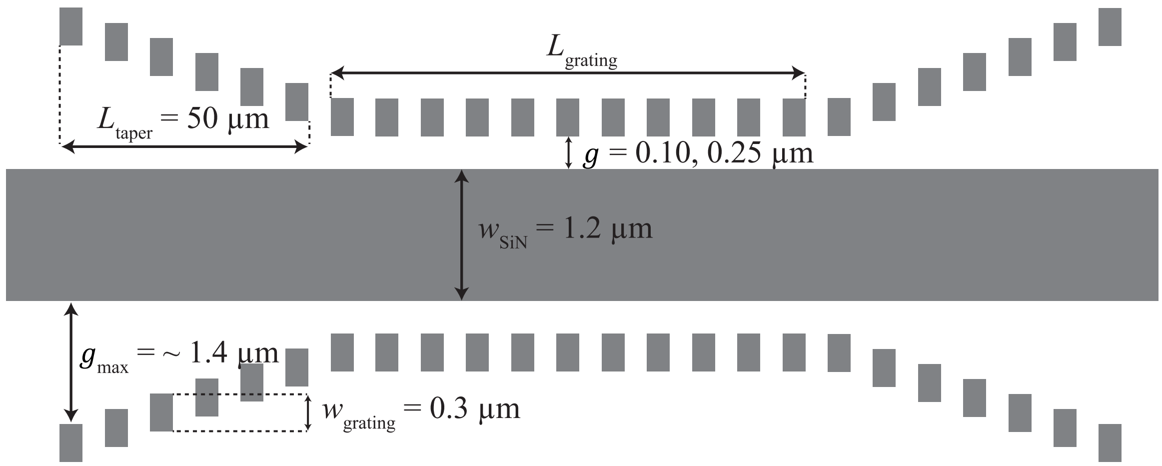

Figure 3.4. Multipiece grating design.

The gaps were chosen as 0.1 and 0.25 μm. The former because it is when the gratings are expected to have similar responses in each wavelength range and the latter because it is when the multipiece gratings are expected to have similar strength as the 0.1-μm-wide O-band gratings. The fabricated multipiece gratings are also expected to be particularly affected by the patterning step, not only being significantly rounded, but also being much narrower than the designed 0.3-μm width. This can have a significant impact on the grating confinement factor and, therefore, on the designed coupling coefficient. Such uncertainty led us to opt for designing strong gratings in case they turned out to be much weaker than estimated. Figure 3.5b shows the theoretical reflectivity as a function of grating length for the chosen multipiece designs and Table 3.2 summarizes the grating lengths that will be used later to make DBR cavities and their respective reflectivities.

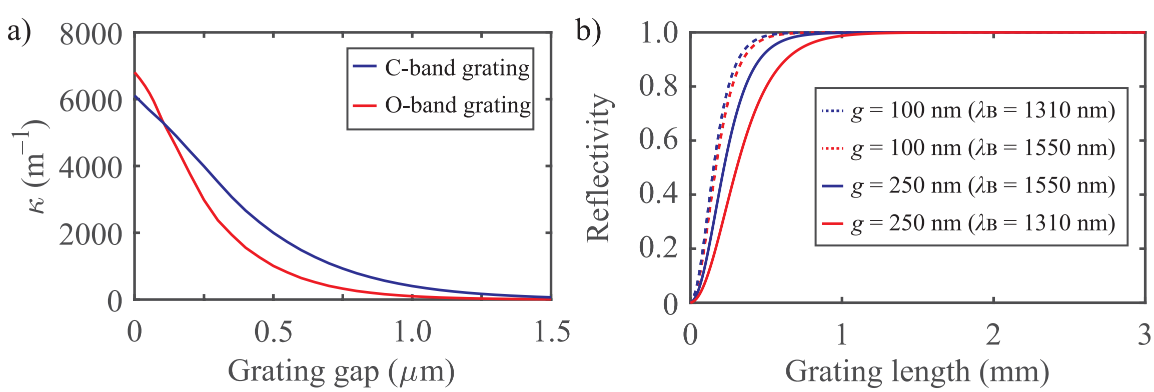

Figure 3.5. a) Grating coupling coefficient as a function of multipiece grating gap and **b)** peak reflectivity as a function of grating length for the chosen grating designs.

Table 3.2. Designed multipiece grating lengths and their respective reflectivities.

Grating gap (μm)	Bragg wavelength (nm)	$\Gamma_{grating}$ (%)	κ (m^{-1})	$L_{grating}$ (mm)	R (%)
0.1	1310	3.22	5763.3	0.50	98.7
				0.75	99.9
				1.00	99.99
				1.25	99.999
				1.50	100
				2.00	
				2.50	
				3.00	
				4.00	
	1550	4.07	5256.3	0.50	97.9
				0.75	99.8
				1.00	99.99
				1.25	99.999
				1.50	99.9999
				2.00	100
				2.50	
				3.00	
				4.00	
0.25	1310	1.61	2881.1	0.50	79.9
				0.75	94.8
				1.00	98.7
				1.25	99.7
				1.50	99.9
				2.00	99.99
				2.50	99.999
				3.00	100
				4.00	
	1550	3.09	3984.2	0.50	92.8
				0.75	98.99
				1.00	99.8
				1.25	99.98
				1.50	99.999
				2.00	100
				2.50	
				3.00	
				4.00	

3.2.3. Effective Index Engineering and Sensitivity

In laser applications, one might prefer to have the gratings under a silica cladding and apply the active gain medium in an oxide window opening between the reflectors. However, in this work we opted for having the entire chip covered with tellurite, which is done in a post-processing step on the uncladded chips produced by the foundry. This approach gives us the flexibility to adjust the reflected wavelength by engineering the fundamental TE mode effective index, which is affected mainly by the tellurite thickness but also by the cladding material. Moreover, it helps to account for fabrication variability and eventual deviations from the designed grating response. Figure 3.6 shows how the effective index and Bragg wavelength vary as a function of tellurite thickness and cladding material for the two waveguide designs shown in Figure 3.1. In addition to air ($n_{\mathrm{Air}} = 1$), and silica ($n_{\mathrm{SiO_2}} = 1.44$), cladding , I have included how the device properties are affected by Cytop ($n_{\mathrm{Cytop}} = 1.33$), a protective fluoropolymer that will be introduced in Section 3.3.2.2. When thinner TeO_2 is used, the cladding has a significant influence on the effective index because of the higher mode overlap with it. As the tellurite thickness increases, the cladding effect asymptotically tends to be negligible due to decreasing mode overlap. However, in the tellurite thickness ranges used in this work, having a cladding on top of the tellurite layer can cause shifts of more than 10 nm in reflected wavelengths.

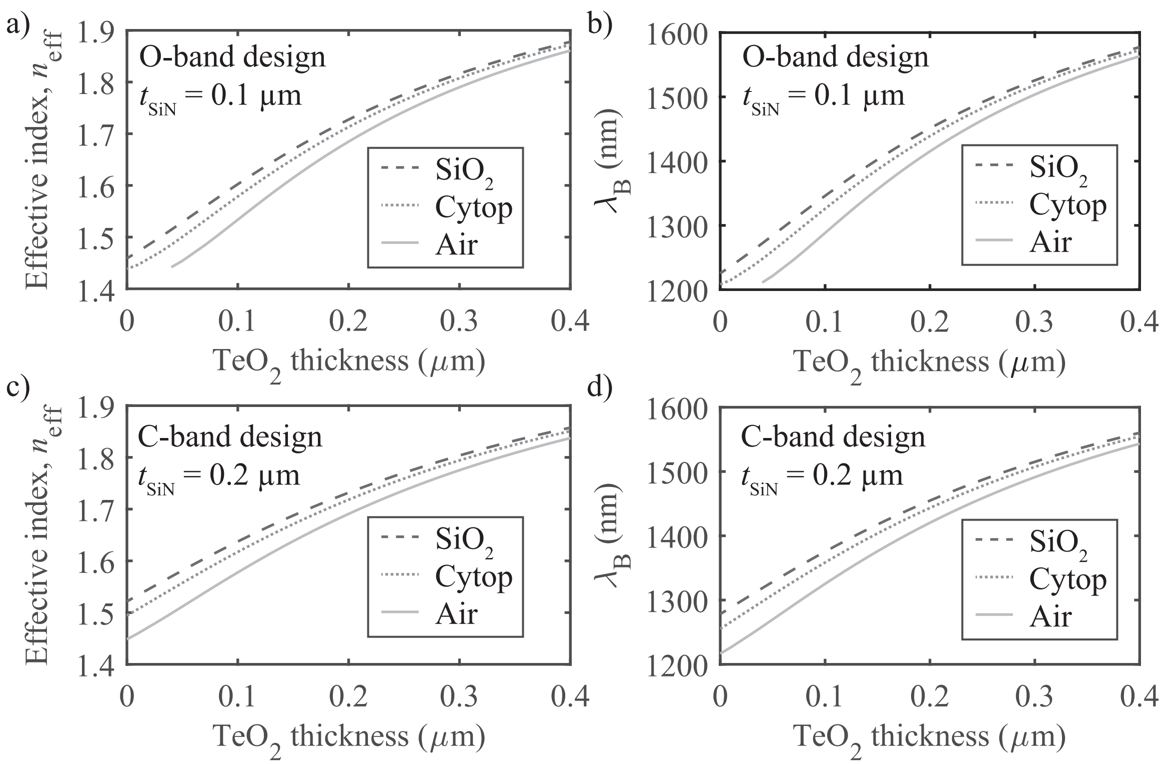

Figure 3.6. a, b) O-band and **c, d)** C-band effective index and Bragg wavelength as a function of tellurite thickness, respectively. The discontinuities in air-cladded O-band designs are due to no mode being supported with less than ~40-nm-thick TeO_2. The SiO_2 and Cytop layers are 0.5-μm-thick and have refractive indices of 1.44 and 1.33, respectively.

For both silicon nitride thicknesses, the effective index (Bragg wavelength) is drastically affected by the tellurite thickness varying by almost 0.5 (400 nm) over a few hundred nanometers. This flexibility comes at the cost of sensitivity: slight variations in the tellurite thickness (or refractive index) can have a significant impact on the reflected wavelength[7]. For instance, if we use the Bragg condition, we find that a mere 0.01 variation in the effective index can shift the grating response by more than 8 nm when the period is 420 nm. As a result, the reflected wavelength is extremely sensitive to fabrication variations, especially in the tellurite properties. Additionally, small variations in effective index across the device are enough to make two reflectors in a DBR cavity not match perfectly, deviating from the expected theoretical transmission spectrum, as we will see in Section 3.5.4.

Figure 3.6b and Figure 3.6d indicate that, in principle, both silicon nitride waveguide thicknesses could work in the O- and C-band with appropriate tellurite thickness. However, for the 0.1-μm-thick nitride waveguide, thicker TeO_2 layers (> 0.3 μm) can promote leakage into slab modes and high bend losses, which are ultimately unwanted if we were to integrate these devices into a circuit on the same chip. On the other hand, for the 0.2-μm-thick SiN gratings to operate in the O-band, very thin tellurite layers are required (< 0.05 μm), yielding an even lower mode overlap, making it challenging to produce active devices in such a configuration.

These simulations also show that gratings on neither waveguide design can operate within the thulium emission band (above 1800 nm) with the same grating period of 420 nm. In Chapter 5, we will apply the same ideas discussed here, but adjust the grating period to achieve sidewall grating-based DBR thulium lasers.

3.2.4. Cavity Variations

For each grating design, we first chose two uniform grating lengths to test their individual responses, as shown in Figure 3.7a. Moreover, we used the method introduced in Section 2.2.4.4 to further study grating properties using symmetrical DBR cavities. To do so, two sets of cavity variations for each grating design are required. The first consists of a fixed grating length and a varying gap between them, as shown in Figure 3.7b. The second set revolves around cavities with varying grating lengths, as per Figure 3.7c. Using Tables 3.1 and 3.2 as a reference, the first set was chosen to have the same gap length variations L_{gap} = 0.5, 1, 1.5, 2, 2.5, 3 mm, whereas the grating lengths were selected as L_{grating} = 3, 2, 1, 1.5 mm for 50- and 100-nm-wide sidewall, 100- and 250-nm-gap multipiece designs, respectively. In the second set, all grating designs have the same grating length variations L_{grating} = 0.5, 0.75, 1, 1.25, 1.5, 1.75, 2, 2.5, 3, 4 mm. The spacing between adjacent devices is 30 μm to avoid crosstalk between them.

In this thesis, when referring to a cavity, we will describe it using the convention $L_{\text{grating,in}} \times L_{\text{grating,out}}$ with the input and output grating lengths in millimeters, respectively. For example, a 4×3 cavity means that the reflectors are 4- and 3-mm-long and the forward-direction output is the one exiting the output grating.

The layout was prepared using Luceda IPKISS, a commercial, Python-based photonic integrated circuit design platform. The layout was visualized and edited in

[7] Here, variations in any material index and geometry will affect the effective index, but once the chips are fabricated by the foundry, the tellurite provides the largest fabrication variability, due to the research-scale nature of the deposition process used.

KLayout. The devices designed for this work (including the devices we will discuss in Chapters 4 and 5 are part of a major fabrication run and make up for approximately one third of the prepared layout with total dimensions of 22 × 22 mm². The total footprint was divided into three chiplets. Then, it was submitted to the LioniX foundry for fabrication.

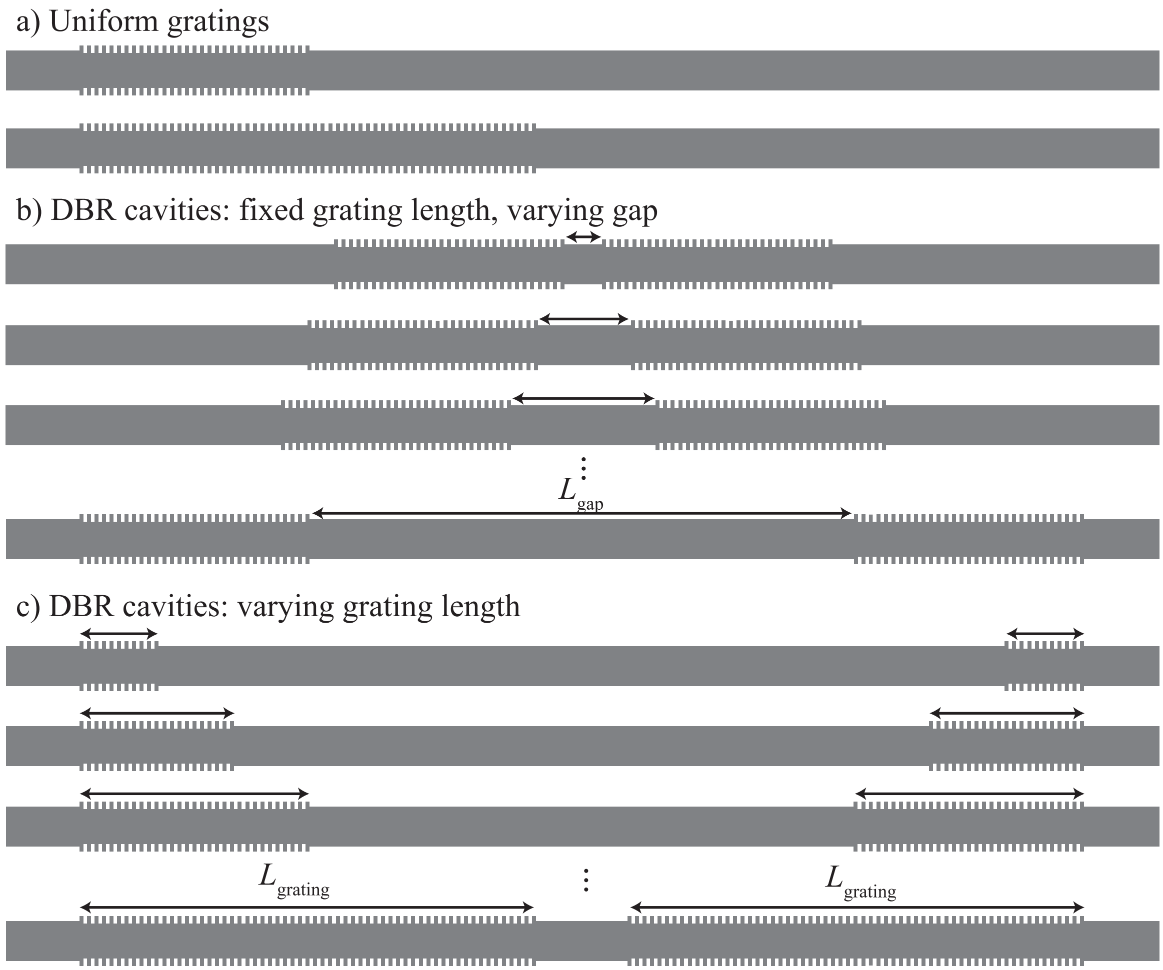

Figure 3.7. Device blocks used to study Bragg grating properties: **a)** uniform gratings, **b)** symmetrical DBR cavities with fixed grating length and varying gap, and **c)** symmetrical DBR cavities with varying grating lengths. The same approach was used for both sidewall and multipiece gratings.

3.3. Fabrication

3.3.1. Silicon Nitride Waveguides and Gratings

In the LioniX foundry, their TriPleX technology was used to fabricate the silicon nitride devices on a silicon wafer with a diameter of 100 mm, covered with an 8-µm-thick thermal oxide layer [53,262]. Their process starts with the deposition of either 0.1- or 0.2- µm-thick silicon nitride thin film via low-pressure chemical vapour deposition (LPCVD). The waveguides and Bragg gratings were then patterned by 248 nm deep ultraviolet (DUV) stepper lithography with 150 nm resolution and reactive ion etching. The wafer underwent an annealing process at > 1100 °C in an N_2 atmosphere to remove hydrogen impurities from the silicon nitride devices and minimize optical losses in the C-band due to absorption caused by Si-H and N-H bonds [86]. The uncladded wafers[8] were stealth-diced into chips, yielding high-quality facets, which are essential to achieve good fiber-chip coupling.

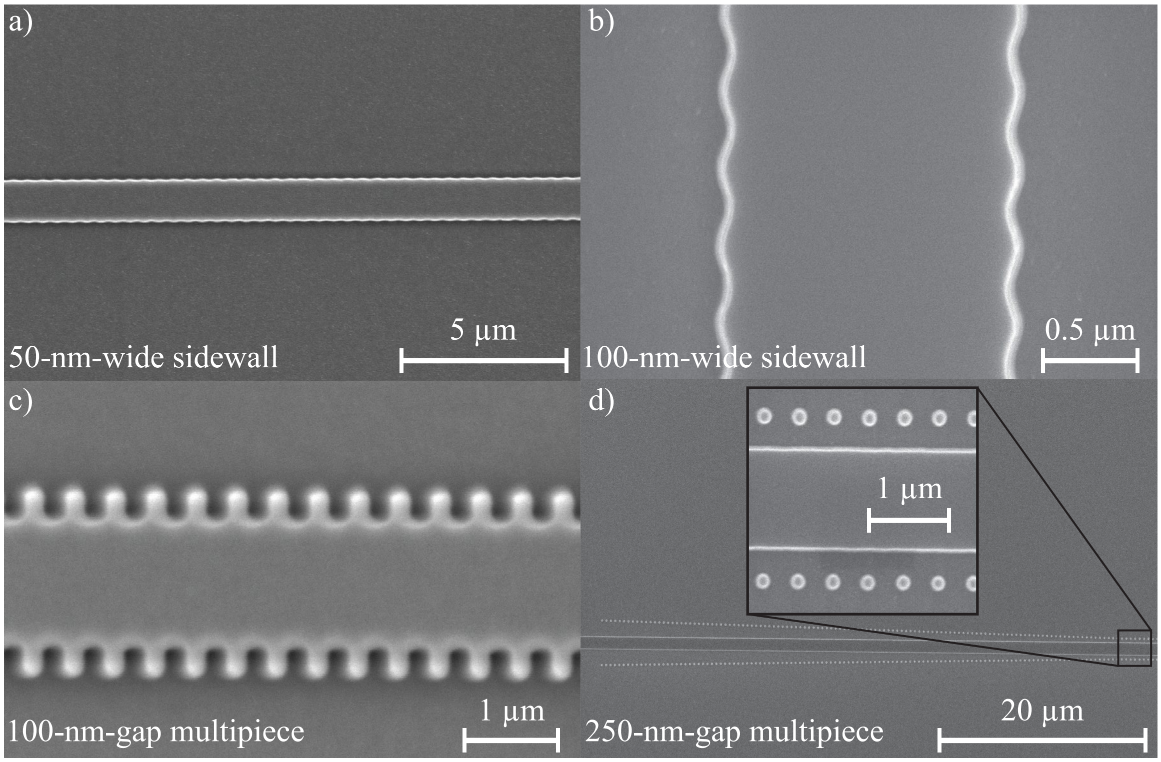

Figure 3.8. Fabricated **a, b)** sidewall and **c, d)** multipiece gratings. The designed rectangular grating features become rounded due to stepper lithography resolution. The 100-nm gap was too narrow and was not patterned properly, making these gratings too strong.

Figure 3.8 shows scanning electron microscopy (SEM) images of the uncladded 0.2-µm-thick silicon nitride devices[9]. In Figures 3.8a,b, the fabricated sidewall gratings exhibit the rounding effect expected from the lithography process. Figure 3.8c shows that the multipiece gratings with gaps of 0.1 µm were not properly fabricated due to resolution limitation, making them essentially extremely wide sidewall gratings Figure 3.8d shows the 0.25-µm gap multipiece grating tapered region and the inset shows a zoomed-in view of the region with a constant gap. With the rounding effect, the designed rectangular pillars became cylinders.

Upon preliminary testing, the transmission properties of all multipiece gratings were found to significantly deviate from the design. They were so strong that the Bragg grating perturbation theory did not predict their behavior. In general, the multipiece gratings promoted a high scattering of wavelengths below the Bragg condition and transmitted

[8] Here, the wafers are coated with a protective resist, which are removed in acetone bath upon receiving at McMaster University, before the post-processing steps.

[9] The chip was coated with a thin gold layer to avoid charge buildup and improve the imagining process.

longer wavelengths, with a response similar to a high-pass filter. As a result, we decided to focus only on the study of sidewall gratings in this work.

3.3.2. POST-PROCESSING

3.3.2.1. Reactive Sputtering of Tellurite Glass

The tellurite films were deposited onto the chips via radio frequency (RF) magnetron reactive sputtering, using a Lesker Pro PVD 200 system. The process used in this work was previously developed by Frankis and an in-depth description can be found in reference [230]. Here, the tellurite films were deposited using a metallic Te target with 3” diameter. Table 3.3 summarizes the deposition parameters[10] used to fabricate the two samples that will be discussed in Section 3.5. The temperatures reported are set on the system heater and not measured directly at the substrate (ambient temperature refers to a deposition carried out with the heater off).

Table 3.3. Sputtering parameters of deposited tellurite films.

Ar flow (sccm)	O_2 flow (sccm)	Process pressure (mTorr)	Te target RF power (W)	Temperature (°C)	Time (min)
12	5.8	3.2	60	20[a]	12
	9.8	2.7	125	150	23

[a]Ambient temperature

3.3.2.2. Spin Coating of Polymer Top-cladding

For testing purposes, we can leave tellurite-coated chips exposed to air without significant degradation, if the sample is properly maintained in a desiccator. However, after the chips were designed and fabricated, we opted to use a protective fluoropolymer, Cytop, as an alternative cladding to silica. It is a straightforward approach to passivate the samples, which can be performed through a simple spin-coating process and is well suited to device testing at this work’s level. The use of Cytop instead of silica avoided developing another fabrication process not readily available at McMaster University or using off-campus facilities. Cytop has a refractive index of 1.33 within both O- and C-bands [263], slightly lower than that of silica (~1.44). With this change, and using slightly oxygen-rich tellurite, thicker TeO_2 films were necessary to make the gratings operate at the desired wavelengths. In the case of the O-band gratings, for instance, it was possible to achieve the desired effective index with more than 0.1-µm-thick tellurite and increase the overlap to 25%.

The Cytop (type CTL-809M) was spun at 1750 rpm, and then baked on a hot plate at 50, 80, and 180 °C for 10, 30, and 30 minutes, respectively. This results in a roughly 1-µm-thick layer on top of the tellurite film.

[10] The discrepancy in parameters is because the first sample was deposited 1.5 years after the second one and after major maintenance being performed on the system. The parameters were altered, but the same deposition steps were used in both cases.

3.4. PASSIVE CHARACTERIZATION SETUP

The waveguides and cavities were characterized on an edge-coupling setup, as shown in Figure 3.9. Tunable lasers (Keysight N7778C) were used to characterize the samples within either 1240–1380 or 1450–1650 nm wavelength range, a resolution of 1 pm and output power of 1 mW. The laser output was adjusted to TE polarization through polarization paddles and coupled in and out of the chip by single-mode tapered fibers with 2.5-µm-diameter spot size, mounted on XYZ stages. The device output was measured by a power meter (Keysight N7742C).

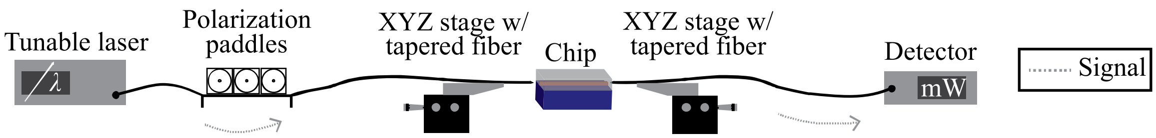

Figure 3.9. Edge coupling setup used to passively characterize devices.

3.5. RESULTS

3.5.1. TELLURITE FILM PROPERTIES

First, ellipsometry measurements were performed on a bare silicon witness piece to find the thickness and refractive index of the deposited tellurite films. This was carried out using a Woollam variable angle spectroscopy ellipsometer. The O-band devices were covered with a 0.109-µm-thick tellurite layer, with a refractive index of 2.04 at 1310 nm. On the other hand, 0.43-µm-thick TeO_2 was applied to the C-band devices, with a refractive index of 2.07 at 1550 nm. It was necessary to use thicker films than designed to make the gratings operate at the desired wavelengths, because the tellurite films were slightly oxygen-rich and had refractive indices < 2.08. Moreover, we chose to substitute the silica cladding with Cytop to facilitate the post-processing steps. These two factors contributed to making the effective indices of fabricated samples lower than designed, and the tellurite thickness was adjusted to account for that.

Next, the films' optical propagation losses were measured on a thermal silica witness sample using a Metricon prism coupling system [264]. Both 0.109- and 0.43-µm-thick films had background loss of (0.2 ± 0.2) dB/cm at 1310 and 1550 nm, respectively. These losses are within the limit of detection of the prism coupling system used. Table 3.4 summarizes the measured films' properties.

Table 3.4. Summary of ellipsometry and prism coupling results for deposited tellurite films.

Thickness (µm)	Refractive index	Background loss (dB/cm)
0.109	2.04 (at 1310 nm)	0.2 ± 0.2 (at 1310 nm)
0.430	2.07 (at 1550 nm)	0.2 ± 0.2 (at 1550 nm)

3.5.2. WAVEGUIDE PROPAGATION LOSSES

The O-band waveguide losses were estimated using the cutback-method. To do so, we measured the insertion loss of waveguides with the same geometry, but varying lengths (10, 22, and 210 mm), on a chip covered with the same tellurite film as the grating-based devices. By linearly fitting the measured insertion loss versus length, we found a background propagation loss of (0.3 ± 0.2) dB/cm and a fiber-to-chip coupling loss of (3.2 ± 0.2) dB/facet, measured at 1310 nm wavelength.

The C-band waveguide losses were estimated through Q-factor measurements [225] of an undercoupled, point-coupled, 0.5-mm bend radius, 1.8-µm gap, microring resonator with the same waveguide geometry covered with a similar tellurite film (0.413-µm-thick, and same background loss from prism coupling measurements). Resonances around 1554 nm were found to have internal Q-factors around 500,000, which correspond to a background propagation loss of (0.7 ± 0.2) dB/cm. Then, by subtracting the propagation losses in a 6-mm-long waveguide from its insertion loss, a fiber-to-chip coupling loss of (4.0 ± 0.5) dB/facet was found.

3.5.3. Uniform Gratings

3.5.3.1. Typical Transmission and Effect of Polymer Top-cladding

After the tellurite deposition, the gratings were tested before and after applying Cytop and the results are shown in Figure 3.10. As expected from the design considerations made in Section 3.2.3, there is a significant shift in reflected wavelengths after the cladding is added. Figure 3.10a,b show that the O-band gratings shift by approximately 30 nm, while the C-band gratings shift by ~10 nm, as shown in Figure 3.10c,d. This is due to the greater mode overlap with the cladding in the former case, as discussed earlier. Moreover, both 50- and 100-nm-wide gratings undergo similar shifts, since they are determined mainly by the variation in effective index. Figure 3.10 also shows the expected widening of the stopband with increasing grating coupling coefficient, when the grating width is increased from 50 (a,c) to 100 nm (b,d).

Interestingly, the measurements show that the gratings become significantly stronger after the addition of Cytop. Mode simulations do not show a significant change in the grating confinement factor as a function of the top cladding and this behavior was not expected. This is partly due to changes in the tellurite density and refractive index during the Cytop baking. In fact, performing the same baking steps described in Section 3.3.2.2 on a witness Si sample covered in TeO_2 deposited at room temperature resulted in a ~ 0.003 increase in tellurite's refractive index. If we return to Equation 2.14, we notice that the grating coupling coefficient is proportional to the difference of the square of the two alternating materials that constitute the gratings, $(n_{\mathrm{TeO_2}}^2 - n_{\mathrm{SiN}}^2)$. Due to the low contrast between the two indices used here ($\lesssim 0.1$), small changes in the tellurite's refractive index can have a significant impact on the coupling coefficient. The variation in κ is more pronounced when the initial tellurite index is closer to that of silicon nitride (~1.99). This can explain why the C-band grating strengths were not affected as much, since the film deposited at a higher temperature was less subject to further changes during the baking process and had a higher initial refractive index. However, using the extinction ratios of each resonance shown in Figure 3.10 to estimate the grating coupling coefficients with air (κ_{air}) and Cytop (κ_{Cytop}) cladding (using Equation 2.36), we find the results summarized in Table 3.5[11]. The necessary increase in tellurite refractive index to achieve these shifts in κ would be in the order of 0.08 and 0.04 for the O- and C- band gratings. These shifts are one order of magnitude greater than that observed in the baked witness sample. Further investigation is needed to determine other contributions that can explain the significant increase in coupling coefficient after applying Cytop. A potential cause can be changes in the tellurite conformity around the gratings after the baking process. However, comparing the results from Table 3.5 to the designed κ values from Table 3.1, we find that κ_{Cytop} is in well agreement with the designed values, and the differences can be attributed mainly to the rounding effect in the fabricated gratings. As mentioned earlier, we opted to design strong gratings expecting they would turn out significantly weaker, which was not the case.

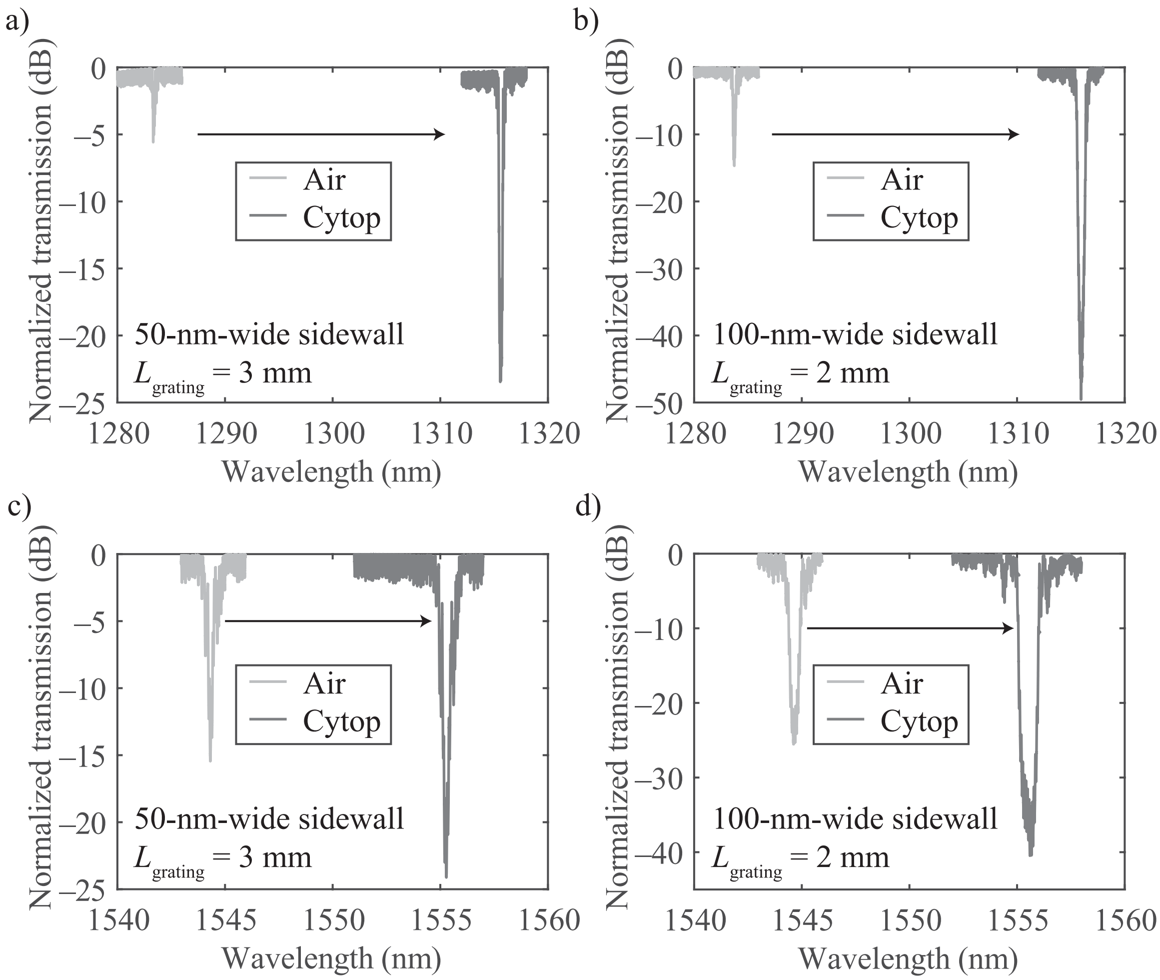

Figure 3.10. Effect of Cytop cladding on **a, b)** O- and **c, d)** C-band 50- and 100-nm-wide sidewall gratings, respectively.

[11] The uncertainties reported were estimated based on the amplitude of the Fabry-Pérot resonances that will be discussed in the next section.

Table 3.5. Estimates of change in grating coupling coefficient after applying Cytop and the necessary shift in tellurite's refractive index to achieve them.

Operating band	Grating width (nm)	κ_{air} (m^{-1})	κ_{Cytop} (m^{-1})	$\kappa_{\text{Cytop}}/\kappa_{\text{air}}$	Necessary Δn_{TeO_2}
O	50	390 ± 50	1110 ± 40	2.85	0.081
O	100	1040 ± 60	2860 ± 60	2.75	0.076
C	50	770 ± 50	1150 ± 50	1.49	0.036
C	100	1660 ± 60	2640 ± 60	1.65	0.048

Table 3.5 also shows that the same grating design has similar strength in both bands, especially after adding the Cytop cladding, agreeing with the trend shown in Figure 3.3. Since the devices will ultimately have a cladding in most applications (including the laser measurements performed in this thesis), we will focus our analysis on the samples with a Cytop cladding.

3.5.3.2. Fabry-Pérot Cavity Formed by Facet Reflections

In Figure 3.10, it is also noticeable that there is significant noise in the spectra outside the grating resonance, especially in the C-band gratings. This is due to reflections off the chip facets, which form a Fabry-Pérot (FP) cavity within the waveguide. Using a simple, plane wave normal incidence approximation, we can use Fresnel coefficients to investigate how this affects the overall device behavior. In this case, the reflectivity R and reflection coefficient r are given by [220]

$$R = |r|^2 = \left|\frac{n_1 - n_2}{n_1 + n_2}\right|^2, \tag{3.1}$$

where n_1 and n_2 are the refractive indices of the two materials that make up an interface. Here, we will consider them to be the designed effective index of the fundamental TE mode for each waveguide geometry (1.56 and 1.83 in the O- and C-band respectively) and the refractive index of air. Making this approximation, we find that 4.8% and 8.6% of light are reflected at each facet when exiting the waveguide, at 1310 and 1550 nm respectively. Next, we can model the facets as partially reflective mirrors and express their behavior using a simple transfer matrix approach [217]:

$$\boldsymbol{T}_{\mathbf{mirror}} = \frac{i}{\sqrt{1-r^2}}\begin{bmatrix} 1 & r \\ r & 1 \end{bmatrix}, \tag{3.2}$$

where $\boldsymbol{T}_{\mathbf{mirror}}$ is the transfer matrix of a partially reflective mirror and i is the imaginary unit. By doing so and, focusing on the spectral response outside the grating stopband for now, we find the response shown in Figure 3.11, which is in good agreement with the measured transmission.

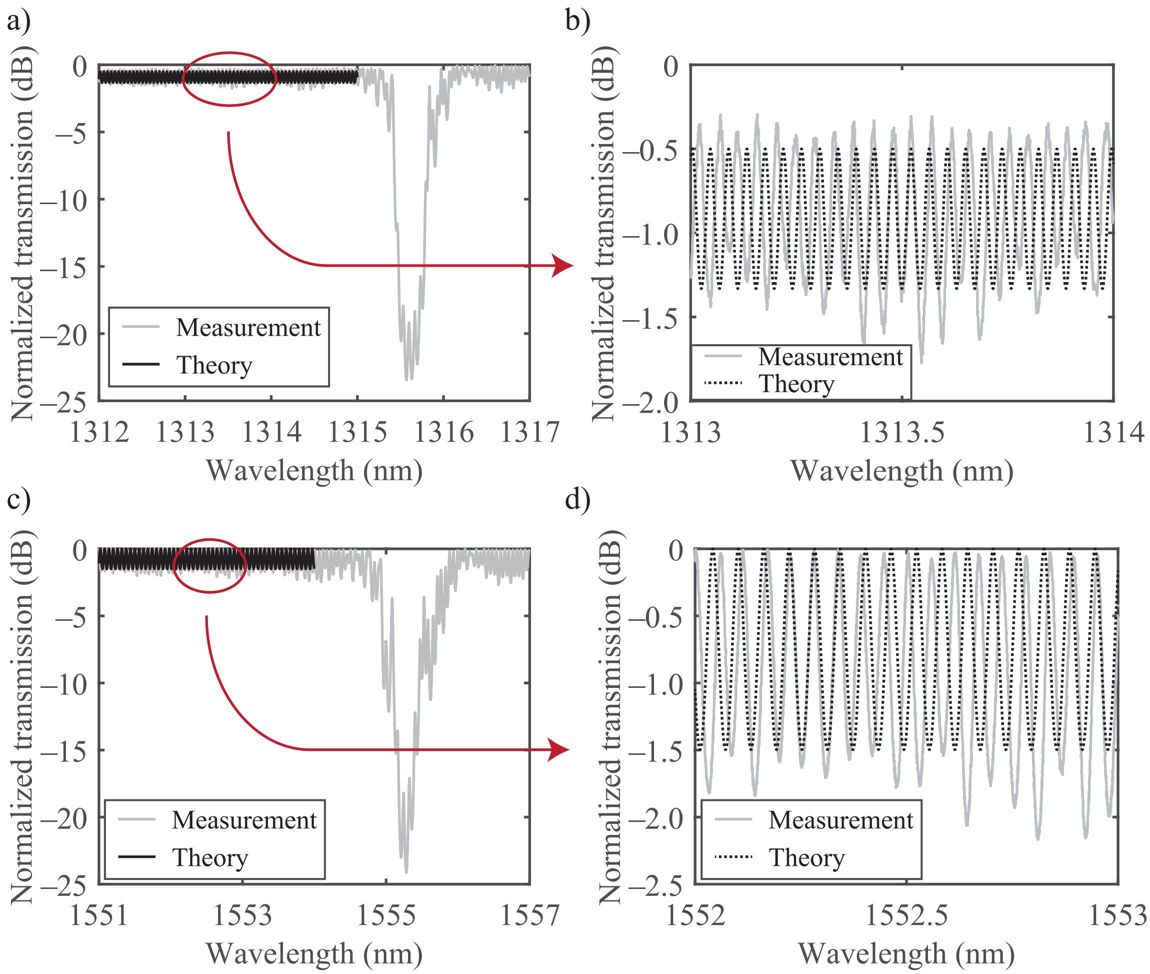

Figure 3.11. Measured and theoretical Fabry-Pérot responses due to facet reflections for fabricated **a, b)** O- and **c, d)** C-band waveguide geometries.

We can now combine the Fabry-Pérot and grating responses, by rewriting Equation 2.39 as

$$\begin{bmatrix} A(z) \\ B(z) \end{bmatrix} = \boldsymbol{T}_{\mathbf{mirror}} \boldsymbol{T}_{\mathbf{offset}} \boldsymbol{T}_{\mathbf{DBR}} \boldsymbol{T}_{\mathbf{offset}} \boldsymbol{T}_{\mathbf{mirror}} \begin{bmatrix} A(0) \\ B(0) \end{bmatrix}, \tag{3.3}$$

where $\boldsymbol{T}_{\mathbf{offset}}$ is the transfer matrix of a 0.5-mm-long straight waveguide that accounts for the offset between the edge coupler and the start of the grating regions, A, B, and $\boldsymbol{T}_{\mathbf{DBR}}$, are the forward- and backward-propagating signal and the DBR transfer matrix, defined in Chapter 2. This equation can easily be adjusted to also study uniform gratings, by changing one of the DBR reflectors length to zero, for instance.

Let us now theoretically analyze how the Fabry-Pérot cavity affects the grating response. To do so, we will focus on C-band 50-nm-wide sidewall gratings, which will provide us with an upper limit on this effect, since the FP resonances are deeper in this waveguide geometry and these gratings are weaker than those with 100-nm width. Figure

3.12a and Figure 3.12b show the theoretical response of an uniform grating[12] in the absence and presence of the Fabry-Pérot effect. Here, in addition to the noise outside the grating stopband, the FP resonances make the grating responses deviate from their typical shape by introducing some new resonances within the stopband. In fact, this theoretical response reproduces well the shape of the measured spectra shown in Figure 3.11a,c[13]. The overall grating properties (extinction ratio, resonance width) are not significantly affected, even though this distortion can introduce some fluctuation in reflectivity values calculated through the extinction ratio.

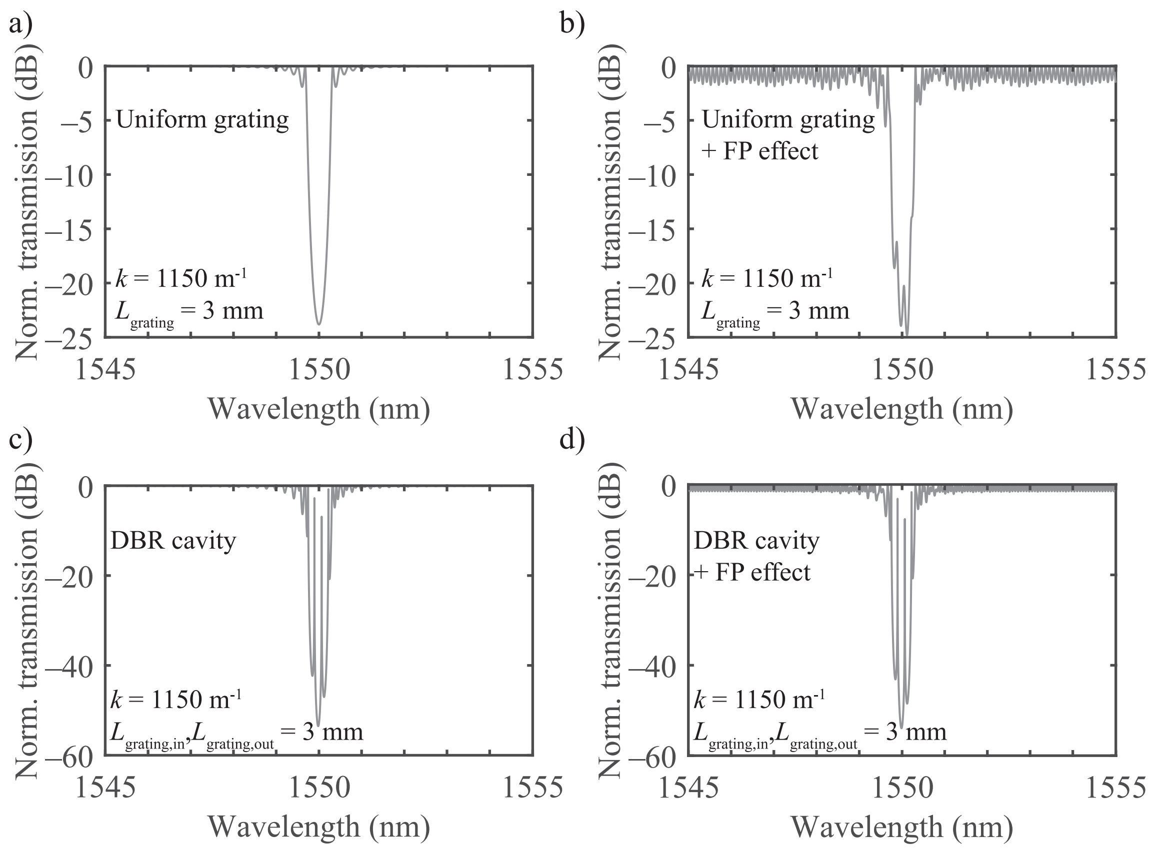

Figure 3.12. a, b) Uniform grating and **c, d)** DBR cavity response without and with the Fabry-Pérot effect from facet reflections.

Figure 3.12c shows the theoretical response of a symmetrical DBR cavity in which the two reflectors are set as the same uniform grating discussed so far. Unlike the uniform grating case, Figure 3.12d shows that within the DBR stopband, there is essentially no influence of the Fabry-Pérot cavity, while outside it behaves similarly to the uniform grating case. This is due to the much stronger reflectivity of the Bragg gratings compared

[12] Here I am considering a grating with same length and estimated coupling coefficient as in the previous sections, but still considering the designed effective index to keep the resonances centered at 1550 nm.

[13] Further deviations observed in the spectra from Figure 3.11 can be explained by the tellurite nonuniformity, which we will discuss in the next section.

to the facets, which makes the DBR cavity inside the FP cavity dominate the effective device response. Therefore, in the analyses that will follow in the remaining of this chapter, we can ignore the Fabry-Pérot effect, especially when the resonances of interest have extinction ratios that are several orders of magnitude larger than that of the FP resonances. Furthermore, the FP effect can be greatly minimized by using an index-matching fluid to fill the air gap between chip and fiber or by optimizing the edge couplers and the effective index at the chip facet to minimize the index contrast between the two regions (tapering the SiN waveguide width or the tellurite thickness using a shadow mask during deposition, for instance).

3.5.4. Symmetrical Distributed Bragg Reflector Cavities

The study of symmetrical DBR cavities can help us broaden our understanding of the gratings' properties. The method described in Chapter 2 first uses the cavities with fixed grating lengths and varying gaps to obtain the grating reflectivity and loss, by calculating the finesse of measured passive cavity response. Then, it relies on finesse measurements of cavities with varying grating lengths and the obtained loss to calculate the reflectivity of other grating lengths. To calculate the finesse, it is necessary to have at least two longitudinal mode resonances within the grating stopband (ideally more for better accuracy). However, the fabricated cavities exhibit responses that significantly deviate from the expected. The measured transmission spectra of four 3×3 50-nm-wide sidewall C-band DBR cavities with varying gaps are shown in Figure 3.13. These results show a broadening of the grating response with irregular oscillations within the stopband, which can be attributed to the fact that the two grating responses are not perfectly matching. Such an effect can be explained by the fluctuations in effective index across the device, driven mainly by nonuniformity in the tellurite film thickness. Frankis has studied the tellurite film uniformity across a 3" wafer using the same process employed in this work [230]. He found that the film thickness can have a ± 2% variation over a few centimeters, while its refractive index can vary in the order of ± 0.2%. For the TeO_2 thicknesses used here, this means a variation of 2 to 9 nm. Using the RSoft mode solver, we find that a 2% variation in tellurite thickness can introduce a variation in the effective index in the order of ±0.003 and ±0.004 in the O- and C-band waveguide geometries, respectively. This, as we will see, is sufficient to completely split the grating responses. Moreover, we find that if the Cytop thickness varies from 1 to 2 μm[14], the n_{eff} varies in the order of $5 \cdot 10^{-6}$, three orders of magnitude lower, showing that the tellurite nonuniformity indeed has a much higher impact on effective index fluctuations. Let us now emulate this effect using the transfer matrix method, considering that each set of grating is subject to slightly different effective indices. Figure 3.14 shows how the response of a C-band, 50-nm sidewall, 3x3 DBR cavity with a 3-mm gap is affected by different effective index mismatches between each grating region. Here, we will use $\kappa = \kappa_{\mathrm{Cytop}}$ from Table 3.5 for both gratings. Then, consider the input

[14] We expect the Cytop to be highly nonuniform near the chip facets due to the spin coating process, which makes it much thicker at the edge of the chip compared to its center, where the thickness is ~1 μm.

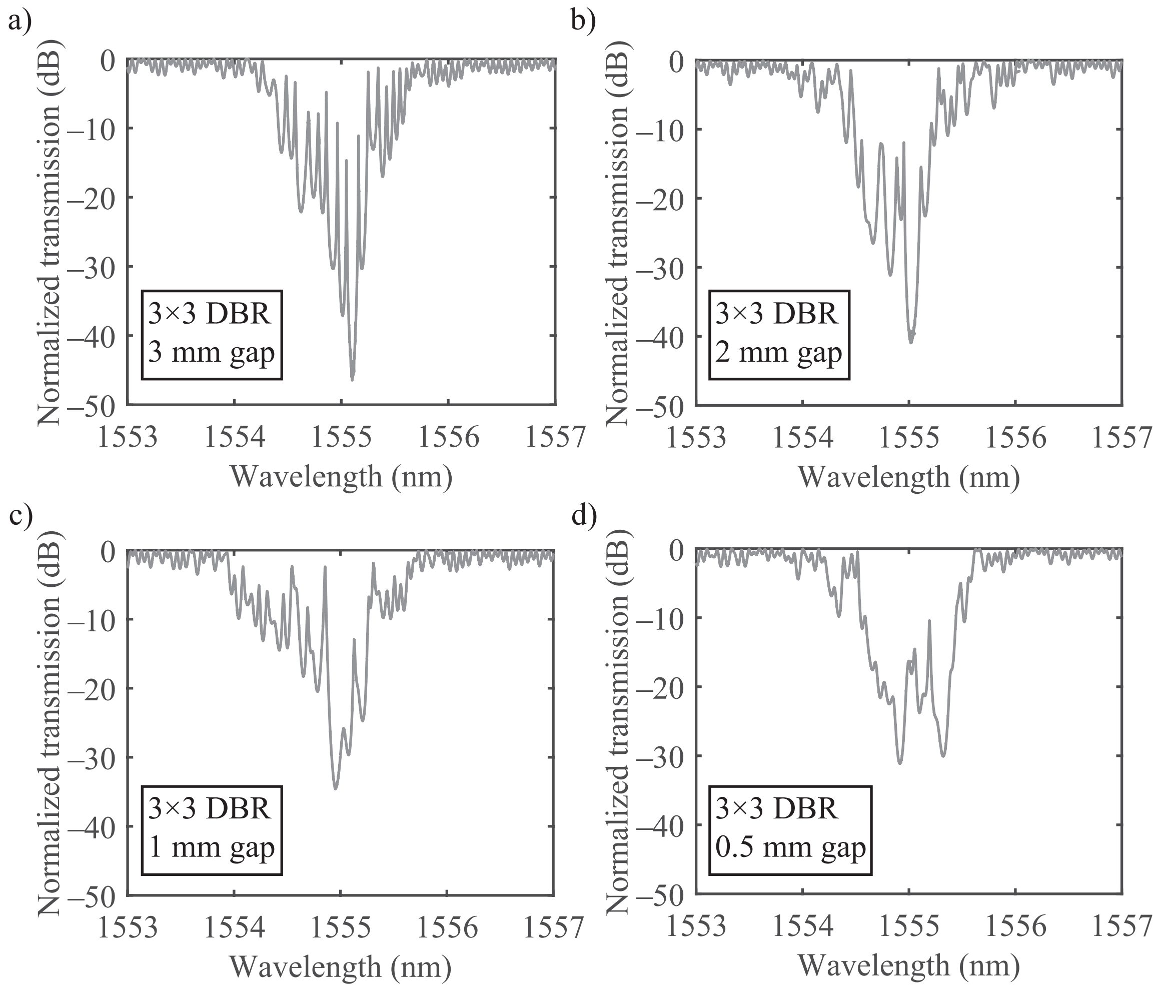

Figure 3.13. Measured transmission spectra of 3×3 DBR cavities with gaps equal to **a)** 3, **b)** 2, **c)** 1, and **d)** 0.5 mm.

grating to be in a region with fixed n_{eff} = 1.85131[15], obtained by applying the Bragg condition to the measured peak reflected wavelength from Figure 3.11. Next, we add different Δn_{eff} values to the output grating region to investigate how the transmission spectrum is affected. From the typical DBR response when the gratings are matching (Figure 3.14a), we notice that a mere fluctuation in the effective index in the order of 0.0001 (Figure 3.14b) is enough to cause a small change in the cavity response. Furthermore, for Δn_{eff} = 0.0003, 0.0005 (Figure 3.14c,d) we observe that the cavity response gets increasingly more deformed and wider as the grating mismatch increases. In fact, note how these two spectra resemble the shape of the measured cavities in Figure 3.13c,d. The Δn_{eff} values considered here are one order of magnitude lower than that of the maximum index shift possible when the tellurite thickness varies by 2%. If we consider this upper-limit scenario, we find that Δn_{eff} = 0.003 is sufficient to completely split the two grating

[15] Dear reader, before you think I have lost my sanity by reporting the effective index with that many significant figures, bear with me because this is necessary for the argument I am trying to make.

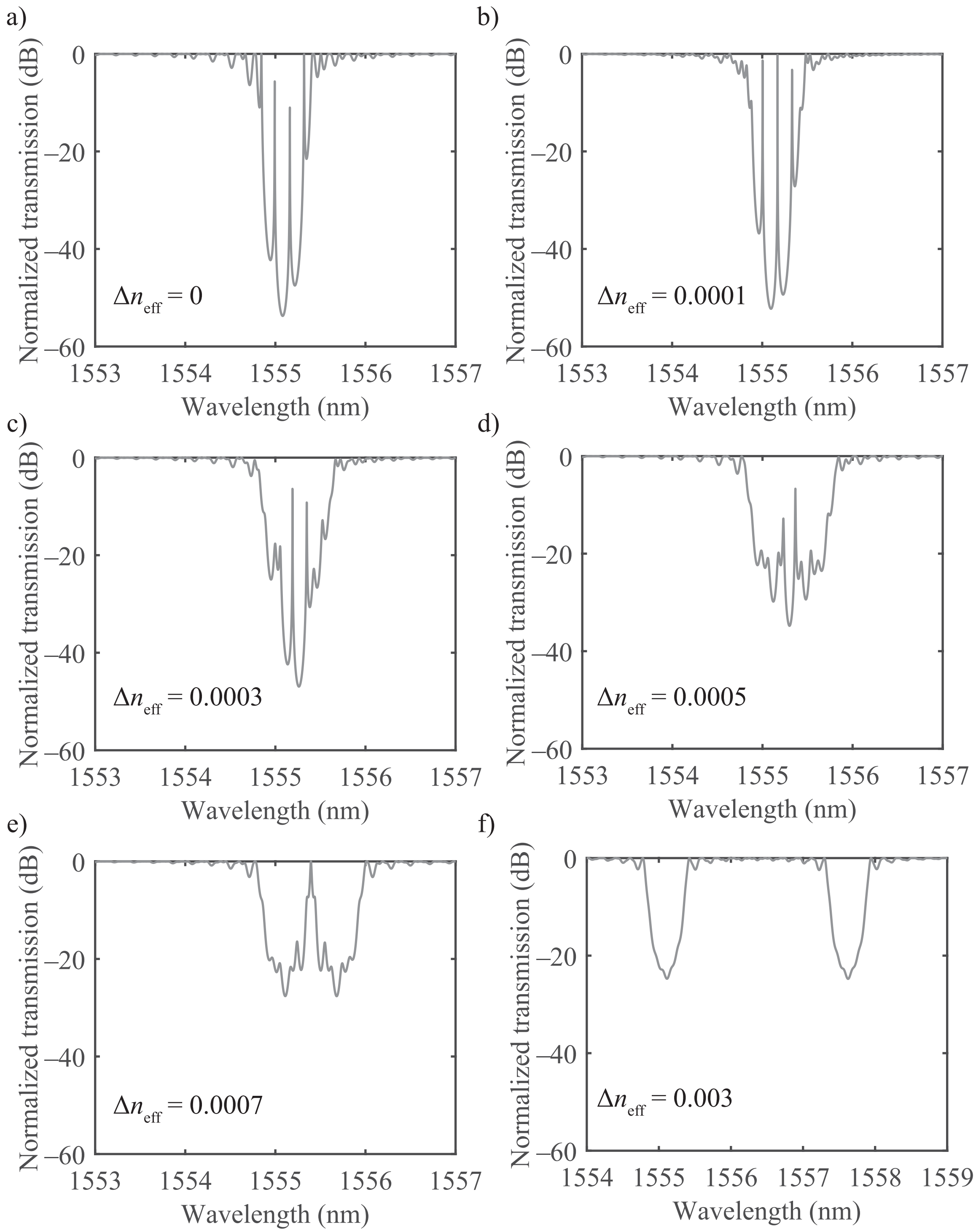

Figure 3.14. Theoretical response of a 3x3 DBR cavity with gap of 3 mm, for effective index mismatch between the two reflectors equal to **a)** 0, **b)** 0.0001, **c)** 0.0003, **d)** 0.0005, **e)** 0.0007, and **f)** 0.003.

resonances, essentially undoing the DBR cavity response and ending up with two uniform gratings instead. Additionally, we observe that the extinction ratios decrease as the grating mismatch increases, much like what can be seen in Figure 3.13. Further distortions in the measured spectra from Figure 3.13 can be attributed to the fact that, in reality, the effective index gradually varies throughout the entire grating (and unperturbed) region, instead of the two fixed indices considered here.

These spectral deviations make it nearly impossible to reliably perform the full study originally planned for this work, since most cavity responses are so distorted it is difficult to extract useful information from their transmission spectrum. In the next section, we will discuss the cavity properties that were able to be extracted from the measured spectra. It was not possible to estimate the grating-induced loss using the proposed method, because the equations involved become invalid when the gratings resonances are not matching well. Alternatively, we attempted to extract these losses by analyzing the difference in insertion loss with varying grating lengths, considering the 100-nm-wide C-band sidewall gratings, which are expected to be the lossiest among the studied variations, due to greater perturbation and confinement factor. It was not observed any significant difference in transmission between a straight waveguide with the same geometry (but no gratings) and a 3×3 cavity (with a total grating length of 6 mm). This suggests an upper grating-induced loss limit within the facet loss uncertainty of ± 0.5 dB, over 6 mm of grating. This implies that the grating-induced losses are < 0.8 dB/cm and potentially well below, but further investigation is needed to determine it with higher precision. As a comparison, losses in the order of 0.08 dB/cm have been reported in alumina waveguide DBR cavities with surface-corrugated gratings on a top silicon dioxide cladding, which are expected to have lower losses than sidewall gratings since they do not introduce topological variation in the waveguide core.

3.5.4.1. Cavity Properties

Tables 3.6 and 3.7 summarize the properties that were possible to be extracted from the measured data for C- and O-band cavities, respectively. The C-band devices operate at around 1555 nm, while the O-band cavities operate near 1315 nm. The symmetrical cavities have the configuration $L_{\text{grating}} \times L_{\text{grating}}$, separated by a gap L_{gap}. The reported free spectral range ($\Delta\lambda_{\text{FSR}}$), full width at half maximum ($\Delta\lambda_{\text{FWHM}}$), Q factor and finesse are the average of 2–4 resonances of each cavity. Due to the lower grating coupling coefficient, the 50-nm-wide sidewall gratings have significantly longer penetration lengths, which make their effective lengths slightly longer than that of the 100-nm-wide gratings with the same cavity configuration. As expected, the free spectral range tends to increase as L_{gap} (and L_{eff}) become shorter. Moreover, as the grating length (reflectivity) increases, less light escapes the cavity, which makes the $\Delta\lambda_{\text{FWHM}}$ generally narrower, increasing both Q factor and finesse. However, this trend tends to saturate for stronger gratings, because of how the reflectivity varies as a function of grating length (see Figure 3.3b). For most cavities studied here, the Q factors usually lie between 1–5·10^5, and the maximum values found were between 9–11·10^5 in the case of strong (100-nm-wide) gratings. There is significant uncertainty in the $\Delta\lambda_{\text{FWHM}}$ of higher-Q cavities (> 5·10^5), because the widths of the resonances approach the measurement resolution.

Table 3.6. Summary of measured properties of C-band symmetrical DBR cavities.

w_{grating} (µm)	L_{grating} (mm)	L_{gap} (mm)	L^{a}_{eff} (mm)	L^{a}_{pen} (mm)	$\Delta\lambda_{\text{FSR}}$ (nm)	$\Delta\lambda_{\text{FWHM}}$ (nm)	Q factor ($\times 10^5$)	Finesse
0.05	0.5	8.0	8.45	0.226	0.064	0.021	0.7	3
	1.25	6.5	7.28	0.388	0.074	0.011	1.4	7
	1.75	5.5	6.34	0.420	0.086	0.010	1.4	11
	2.00	5.0	5.85	0.426	0.082	0.011	1.4	7
	2.50	4.0	4.86	0.432	0.080	0.010	1.6	8
	3.00	3.0	3.87	0.434	0.100	0.003	4.9	37
0.1	0.50	8.0	8.31	0.156	0.067	0.014	1.1	5
	0.75	7.5	7.84	0.170	0.070	0.006	2.4	10
	1.00	7.0	7.35	0.174	0.076	0.003	5.1	26
	1.25	6.5	6.85	0.175	0.082	0.002	6.0	36
	1.50	6.0	6.35	0.175	0.087	0.002	10	48
	1.75	5.5	5.85	0.175	0.094	0.002	9.0	55
	2.00	5.0	5.35	0.175	0.102	0.002	9.1	60
	2.50	4.0	4.35	0.175	0.189	0.002	6.9	72

^{a}Calculated using estimated coupling coefficients from Table 3.5.

Table 3.7. Summary of measured properties of O-band symmetrical DBR cavities.

w_{grating} (µm)	L_{grating} (mm)	L_{gap} (mm)	L^{a}_{eff} (mm)	L^{a}_{pen} (mm)	$\Delta\lambda_{\text{FSR}}$ (nm)	$\Delta\lambda_{\text{FWHM}}$ (nm)	Q factor ($\times 10^5$)	Finesse
50	0.50	8.0	8.45	0.226	0.053	0.020	0.6	3
	0.75	7.5	8.11	0.303	0.056	0.019	0.7	3
	1.00	7.0	7.71	0.356	0.059	0.012	1.1	5
	1.25	6.5	7.28	0.388	0.062	0.008	1.6	7
	1.50	6.0	6.82	0.408	0.066	0.011	1.4	7
	1.75	5.5	6.34	0.420	0.070	0.006	2.4	13
	2	5	5.85	0.426	0.077	0.005	2.9	17
	2.5	4	4.86	0.432	0.087	0.005	2.7	18
	3	2	2.87	0.434	0.145	0.005	2.5	28
100	0.5	8	8.33	0.164	0.055	0.005	2.8	14
	0.75	7.5	7.86	0.182	0.06	0.004	3.8	17
	1	7	7.37	0.187	0.062	0.003	3.9	18
	1.25	6.5	6.88	0.189	0.067	0.002	11	23
	1.5	6	6.38	0.189	0.073	0.003	4.1	25

^{a}Calculated using estimated coupling coefficients from Table 3.5.

3.6. Summary

In this chapter, we discussed the main steps involved in designing sidewall and multipiece Bragg gratings, as well as considerations regarding fabrication constraints. The effective index of the fundamental mode was engineered so that the same designs could operate at either the O- or C-band depending on the silicon nitride and tellurite thicknesses. We combined the theory introduced in Chapter 2 with RSoft finite element method simulations to guide the design choices. Several symmetrical DBR cavities were designed with varying grating and cavity lengths to study their optical properties. The silicon nitride chips were fabricated at the LioniX foundry and post-processed at McMaster University to add the tellurite and Cytop layers. The devices were characterized in an edge-coupling setup using tunable lasers. Distortions to the expected theoretical response of the DBR cavities made the data analysis extremely challenging, significantly affecting the planned study. These distortions can be attributed mainly to variations in effective index across the devices, primarily caused by the tellurite film nonuniformity. Using uniform grating transmission spectra, it was possible to estimate the grating coupling coefficients as 1110 and 1150 m^{-1} for O- and C-band 50-nm-wide sidewall gratings. The 100-nm-wide gratings had coupling coefficients around 2640 and 2860 m^{-1} in the O- and C-band respectively. These values were used to investigate Fabry-Pérot resonances caused by facet reflections, as well as the effects of the tellurite thickness variation and the penetration and effective lengths of the DBR cavities. Measured transmission spectra of symmetrical DBR cavities were used to estimate properties such as free spectral range, Q factor, and finesse. Most cavities exhibited Q factors in the order of $1–3 \cdot 10^5$ and finesses within 3–40.

In Chapters 4 and 5, we will use similar sidewall grating designs to achieve erbium- and thulium-doped tellurite DBR lasers operating around 1550 and 1900 nm wavelengths.

4. Erbium Lasers

Reproduced with permission from Springer Nature (license number: 5805970415562), as well as B. L. Segat Frare, P. Torab Ahmadi, B. Hashemi, D. B. Bonneville, H. M. Mbonde, H. C. Frankis, A. P. Knights, P. Mascher, and J. D. B. Bradley, "*On-chip hybrid erbium-doped tellurium oxide-silicon nitride distributed Bragg reflector lasers*", Applied Physics B 129:158 (2023).

DOI: https://doi.org/10.1007/s00340-023-08099-4

This chapter reproduces a published manuscript on erbium-doped tellurite distributed Bragg reflector lasers. The only changes made to the original work include some minor adjustments to the figure dimensions and coloring schemes, and revised text formatting and numbering to match the thesis, to match the flow of the other chapters. Here, we use the Bragg grating designs and fabrication steps introduced in Chapter 3 to demonstrate asymmetrical distributed Bragg reflector lasers with high emission directionality. These devices represent the first erbium-based lasers with emission in the important telecom C-band (1530–1565 nm) demonstrated in the hybrid tellurite-silicon nitride platform. Moreover, they establish the groundwork to design and build, in the future, optimized on-chip erbium-doped tellurite lasers with high efficiency and output power. In Chapter 6, we investigate routes to optimize these devices using the laser model that is presented in Chapter 2.

Abstract: *We demonstrate integrated on-chip erbium-doped tellurite ($TeO_2:Er^{3+}$) waveguide lasers fabricated on a wafer-scale silicon nitride platform. A 0.352-µm-thick $TeO_2:Er^{3+}$ coating was deposited as an active medium on 0.2-µm-thick, 1.2- and 1.6-µm-wide, and 22-mm-long silicon nitride waveguides with sidewall-patterned asymmetrical distributed Bragg reflector cavities. The lasers yield efficiencies between 0.06 and 0.36%, lasing threshold ranging from 13 to 26 mW, and emission within the C-band (1530–1565 nm). These results establish new opportunities for this hybrid tellurite glass-silicon nitride platform, such as the co-integration of passive components and light sources in the telecom window, and provide the foundation for the development of efficient, compact, and high-output-power on-chip erbium-doped tellurite waveguide lasers.*

4.1. INTRODUCTION

Rare-earth-doped fiber lasers have achieved remarkable success over the past few decades in delivering reliable solutions for various applications, including material processing, medicine, and defense [11]. They possess desirable characteristics such as stability, high output power, narrow linewidth, low cost, and scalability [8]. Among them, erbium-doped lasers stand out due to their high efficiency, compatibility with telecommunication networks, and ability to emit eye-safe radiation in the C-band [265]. In the field of integrated photonics, planar glass lasers aim to bring the advantages of fibers to a chip-scale, while monolithically integrating an active gain medium onto the chip. With the current mature complementary metal-oxide semiconductor (CMOS) processing capabilities, it is possible to reliably fabricate small features such as Bragg gratings that can be used to define optical cavities on silicon chips. Bragg-grating-based devices are well-established in both fibers and chips [8,159,168,179,265–268] and offer great control and flexibility over cavity designs, enabling precise tuning of their optical responses. These devices can be monolithically integrated into waveguides to create compact, efficient, and narrow linewidth lasers [66,159,269]. They can be employed in many applications, including sensing [270], integrated LiDAR systems [100], telecommunications [271], and microwave photonics [272].

Tellurium dioxide (TeO_2) is a glass with a relatively high refractive index ($n_{\mathrm{TeO_2}}$= 2.08 at 1550 nm) and is highly transparent from visible to mid-infrared wavelengths. It also has strong nonlinear [72] and acousto-optic [70,71] effects, as well as high rare-earth solubility and large emission cross sections, making it an excellent candidate for a gain medium in integrated photonics [73–75]. Additionally, it can be processed at low temperatures (< 200 °C), which is an advantage for post-processing fabrication on photonic integrated circuit platforms [76,77,90,273]. Vu et al. demonstrated high gain erbium-doped tellurite waveguide amplifiers and lasing due to chip facet reflections [84]. However, further development was required for etching smooth waveguides when it is doped with erbium [73] and high-resolution features suitable for integrated cavities and on-chip lasing.

Hybrid integration approaches, such as erbium-doped Al_2O_3 on silicon nitride (SiN) waveguides, have been successfully employed to achieve distributed Bragg reflector (DBR) lasers on photonics integrated circuit (PIC) platforms [68,207]. In these cases, the wafer-scale, low-cost and mature processing of SiN PICs is leveraged, while the gain medium is applied without the need for an etching step. SiN is a CMOS-compatible material with several advantages [37,38], including low propagation loss (<0.1 dB/cm) within SiN's transparency window from visible to mid-infrared, high nonlinear figure of merit, low cost, small feature sizes available in large-scale production, and relatively high refractive index (n_{SiN} = 1.98), essential for developing compact devices [64]. We have developed a hybrid silicon nitride-tellurite glass platform that combines the advantages of both materials [86]. When tellurite is applied on top of thin SiN waveguides, the optical mode is expanded into the TeO_2 layer due to its slightly higher refractive index than SiN. Consequently, it is possible to achieve more than 50% of mode confinement in the gain medium, with the potential for same-chip integration with passive and nonlinear devices

[72]. We have demonstrated gain on this platform with erbium-doped TeO_2 ($TeO_2:Er^{3+}$) [87], as well as optical amplifiers and microring lasers with thulium-doped tellurite [88,89].

Here, we demonstrate $TeO_2:Er^{3+}$ DBR lasers monolithically integrated on a SiN chip. By varying the grating period and strength, lasing is achieved at wavelengths across the C-band. Asymmetrical cavities were used to promote high emission directionality, with a maximum forward efficiency of 0.33%. These results build upon our previous work and pave the way for the development of efficient and low-cost erbium-doped tellurite glass lasers in PICs.

4.2. Experimental Details

4.2.1. Device Design

Figure 4.1a illustrates the DBR cavities investigated in this work. The SiN thickness (t_{SiN}) was chosen to be 0.2 μm to allow for sufficient overlap with the active medium [86]. The designed $TeO_2:Er^{3+}$ thickness ($t_{TeO_2:Er^{3+}}$) was selected as 0.35 μm to account for fabrication variability, so that the Bragg condition can be matched within the optimal tellurite thickness range of 0.25 μm < $t_{TeO_2:Er^{3+}}$ < 0.45 μm that enables lateral mode confinement and integration with tight bend radii (< 300 μm) [86]. The total device length, L_{total} = 22 mm, is the length of the chip, defined by the lithography reticle size, and is such that the cavity is long enough for the total gain to overcome the roundtrip losses. The waveguide width (w_{SiN}) was chosen as either 1.2 μm (close to the single mode cutoff) or 1.6 μm (further into multimode operation) [86]. Single-mode operation is desirable to maximize the power coupled into the fundamental mode, because the Bragg response is sensitive to the mode effective index and other modes are not reflected. However, wider waveguides tend to have lower propagation losses due to less interaction with the sidewalls [274], which can alleviate the amount of gain required to achieve lasing.

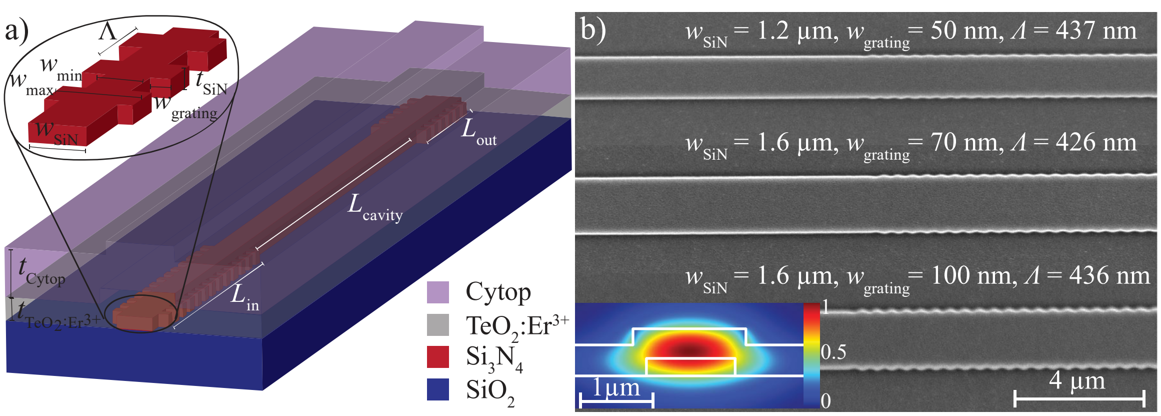

Figure 4.1. a) Diagram of a $TeO_2:Er^{3+}$-Si_3N_4 DBR cavity. **b)** Scanning electron microscope image of fabricated Si_3N_4 waveguide gratings showing the transition between a straight section and a corrugated section for the different grating designs analyzed in this work. Inset: electric field profile for the 1550-nm fundamental TE mode in a hybrid $TeO_2:Er^{3+}$-Si_3N_4 waveguide showing strong overlap with both the $TeO_2:Er^{3+}$ gain layer and the Si_3N_4 strip.

The devices were designed using a finite element method mode solver (Synopsys RSoft) to extract parameters such as the effective index and mode overlap fractions with the gain medium and SiN grating features. The grating strengths were then estimated using the transfer-matrix method [195]. 2D mode simulations were performed with the selected SiN waveguide geometry and TeO_2:Er^{3+} thickness to determine the effective index n_{eff} and the power confinement factor in the grating ($0 < \Gamma_{\mathrm{grating}} < 1$) of the fundamental mode for several grating widths (w_{grating}). The grating period Λ was chosen using the first-order Bragg condition [218]:

$$\Lambda = \frac{\lambda_0}{2n_{\mathrm{eff}}}, \tag{4.1}$$

where λ_0 is the target laser wavelength, set to 1550 nm. The DBR cavities investigated are asymmetrical, with the length of the input grating (L_{in}) being longer than that of the output grating (L_{out}). This results in a higher reflection coefficient R at the input to promote directional laser emission through the output facet. The grating lengths $L = L_{\mathrm{in}}, L_{\mathrm{out}}$ were used to estimate R at λ_0 for each set of gratings [218]:

$$R = \tanh^2(\kappa L), \tag{4.2}$$

with κ being the coupling coefficient, given by [218]:

$$\kappa = \frac{\Gamma_{\mathrm{grating}}\left(n^2_{\mathrm{TeO_2:Er^{3+}}} - n^2_{\mathrm{SiN}}\right)}{\lambda_0 n_{\mathrm{eff}}} \sin(\pi D), \tag{4.3}$$

where $n_{\mathrm{TeO_2:Er^{3+}}}$ is the refractive index of the TeO_2:Er^{3+} film and $D = 0.5$ is the duty cycle. The $w_{\mathrm{grating}} = 50, 70, 100$ nm was chosen so that $R > 0.9$ for a grating length of ~ 3 mm, resulting in a cavity length, L_{cavity}, that was at least 10 mm for all devices. Within the grating region, the waveguide width varies between a minimum (w_{min}) and maximum (w_{max}) value to match the n_{eff} of the straight and corrugated sections. The waveguides include an offset $L_{\mathrm{offset}} = (0.520 \pm 0.005)$ mm from each chip facet before the grating region starts. The 1.6-µm-wide waveguides also have a 0.25-mm-long edge coupler within this offset that is linearly tapered to a width of 1.2 µm at the chip facet, to keep the facet losses consistent among all devices. L_{cavity} is then defined by $L_{\mathrm{cavity}} = L_{\mathrm{total}} - (2L_{\mathrm{offset}} + L_{\mathrm{in}} + L_{\mathrm{out}})$.

4.2.2. FABRICATION

The silicon nitride chips were fabricated at the LioniX foundry through their commercially available process, described in [262]. The SiN waveguides and grating features were defined using stepper lithography and reactive ion etching. The wafers were left unclad, then stealth-diced into chips to achieve high-quality facets. As shown in Figure 4.1b, due to resolution limitations, the fabricated grating features are rounded instead of the designed rectangular shape [260]. Next, the chips were transferred from the foundry and deposition of the TeO_2:Er^{3+} film was carried out via radio frequency (RF) reactive co-sputtering. The deposition was performed at 150 °C, under a process pressure of 2.8 mTorr, in an Ar and O_2 atmosphere with gas flows of 12 and 10.2 sccm, respectively, using a Lesker PVD Pro 200 system. RF powers of 125 and 60 W were applied to 3” metallic Te and Er targets, respectively. Further details about the $TeO_2:Er^{3+}$ sputtering process can be found in [86]. A 1-µm-thick Cytop fluoropolymer layer ($n_{Cytop} = 1.33$) was spin-coated onto the chips as a top cladding.

4.2.3. Characterization

The devices were characterized on the setup illustrated in Figure 4.2. A 1470 nm laser diode was used as a forward pump, followed by polarization paddles and a 1480/1550 nm wavelength division multiplexer (WDM). Next, the pump was launched into the waveguide through a tapered fiber with a spot diameter of 2.5 µm mounted on an XYZ stage. A backward pump with the same configuration was also used to perform double-sided pumping and increase the amount of power coupled to the device. The emitted laser signal at each facet was coupled to the same fibers and WDMs followed by an optical switch which was used for measuring forward and backward laser emissions separately. A free space 1500 nm edge pass filter was employed to filter the residual pump light and a 50/50 splitter was used to measure the laser power with a detector while the laser emission spectrum could be observed on an optical spectrum analyzer.

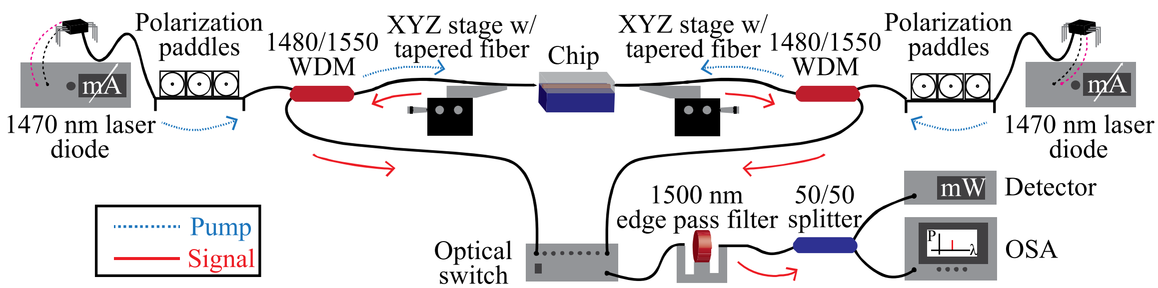

Figure 4.2. Experimental setup used for the $TeO_2:Er^{3+}$-coated SiN DBR laser measurements.

The laser power was measured as a function of the pump power, which was controlled by a current source that feeds the diodes. The launched (on-chip) pump power was calculated by removing the chip, measuring the incident power at the tapered fiber output with a power meter, and subtracting the facet loss, which was determined by measuring the fiber-chip-fiber insertion loss. The amplified stimulated emission (ASE) power was evaluated by measuring the emitted signal from a straight waveguide with equal geometries and no gratings, on the same chip. The ASE power was then subtracted from the measured signal power at the detector to determine the laser output power. The on-chip laser power was determined by taking into account all the system losses from the tapered fiber to the detector as well as the facet losses.

4.3. Results

4.3.1. Film and Passive Waveguide Properties

The $TeO_2:Er^{3+}$ deposition was carried out for 18.5 min, resulting in a 0.352-µm-thick film. A bare Si witness piece was used to measure a refractive index of 2.04 at 1550 nm wavelength through ellipsometry. The film losses were characterized on a thermal SiO_2 witness sample with a Metricon prism coupling system [264], yielding a background loss of (1.1 ± 0.3) dB/cm at 1620 nm. The same technique was applied to measure the losses at several wavelengths between 1510 and 1560 nm. The Er^{3+} concentration was then estimated to be $2.4 \cdot 10^{20}$ ions/cm^3 by fitting the losses to their corresponding absorption cross sections [84]. In addition, the excited-state lifetime of Er^{3+} was found to be (620 ± 20) µs, by fitting the back-emitted ASE signal intensity from the waveguide as a function of time with a 50-Hz square-wave-modulated 1470-nm pump.

Point-coupled microring resonators (500-µm diameter, 1.2-µm gap) with the same tellurite and Cytop layers and waveguide geometry were used to extract the background loss of the devices at 1620 nm through Q-factor measurements [225], resulting in propagation losses of (1.0 ± 0.2) dB/cm and (0.8 ± 0.2) dB/cm for 1.2- and 1.6-µm-wide waveguides respectively. Lastly, the background loss was subtracted from the total insertion loss measured at 1620 nm to estimate a fiber-to-chip facet loss of (3.5 ± 0.5) dB/facet for each device.

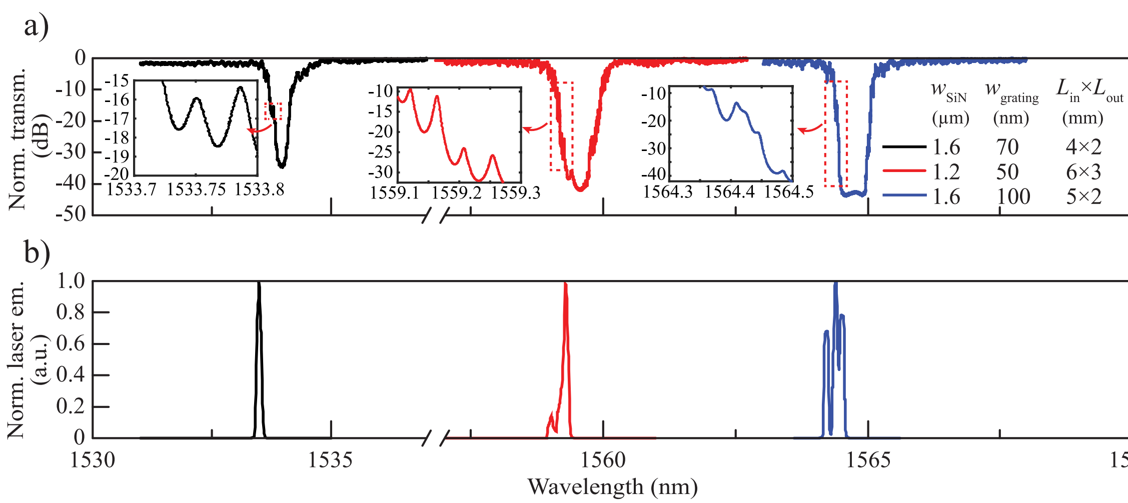

Figure 4.3. a) Passive transmission (unpumped) and **b)** corresponding laser emission spectra of DBR cavities with different grating designs.

Figure 4.3a shows normalized passive transmission measurements for the most efficient device for each grating width, measured from the same sample and with the pump off. The extinction ratios are greater than –30 dB and the flat response around –40 dB is due to the limit of detection of the power meter. The cavity transmission spectra represent the combined response of both sets of reflectors, which is dominated by the input gratings (R > 99.5%). This indicates that the overall grating strengths agree with the designed values, even though these measurements do not allow us to directly calculate the reflection coefficient of each individual set of gratings. Furthermore, the Q-factors of the resonances were estimated to be in the range of (0.5–2)·10^5 by dividing each resonance's peak wavelength by its full width half maximum.

4.3.2. Laser Measurements

We observed lasing within the wavelength range of 1533 to 1565 nm, as shown in the normalized emission spectra in Figure 4.3b. Lasing occurred in all the devices tested, except for one that was damaged during handling. Multimode lasing was observed in most of the devices, corresponding to different longitudinal modes inside the cavity. The strong grating responses caused the devices to lase at the edge of the reflection bandwidths.

In Figure 4.4, the efficiency curve of the device with the lowest lasing threshold is presented. The device consisted of a 1.2-µm-wide waveguide and 50-nm-wide gratings with a period of 437 nm, and lengths L_{in} = 6 mm and L_{out} = 3 mm. The cavity asymmetry introduced high directionality in the output, which is evident by comparing the forward and backward laser emissions. The forward slope efficiency is η_{fwd} = 0.26%, while the backward laser emission is η_{bwd} = 0.01%, for a total efficiency of 0.27%. Both forward and backward directions exhibited similar lasing thresholds (P_{th}) of P_{th}^{fwd} = 13 and P_{th}^{bwd} = 11 mW, respectively, as estimated through a linear fit of the experimental data. The maximum forward on-chip laser power was 0.13 and 0.28 mW for single- and double-side pumping, respectively.

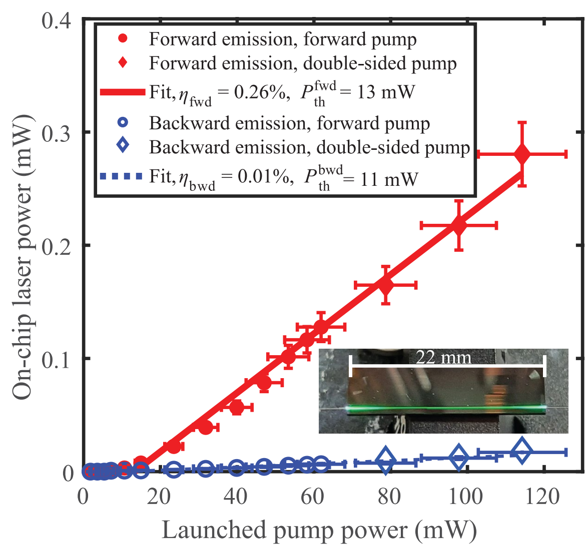

Figure 4.4. Laser efficiency curve of a DBR laser with w_{SiN} = 1.2 µm, $w_{grating}$ = 50 nm, Λ = 437 nm, L_{in} = 6 mm, L_{out} = 3 mm. A linear fit gives a total efficiency of 0.27%, of which 0.26% corresponds to forward emission, and a threshold pump power of approximately 13 mW. Inset: lasing device. Typical Er^{3+} green emission can be seen due to higher order excited states because of upconversion when pumped.

Table 4.1 summarizes the laser results of all the devices tested. The lasing wavelengths observed are dependent on the effective index and grating period. In the high reflectivity regime, by keeping L_{in} constant and increasing L_{out}, the transmission coefficient of the output grating is reduced, leading to lower forward laser efficiency and, therefore, lower overall efficiency as well.

Table 4.1. Summary of DBR laser designs and results

<table>
<tr><th>w_{SiN} (µm)</th><th>w_{grating} (nm)</th><th>w_{min} (µm)</th><th>w_{max} (µm)</th><th>Λ (nm)</th><th>L_{in} (mm)</th><th>$R_{\mathrm{in}}{}^{a}$ (%)</th><th>L_{out} (mm)</th><th>$R_{\mathrm{out}}{}^{a}$ (%)</th><th>L_{cavity} (mm)</th><th>$\lambda_{\mathrm{emission}}$ (nm)</th><th>η_{fwd} (%)</th><th>η_{bwd} (%)</th><th>$P_{\mathrm{th}}^{\mathrm{fwd}}$ (mW)</th></tr>
<tr><td rowspan="2">1.2</td><td rowspan="2">50</td><td rowspan="2">1.175</td><td rowspan="2">1.225</td><td rowspan="2">437</td><td rowspan="2">6</td><td rowspan="2">99.99</td><td>3</td><td>98</td><td>12</td><td>1559.0
1559.3</td><td>0.26</td><td>0.01</td><td>13</td></tr>
<tr><td>4</td><td>99.7</td><td>11</td><td>1558.6
1558.8</td><td>0.06</td><td><0.01</td><td>26</td></tr>
<tr><td rowspan="4">1.6</td><td rowspan="2">70</td><td rowspan="2">1.565</td><td rowspan="2">1.635</td><td rowspan="2">426</td><td rowspan="2">4</td><td rowspan="2">99.7</td><td>2</td><td>90</td><td>15</td><td>1533.5</td><td>0.33</td><td>0.03</td><td>17</td></tr>
<tr><td>3</td><td>98</td><td>14</td><td>1533.3</td><td>0.11</td><td>0.02</td><td>16</td></tr>
<tr><td rowspan="2">100</td><td rowspan="2">1.550</td><td rowspan="2">1.650</td><td rowspan="2">436</td><td rowspan="2">5</td><td rowspan="2">100</td><td>2</td><td>98</td><td>14</td><td>1564.2
1564.4
1564.5</td><td>0.09</td><td>0.07</td><td>17</td></tr>
<tr><td>3.5</td><td>99.95</td><td>12.5</td><td>-</td><td>-</td><td>-</td><td>-</td></tr>
</table>

[a]Designed values

Although hybrid lasers on SiN have been demonstrated with one order of magnitude higher efficiencies [68,207], the lasing thresholds achieved here are comparable to those of similar erbium-doped aluminum oxide DBR lasers first reported in [68,207]. The low efficiencies (< 1%) can be attributed mainly to the high background losses, incomplete activation of Er^{3+} ions [87], and high reflection coefficient of the output gratings, which can be reduced by choosing shorter values for L_{out}. Studying devices with just one set of uniform gratings as well as weaker reflectors will allow for further characterizing the gratings' passive response [211]. The background losses reported here are dominated by the tellurite losses, which can be improved by varying the TeO_2:Er^{3+} sputtering parameters, namely the O_2 flow to adjust the film stoichiometry. Despite the fact that the TeO_2:Er^{3+} film used in this work has a relatively higher loss (> 1 dB/cm), we have demonstrated losses down to ≤ 0.1 dB/cm using the same fabrication process [86,87]. We expect to achieve higher performance lasers by optimizing the Er^{3+} doping concentration and fraction of active ions, waveguide cross section geometry, and cavity parameters, such as the grating width, length, and period. Furthermore, the devices' operating wavelength can be adjusted by changing the gratings' period to achieve lasing with different rare earths, such as ytterbium, praseodymium, thulium, as well as erbium-ytterbium co-doping.

4.4. Conclusion

We demonstrate erbium DBR lasers on a $TeO_2:Er^{3+}$-coated SiN hybrid platform. The silicon nitride waveguides were fabricated through a standard wafer-scale foundry process and the $TeO_2:Er^{3+}$ layer was reactively co-sputtered using a straightforward low temperature step. High output directionality was achieved using asymmetrical cavities, with a maximum total laser efficiency of 0.36% and minimum pump power threshold of 13 mW. Lasing at wavelengths between 1533 and 1565 nm was observed in several devices with varying waveguide widths, and grating widths, periods and lengths. These results serve as a basis for understanding the grating response in such hybrid waveguides and optimizing the cavity and grating properties for improved performance in future designs. The simplicity and versatility of this platform make it attractive for the integration of active and passive devices on a single chip. Overall, these results represent significant initial steps toward the realization of reliable, efficient, and high-output-power integrated erbium-doped tellurite lasers for applications in communications and sensing.

5. Thulium Laser

This chapter is a manuscript currently under preparation for submission to a peer-reviewed journal with the working title "*A thulium-doped tellurite distributed Bragg reflector waveguide laser on a silicon nitride chip*". Printed with permission from B. L. Segat Frare, B. Hashemi, N. Majidian Taleghani, P. Torab Ahmadi, D. B. Bonneville, H. M. Mbonde, H. C. Frankis, P. Mascher, P. Ravi Selvaganapathy, and J. D. B. Bradley.

This chapter includes a draft of a manuscript to be submitted to a peer-reviewed journal on thulium-doped tellurite DBR lasers. Here, we adapt the sidewall grating designs discussed in Chapters 3 and 4 to operate at wavelengths near 2 µm, by adjusting the grating period. As a result, we were able to demonstrate a thulium laser operating at 1875 nm and with slope efficiency of 5%, which is more than ten times higher than that of the erbium lasers discussed in Chapter 4. This laser represents the first thulium-based distributed Bragg reflector laser achieved in the hybrid tellurite-silicon nitride platform, in addition to microring resonator lasers reported by Miarabbas Kiani [89]. Similarly to the DBR lasers obtained in the previous chapter, there is still much room for improvement by optimizing the cavity and grating design. In Chapter 6, we will use the thulium laser model introduced in Chapter 2 to study how these lasers can be optimized in future design iterations. The results reported here combined with the optimization discussions from Chapter 6 pave the way for the development of efficient, high-power thulium-doped tellurite on-chip lasers.

Abstract: *We show a distributed Bragg reflector laser operating at 1875 nm, using a hybrid silicon nitride chip covered with thulium-doped tellurite glass. The hybrid laser consists of nominally 50-nm-wide sidewall gratings directly patterned on a 1.2-µm-wide, 0.2-µm-thick, and 22-mm-long silicon nitride waveguide on a thermally-oxidized silicon substrate fabricated at a foundry. Then, a low-temperature post-processed 0.39-µm-thick thulium-doped tellurium dioxide layer was deposited onto the chip by reactive radio frequency magnetron co-sputtering. The laser includes 6- and 4-mm-long gratings separated by a 11-mm gap to form an asymmetrical cavity and promote directional lasing off the shorter reflector. We obtain a maximum on-chip output power of 4.5 mW and lasing threshold of 20 mW when pumping at 1610 nm. A total slope efficiency of 5% was achieved, as well as a thermal tunability of the laser wavelength of 32.3 pm/°C. These results are a step towards simple, compact, high-power, and tunable on-chip thulium-based tellurite lasers for silicon-based photonic integrated circuits.*

5.1. INTRODUCTION

The ever-growing data traffic worldwide has pressured for the expansion of telecommunication networks beyond the original (1260–1360 nm) and conventional (1530–1565 nm) bands to ensure the future demand can be met [158]. One alternative is the exploration of other transmission bands, from which wavelengths around 2 µm stand out as potential candidates because they allow for high bandwidth and low-loss transmission, while also being eye-safe [158,184]. In light of this, thulium-based amplifiers and light sources are of interest due to their ultra broadband emission from 1.6 to 2.2 µm and potential to achieve high gain and output powers [185–187]. Thulium-doped fiber amplifiers and high power lasers have been extensively studied [156,158,184], with applications that go beyond telecommunications, including remote and environmental sensing, military, spectroscopy, and minimally invasive surgery [184,275–277].

Over the past decade, numerous devices operating near 2 µm wavelength have also been demonstrated in integrated photonics [88–90,185–188]. On-chip thulium light sources are useful for applications including LiDAR [185,278], sensing [279], and medical diagnostics [280], but have not been extensively studied in thulium-based photonic integrated circuits (PICs). Particularly, distributed Bragg reflector (DBR) lasers are attractive because they allow for simple, compact, and highly customizable cavity designs, which can be monolithically fabricated on chips [66,159,269]. The development of thulium-based DBR on-chip lasers can enable high-power light sources with directional output, as well as lead to achieving integrated distributed feedback (DFB) lasers with single-mode, narrow linewidth output.

Amorphous tellurium dioxide is a glass with a relatively high refractive index ($n_{\mathrm{TeO_2}} \sim 2$ at 2 µm) and excellent optical properties, including transparency from visible to mid-infrared wavelengths. It is also an excellent rare-earth host material with broad emission bandwidths due to its low phonon energies [86,281]. Tellurite fiber lasers have been extensively studied [78,79,282–284] and on-chip tellurite waveguide lasers and amplifiers have been demonstrated with low background losses and high gain [73,84]. However, it has been shown that patterning rare-earth-doped TeO_2 requires additional processing steps. This is due to the formation of rough surfaces with grassing effects that significantly increase the propagation losses when etched [73]. We have developed a hybrid platform that combines tellurite with low loss silicon nitride (SiN) chips that are compatible with complementary metal-oxide semiconductor (CMOS) technology, using simple low-temperature post-processing steps. With this approach, it is possible to add active functionalities that are generally not readily available in all silicon nitride-based foundry platforms. At the same time, the hybrid platform maintains the advantages of silicon nitride, such as compactness, low cost, and mature fabrication techniques with small feature sizes in wafer-scale processing. We have demonstrated on-chip rare-earth lasers and amplifiers, including erbium DBR lasers [285] and amplifiers [87], as well as thulium microring lasers [89] and amplifiers [88].

In this work, we show a proof-of-concept DBR laser using a SiN waveguide covered with thulium-doped tellurite (TeO_2:Tm^{3+}). We observed highly directional maximum on-chip output power of 4.5 mW. The total device slope efficiency and threshold are 5.0% and 20 mW respectively. Moreover, we tested the laser's temperature response, finding a thermal sensitivity of 32.3 pm/°C. These results pave the way for the development of optimized $TeO_2:Tm^{3+}$-SiN laser cavities, sensors, and tunable lasers in this platform.

5.2. Experimental Details

5.2.1. Device Design

The platform used here is illustrated in Figure 5.1a. It consists of a strip silicon nitride (n_{SiN} ~ 1.98) waveguide with width w_{SiN} = 1.2 µm (close to the single-mode cutoff) and thickness t_{SiN} = 0.2 µm, covered with a $TeO_2:Tm^{3+}$ layer with thickness $t_{\mathrm{TeO_2:Tm^{3+}}}$ = 0.39 µm. This structure forms a hybrid waveguide that expands the optical mode into the tellurite layer due to the small refractive index contrast of ≲ 0.1 between the two materials [86]. In this case, the composite structure resembles a rib waveguide, and it is possible to achieve more than 50% mode overlap with the active gain medium [86]. A ~1-µm-thick fluoropolymer (Cytop, n_{Cytop} = 1.33) top cladding is used to passivate the sample.

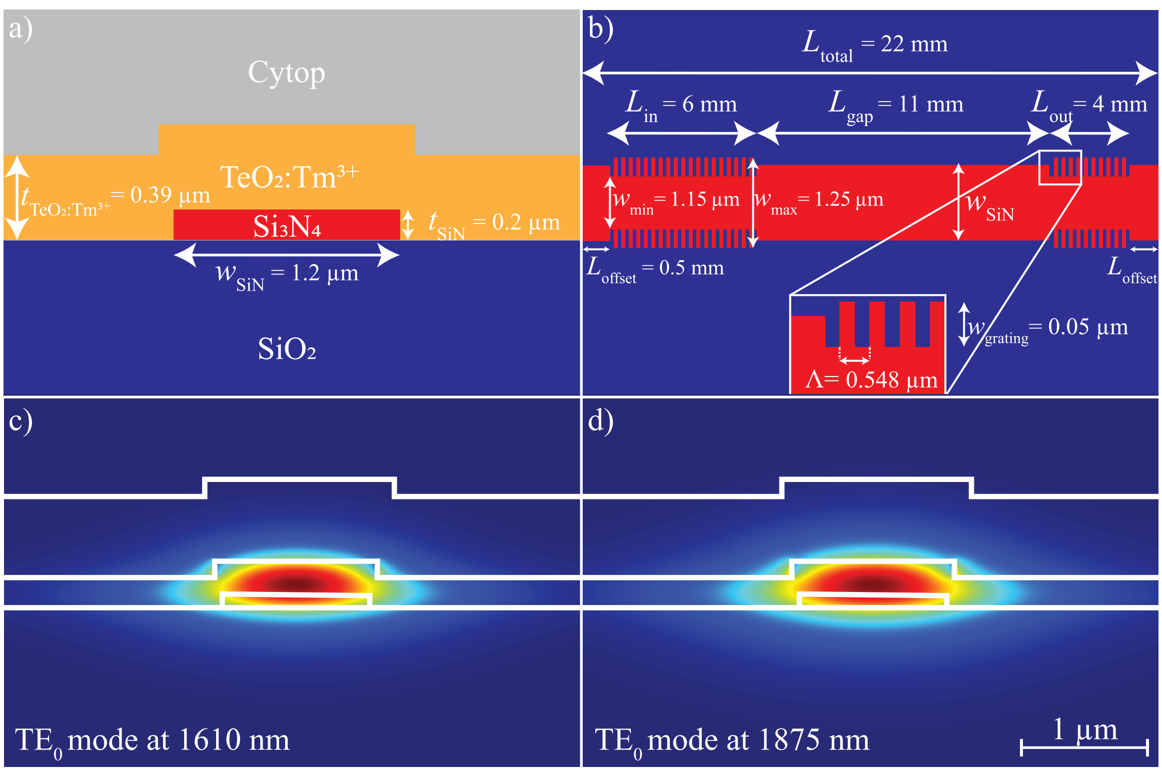

Figure 5.1. a) $TeO_2:Tm^{3+}$-Si_3N_4 hybrid laser waveguide cross section and **b)** top-view summarizing the cavity design. **c, d)** Electric field profile for the fundamental TE mode at 1610 and 1875 nm, respectively.

The grating design follows the approach that we previously reported in [285]. We used a commercial finite element mode solver (Synopsys RSoft) to estimate the effective index (n_{eff}) of the fundamental transverse electric (TE_0) to be between 1.7–1.75 for tellurite thicknesses within 0.35 and 0.4 μm. This $TeO_2:Tm^{3+}$ thickness range enables lateral mode confinement and eventual integration with tight bend radii (< 0.3 mm). Using the Bragg condition ($\Lambda = \lambda_B/2n_{eff}$), we chose a grating period (Λ) of 0.548 μm to achieve a device operating wavelength (λ_B) around the peak emission of thulium (1.85–1.91 μm) [252] for the tellurite thickness interval considered. The grating width $w_{grating}$ was chosen as 0.05 μm to achieve strong DBR mirrors (> 90% reflectivity) over a few millimeters. The device investigated here consists of an asymmetrical DBR cavity (different grating lengths), defined by two sets of gratings with lengths L_{in} = 6 mm and L_{out} = 4 mm, as shown in Figure 5.1b. The first reflector is designed to reflect 100% at λ_B, while the second has a designed reflectivity of > 99%, to promote directional laser output. The strong gratings were chosen to ensure roundtrip gain in the first proof-of-concept device. The total device length is L_{total} = 22 mm, which is the chip length defined by the stepper lithography reticle size. The grating regions are separated from the chip facets by an offset with length L_{offset} = 0.5 mm. Within the grating regions, the waveguide width is modulated between a minimum (w_{min}) and maximum (w_{max}) widths such that the corrugation is centered at the nominal waveguide width, w_{SiN}. The two gratings are separated by a distance L_{gap} = 11 mm.

5.2.2. Fabrication

The silicon nitride chip was fabricated at the LioniX foundry, using their TriPleX platform [53]. The silicon nitride layer was deposited on a thermally-oxidized 4" Si wafer via low-pressure chemical vapor deposition (LPCVD). Then, the waveguide and Bragg gratings were patterned using 248 nm deep UV stepper lithography, followed by reactive ion etching. Stealth dicing was used to cut the uncladded wafer into chips with high-optical-quality end facets. The chips were then transferred from the foundry and post-processing steps were carried out at the Centre for Emerging Device Technologies (CEDT) at McMaster University. First, a $TeO_2:Tm^{3+}$ film was deposited onto the chips via reactive RF magnetron co-sputtering using the process previously reported in [86,88,89] using a Lesker Pro PVD 200 system. We carried out the deposition at room temperature, in an argon and oxygen atmosphere with 12 and 10.2 sccm flows, respectively, at a process pressure of 3 mTorr. We applied RF powers of 125 and 85 W to 3"-diameter Te and Tm metallic targets, respectively. Lastly, the sample was spin-coated with Cytop fluoropolymer (1750 rpm, baked at 50, 80, and 180 °C for 10, 30, and 30 minutes respectively).

5.2.3. Characterization

Figure 5.2 shows the experimental setup used to characterize the $TeO_2:Tm^{3+}$-Si_3N_4 DBR laser. To pump it, the output of a tunable 1510–1640 nm laser (Agilent 8164A) set at 1610 nm was amplified by an L-band erbium-ytterbium-co-doped fiber amplifier (EYDFA, Optilab EYDFA-L-37-1). The pump light was coupled to an L-band fiber isolator (for protection from reflections), a 3-pad polarization controller (set to TE polarization), and a 1600/1900 nm wavelength division multiplexer (WDM). The light was coupled in and out of the chip using tapered fibers with 2.5-µm-diameter spot size. The forward and backward laser emission from the chip were collected by the same fibers and separated from the residual pump by the WDMs and a free-space (2000 ± 250) nm band-pass filter (Thorlabs FB2000-500). A 50/50 power splitter was used to simultaneously record the output powers and spectra using a power meter and a Fourier transform optical spectral analyzer (OSA, Thorlabs OSA205C).

Passive measurements were carried out using the same setup, by connecting either the tunable 1510–1640 nm laser or a tunable 1850–2020 nm laser directly to the polarization paddles and bypassing the WDM on the input side. The output was collected by the tapered fiber and sent directly to the power meter.

We also investigated the laser's thermal tunability by mounting the chip on a Peltier thermoelectric module. The temperature was controlled by adjusting the applied voltage and measured using a thermistor at the plate surface which was assumed to be the same as on the chip after a few minutes.

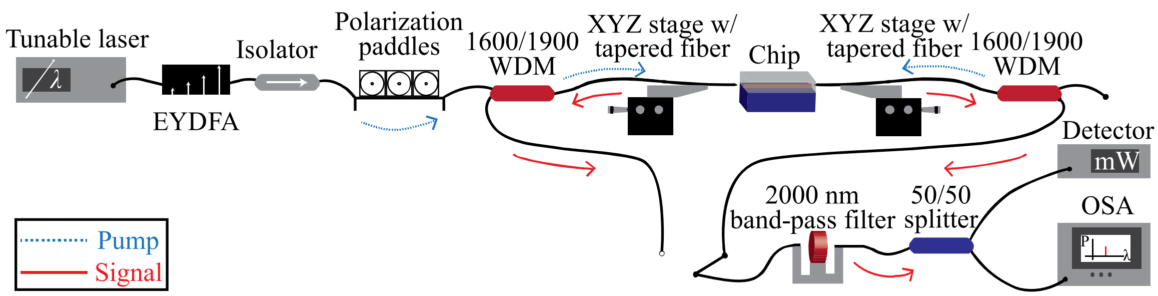

Figure 5.2. Experimental setup used to characterize the $TeO_2:Tm^{3+}$ distributed Bragg reflector laser.

5.3. Results

5.3.1. Film and Passive Waveguide Properties

A bare Si witness sample included in the deposition was used to characterize the tellurite film via ellipsometry and Rutherford backscattering spectrometry. The former was used to find a film thickness of 0.39 µm and a refractive index of 1.98 at 1.9 µm wavelength, while the latter was used to find a thulium concentration of $3.6 \cdot 10^{20}$ ions/cm^3. A thermal oxide sample was also used as witness sample, to measure the tellurite film background loss using a Metricon prism-coupling system, resulting in (0.4 ± 0.4) dB/cm at 1500 nm, where the thulium absorption is negligible.

The waveguide background and facet losses were found using the cutback method on three devices with same cross section design and covered with the same tellurite film: 6- and 10-mm-long straight waveguides and a 67-mm-long paperclip structure with minimum bend radius of 0.65 mm. By linearly fitting the insertion loss versus waveguide length for the three devices, we found a background loss (slope) of (0.6 ± 0.3) dB/cm at both 1500 and 1900 nm, where the thulium absorption is low. Moreover, the facet losses (y-intercept) were estimated as (3.4 ± 0.5) and (2.9 ± 0.5) dB/facet at 1610 and 1900 nm, respectively.

5.3.2. Laser Measurements

Figure 5.3a shows the normalized forward laser emission at 1875.1 nm with a launched pump power of 100 mW at 1610 nm. The passive transmission spectrum measured with a tunable laser around 2 µm in the absence of pump light is shown in the inset. The flat DBR response at a level of –20 dB between approximately 1875 and 1877 nm is caused by the strong grating response, dominated by the longer reflector, which resulted in reaching the limit of detection of the photodetector used. The strong gratings used here promoted multimode lasing near the edge of the grating stopband rather than at its center. The laser linewidth and multimode behavior could not be fully resolved with the OSA used here and require further measurements to be fully understood. Figure 5.3b shows the laser efficiency curve for the forward and backward directions. We observe a highly directional output, with 4.7% and 0.3% efficiency in the forward and backward direction, respectively, for a total device efficiency of 5%. The lasing threshold is around 20 mW of on-chip pump power, in both cases. The maximum observed on-chip laser power was 4.5 and 0.3 mW in the forward and backward direction, respectively. This means that more than 93% of the laser output is emitted from the weaker grating. The efficiency obtained here is about half of that of TeO_2:Tm^{3+}-Si_3N_4 microring resonator lasers reported by Miarabbas Kiani et al. (11%) [89], although the same maximum output power was achieved due to improved facet losses here, which enabled higher launched pump powers. The lasing thresholds are also comparable. Moreover, this laser has an efficiency an order of magnitude higher than the erbium-based DBR lasers previously demonstrated in this platform (0.36%) [285]. However, thulium DBR lasers have been demonstrated with higher efficiencies (up to 23%) and output powers (up to 387 mW) in a similar hybrid platform that used alumina instead of tellurite [185], although higher lasing thresholds were observed (65 mW) due to the weaker gratings (70% reflectivity on both DBRs) used there.

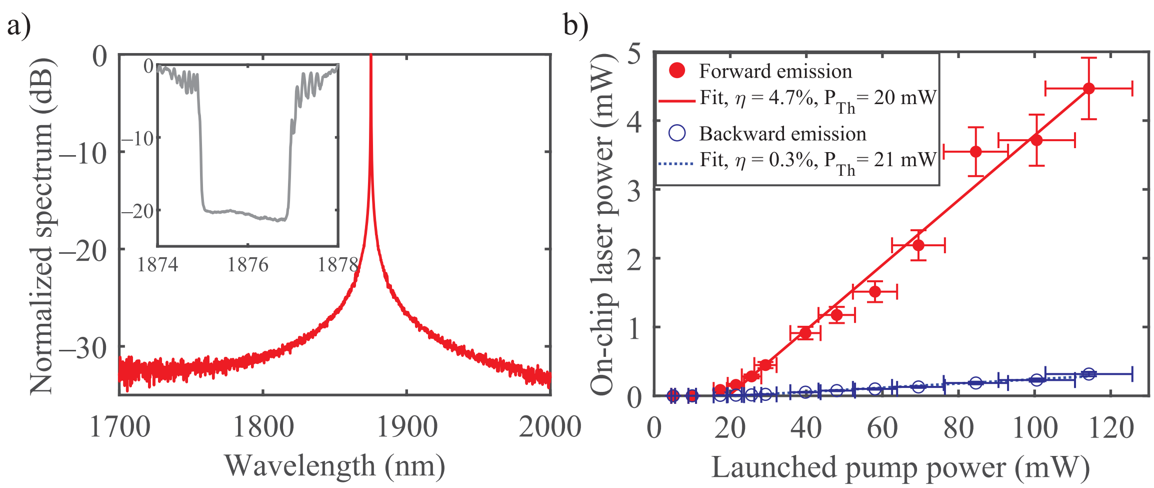

Figure 5.3. a) Laser emission spectrum. Inset: transmission spectrum of the unpumped device. **b)** Laser efficiency curve.

Figure 5.4a shows how the laser emission spectrum shifts as a function of temperature, while Figure 5.4b shows a linear fit of the peak laser emission wavelength

(λ_{laser}), yielding a 32.3 pm/°C thermal sensitivity. A maximum shift of 1.55 nm was observed between 19.8 and 69.9 °C. This sensitivity is in good agreement with what we previously reported in tellurite microcavity resonator sensors [286]. On one hand, the thermal sensitivity observed here is roughly double the reported sensitivities in low-confinement SiN Bragg gratings surrounded by silica (15 pm/°C) [287] and high-confinement SiN demultiplexers on buried oxide exposed to air (18.5 pm/°C) [288]. On the other hand, it is approximately a third of the typical sensitivity of ~ 100 pm/°C in silicon waveguides [289], such as the silicon-on-insulator rib waveguides with a thermal shift of 80 pm/°C previously reported by Homampour et al. [290]. These sensitivities are mainly affected by the thermo-optical coefficient (dn/dT) of the different materials, $dn/dT_{\text{SiO}_2} \sim 0.95{\cdot}10^{-5}$/°C $< dn/dT_{\text{Si}_3\text{N}_4} \sim 2.45{\cdot}10^{-5}$/°C $< dn/dT_{\text{TeO}_2} \sim 5.9{\cdot}10^{-5}$/°C $< dn/dT_{\text{Si}} \sim 18.6{\cdot}10^{-5}$/°C [286,287,290]. Understanding the behavior of DBR lasers in this hybrid tellurite-silicon nitride platform across a wide range of temperature is crucial for the development of components that require high wavelength selectivity, such as modulators and switches, and can also help to account for slight fabrication variations to ensure the devices operate at the target wavelength [291].

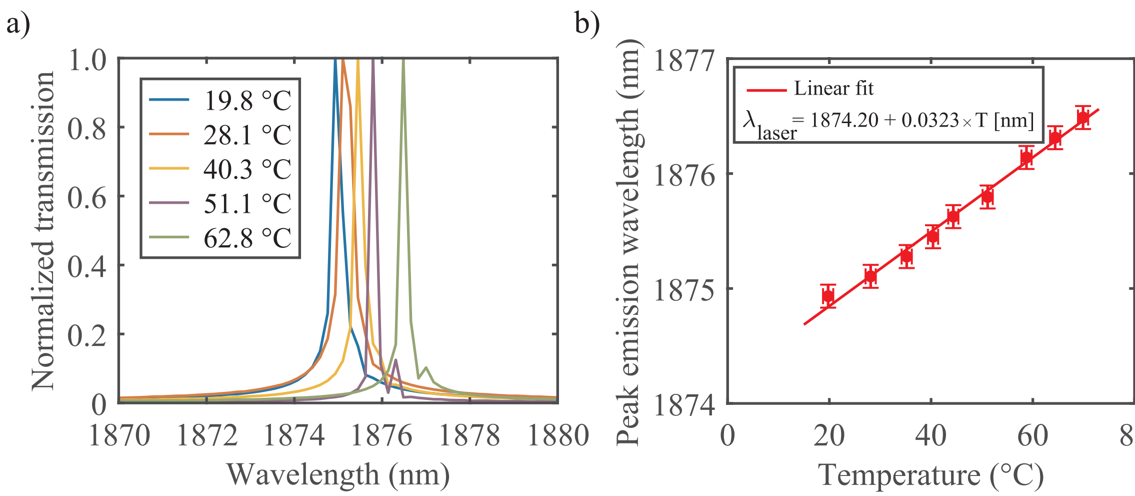

Figure 5.4. a) Laser emission spectra for different temperatures and **b)** peak emission wavelength as a function of temperature.

These results pave the way for the development of fully integrated tunable lasers by adding on-chip heaters [292], as well as Bragg-grating-based sensors in this platform. Distributed feedback lasers can be investigated to achieve single-mode operation and narrow linewidths. Moreover, there is room to improve the TeO_2:Tm^{3+}-Si_3N_4 DBR laser performance beyond this first proof of concept demonstration by optimizing the cavity design (including the grating width, DBR length and cavity size), reducing background losses (for instance by increasing the waveguide width between the gratings to minimize scattering [274]), and optimizing the concentration and activation of thulium ions.

5.4. CONCLUSION

We have demonstrated highly directional lasing in an asymmetrical distributed Bragg reflector cavity on a silicon nitride chip coated with thulium-doped tellurite glass. We measured a slope efficiency of 5% and demonstrated thermal tuning of the laser wavelength across 1.55 nm over a 50 °C span. This proof-of-concept laser can be optimized, enabling high-power tellurite on-chip lasers in commercial silicon-based platforms using a single, low-temperature post-processing step. These lasers can be used in applications including LiDAR, sensing, as well as telecommunications.

6. Laser Optimization

In this chapter, we combine the laser model introduced in Chapter 2 with the experimental results from Chapters 3–5 to analyze how different parameters (grating and cavity lengths, background loss, excited-state lifetime, and concentration) affect the lasers' performance. In fact, we find that the performance of both erbium and thulium lasers can be greatly improved by adjusting these parameters. The results presented here can provide us with insights on how to optimize erbium- and thulium-based distributed Bragg reflector lasers in the tellurite-silicon nitride hybrid platform.

6.1. Introduction and General Modeling Considerations

In Chapter 2, we built a laser model that uses the shooting method to solve coupled mode theory equations combined with a rare-earth rate equation gain model. Now it is finally the time to use it and broaden our understanding of distributed Bragg reflector (DBR) lasers in the hybrid tellurite-silicon nitride platform used in this work. As we progress through this chapter, we will refer back to the laser results discussed in Chapters 4 and 5, showing that the model is generally in good agreement with the results achieved and that the trends obtained here agree with what we predicted in previous chapters.

For both erbium and thulium lasers, we will follow a similar approach and use the same starting point. In all the simulations, we will consider gratings with coupling coefficient $\kappa = 1150\ \text{m}^{-1}$ obtained in Chapter 3 for 50-nm-wide sidewall C-band gratings[16]. Moreover, we will consider a baseline background loss of 0.5 dB/cm at both pump and signal wavelengths, which are the minimum losses that we typically observe in this platform [85]. Furthermore, we will consider that the two grating responses are perfectly matching and that the lasing occurs at the Bragg wavelength. As we have seen in Chapters 3–5, this often might not be the case, but it eliminates random effects of the tellurite non-uniformity and lasing at the edge of the reflection band of strong gratings, providing us with an upper limit of the lasers' performance. We will also consider the input grating to have a fixed length of 4 mm, with a reflectivity of ~ 99.9%. All the erbium laser simulations are performed at 1550 nm wavelength, while the thulium lasers are simulated at 1875 nm (near the peak emission cross section, but also the same wavelength reported in Chapter 5).

First, we will analyze how the laser efficiency varies with the length (reflectivity) of the output grating ($L_{\text{grating,out}}$), considering a fixed device length of 20 mm (similar to what we had in Chapters 4 and 5). The gap (L_{gap}) between the two reflectors can be calculated as $L_{\text{gap}} = 20 - 4 - L_{\text{grating,out}}$, in millimeters. Then, we will choose our optimized cavity as the one with the highest efficiency. Next, we will analyze how several parameters (including device length, background loss, excited-state lifetime, and rare earth

[16] The gratings operating near 2 μm wavelength must be redesigned accordingly to maintain the same coupling coefficient of 1150 m^{-1}, but this assumption will make it easier to directly compare the results in this chapter.

ion concentration) affect the performance of the chosen cavity design, one parameter at a time and always using the aforementioned baseline parameters.

All the simulations were carried out using a 0.1 mm step size along the direction of propagation (z), a maximum number of iterations of 3000 and a tolerance of 0.001 for the magnitude of the backward-propagating laser electric field (which translates to 1 μW resolution in the calculations). Additionally, I have considered only single-sided pump from the input grating facet, as this is the preferred configuration for most applications. The slope efficiencies and lasing thresholds were obtained by simulating the laser output power for four different launched pump powers (25, 50, 75, and 100 mW) and performing a linear fit to the data points. Due to the strong grating on the input side, the backward laser emissions were found to be negligible compared to the forward emission (as we have also seen in Chapters 4 and 5). As a result, we will assume here that the total laser efficiency is simply the forward laser emission. The Matlab codes used are available in Appendices III and IV. Most figures in this chapter are connected scattered plots, in which the lines connecting the simulation results were added as guides to help visualize the trends obtained.

6.2. Erbium Laser Modeling and Optimization

In the erbium laser simulations, I have also considered a baseline excited-state lifetime of 0.62 ms (from Chapter 4), and a concentration of $2.5 \cdot 10^{20}$ ions/cm^3 with 20% of quenched ions (assumed from our previous results reported in [87]). The other spectroscopy parameters were summarized in Chapter 2 (see Table 2.1).

The cross section uniform mesh used to obtain the electric field mode profile for the pump (1470 nm) and laser (1550 nm) wavelengths is 400-points-wide and 200-points-tall, with 10×10 nm² mesh elements (the total simulated cross section is 4-μm-wide, 2-μm-tall). This means that as we propagate the signal and pump powers across the direction of propagation, the rate equations and pump/signal powers are calculated in 80,000 mesh elements at each step along z. With this configuration, it took 0.5–2 h to obtain each laser efficiency curve, using an upgraded Dell G3 15 laptop with an Intel i5-8300H processor, 32 GB of random-access memory (RAM), and a Crucial MX500 solid-state drive (SSD). This computational time is highly dependent on the initial guess and the correction factor, which were adjusted on a case-by-case basis after a few trial-and-error attempts for each device configuration. For devices with relatively higher efficiency (more than 1%), the starting backward laser power guess was typically around $1\text{–}5 \cdot 10^{-6}$ W with a correction factor of $1 \cdot 10^{-7}$ W. For low-efficiency lasers, they were both set as $1 \cdot 10^{-8}$ W.

6.2.1. Grating Length

Figure 6.1 shows how the laser efficiency and threshold vary as a function of the output grating length and reflectivity (R). The maximum efficiency was found to be 9%, which happened when $L_{\text{grating,out}}$ = 0.85 mm (R = 57%), as per Figure 6.1a,b. This corresponds to a maximum output power of 8.6 mW when the launched pump power is 100 mW. No lasing was observed when $L_{\text{grating,out}} \lesssim 0.6$ mm (R = 36%), which is supported by the sharp increase in lasing threshold for weaker gratings (Figure 6.1c,d). When the grating length is increased from the peak efficiency, the device performance starts to decrease, while the lasing threshold also decreases, because when less light leaks out of the cavity it becomes easier to achieve sufficient gain to overcome the roundtrip losses. In particular, when the grating becomes too strong, around $L_{\text{grating,out}}$ ~ 2.25 mm (R = 98%), the efficiency drops below 1%. This agrees with the results obtained in Chapter 4.

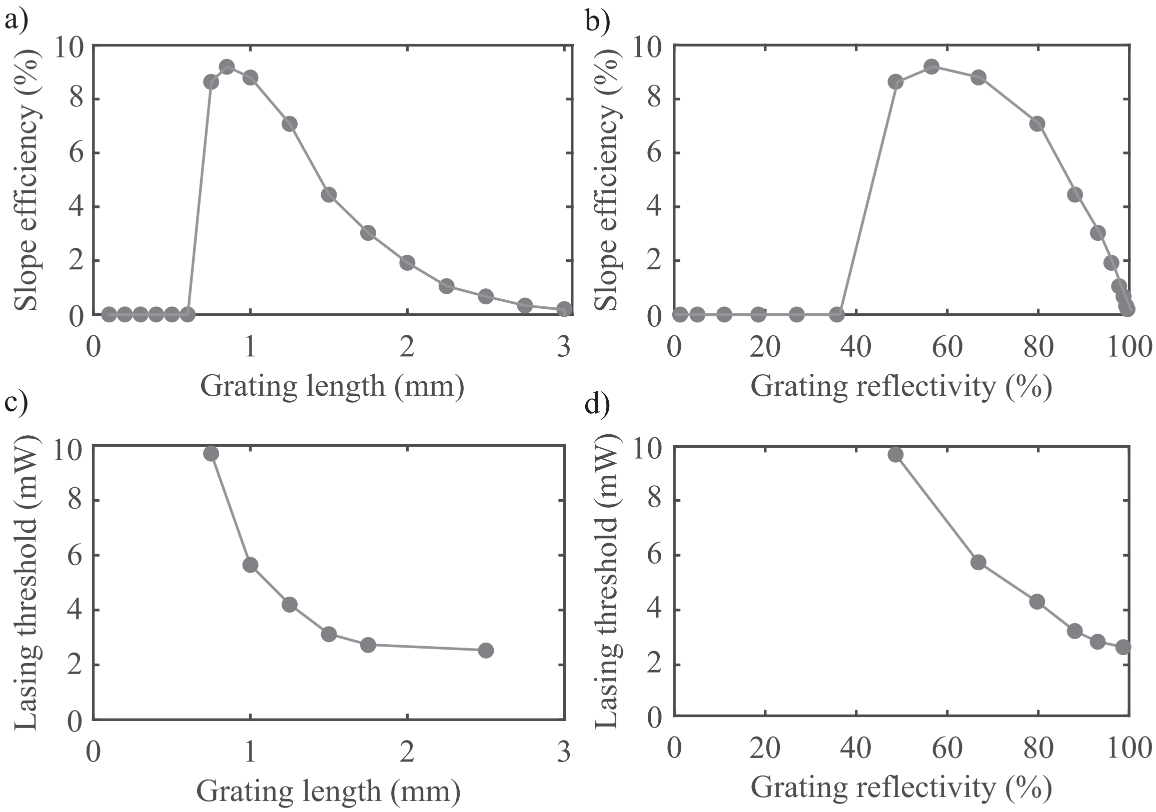

Figure 6.1. TeO_2:Er^{3+}-Si_3N_4 DBR laser **a, b)** slope efficiency and **c, d)** threshold as a function of grating length and reflectivity, respectively.

Figure 6.2a shows how the total laser power is distributed along the cavity, as well as the contribution of the forward- and backward-propagating powers, when the device with highest efficiency is pumped with 100 mW at 1470 nm wavelength. The pump power varies across the cavity as in Figure 6.2b, indicating that ~70 mW of unabsorbed pump power exits the cavity.

The gain and absorption coefficients vary across the cavity as indicated by Figure 6.3a and Figure 6.3b, respectively. The figure shows their magnitude with and without the inclusion of the background losses (0.5 dB/cm). Throughout most of the cavity, the gain coefficient lies between 1–1.5 dB/cm, which translates to a net gain coefficient of 0.5–1 dB/cm when we consider the losses.

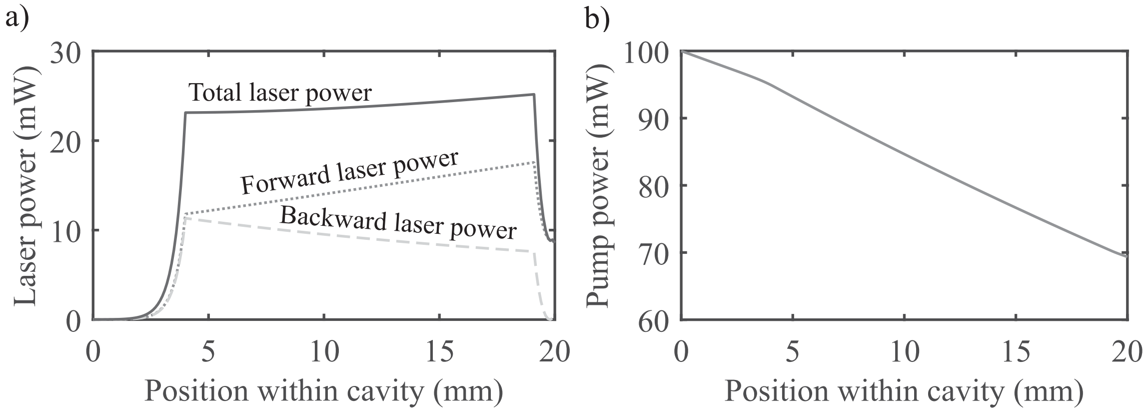

Figure 6.2. $TeO_2:Er^{3+}$-Si_3N_4 DBR **a)** laser and **b)** pump power distribution along the cavity.

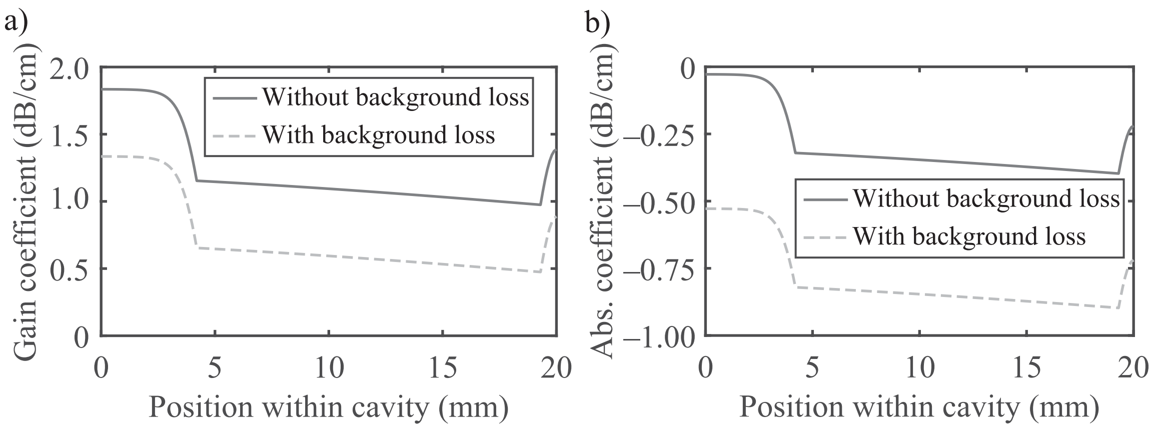

Figure 6.3.a) Gain and **b)** absorption coefficients along the $TeO_2:Er^{3+}$-Si_3N_4 DBR laser cavity.

In the following sections, 6.2.2–6.2.5, we will fix the output grating length as 0.85 mm and analyze how the laser efficiency and threshold vary with the device length, background loss, excited-state lifetime, concentration, and quenching fraction. In all these analyses, we will always use this optimized cavity design with the same parameters considered here (20-mm-long device, 0.5 dB/cm background loss, 0.62 ms lifetime, $2.5\cdot10^{20}$ ions/cm^3 concentration with 20% quenching) and vary only the quantity of interest at a time, such that we can compare the results with what we have seen so far. In reality, as we vary the other parameters, the optimal grating and cavity lengths will also vary and, ideally, for each parameter sweep we should re-optimize the grating and cavity lengths to obtain the best cavity configurations. Here, we opt to fix the cavity configuration for simplicity, so we can study how other parameters affect the laser performance around a fixed configuration used as a reference.

6.2.2. Cavity Length

When the total erbium DBR laser cavity length varies from 10 to 100 mm, we find the trends shown in Figure 6.4. The efficiency reaches a maximum of ~15% when the device length is increased to 40 mm and then decreases with increasing lengths. For a 10-mm-long device, no lasing was observed with up to 100 mW launched pump power. The simulations also suggest that there is a minimum lasing threshold power when the efficiency is maximum, which slightly increases as we deviate from the optimized device length.

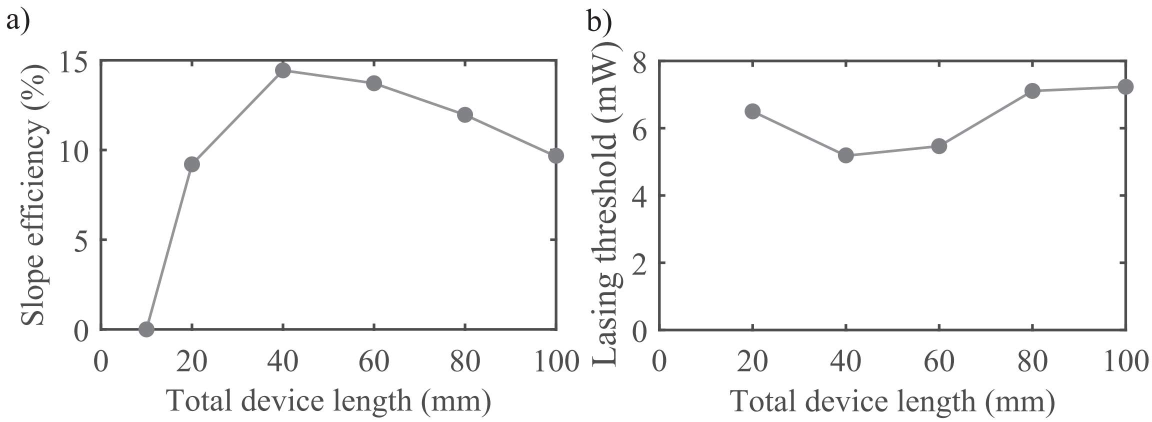

Figure 6.4. $TeO_2:Er^{3+}$-Si_3N_4 DBR laser **a)** slope efficiency and **b)** lasing threshold as a function of the total device length.

6.2.3. Background Loss

If we now look at the device performance as function of the background loss (assumed to be the same at the pump and signal wavelengths), we find that the laser efficiency can be increased up to 30% when the losses are 0.01 dB/cm, in the order of state-of-the-art ultralow loss waveguides [293]. Figure 6.5a shows that this efficiency drops significantly with increasing background losses, reaching ~2% when the loss is 1 dB/cm. This also explains why the laser efficiencies obtained in Chapter 4 are relatively low, since that sample had a background loss of (1.1 ± 0.3) dB/cm (in addition to the strong gratings mentioned earlier). Conversely, the lasing threshold significantly increases with increasing background loss, as seen in Figure 6.5b. This also agrees reasonably with the threshold pump powers observed in Chapter 4, between 13 and 26 mW.

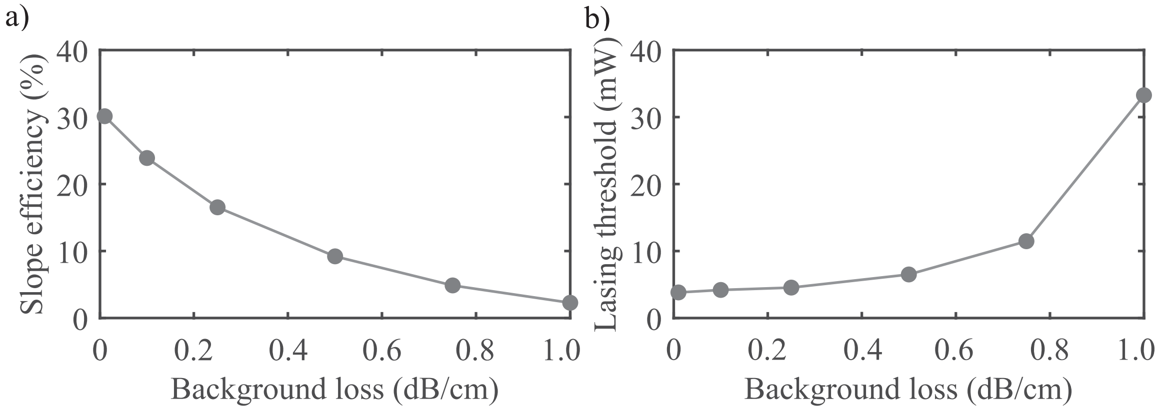

Figure 6.5. $TeO_2:Er^{3+}$-Si_3N_4 DBR laser **a)** slope efficiency and **b)** lasing threshold as a function of the background loss.

6.2.4. Excited-state Lifetime

The simulations suggest that the erbium excited-state lifetime does not have a major effect on the laser efficiency, as shown in Figure 6.6a. However, it greatly affects the necessary pump power to achieve lasing (see Figure 6.6b). When the lifetime increases from 0.1 to 0.5 ms, the lasing threshold drops to a third of the initial value of almost 30 mW. This effect tends to saturate, however, if the lifetime is further increased above 0.5 ms. The measured lifetime from Chapter 4 (0.62 ms) is long enough to enable relatively low lasing thresholds. Nonetheless, it is important to keep in mind that lifetime is impacted by concentration, fraction of quenched ions, and impurities, such as those of the OH^- group. These effects are not taken into account here, since we are varying one parameter at a time.

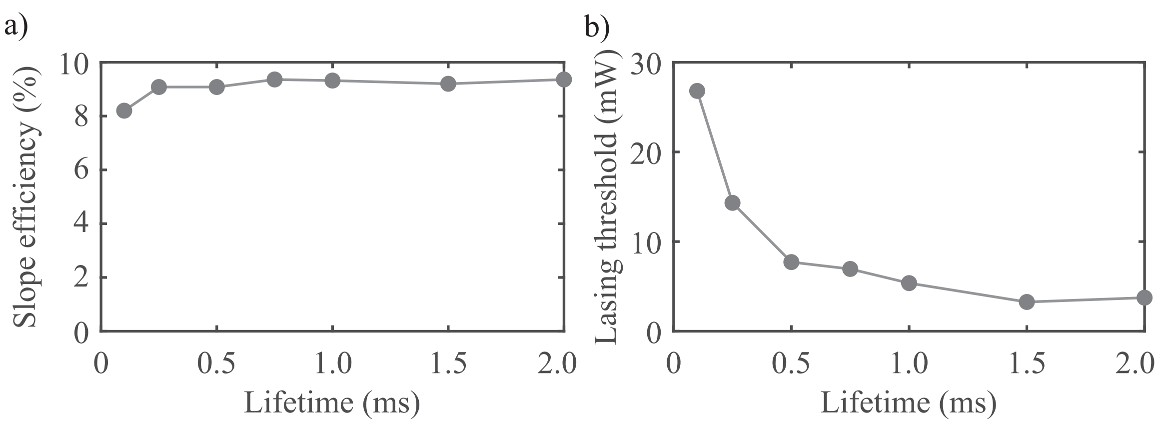

Figure 6.6. $TeO_2:Er^{3+}$-Si_3N_4 DBR laser **a)** slope efficiency and **b)** lasing threshold as a function of the erbium excited-state lifetime.

6.2.5. ERBIUM CONCENTRATION AND QUENCHING

The laser performance as a function of erbium concentration for different quenching fractions (0, 20, and 40%) are shown in Figure 6.7. In reality, the quenching ratio increases with increasing concentration, but here we consider the two parameters separately to understand their individual contributions (and for simplicity). No lasing was observed with $1\cdot10^{20}$ cm^{-3} concentration (even with 0% quenching) or with $2\cdot10^{20}$ cm^{-3} concentration and 40% of quenched ions. While the higher concentrations tend to increase the laser efficiency, the increase in quenched ions tend to significantly reduce their efficiencies. For relatively lower concentrations, the fraction of quenched ions also has a significant impact on the lasing threshold, which tends to be less pronounced with higher concentrations. In our works, we usually observe that erbium concentrations between $2–3\cdot10^{20}$ cm^{-3} give us the best balance between gain coefficient, fraction of quenched ions, and excited-state lifetime [230].

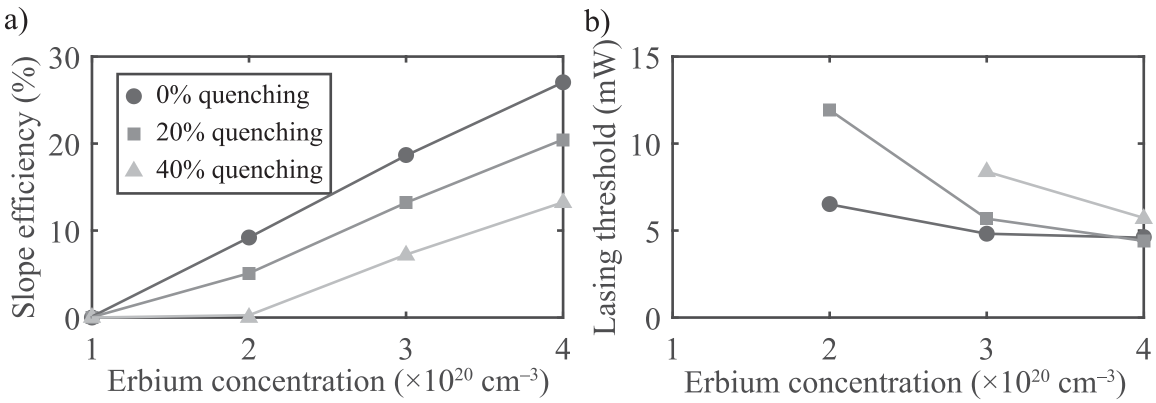

Figure 6.7. $TeO_2:Er^{3+}$-Si_3N_4 DBR laser **a)** slope efficiency and **b)** lasing threshold as a function of erbium concentration, with different fraction of quenched ions.

6.3. THULIUM LASER MODELING AND OPTIMIZATION

In the thulium laser simulations, the baseline parameters were chosen as 0.3 ms excited-state lifetime and $4\cdot10^{20}$ ions/cm^3 concentration (both assumed from our previous optimization work [253]). As previously discussed in Chapter 2, quenching is not as detrimental to thulium as it is to erbium in the concentrations considered here, so no fraction of quenched ions is considered here. Instead, the lifetime value used can in part be considered to account for the influence of quenching. The other spectroscopy parameters were summarized in Chapter 2 (see Table 2.2).

When I introduced the rate equation model for thulium in Chapter 2, I mentioned that the equations were nonlinear (due to the cross relaxation terms) and no analytical solution was available. As a result, a numerical solution was implemented. However, when this approach was added to the full laser model used for the erbium laser simulations, it drastically increased the computation time. While the erbium simulations would take up to

~2 hours to run, the thulium simulations were drastically increased to days. For the sake of achieving less-prohibitive computational costs, a simplification was made. Instead of using a cross sectional mesh as we did for erbium, here we simply considered the confinement factor in the tellurite layer and the mode effective area in the laser model. By doing so, instead of solving the rate equations 80,000 times for each point along the cavity, we only solve it once. This reduced the computation time from days to a few minutes. The main disadvantage of this simplification is that it overestimates the gain and absorption coefficients, since it does not take into account the nuances of the electric field intensity distribution across the tellurite layer and assumes that it is constant in the entire overlap region. Further investigation is necessary to assess how much this approach deviates from the more complete model. However, for the purposes of this work, where a qualitatively analysis is prioritized to provide insights for future designs, this is a fair trade considering the drastic reduction in simulation time. To adapt the laser model, we follow a relatively simple process: we substitute the normal pump and laser intensity distributions with the tellurite mode overlap. They were estimated as 0.633 and 0.573 for the pump (1610 nm) and laser (1875 nm) wavelengths, respectively, using RSoft. Then, instead of using the mesh element area, I used the effective mode areas of $1.245\cdot10^{-12}$ and $1.619\cdot10^{-12}$ m² for the pump and laser wavelengths, also obtained via RSoft simulations. Further details can be found in Appendix IV. Similar initial guesses and correction factors as in the erbium model were used here.

6.3.1. Grating Length

The laser slope efficiency and threshold as a function of the output grating length and reflectivity are shown in Figure 6.8. A maximum efficiency of 49% was observed when $L_{\text{grating,out}}$ = 0.5 mm (R = 27%), with a lasing threshold around 5 mW of on-chip pump power. This device configuration suggests a maximum laser output of 47 mW when pumped with 100 mW at 1610 nm wavelength. Similarly to the erbium case, the efficiency and threshold tend to decrease with increasing grating length (reflectivity), and no lasing was observed for shorter gratings. This cavity design was chosen as a baseline for the remaining simulations in this chapter.

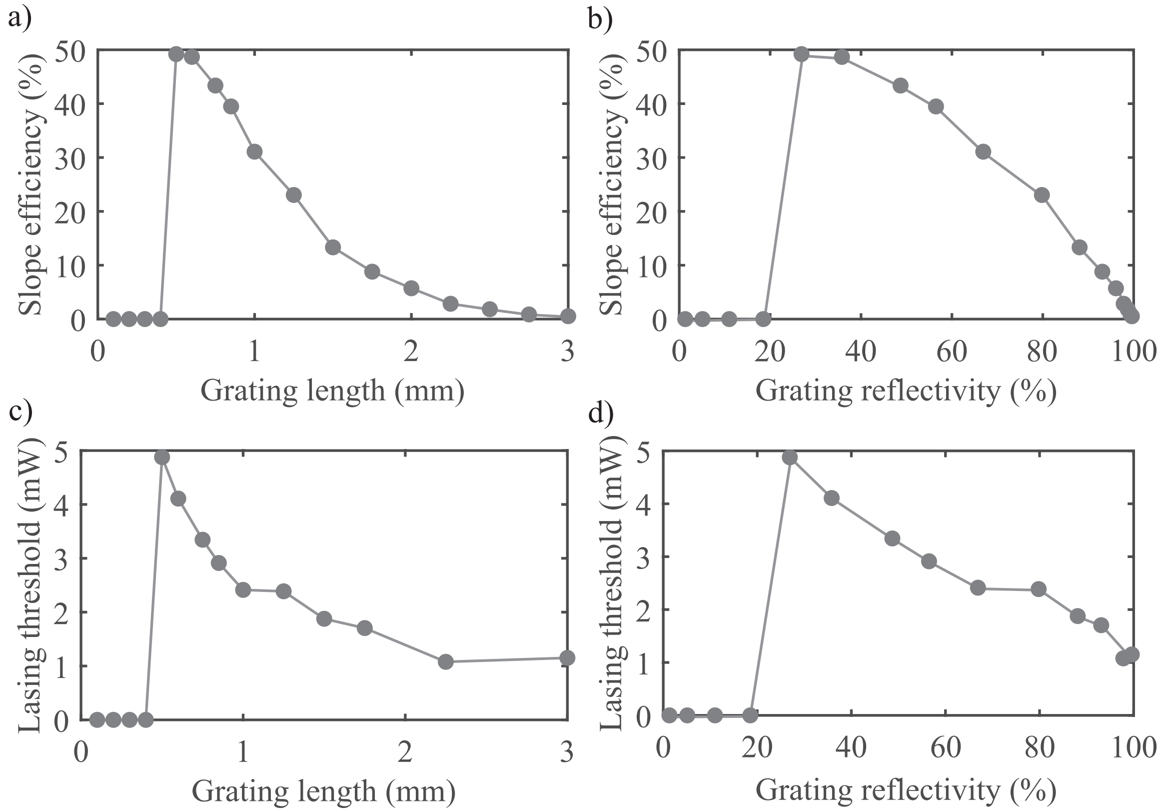

Figure 6.8. TeO_2:Tm^{3+}-Si_3N_4 DBR laser **a, b)** slope efficiency and **c, d)** lasing threshold as a function of grating length and reflectivity, respectively.

Figure 6.9 shows the laser and pump power distributions throughout the cavity when the device is pumped with 100 mW power. While in the erbium laser the total laser power tended to be constant in the region between the gratings, here we observe a significant increase along the forward direction, due to the higher gain obtained from thulium compared to erbium (mainly because of the low overlap between absorption and emission cross sections in thulium). About half of the launched pump power exits the cavity without being absorbed.

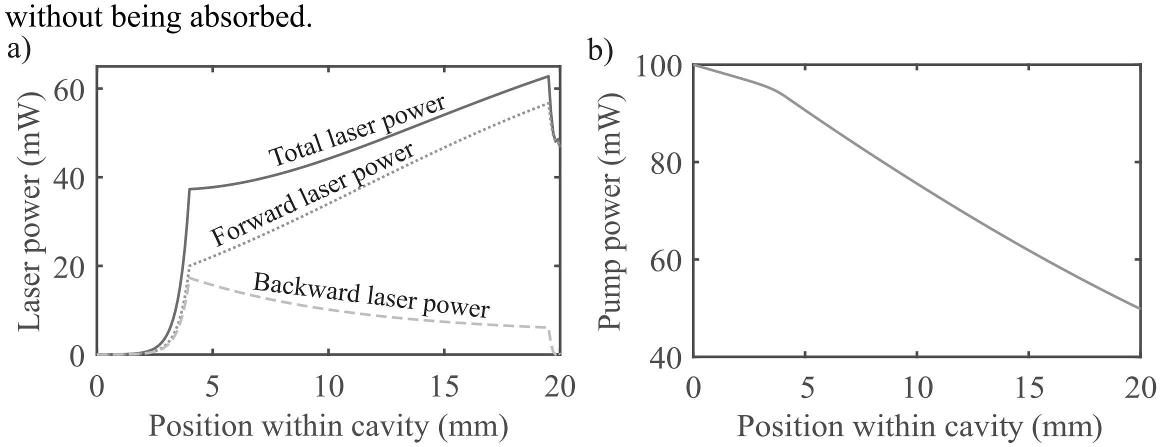

Figure 6.9. TeO_2:Tm^{3+}-Si_3N_4 DBR **a)** laser and **b)** pump power distributions along the cavity.

The gain and absorption coefficient distributions throughout the cavity are shown in Figure 6.10. As expected, these are significantly higher than those of erbium (even when the background loss is considered) and explain the higher efficiencies and output powers achievable with thulium.

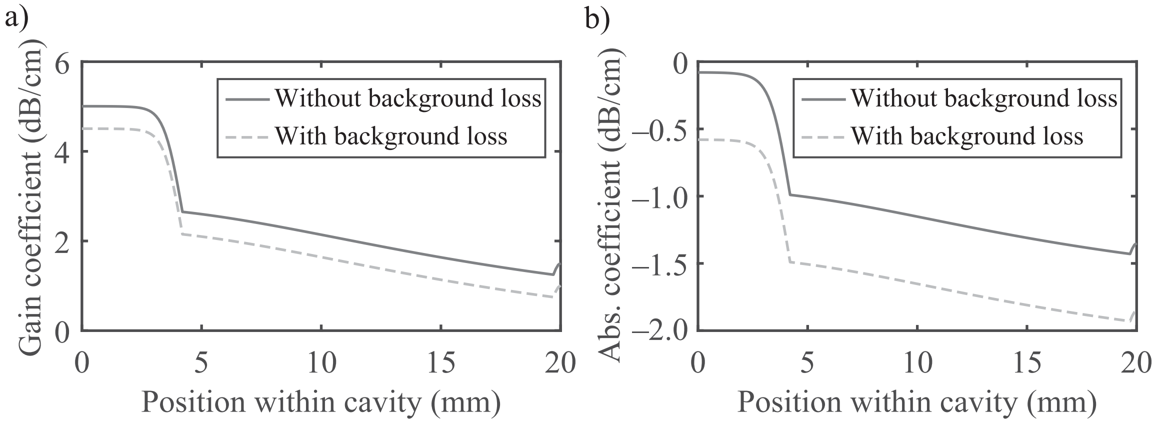

Figure 6.10. a) Gain and **b)** absorption coefficients along the $TeO_2:Tm^{3+}$-Si_3N_4 DBR laser cavity.

6.3.2. Cavity Length

Similarly to the erbium case, the efficiency can be further improved by increasing the total device length until ~40 mm, where a peak efficiency of 64% is expected. Moving away from this length leads to a gradual decrease in efficiency, as shown in Figure 6.11. In this configuration, a minimum lasing threshold of 4.3 mW launched pump power is expected. Unlike the erbium cavities, the simulations suggest that a 10-mm-long device can lase, but requiring higher pump powers.

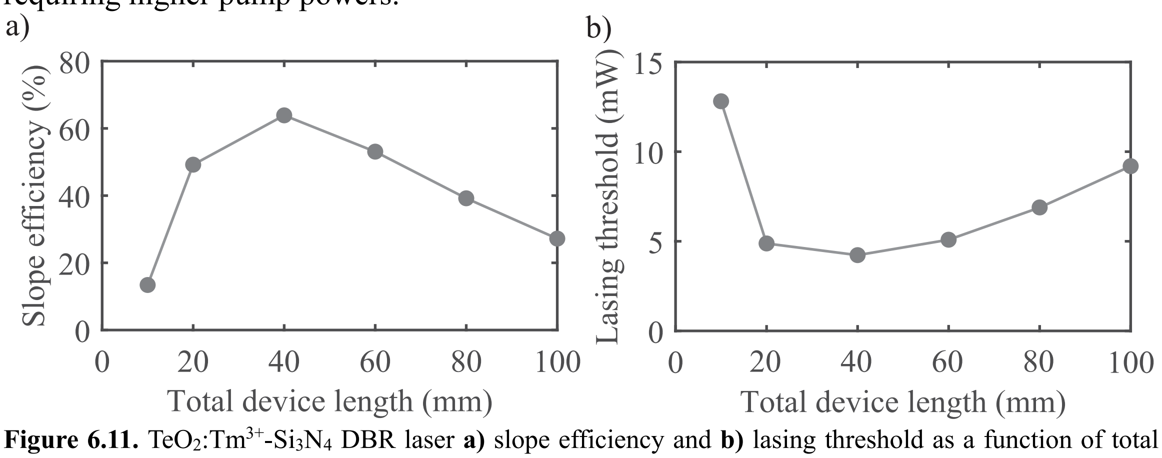

Figure 6.11. $TeO_2:Tm^{3+}$-Si_3N_4 DBR laser **a)** slope efficiency and **b)** lasing threshold as a function of total device length.

6.3.3. BACKGROUND LOSS

As the background loss is varied, we see a significant increase in efficiency up to 83% when the loss is 0.01 dB/cm (see Figure 6.12). You might be surprised with the high efficiencies reported so far (well above 50%), but thulium waveguide lasers with efficiencies between 50–80% (and above) have been demonstrated using different platforms and types of cavities, as discussed in reference [187]. The lasing threshold increases by more than three times and the efficiency drops to 11% as the background loss increases from 0.01 to 2 dB/cm.

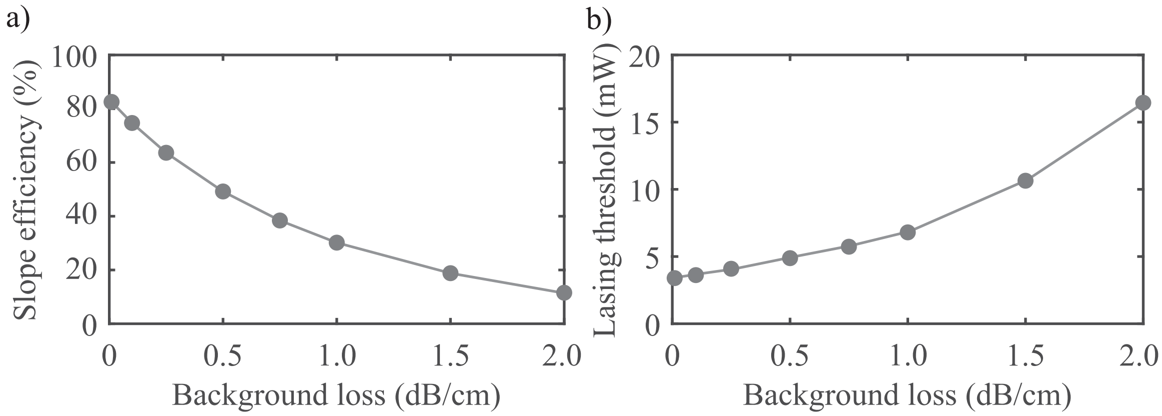

Figure 6.12. $TeO_2:Tm^{3+}$-Si_3N_4 DBR laser **a)** slope efficiency and **b)** lasing threshold as a function of background loss.

6.3.4. EXCITED STATE LIFETIME

Just like in the erbium lasers, the thulium excited-state lifetime does not significantly impact the laser efficiency, but it greatly impacts the lasing threshold, as we can see in Figure 6.13. The threshold is reduced from 14 to 0.8 mW as the lifetime varies from 0.1 to 2 ms. However, for lifetimes longer than 0.5 ms this effect tends to saturate, with diminishing returns.

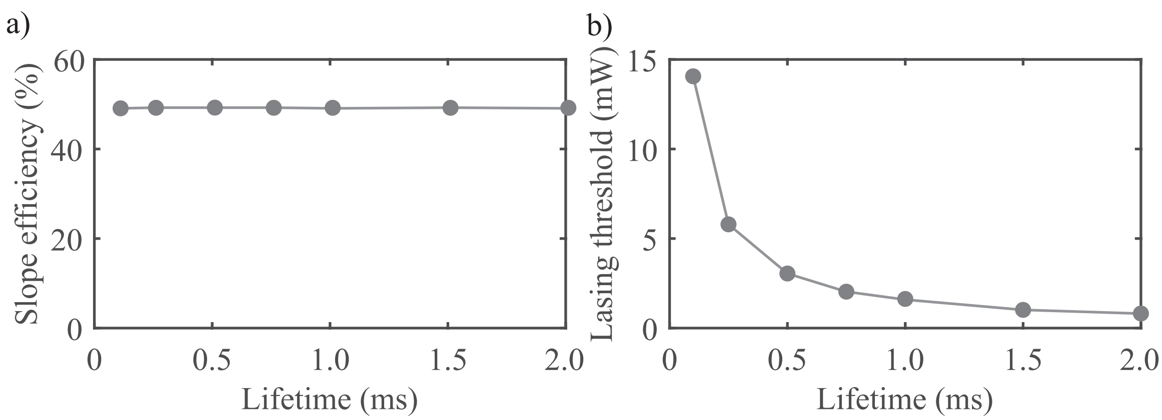

Figure 6.13. $TeO_2:Tm^{3+}$-Si_3N_4 DBR laser **a)** slope efficiency and **b)** lasing threshold as a function of thulium excited-state lifetime.

6.3.5. THULIUM CONCENTRATION

Figure 6.14 shows how the laser performance varies with thulium concentration. As expected, increasing the rare earth concentration leads to an increase in in efficiency and reduction in threshold. However, in previous works, our group has found that thulium concentrations between $4–5 \cdot 10^{20}$ cm^{-3} have the best performance in optical amplifiers [253]. The results indicated that further increasing the concentration made quenching become gradually non-negligible, such that a maximum gain was obtained with $4 \cdot 10^{20}$ ions/cm^3 concentration, which was slightly reduced when the thulium ion concentration was increased to 5 and $6 \cdot 10^{20}$ ions/cm^3. In my simulations, no lasing was observed when the concentration is $1 \cdot 10^{20}$ cm^{-3} with up to 100 mW of launched pump power.

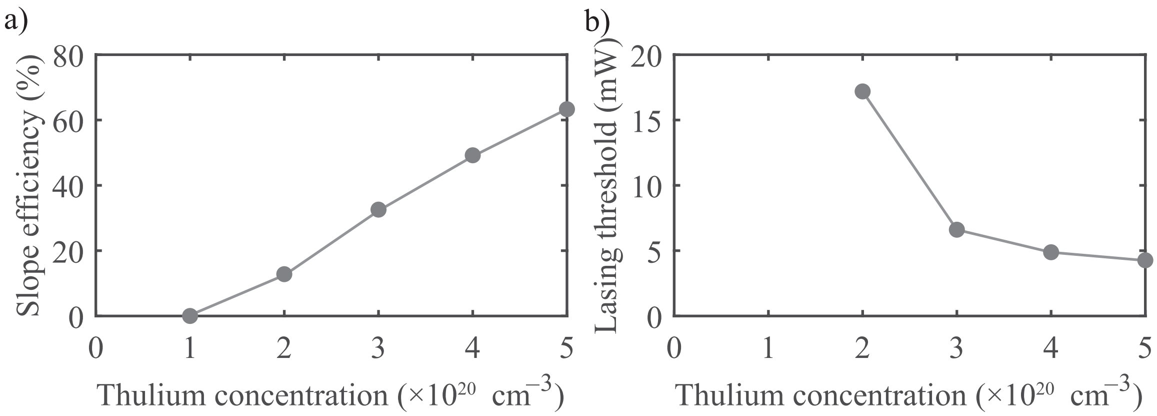

Figure 6.14. $TeO_2:Tm^{3+}$-Si_3N_4 DBR laser **a)** slope efficiency and **b)** lasing threshold as a function of thulium concentration.

6.4. DISCUSSION AND CONCLUSION

In this chapter, we used a laser model that combines the shooting method with coupled mode theory and a rare earth rate equation gain model to investigate how different parameters (grating and device lengths, background loss, excited-state lifetime, rare earth ion concentration, and quenching fraction) affect the performance of hybrid $TeO_2:Er^{3+}$-Si_3N_4 and $TeO_2:Tm^{3+}$-Si_3N_4 distributed Bragg reflector lasers. The results presented here are not an exhaustive optimization (e.g., the grating geometry/coupling coefficient can be optimized, as well as the grating reflectivity for longer devices). However, they suggest that both the erbium and thulium lasers achieved in Chapters 4 and 5 can be greatly optimized, with the potential to yield efficiencies and output powers that are more than one order of magnitude higher than the ones demonstrated experimentally in this thesis. More important than the exact numbers obtained here are the trends and qualitative analyses of how each parameter affects the laser performance. The simulations performed here provide us with insights on different design directions to enhance the laser performances. A significant improvement is expected by simply redesigning the cavities with different output grating and device length. However, further improvements can be made my optimizing the background losses of this platform (perhaps by using multimode waveguides in the gap region between gratings, which are expected to have lower losses) or the spectroscopic properties of erbium and thulium in tellurite glass (e.g. by annealing the samples to enhance the ion activation). One important route to explore in the future is the use of different waveguide cross sections that allow for increased overlap with the tellurite layer and larger mode area, which can potentially enable higher power lasers. The convergence of the model used here can be improved by exploring efficient methods to determine the initial guess and the guess update procedure. The model can also be adjusted and applied to other pump wavelengths and rare earth ion dopants to investigate lasing at other wavelengths. By optimizing these lasers, it is possible to achieve competitive high-power lasers in this hybrid tellurite-silicon nitride platform, which can be easily integrated with other passive, active, and nonlinear devices that our group has already demonstrated.

7. Conclusion

In this final chapter, I briefly summarize the main findings of this work. Then, I share some insights and suggestions on potential directions for future research on Bragg-grating based lasers in the hybrid tellurite-silicon nitride platform.

7.1. Summary

The goals of this thesis were to investigate the properties of Bragg gratings and distributed Bragg reflector (DBR) cavities in a hybrid tellurite-silicon nitride integrated photonics platform and demonstrate on-chip rare-earth DBR lasers by doping the tellurite layer.

This work covered all aspects from design to fabrication and characterization of DBR cavities. Sidewall and multipiece gratings operating at standard telecom wavelengths around 1.3 and 1.5 μm were investigated. While the sidewall gratings were found to work in good agreement with the designed properties, the multipiece gratings turned out to be too strong and require a future redesign to adjust their performance. The main challenge in studying these devices came from the (undoped) tellurite layer non-uniformity across the samples, which impacted their passive properties by causing a random, partial mismatch between the two DBR gratings. The coupling coefficients of 50-nm-wide gratings were estimated as 1110 and 1150 m^{-1} in the O- and C-band respectively. For the 100-nm-wide sidewall gratings, they were found to be 2640 and 2860 m^{-1}. Several symmetrical DBR cavities were characterized, typically yielding quality factors between $1–3 \cdot 10^5$ and finesses around 3–40.

We also employed similar sidewall grating designs to make asymmetrical DBR cavities and demonstrate rare-earth-doped tellurite lasers. Erbium lasers were achieved at wavelengths between 1533 and 1565 nm with different cavity designs. The maximum laser efficiency obtained was 0.36%, while the minimum pump power lasing threshold was 13 mW at 1470 nm wavelength. Moreover, a thulium laser was demonstrated with a total slope efficiency of 5%, maximum on-chip output power of 4.5 mW, and lasing threshold of 20 mW when pumped at 1610 nm. We also characterized the thulium laser thermal tunability using an external heater, finding a sensitivity of 32.3 pm/°C. The cavities used in both erbium and thulium lasers included two strong Bragg reflectors, to improve the chance of lasing in these first proof-of-concept devices, but which caused the lasing to occur generally at the edge of the grating stopband and the efficiencies and output powers to be relatively low, suggesting room for performance improvement.

The aforementioned results were used to investigate routes to optimize the cavity designs, using a shooting-method-based laser model that combined coupled-mode theory with a rare-earth rate equation gain model. We found that by simply adjusting the length of the output grating, it is possible to significantly increase the laser efficiency. However, the devices can be further optimized by adjusting their total length, reducing the background loss, and further investigating and accounting for the spectroscopic properties of the rare earths in the tellurite host material. It is also possible to explore large mode area waveguide designs and larger overall cavity volumes for high power handling.

These findings pave the way for the development of optimized, efficient on-chip tellurite lasers, which can be easily integrated with other passive, active, and nonlinear photonic devices in the same chip. However, there is still much room for improvement and further research to broaden our understanding of Bragg-grating-based devices and lasers in the simple, low-cost, and scalable hybrid platform used here.

7.2. OUTLOOK AND FUTURE WORK

In this section, I propose future research directions that can build upon this work, based on the things I have learned during this project and insights from discussions with my colleagues, supervisor, and supervisory committee.

The first (and most straightforward) route is to fabricate new devices with the optimized grating and cavity lengths discussed in Chapter 6. By doing this, it is expected at least one order of magnitude improvement in the lasers' performance, both for erbium and thulium devices. Further optimizations include reducing the background loss and enhancing the ion activation in tellurite. The former can be explored by using wide, multimode waveguide sections in the region between the gratings, while the latter can be investigated with a careful study of the influence of temperature and deposition rate on the spectroscopy properties of sputtered rare-earth-doped tellurite. Post-deposition annealing also deserves a comprehensive study, even though it is limited to low temperatures due to crystallization of tellurite at high temperatures. Still, short annealing steps in the 200–400 °C range can be studied.

There is also plenty of room to explore other grating designs and geometries. For instance, using a grating with large coupling coefficient (wide stopband) on the input side and one with narrow stopband at the output can help minimize the resonance mismatch due to tellurite nonuniformity, and potentially enable single-mode lasers. I have not had a chance to measure the linewidth of the lasers achieved here, but this is another important measurement to explore in future, optimized devices. Multipiece gratings can also be explored with wider gaps between the grating features and the waveguide to reduce their strength, even though the tellurite might not conform well between the pillars because of the directionality of the sputtering process. The gratings can also be integrated with on-chip heaters to achieve cavities with integrated tunability.

It is also possible to enclose the DBR cavities inside a second DBR cavity (or a simple uniform grating at the output) that operates at the pump wavelength. This would give the pump wavelength a chance to recirculate in the cavity, allowing for better pump absorption and potentially higher efficiencies. Moreover, this would act as an on-chip pump filter, which would help with collecting a pure laser output signal without the need for additional external filters. One way to make such a cavity more compact would be to maintain the sidewall DBR designs similarly to what we have used in this thesis, but simultaneously use multipiece gratings with a different period overlapping with the sidewall grating region to reflect the pump. Another alternative is to use exclusively sidewall gratings, but make the features on each side of the waveguide have a different period to reflect the pump and signal wavelengths at the same time.

Bragg gratings can also be used to achieve distributed feedback (DFB) lasers, for single mode operation and narrow linewidths. In this case, the gratings should be made weaker (e.g. by exploring narrower sidewall gratings, between 10- and 50-nm wide), because these devices require the gratings to run across the entire device length and the designs used here reach 100% reflectivity after a few millimeters.

Another interesting research route is to apply the same concepts explored here on a silicon-on-insulator platform, instead of silicon nitride. One of the main challenges in that approach is that the optical mode is highly confined in standard 220-nm-thick silicon waveguides. One alternative is using thin silicon waveguides with low mode confinement, similar to what we did in this work on silicon nitride. In particular, the foundry that usually fabricates our silicon chips (Advanced Micro Foundry, AMF) has the capability of fabricating 90-nm-thick silicon waveguides (even though this layer is typically offered only as a slab layer and not optimized to produce ridge waveguides). By using a thin silicon layer, similar hybrid tellurite waveguides can be achieved, and many of the design considerations explored here translate to silicon straightforwardly. The main challenge here is achieving similar low losses in silicon as in silicon nitride. I truly believe that this can be achieved by properly engineering the waveguide cross section (again, using multimode waveguides between the reflectors) and optimizing the fabrication process to produce high quality patterning in the thin silicon layer. This is an exciting research direction that can enable rare-earth lasers and amplifiers directly on silicon, which can be easily integrated with the mature library of silicon-on-insulator components.

Lastly, these considerations can be expanded to other wavelengths, by using different rare-earth dopants. Lasers operating around 1.0 μm can be achieved in ytterbium- and neodymium-doped tellurite, while O-band lasers (around 1.3 μm) can potentially be demonstrated by exploring praseodymium- and neodymium-doped tellurite. However, further spectroscopy work is needed to better understand tellurite's luminescence properties when doped with Pr or Nd. Holmium doping can also be explored for emission beyond 2.0 μm. Furthermore, co-doping can be investigated to enhance the performance of these lasers. In particular, erbium-ytterbium and praseodymium-ytterbium can be studied to enhance light emission around 1.5 and 1.3 μm wavelengths, respectively.

– THE END.

Bibliography

1. Y. N. Harari, *Sapiens: A Brief History of Humankind* (Signal, 2016).
2. G. Gillespie, "Technology of communication timeline," https://eagle.northwestu.edu/faculty/gary-gillespie/technology-of-communication-timeline/.
3. V. Moeyaert and G. Maier, "Network technologies for broadband access," 13th Int. Conf. Transparent Opt. Netw. Stockholm, Sweden, 1–5 (2011).
4. L. Grzybowski, M. Hasbi, and J. Liang, "Transition from copper to fiber broadband: the role of connection speed and switching costs," Inf. Econ. Policy 42, 1–10 (2018).
5. W. A. Gambling, "The rise and rise of optical fibers," IEEE J. Sel. Top. Quantum Electron. 6(6), 1084–1093 (2000).
6. C. David. Chaffee, *The Rewiring of America: The Fiber Optics Revolution* (Academic Press, 1988).
7. P. Urquhart, "Review of rare earth doped fibre lasers and amplifiers," IEE Proc. 135(6), (1988).
8. M. N. Zervas and C. A. Codemard, "High power fiber lasers: a review," IEEE J. Sel. Top. Quantum Electron. 20(5), (2014).
9. D. Brida, G. Krauss, A. Sell, and A. Leitenstorfer, "Ultrabroadband Er:fiber lasers," Laser Photonics Rev. 8(3), 409–428 (2014).
10. P. D. Dragic, M. Cavillon, and J. Ballato, "Materials for optical fiber lasers: a review," Appl. Phys. Rev. 5(041301), (2018).
11. W. Shi, Q. Fang, X. Zhu, R. A. Norwood, and N. Peyghambarian, "Fiber lasers and their applications [Invited]," Appl. Opt. 53(28), 6554–6568 (2014).
12. L. Thylén and L. Wosinski, "Integrated photonics in the 21st century," Photonics Res. 2(2), 75–81 (2014).
13. S. E. Miller, "Integrated optics: an introduction," Bell Syst. Tech. J. 48(7), 2059–2069 (1969).
14. E. A. J. Marcatili, "Dielectric rectangular waveguide and directional coupler for integrated optics," Bell Syst. Tech. J. 48(7), 2071–2102 (1969).
15. P. K. Tien, "Light waves in thin films and integrated optics," Appl. Opt. 10(11), 2395–2413 (1971).
16. P. K. Tien, "Integrated optics and new wave phenomena in optical waveguides," Rev. Mod. Phys. 49(361), (1977).
17. Z. Fang and C. Z. Zhao, "Recent progress in silicon photonics: a review," ISRN Opt. 2012(428690), 1–27 (2012).
18. J. D. Musgraves, J. Hu, and L. Calvez, *Springer Handbook of Glass* (Springer, 2019).
19. J. D. B. Bradley, F. Ay, K. Wörhoff, and M. Pollnau, "Fabrication of low-loss channel waveguides in Al_2O_3 and Y_2O_3 layers by inductively coupled plasma reactive ion etching," Appl. Phys. B Lasers Opt. 89, 311–318 (2007).
20. W. A. Hendriks, L. Chang, C. I. Van Emmerik, J. Mu, M. De Goede, M. Dijkstra, and S. M. Garcia-Blanco, "Rare-earth ion doped Al2O3 for active integrated photonics," Adv. Phys. X 6(1), 1833753 (2021).
21. B. Gholipour, S. R. Elliott, M. J. Müller, M. Wuttig, D. W. Hewak, B. E. Hayden, Y. Li, S. S. Jo, R. Jaramillo, R. E. Simpson, J. Tominaga, Y. Cui, A. Mandal, B. J. Eggleton, M. Rochette, M. Rezaei, I. Alamgir, H. M. Shamim, R. Kormokar, A. Anjum, G. T. Zeweldi, T. S. Karnik, J. Hu, S. O. Kasap, G. Belev, and A. Reznik, "Roadmap on chalcogenide photonics," J. Phys. Photonics 5(012501), (2023).
22. J.-E. Broquin and S. Honkanen, "Integrated photonics on glass: A review of the ion-exchange technology achievements," Appl. Sci. 11(4472), (2021).
23. F. Gardillou, L. Bastard, and J. E. Broquin, "4.25 dB gain in a hybrid silicate/phosphate glasses optical amplifier made by wafer bonding and ion-exchange techniques," Appl. Phys. Lett. 85(22), 5176–5178 (2004).

24. S. Blaize, L. Bastard, C. Cassagnètes, and J. E. Broquin, "Multiwavelengths DFB waveguide laser arrays in Yb-Er codoped phosphate glass substrate," IEEE Photonics Technol. Lett. 15(4), 516–518 (2003).
25. A. Yi, C. Wang, L. Zhou, Y. Zhu, S. Zhang, T. You, J. Zhang, and X. Ou, "Silicon carbide for integrated photonics," Appl. Phys. Rev. 9(031302), (2022).
26. L. Splitthoff, M. A. Wolff, T. Grottke, and C. Schuck, "Tantalum pentoxide nanophotonic circuits for integrated quantum technology," Opt. Express 28(8), 11921 (2020).
27. X.-Y. Han, Z.-L. Wu, S.-C. Yang, F.-F. Shen, Y.-X. Liang, L.-H. Wang, J.-Y. Wang, J. Ren, L.-Y. Jia, H. Zhang, S.-H. Bo, G. Morthier, and M.-S. Zhao, "Recent progress of imprinted polymer photonic waveguide devices and applications," Polymers 10(603), (2018).
28. R. Butté and N. Grandjean, "III-nitride photonic cavities," Nanophotonics 9(3), 569–598 (2020).
29. N. Li, C. P. Ho, S. Zhu, Y. H. Fu, Y. Zhu, and L. Y. T. Lee, "Aluminium nitride integrated photonics: a review," Nanophotonics 10(9), 2347–2387 (2021).
30. D. Zhu, L. Shao, M. Yu, R. Cheng, B. Desiatov, C. J. Xin, Y. Hu, J. Holzgrafe, S. Ghosh, A. Shams-Ansari, E. Puma, N. Sinclair, C. Reimer, M. Zhang, and M. Lončar, "Integrated photonics on thin-film lithium niobate," Adv. Opt. Photonics 13(2), 242 (2021).
31. Y. Qi and Y. Li, "Integrated lithium niobate photonics," Nanophotonics 9(6), 1287–1320 (2020).
32. M. G. Vazimali and S. Fathpour, "Applications of thin-film lithium niobate in nonlinear integrated photonics," Adv. Photonics 4(3), (2022).
33. Y. Jia, J. Wu, X. Sun, X. Yan, R. Xie, L. Wang, Y. Chen, and F. Chen, "Integrated Photonics Based on Rare-Earth Ion-Doped Thin-Film Lithium Niobate," Laser Photonics Rev. 16(9), 2200059 (2022).
34. G. Chen, N. Li, J. D. Ng, H. L. Lin, Y. Zhou, Y. H. Fu, L. Y. T. Lee, Y. Yu, A. Q. Liu, and A. J. Danner, "Advances in lithium niobate photonics: development status and perspectives," Adv. Photonics 4(3), (2022).
35. T. D. Bucio, C. Lacava, M. Clementi, J. Faneca, I. Skandalos, A. Baldycheva, M. Galli, K. Debnath, P. Petropoulos, and F. Gardes, "Silicon nitride photonics for the near-infrared," IEEE J. Sel. Top. Quantum Electron. 26(2), (2020).
36. C. Xiang, W. Jin, and J. E. Bowers, "Silicon nitride passive and active photonic integrated circuits: trends and prospects," Photonics Res. 10(6), (2022).
37. D. J. Blumenthal, R. Heideman, D. Geuzebroek, A. Leinse, and C. Roeloffzen, "Silicon nitride in silicon photonics," Proc. IEEE 106(12), 2209–2231 (2018).
38. T. Sharma, J. Wang, B. K. Kaushik, Z. Cheng, R. Kumar, Z. Wei, and X. Li, "Review of recent progress on silicon nitride-based photonic integrated circuits," IEEE Access 8, 195436–195446 (2020).
39. M. Tang, J. S. Park, Z. Wang, S. Chen, P. Jurczak, A. Seeds, and H. Liu, "Integration of III-V lasers on Si for Si photonics," Prog. Quantum Electron. 66, 1–18 (2019).
40. Z. Yan, Y. Han, L. Lin, Y. Xue, C. Ma, W. K. Ng, K. S. Wong, and K. M. Lau, "A monolithic InP/SOI platform for integrated photonics," Light Sci. Appl. 10(200), (2021).
41. M. Smit, K. Williams, and J. van der Tol, "Past, present, and future of InP-based photonic integration," APL Photonics 4(050901), (2019).
42. F. A. Kish, D. Welch, R. Nagarajan, J. L. Pleumeekers, V. Lal, M. Ziari, A. Nilsson, M. Kato, S. Murthy, P. Evans, S. W. Corzine, M. Mitchell, P. Samra, M. Missey, S. DeMars, R. P. Schneider, M. S. Reffle, T. Butrie, J. T. Rahn, M. Van Leeuwen, J. W. Stewart, D. J. H. Lambert, R. C. Muthiah, H. S. Tsai, J. S. Bostak, A. Dentai, K. T. Wu, H. Sun, D. J. Pavinski, J. Zhang, J. Tang, J. McNicol, M. Kuntz, V. Dominic, B. D. Taylor, R. A. Salvatore, M. Fisher, A. Spannagel, E. Strzelecka, P. Studenkov, M. Raburn, W. Williams, D. Christini, K. J. Thomson, S. S. Agashe, R. Malendevich, G. Goldfarb, S. Melle, C. Joyner, M. Kaufman, and S. G. Grubb, "Current status of large-scale InP photonic integrated circuits," IEEE J. Sel. Top. Quantum Electron. 17(6), 1470–1489 (2011).
43. K. A. Williams, E. A. J. M. Bente, D. Heiss, Y. Jiao, K. Ławniczuk, X. J. M. Leijtens, J. J. G. M. van der Tol, and M. K. Smit, "InP photonic circuits using generic integration [Invited]," Photonics Res. 3(5), (2015).
44. H. Zhao, S. Pinna, F. Sang, B. Song, S. T. S. Brunelli, L. A. Coldren, and J. Klamkin, "High-power indium phosphide photonic integrated circuits," IEEE J. Sel. Top. Quantum Electron. 25(6), (2019).

45. N. Li, G. Chen, D. K. T. Ng, L. W. Lim, J. Xue, C. P. Ho, Y. H. Fu, and L. Y. T. Lee, "Integrated lasers on silicon at communication wavelength: a progress review," Adv. Opt. Mater. 10(2201008), (2022).
46. C. Op de Beeck, B. Haq, L. Elsinger, A. Gocalinska, E. Pelucchi, B. Corbett, G. Roelkens, and B. Kuyken, "Heterogeneous III-V on silicon nitride amplifiers and lasers via microtransfer printing," Optica 7(5), 386 (2020).
47. B. Stern, X. Ji, A. Dutt, and M. Lipson, "Compact narrow-linewidth integrated laser based on low-loss silicon nitride ring resonator," in *2018 Conference on Lasers and Electro-Optics, CLEO 2018 - Proceedings* (Institute of Electrical and Electronics Engineers Inc., 2018).
48. X. Zhang, X. Liu, R. Ma, Z. Chen, Z. Yang, Y. Han, B. Wang, S. Yu, R. Wang, and X. Cai, "Heterogeneously integrated III–V-on-lithium niobate broadband light sources and photodetectors," Opt. Lett. 47(17), 4564 (2022).
49. C. Op de Beeck, F. M. Mayor, S. Cuyvers, S. Poelman, J. F. Herrmann, O. Atalar, T. P. McKenna, B. Haq, W. Jiang, J. D. Witmer, G. Roelkens, A. H. Safavi-Naeini, R. Van Laer, and B. Kuyken, "III/V-on-lithium niobate amplifiers and lasers," Optica 8(10), 1288 (2021).
50. A. J. Maker and A. M. Armani, "Low-loss silica-on-silicon waveguides," Opt. Lett. 36(19), 3729–3731 (2011).
51. M. Kawachi, "Silica waveguides on silicon and their application to integrated-optic components," Opt. Quantum Electron. 22, 391–416 (1990).
52. L. Chrostowski, H. Shoman, M. Hammood, H. Yun, J. Jhoja, E. Luan, S. Lin, A. Mistry, D. Witt, N. A. F. Jaeger, S. Shekhar, H. Jayatilleka, P. Jean, S. B. -de Villers, J. Cauchon, W. Shi, C. Horvath, J. N. Westwood-Bachman, K. Setzer, M. Aktary, N. S. Patrick, R. J. Bojko, A. Khavasi, X. Wang, T. Ferreira de Lima, A. N. Tait, P. R. Prucnal, D. E. Hagan, D. Stevanovic, and A. P. Knights, "Silicon photonic circuit design using rapid prototyping foundry process design kits," IEEE J. Sel. Top. Quantum Electron. 25(5), 1–26 (2019).
53. K. Wörhoff, R. G. Heideman, A. Leinse, and M. Hoekman, "TriPleX: a versatile dielectric photonic platform," Adv. Opt. Technol. 4(2), 189–207 (2015).
54. S. Y. Siew, B. Li, F. Gao, H. Y. Zheng, W. Zhang, P. Guo, S. W. Xie, A. Song, B. Dong, L. W. Luo, C. Li, X. Luo, and G. Q. Lo, "Review of silicon photonics technology and platform development," J. Light. Technol. 39(13), 4374–4389 (2021).
55. P. P. Absil, P. De Heyn, H. Chen, P. Verheyen, G. Lepage, M. Pantouvaki, J. De Coster, A. Khanna, Y. Drissi, D. Van Thourhout, and J. Van Campenhout, "Imec iSiPP25G silicon photonics: a robust CMOS-based photonics technology platform," Silicon Photonics X 9367, (2015).
56. R. Soref, "The past, present, and future of silicon photonics," IEEE J. Sel. Top. Quantum Electron. 12(6), 1678–1687 (2006).
57. W. Bogaerts, M. Fiers, and P. Dumon, "Design challenges in silicon photonics," IEEE J. Sel. Top. Quantum Electron. 20(4), (2014).
58. H. Moriceau, F. Mazen, C. Braley, F. Rieutord, A. Tauzin, and C. Deguet, "Smart Cut^{TM}: Review on an attractive process for innovative substrate elaboration," Nucl. Instrum. Methods Phys. Res. Sect. B Beam Interact. Mater. At. 277, 84–92 (2012).
59. W. N. Ye and Y. Xiong, "Review of silicon photonics: history and recent advances," J. Mod. Opt. 60(16), 1299–1320 (2013).
60. A. Novack, M. Streshinsky, R. Ding, Y. Liu, A. E. J. Lim, G. Q. Lo, T. Baehr-Jones, and M. Hochberg, "Progress in silicon platforms for integrated optics," Nanophotonics 3(4–5), 205–214 (2014).
61. G. T. Reed and A. P. Knights, *Silicon Photonics* (Wiley, 2004).
62. Q. Wilmart, H. El Dirani, N. Tyler, D. Fowler, S. Malhouitre, S. Garcia, M. Casale, S. Kerdiles, K. Hassan, C. Monat, X. Letartre, A. Kamel, M. Pu, K. Yvind, L. K. Oxenløwe, W. Rabaud, C. Sciancalepore, B. Szelag, and S. Olivier, "A versatile silicon-silicon nitride photonics platform for enhanced functionalities and applications," Appl. Sci. 9(255), (2019).
63. A. Rahim, E. Ryckeboer, A. Z. Subramanian, S. Clemmen, B. Kuyken, A. Dhakal, A. Raza, A. Hermans, M. Muneeb, S. Dhoore, Y. Li, U. Dave, P. Bienstman, N. Le Thomas, G. Roelkens, D. Van

Thourhout, P. Helin, S. Severi, X. Rottenberg, and R. Baets, "Expanding the silicon photonics portfolio with silicon nitride photonic integrated circuits," J. Light. Technol. 35(4), 639–649 (2017).

64. Y. Liu, Z. Qiu, X. Ji, A. Lukashchuk, J. He, J. Riemensberger, M. Hafermann, R. N. Wang, J. Liu, C. Ronning, and T. J. Kippenberg, "A photonic integrated circuit-based erbium-doped amplifier," Science 376, 1309–1313 (2022).
65. L. Agazzi, J. D. B. Bradley, M. Dijkstra, F. Ay, G. Roelkens, R. Baets, K. Wörhoff, and M. Pollnau, "Monolithic integration of erbium-doped amplifiers with silicon-on-insulator waveguides," Opt. Express 18(26), 27703–27711 (2010).
66. Purnawirman, N. Li, E. S. Magden, G. Singh, N. Singh, A. Baldycheva, E. S. Hosseini, J. Sun, M. Moresco, T. N. Adam, G. Leake, D. Coolbaugh, J. D. B. Bradley, and M. R. Watts, "Ultra-narrow-linewidth Al_2O_3:Er^{3+} lasers with a wavelength-insensitive waveguide design on a wafer-scale silicon nitride platform," Opt. Express 25(12), 13705 (2017).
67. E. S. Hosseini, Purnawirman, J. D. B. Bradley, J. Sun, G. Leake, T. N. Adam, D. D. Coolbaugh, and M. R. Watts, "CMOS-compatible 75 mW erbium-doped distributed feedback laser," Opt. Lett. 39(11), 3106–3109 (2014).
68. Purnawirman, J. Sun, T. N. Adam, G. Leake, D. Coolbaugh, J. D. B. Bradley, E. S. Hosseini, and M. R. Watts, "C- and L-band erbium-doped waveguide lasers with wafer-scale silicon nitride cavities," Opt. Lett. 38(11), 1760–1762 (2013).
69. S. J. Madden and K. T. Vu, "High-performance integrated optics with tellurite glasses: status and prospects," Int. J. Appl. Glass Sci. 3(4), 289–298 (2012).
70. R. Botter, B. L. Segat Frare, B. Hashemi, K. Ye, Y. Klaver, J. D. B. Bradley, and D. Marpaung, "Observation and enhancement of stimulated Brillouin scattering in tellurite covered silicon nitride waveguides," Opt. Open Prepr. (2023).
71. W. A. Bonner, S. Singh, L. G. V. Uitert, and A. W. Warner, "High quality tellurium dioxide for acousto-optics and non-linear applications," J. Electron. Mater. (1), 154–164 (1972).
72. S. J. Madden and K. T. Vu, "Very low loss reactively ion etched Tellurium Dioxide planar rib waveguides for linear and non-linear optics," Opt. Express 17(20), 17645–17651 (2009).
73. K. Vu and S. Madden, "Tellurium dioxide Erbium doped planar rib waveguide amplifiers with net gain and 2.8dB/cm internal gain," Opt. Express 18(18), 19192–19200 (2010).
74. E. A. Anashkina and A. Andrianov, "Erbium-doped tellurite glass microlaser in C-Band and L-Band," J. Light. Technol. 39(11), 3568–3574 (2021).
75. S. Marjanovic, J. Toulouse, H. Jain, C. Sandmann, V. Dierolf, A. R. Kortan, N. Kopylov, and R. G. Ahrens, "Characterization of new erbium-doped tellurite glasses and fibers," in *Journal of Non-Crystalline Solids* (2003), 322(1–3), pp. 311–318.
76. N. Li, D. Vermeulen, Z. Su, E. S. Magden, M. Xin, N. Singh, A. Ruocco, J. Notaros, C. V. Poulton, E. Timurdogan, C. Baiocco, and M. R. Watts, "Monolithically integrated erbium-doped tunable laser on a CMOS-compatible silicon photonics platform," Opt. Express 26(13), 16200 (2018).
77. J. Notaros, N. Li, C. V. Poulton, Z. Su, M. J. Byrd, E. S. Magden, E. Timurdogan, C. Baiocco, N. M. Fahrenkopf, and M. R. Watts, "CMOS-compatible optical phased array powered by a monolithically-integrated erbium laser," J. Light. Technol. 37(24), 5982–5987 (2019).
78. M. C. Falconi, D. Laneve, and F. Prudenzano, "Advances in mid-IR fiber lasers: tellurite, fluoride and chalcogenide," Fibers 5(23), (2017).
79. E. A. Anashkina, "Laser sources based on rare-earth ion doped tellurite glass fibers and microspheres," Fibers 8(30), (2020).
80. A. Jha, B. D. O. Richards, G. Jose, T. T. Fernandez, C. J. Hill, J. Lousteau, and P. Joshi, "Review on structural, thermal, optical and spectroscopic properties of tellurium oxide based glasses for fibre optic and waveguide applications," Int. Mater. Rev. 57(6), 357–382 (2012).
81. A. Mori, "Tellurite-based fibers and their applications to optical communication networks," J. Ceram. Soc. Jpn. 116(10), 1040–1051 (2008).
82. B. Richards, A. Jha, Y. Tsang, D. Binks, J. Lousteau, F. Fusari, A. Lagatsky, C. Brown, and W. Sibbett, "Tellurite glass lasers operating close to 2 μm," Laser Phys. Lett. 7(3), 177–193 (2010).
83. S. Shen, A. Jha, X. Liu, M. Naftaly, K. Bindra, H. J. Bookey, and A. K. Kar, "Tellurite glasses for broadband amplifiers and integrated optics," J. Am. Ceram. Soc. 85(6), (2002).

84. K. Vu, S. Farahani, and S. Madden, "980nm pumped erbium doped tellurium oxide planar rib waveguide laser and amplifier with gain in S, C and L band," Opt. Express 23(2), 747–755 (2015).
85. H. C. Frankis, K. Miarabbas Kiani, D. Su, R. Mateman, A. Leinse, and J. D. B. Bradley, "High-Q tellurium-oxide-coated silicon nitride microring resonators," Opt. Lett. 44(1), 118–121 (2019).
86. H. C. Frankis, K. Miarabbas Kiani, D. B. Bonneville, C. Zhang, S. Norris, R. Mateman, A. Leinse, N. D. Bassim, A. P. Knights, and J. D. B. Bradley, "Low-loss TeO_2-coated Si_3N_4 waveguides for application in photonic integrated circuits," Opt. Express 27(9), 12529–12540 (2019).
87. H. C. Frankis, H. M. Mbonde, D. B. Bonneville, C. Zhang, R. Mateman, A. Leinse, and J. D. B. Bradley, "Erbium-doped TeO_2-coated Si_3N_4 amplifiers with 5 dB net gain waveguide," Photonics Res. 8(2), 127–134 (2020).
88. K. Miarabbas Kiani, H. C. Frankis, H. M. Mbonde, R. Mateman, A. Leinse, A. P. Knights, and J. D. B. Bradley, "Thulium-doped tellurium oxide waveguide amplifier with 7.6 dB net gain on a silicon nitride chip," Opt. Lett. 44(23), 5788–5791 (2019).
89. K. Miarabbas Kiani, H. C. Frankis, R. Mateman, A. Leinse, A. P. Knights, and J. D. B. Bradley, "Thulium-doped tellurium oxide microring lasers integrated on a low-loss silicon nitride platform," Opt. Mater. Express 11(11), 3656–3665 (2021).
90. K. Miarabbas Kiani, H. C. Frankis, C. M. Naraine, D. B. Bonneville, A. P. Knights, and J. D. B. Bradley, "Lasing in a hybrid rare-earth silicon microdisk," Laser Photonics Rev. 16(1), (2022).
91. B. R. Koch, E. J. Norberg, B. Kim, J. Hutchinson, J.-H. Shin, G. Fish, and A. Fang, "Integrated silicon photonic laser sources for telecom and datacom," Opt. Fiber Commun. Conf. Expo. Natl. Fiber Opt. Eng. Conf. OFCNFOEC (2013).
92. H. Kim, W. J. Lee, A. C. Farrell, A. Balgarkashi, and D. L. Huffaker, "Telecom-wavelength bottom-up nanobeam lasers on silicon-on-insulator," Nano Lett. 17, 5244–5250 (2017).
93. N. L. Kazanskiy, M. A. Butt, and S. N. Khonina, "Optical computing: status and perspectives," Nanomaterials 12(2171), (2022).
94. R. Gupta, R. Singh, A. Gehlot, S. V. Akram, N. Yadav, R. Brajpuriya, A. Yadav, Y. Wu, H. Zheng, A. Biswas, E. Suhir, V. S. Yadav, T. Kumar, and A. S. Verma, "Silicon photonics interfaced with microelectronics for integrated photonic quantum technologies: a new era in advanced quantum computers and quantum communications?," Nanoscale 15, 4682–4693 (2022).
95. V. A. Pammi, K. Alfaro-Bittner, M. G. Clerc, and S. Barbay, "Photonic computing with single and coupled spiking micropillar lasers," IEEE J. Sel. Top. Quantum Electron. 26(1), (2020).
96. Y. Shi, C. Wan, C. Dai, Z. Wang, S. Wan, G. Zheng, S. Zhang, and Z. Li, "Augmented reality enabled by on-chip meta-holography multiplexing," Laser Photonics Rev. 16(2100638), (2022).
97. J. Xiong, E. L. Hsiang, Z. He, T. Zhan, and S. T. Wu, "Augmented reality and virtual reality displays: emerging technologies and future perspectives," Light Sci. Appl. 10(216), (2021).
98. Y. Liu, Y. Shi, Z. Wang, and Z. Li, "On-chip integrated metasystem with inverse-design wavelength demultiplexing for augmented reality," ACS Photonics 10, 1268–1274 (2023).
99. C.-P. Hsu, B. Li, B. Solano-Rivas, A. R. Gohil, P. H. Chan, A. D. Moore, and V. Donzella, "A review and perspective on optical phased array for automotive LiDAR," IEEE J. Sel. Top. Quantum Electron. 27(1), (2021).
100. K. Sayyah, R. Sarkissian, P. Patterson, B. Huang, O. Efimov, D. Kim, K. Elliott, L. Yang, and D. Hammon, "Fully integrated FMCW LiDAR optical engine on a single silicon chip," J. Light. Technol. 40(9), 2763–2772 (2022).
101. N. Dostart, B. Zhang, A. Khilo, M. Brand, K. Al Qubaisi, D. Onural, D. Feldkhun, K. H. Wagner, and M. A. Popović, "Serpentine optical phased arrays for scalable integrated photonic lidar beam steering," Optica 7(6), 726 (2020).
102. K. W. Cho, W. H. Lee, B. S. Kim, and D. H. Kim, "Sensors in heart-on-a-chip: a review on recent progress," Talanta 219(121269), (2020).
103. M. C. Estevez, M. Alvarez, and L. M. Lechuga, "Integrated optical devices for lab-on-a-chip biosensing applications," Laser Photonics Rev. 6(4), 463–487 (2012).
104. C. Vannahme, S. Klinkhammer, U. Lemmer, and T. Mappes, "Plastic lab-on-a-chip for fluorescence excitation with integrated organic semiconductor lasers," Opt. Express 19(9), (2011).

105. B. Schwarz, P. Reininger, D. Ristanić, H. Detz, A. M. Andrews, W. Schrenk, and G. Strasser, "Monolithically integrated mid-infrared lab-on-a-chip using plasmonics and quantum cascade structures," Nat. Commun. 5(4085), (2014).
106. D. K. Shin, B. M. Henson, R. I. Khakimov, J. A. Ross, C. J. Dedman, S. S. Hodgman, K. G. H. Baldwin, and A. G. Truscott, "Widely tunable, narrow linewidth external-cavity gain chip laser for spectroscopy between 1.0 – 1.1 μm," Opt. Express 24(24), 27403 (2016).
107. J. Yang, M. Tang, S. Chen, and H. Liu, "From past to future: on-chip laser sources for photonic integrated circuits," Light Sci. Appl. 12(16), (2023).
108. D. Liang and J. E. Bowers, "Recent progress in lasers on silicon," Nat. Photonics 4, 511–517 (2010).
109. Z. Zhou, X. Ou, Y. Fang, E. Alkhazraji, R. Xu, Y. Wan, and J. E. Bowers, "Prospects and applications of on-chip lasers," eLight 3(1), (2023).
110. M. T. Hill and M. C. Gather, "Advances in small lasers," Nat. Photonics 8, (2014).
111. G. Spektor, D. Carlson, Z. Newman, J. L. Skarda, N. Sapra, L. Su, S. Jammi, A. R. Ferdinand, A. Agrawal, J. Vučković, and S. B. Papp, "Universal visible emitters in nanoscale integrated photonics," Optica 10(7), 871 (2023).
112. C. A. A. Franken, W. A. P. M. Hendriks, L. V. Winkler, M. Dijkstra, A. R. do Nascimento, A. van Rees, M. R. S. Mardani, R. Dekker, J. van Kerkhof, P. J. M. van der Slot, S. M. García-Blanco, and K.-J. Boller, "Hybrid integrated near UV lasers using the deep-UV Al_2O_3 platform," ArXiv Prepr. (2023).
113. D. J. Blumenthal, "Photonic integration for UV to IR applications," APL Photonics 5(020903), (2020).
114. A. Siddharth, T. Wunderer, G. Lihachev, A. S. Voloshin, C. Haller, R. N. Wang, M. Teepe, Z. Yang, J. Liu, J. Riemensberger, N. Grandjean, N. Johnson, and T. J. Kippenberg, "Near ultraviolet photonic integrated lasers based on silicon nitride," APL Photonics 7(046108), (2022).
115. N. Chauhan, A. Isichenko, K. Liu, J. Wang, Q. Zhao, R. O. Behunin, P. T. Rakich, A. M. Jayich, C. Fertig, C. W. Hoyt, and D. J. Blumenthal, "Visible light photonic integrated Brillouin laser," Nat. Commun. 12(4685), (2021).
116. C. Khurmi, S. Thoday, T. M. Monro, G. Chen, and D. G. Lancaster, "Visible laser emission from a praseodymium-doped fluorozirconate guided-wave chip," Opt. Lett. 42(17), 3339 (2017).
117. F. Tabataba-Vakili, B. Alloing, B. Damilano, H. Souissi, C. Brimont, L. Doyennette, T. Guillet, X. Checoury, M. El Kurdi, S. Chenot, E. Frayssinet, J.-Y. Duboz, F. Semond, B. Gayral, and P. Boucaud, "Monolithic integration of ultraviolet microdisk lasers into photonic circuits in a III-nitride-on-silicon platform," Opt. Lett. 45(15), 4276 (2020).
118. M. S. Vitiello and P. De Natale, "Terahertz quantum cascade lasers as enabling quantum technology," Adv. Quantum Technol. 5(2100082), (2022).
119. H. Nguyen-Van, A. N. Baranov, Z. Loghmari, L. Cerutti, J. B. Rodriguez, J. Tournet, G. Narcy, G. Boissier, G. Patriarche, M. Bahriz, E. Tournié, and R. Teissier, "Quantum cascade lasers grown on silicon," Sci. Rep. 8(7206), (2018).
120. A. Spott, J. Peters, M. L. Davenport, E. J. Stanton, C. D. Merritt, W. W. Bewley, I. Vurgaftman, C. S. Kim, J. R. Meyer, J. Kirch, L. J. Mawst, D. Botez, and J. E. Bowers, "Quantum cascade laser on silicon," Optica 3(5), 545 (2016).
121. Y. Yao, A. J. Hoffman, and C. F. Gmachl, "Mid-infrared quantum cascade lasers," Nat. Photonics 6(7), 432–439 (2012).
122. Y. Liang, C. Li, Y. Z. Huang, and Q. Zhang, "Plasmonic nanolasers in on-chip light sources: prospects and challenges," ACS Nano 14, 14375–14390 (2020).
123. Y. L. Ho, J. K. Clark, A. S. A. Kamal, and J. J. Delaunay, "On-chip monolithically fabricated plasmonic-waveguide nanolaser," Nano Lett. 18, 7769–7776 (2018).
124. V. J. Sorger, R. F. Oulton, R. M. Ma, and X. Zhang, "Toward integrated plasmonic circuits," MRS Bull. 37(8), 728–738 (2012).
125. J. C. Norman, D. Jung, Z. Zhang, Y. Wan, S. Liu, C. Shang, R. W. Herrick, W. W. Chow, A. C. Gossard, and J. E. Bowers, "A review of high-performance quantum dot lasers on silicon," IEEE J. Quantum Electron. 55(2), (2019).

126. V. Cao, J. S. Park, M. Tang, T. Zhou, A. Seeds, S. Chen, and H. Liu, "Recent progress of quantum dot lasers monolithically integrated on Si platform," Front. Phys. 10, (2022).
127. W. Xie, T. Stöferle, G. Rainò, T. Aubert, S. Bisschop, Y. Zhu, R. F. Mahrt, P. Geiregat, E. Brainis, Z. Hens, and D. Van Thourhout, "On-chip integrated quantum-dot–silicon-nitride microdisk lasers," Adv. Mater. 29(1604866), (2017).
128. Z. Mi, J. Yang, P. Bhattacharya, G. Qin, and Z. Ma, "High-performance quantum dot lasers and integrated optoelectronics on Si," Proc. IEEE 97(7), 1239–1249 (2009).
129. A. Malik, J. Guo, M. A. Tran, G. Kurczveil, D. Liang, and J. E. Bowers, "Widely tunable, heterogeneously integrated quantum-dot O-band lasers on silicon," Photonics Res. 8(10), 1551 (2020).
130. R. Yi, X. Zhang, F. Zhang, L. Gu, Q. Zhang, L. Fang, J. Zhao, L. Fu, H. H. Tan, C. Jagadish, and X. Gan, "Integrating a nanowire laser in an on-chip photonic waveguide," Nano Lett. 22, 9920–9927 (2022).
131. E. Bermúdez-Ureña, G. Tutuncuoglu, J. Cuerda, C. L. C. Smith, J. Bravo-Abad, S. I. Bozhevolnyi, A. FontcubertaMorral, F. J. García-Vidal, and R. Quidant, "Plasmonic waveguide-integrated nanowire laser," Nano Lett. 17, 747–754 (2017).
132. Q. Bao, W. Li, P. Xu, M. Zhang, D. Dai, P. Wang, X. Guo, and L. Tong, "On-chip single-mode CdS nanowire laser," Light Sci. Appl. 9(42), (2020).
133. B. Mayer, L. Janker, B. Loitsch, J. Treu, T. Kostenbader, S. Lichtmannecker, T. Reichert, S. Morkötter, M. Kaniber, G. Abstreiter, C. Gies, G. Koblmüller, and J. J. Finley, "Monolithically integrated high-β nanowire lasers on silicon," Nano Lett. 16, 152–156 (2016).
134. Q. Zhang, R. Su, W. Du, X. Liu, L. Zhao, S. T. Ha, and Q. Xiong, "Advances in small perovskite-based lasers," Small Methods 1(1700163), (2017).
135. P. J. Cegielski, S. Neutzner, C. Porschatis, H. Lerch, J. Bolten, S. Suckow, A. R. S. Kandada, B. Chmielak, A. Petrozza, T. Wahlbrink, and A. L. Giesecke, "Integrated perovskite lasers on a silicon nitride waveguide platform by cost-effective high throughput fabrication," Opt. Express 25(12), 13199 (2017).
136. P. J. Cegielski, A. L. Giesecke, S. Neutzner, C. Porschatis, M. Gandini, D. Schall, C. A. R. Perini, J. Bolten, S. Suckow, S. Kataria, B. Chmielak, T. Wahlbrink, A. Petrozza, and M. C. Lemme, "Monolithically integrated perovskite semiconductor lasers on silicon photonic chips by scalable top-down fabrication," Nano Lett. 18, 6915–6923 (2018).
137. S. Wang, Y. Liu, G. Li, J. Zhang, N. Zhang, S. Xiao, and Q. Song, "Lead halide perovskite based microdisk lasers for on-chip integrated photonic circuits," Adv. Opt. Mater. 6(1701266), (2018).
138. J. D. B. Bradley and M. Pollnau, "Erbium-doped integrated waveguide amplifiers and lasers," Laser Photonics Rev. 5(3), 368–403 (2011).
139. Z. Chen, "Global rare earth resources and scenarios of future rare earth industry," J. Rare Earths 29(1), 1–6 (2011).
140. T. Zhong and P. Goldner, "Emerging rare-earth doped material platforms for quantum nanophotonics," Nanophotonics 8(11), (2019).
141. A. J. Steckl and J. M. Zavada, "Photonic applications of rare-earth-doped materials," MRS Bull. 24, 16–17 (1999).
142. G. Charalampides, K. I. Vatalis, B. Apostoplos, and B. Ploutarch-Nikolas, "Rare earth elements: industrial applications and economic dependency of Europe," Procedia Econ. Finance 24, 126–135 (2015).
143. M. K. Hossain, M. I. Khan, and A. El-Denglawey, "A review on biomedical applications, prospects, and challenges of rare earth oxides," Appl. Mater. Today 24(101104), (2021).
144. R. Ganguli and D. R. Cook, "Rare earths: a review of the landscape," MRS Energy Sustain. 5(6), (2018).
145. A. J. Kenyon, "Recent developments in rare-earth doped materials for optoelectronics," Prog. Quantum Electron. 26, 225–284 (2002).
146. Y. Kotaki and H. Ishikawa, "Wavelength tunable DFB and DBR lasers for coherent optical fibre communications," IEE Proc. 138(2), (1991).

147. S. Addanki, I. S. Amiri, and P. Yupapin, "Review of optical fibers-introduction and applications in fiber lasers," Results Phys. 10, 743–750 (2018).
148. P. D. Brazitikos, D. J. D'Amico, M. T. Bernal, and A. W. Walsh, "Erbium:YAG laser surgery of the vitreous and retina," Ophthalmology 102(2), 278–290 (1995).
149. T. A. Wollin and J. D. Denstedt, "The Holmium laser in urology," J. Clin. Laser Med. Surg. 16(1), 13–20 (1998).
150. H. Watanabe, I. Ishikawa, M. Suzuki, and K. Hasegawa, "Clinical assessments of the Erbium:YAG laser for soft tissue surgery and scaling," J. Clin. Laser Med. Surg. 14(2), 67–75 (1996).
151. A. H. H. Tan and P. J. Gilling, "Holmium laser prostatectomy: current techniques," Urology 60(1), 152–156 (2002).
152. R. Kaufmann and R. Hibst, "Pulsed Erbium:YAG laser ablation in cutaneous surgery," Lasers Surg. Med. 19(3), 324–330 (1996).
153. K. Washio, "Neodymium-doped solid-state lasers and their applications to materials processing," Mater. Chemlstty Phys. 31(1–2), 57–66 (1992).
154. P. Wang, X. Chen, Q. Pan, B. Madigan, and J. Long, "Laser welding dissimilar materials of aluminum to steel: an overview," Int. J. Adv. Manuf. Technol. 87(9–12), 3081–3090 (2016).
155. J. A. Ga-Orza, "Welding of aluminium alloys with high-power Nd:YAG lasers," Weld. Int. 13(4), 282–284 (1999).
156. P. Kronenberg and O. Traxer, "The laser of the future: reality and expectations about the new thulium fiber laser-a systematic review," Transl. Androl. Urol. 8(4), S398–S417 (2019).
157. M. Guney, B. Tunc, and M. Gulsoy, "Investigating the ablation efficiency of a 1940-nm thulium fibre laser for intraoral surgery," Int. J. Oral Maxillofac. Surg. 43, 1015–1021 (2014).
158. Z. Li, A. M. Heidt, J. M. O. Daniel, Y. Jung, S. U. Alam, and D. J. Richardson, "Thulium-doped fiber amplifier for optical communications at 2μm," Opt. Express 21(8), (2013).
159. E. H. Bernhardi, H. A. G. M. Van Wolferen, L. Agazzi, M. R. H. Khan, C. G. H. Roeloffzen, K. Wörhoff, M. Pollnau, and R. M. De Ridder, "Ultra-narrow-linewidth, single-frequency distributed feedback waveguide laser in Al_2 O_3:Er^{3+} on silicon," Opt. Lett. 35(14), (2010).
160. S. A. Vázquez-Córdova, M. Dijkstra, E. H. Bernhardi, F. Ay, K. Wörhoff, J. L. Herek, S. M. García-Blanco, and M. Pollnau, "Erbium-doped spiral amplifiers with 20 dB of net gain on silicon," Opt. Express 22(21), 25993–26004 (2014).
161. R. Paschotta, "Optical Resonators," https://www.rp-photonics.com/optical_resonators.html.
162. G. Della Valle, A. Festa, G. Sorbello, K. Ennser, C. Cassagnetes, D. Barbier, and S. Taccheo, "Single-mode and high power waveguide lasers fabricated by ion-exchange," Opt. Express 16(16), (2008).
163. G. Della Valle, S. Taccheo, R. Osellame, A. Festa, G. Cerullo, and P. Laporta, "1.5 μm single longitudinal mode waveguide laser fabricated by femtosecond laser writing," Opt. Express 15(6), (2007).
164. D. L. Veasey, D. S. Funk, P. M. Peters, N. A. Sanford, G. E. Obarski, N. Fontaine, M. Young, A. P. Peskin, W.-C. Liu, S. N. Houde-Walter, and J. S. Hayden, "Yb/Er-codoped and Yb-doped waveguide lasers in phosphate glass," J. Non-Cryst. Solids 263 & 264, (2000).
165. T. Kitagawa, K. Hattori, M. Shimizu, Y. Ohmori, and M. Kobayashi, "Guided-wave laser based on erbium-doped silica planar lightwave circuit," Electron. Lett. 27(4), (1991).
166. H. Guan, A. Novack, T. Galfsky, Y. Ma, S. Fathololoumi, A. Horth, T. N. Huynh, J. Roman, R. Shi, M. Caverley, Y. Liu, T. Baehr-Jones, K. Bergman, and M. Hochberg, "Widely-tunable, narrow-linewidth III-V/silicon hybrid external-cavity laser for coherent communication," Opt. Express 26(7), 7920 (2018).
167. Y. Xu, P. Maier, M. Blaicher, P. I. Dietrich, P. Marin-Palomo, W. Hartmann, Y. Bao, H. Peng, M. R. Billah, S. Singer, U. Troppenz, M. Moehrle, S. Randel, W. Freude, and C. Koos, "Hybrid external-cavity lasers (ECL) using photonic wire bonds as coupling elements," Sci. Rep. 11(16426), (2021).
168. A. J. Zilkie, P. Seddighian, B. J. Bijlani, W. Qian, D. C. Lee, S. Fathololoumi, J. Fong, R. Shafiiha, D. Feng, B. J. Luff, X. Zheng, J. E. Cunningham, A. V. Krishnamoorthy, and M. Asghari, "Power-efficient III-V/silicon external cavity DBR lasers," Opt. Express 20(21), (2012).
169. D. J. M Stothard, J.-M. Hopkins, and M. H. Dunn, "Stable, continuous-wave, intracavity, optical parametric oscillator pumped by a semiconductor disk laser (VECSEL)," Opt. Express 17(13), (2009).

170. L. Fan, M. Fallahi, A. R. Zakharian, J. Hader, J. V. Moloney, R. Bedford, J. T. Murray, W. Stolz, and S. W. Koch, "Extended tunability in a two-chip VECSEL," IEEE Photonics Technol. Lett. 19(8), 544–546 (2007).
171. D. Liang, X. Huang, G. Kurczveil, M. Fiorentino, and R. G. Beausoleil, "Integrated finely tunable microring laser on silicon," Nat. Photonics 10(11), 719–722 (2016).
172. J. Van Campenhout, P. Rojo-Romeo, P. Regreny, C. Seassal, D. Van Thourhout, S. Verstuyft, L. Di Cioccio, J. Fedeli, C. Lagahe, and R. Baets, "Electrically pumped InP-based microdisk lasers integrated with a nanophotonic silicon-on-insulator waveguide circuit," Opt. Express 15(11), (2007).
173. Q. Luo, C. Yang, Z. Hao, R. Zhang, R. Ma, D. Zheng, H. Liu, X. Yu, F. Gao, F. Bo, Y. Kong, G. Zhang, and J. Xu, "Integrated ytterbium-doped lithium niobate microring lasers," Opt. Lett. 47(6), 1427 (2022).
174. J. Guan, C. Li, R. Gao, H. Zhang, J. Lin, M. Li, M. Wang, L. Qiao, L. Deng, and Y. Cheng, "Monolithically integrated narrow-bandwidth disk laser on thin-film lithium niobate," Opt. Laser Technol. 168(109908), (2024).
175. S. Matsuo and T. Segawa, "Microring-resonator-based widely tunable lasers," IEEE J. Sel. Top. Quantum Electron. 15(3), 545–554 (2009).
176. J. Van Campenhout, L. Liu, P. Rojo Romeo, D. Van Thourhout, C. Seassal, P. Regreny, L. Di Cioccio, J. M. Fedeli, and R. Baets, "A compact SOI-integrated multiwavelength laser source based on cascaded InP microdisks," IEEE Photonics Technol. Lett. 20(16), 1345–1347 (2008).
177. S. Yu, Z. Fang, Z. Wang, Y. Zhou, Q. Huang, J. Liu, R. Wu, H. Zhang, M. Wang, and Y. Cheng, "On-chip single-mode thin-film lithium niobate Fabry–Perot resonator laser based on Sagnac loop reflectors," Opt. Lett. 48(10), 2660 (2023).
178. Y. Zhang, S. Yang, H. Guan, A. E.-J. Lim, G.-Q. Lo, P. Magill, T. Baehr-Jones, and M. Hochberg, "Sagnac loop mirror and micro-ring based laser cavity for silicon-on-insulator," Opt. Express 22(15), 17872 (2014).
179. E. S. Magden, N. Li, Purnawirman, J. D. B. Bradley, N. Singh, A. Ruocco, G. S. Petrich, G. Leake, D. D. Coolbaugh, E. P. Ippen, M. R. Watts, and L. A. Kolodziejski, "Monolithically-integrated distributed feedback laser compatible with CMOS processing," Opt. Express 25(15), 18058 (2017).
180. T. Kitagawa, F. Bilodeau, B. Malo, S. Thériault, J. Albert, D. C. Jihnson, K. O. Hill, K. Hattori, and Y. Hibino, "Single-frequency Er^{3+}-doped silica-based planar waveguide laser with integrated photo-imprinted Bragg reflectors," Electron. Lett. 30(16), (1994).
181. B. K. Das, H. Suche, and W. Sohler, "Single-frequency Ti:Er:$LiNbO_3$ distributed Bragg reflector waveguide laser with thermally fixed photorefractive cavity," Appl. Phys. B 73, 439–442 (2001).
182. S. Guldberg-Kjær, J. Hübner, M. Kristensen, C. Laurent-Lund, M. Rysholt Poulsen, and M. W. Sckerl, "Planar waveguide laser in Er/Al-doped germanosilicate," Electron. Lett. 35(4), 302–303 (1999).
183. D. Kharas, J. J. Plant, W. Loh, R. B. Swint, S. Bramhavar, C. Heidelberger, S. Yegnanarayanan, and P. W. Juodawlkis, "High-power (>300 mW) on-chip laser with passively aligned silicon-nitride waveguide DBR cavity," IEEE Photonics J. 12(6), (2020).
184. S. Christensen, G. Frith, and B. Samson, "Developments in thulium-doped fiber lasers offer higher powers," SPIE Newsroom (2008).
185. N. Li, Purnawirman, Z. Su, E. Salih Magden, P. T. Callahan, K. Shtyrkova, M. Xin, A. Ruocco, C. Baiocco, E. P. Ippen, F. X. Kärtner, J. D. B. Bradley, D. Vermeulen, and M. R. Watts, "High-power thulium lasers on a silicon photonics platform," Opt. Lett. 42(6), 1181 (2017).
186. E. Kifle, P. Loiko, C. Romero, J. R. Vázquez de Aldana, M. Aguiló, F. Díaz, P. Camy, U. Griebner, V. Petrov, and X. Mateos, "Watt-level ultrafast laser inscribed thulium waveguide lasers," Prog. Quantum Electron. 72(100266), (2020).
187. K. van Dalfsen, S. Aravazhi, C. Grivas, S. M. García-Blanco, and M. Pollnau, "Thulium channel waveguide laser with 1.6 W of output power and ∼80% slope efficiency," Opt. Lett. 39(15), 4380 (2014).
188. Z. Su, N. Li, E. Salih Magden, M. Byrd, Purnawirman, T. N. Adam, G. Leake, D. Coolbaugh, J. D. B. Bradley, and M. R. Watts, "Ultra-compact and low-threshold thulium microcavity laser monolithically integrated on silicon," Opt. Lett. 41(24), 5708 (2016).

189. N. Singh, J. Lorenzen, M. Sinobad, K. Wang, A. C. Liapis, H. C. Frankis, S. Haugg, H. Francis, J. Carreira, M. Geiselmann, M. A. Gaafar, T. Herr, J. D. B. Bradley, Z. Sun, S. M. Garcia-Blanco, and F. X. Kärtner, "Silicon photonics-based high-energy passively Q-switched laser," Nat. Photonics 18(5), 485–491 (2024).
190. J. Söchtig, H. Schütz, R. Widmer, R. Corsini, D. Hiller, C. Carmannini, G. Consonni, S. Bosso, and L. Gobbi, "Monolithically integrated DBR waveguide laser and intensity modulator in erbium doped $LiNbO_3$," Electron. Lett. 32(10), (1996).
191. P. Madasamy, G. N. Conti, P. Poyhonen, Y. Hu, M. M. Morell, D. F. Geraghty, S. Honkanen, and N. Peyghambarian, "Waveguide distributed Bragg reflector laser arrays in erbium doped glass made by dry Ag film ion exchange," Opt. Eng. 41(5), 1084 (2002).
192. D. J. Griffiths, *Introduction to Electrodynamics* (Cambridge University Press, 2023).
193. R. G. Hunsperger, *Integrated Optics* (Springer New York, 2009).
194. R. Paschotta, "Effective Refractive Index," .
195. L. Chrostowski and M. Hochberg, *Silicon Photonics Design* (Cambridge University Press, 2015).
196. C. Peng, C. Yang, H. Zhao, L. Liang, C. Zheng, C. Chen, L. Qin, and H. Tang, "Optical waveguide refractive index sensor for biochemical sensing," Appl. Sci. 13(3829), (2023).
197. Y. Lyu, *Finite Element Method* (Springer, 2022).
198. M. Koshiba, "Optical waveguide theory by the finite element method," IEICE Trans. Electron. E97-C(7), 625–635 (2014).
199. J. N. Reddy, *Introduction to the Finite Element Method* (McGraw-Hill Education, 2019).
200. K. Y. You, *Emerging Waveguide Technology* (InTech, 2018).
201. B. S. Ahluwalia, Ø. I. Helle, and O. G. Hellesø, "Rib waveguides for trapping and transport of particles," Opt. Express 24(5), 4477 (2016).
202. K. P. Yap, A. Delâge, J. Lapointe, B. Lamontagne, J. H. Schmid, P. Waldron, S. Janz, and B. A. Syrett, "Correlation of scattering loss, sidewall roughness and waveguide width in silicon-on-insulator (SOI) ridge waveguides," J. Light. Technol. 27(18), 3999–4008 (2009).
203. M. H. P. Pfeiffer, C. Herkommer, J. Liu, T. Morais, M. Zervas, M. Geiselmann, and T. J. Kippenberg, "Photonic damascene process for low-loss, high-confinement silicon nitride waveguides," IEEE J. Sel. Top. Quantum Electron. 24(4), (2018).
204. H. M. Mbonde, H. C. Frankis, and J. D. B. Bradley, "Enhanced nonlinearity and engineered anomalous dispersion in TeO2-coated Si_3N_4 Waveguides," IEEE Photonics J. 12(2), (2020).
205. S. Yliniemi, J. Albert, Q. Wang, and S. Honkanen, "UV-exposed Bragg gratings for laser applications in silver-sodium ion-exchanged phosphate glass waveguides," Opt. Express 14(7), 2898 (2006).
206. G. D. Marshall, M. Ams, and M. J. Withford, "Direct laser written waveguide-Bragg gratings in bulk fused silica," Opt. Lett. 31(18), (2006).
207. M. Belt and D. J. Blumenthal, "Erbium-doped waveguide DBR and DFB laser arrays integrated within an ultra-low-loss Si 3 N 4 platform," Opt. Express 22(9), 10655–10660 (2014).
208. G. Jiang, R. Chen, Q. Zhou, J. Yang, M. Wang, and X. Jiang, "Slab-modulated sidewall bragg gratings in silicon-on-insulator ridge waveguides," IEEE Photonics Technol. Lett. 23(1), 6–8 (2011).
209. S. Zamek, D. T. H. Tan, M. Khajavikhan, M. Ayache, M. P. Nezhad, and Y. Fainman, "Compact chip-scale filter based on curved waveguide Bragg gratings," Opt. Lett. 35(20), (2010).
210. X. Wang, W. Shi, H. Yun, S. Grist, N. A. F. Jaeger, and L. Chrostowski, "Narrow-band waveguide Bragg gratings on SOI wafers with CMOS-compatible fabrication process," Opt. Express 20(14), 15547 (2012).
211. E. H. Bernhardi, Q. Lu, H. A. G. M. Van Wolferen, K. Wörhoff, R. M. de Ridder, and M. Pollnau, "Monolithic distributed Bragg reflector cavities in Al_2O_3 with quality factors exceeding 10^6," Photonics Nanostructures - Fundam. Appl. 9(3), 225–234 (2011).
212. H. A. Haus and W. Huang, "Coupled-mode theory," Proc. IEEE 79(10), (1991).
213. A. Yariv, *Quantum Electronics* (Wiley, 1991).
214. A. Yariv and H. W. Yen, "Bragg amplification and oscillation in periodic optical media," Opt. Commun. 10(2), (1973).
215. A. Yariv and M. Nakamura, "Periodic structures for integrated optics," IEEE J. Quantum Electron. QE-13(4), (1977).

216. A. Yariv, "Coupled-mode theory for guided-wave optics," IEEE J. Quantum Electron. QE-9(9), (1973).
217. T. E. Murphy, "Design, fabrication and measurement of integrated Bragg grating optical filters," Massachusetts Institute of Technology (MIT) (2001).
218. E. H. Bernhardi, "Bragg-grating-based rare-earth-ion-doped channel waveguide lasers and their applications," University of Twente (2012).
219. T. G. Mackay and A. Lakhtakia, *The Transfer-Matrix Method in Electromagnetics and Optics* (Morgan & Claypool, 2020), 1.
220. I. R. Kenyon, *The Light Fantastic* (Oxford University Press, 2011), 1.
221. D. I. Babic and S. W. Corzine, "Analytic expressions for the reflection delay, penetration depth, and absorptance of quarter-wave dielectric mirrors," IEEE J. Quantum Electron. 28(2), (1992).
222. D. G. Rabus and C. Sada, *Integrated Ring Resonators: A Compendium* (Springer, 2020), 127.
223. B. E. A. Saleh and M. C. Teich, *Fundamentals of Photonics* (Wiley, 1991).
224. G. Tittelbach, B. Richter, and W. Karthe, "Comparison of three transmission methods for integrated optical waveguide propagation loss measurement," Pure Appl. Opt. 2, 683–706 (1993).
225. K. Preston, B. Schmidt, and M. Lipson, "Polysilicon photonic resonators for large-scale 3D integration of optical networks," Opt. Express 15(25), 17283–17290 (2007).
226. N. Daldosso, M. Melchiorri, F. Riboli, F. Sbrana, L. Pavesi, G. Pucker, C. Kompocholis, M. Crivellari, P. Bellutti, and A. Lui, "Fabrication and optical characterization of thin two-dimensional Si_3N_4 waveguides," Mater. Sci. Semicond. Process. 7, 453–458 (2004).
227. J. T. Verdeyen, *Laser Electronics* (Prentice Hall, 1995).
228. J. D. B. Bradley, "AI_2O_3:ER^{3+} as a gain platform for integrated optics," University of Twente (2009).
229. C. A. Evans, Z. Ikonić, B. Richards, P. Harrison, and A. Jha, "Theoretical modeling of a ~ 2 µm Tm^{3+}-doped tellurite fiber laser: the influence of cross relaxation," J. Light. Technol. 27(18), 4026–4032 (2009).
230. H. C. Frankis, "Low-loss tellurium oxide devices integrated on silicon and silicon nitride photonic circuit platforms," McMaster University (2021).
231. L. Agazzi, "Spectroscopic excitation and quenching processes in rare-earth-ion-doped Al_2O_3 and their impact on amplifier and laser performance," University of Twente (2012).
232. R. J. Singh, *Solid State Physics* (Pearson, 2012).
233. Thorlabs, "Erbium-doped SM and LMA optical fiber," https://www.thorlabs.com/NewGroupPage9.cfm?ObjectGroup_ID=1504.
234. M. A. Khamis and K. Ennser, "Theoretical model of a thulium-doped fiber amplifier pumped at 1570 nm and 793 nm in the presence of cross relaxation," J. Light. Technol. 34(24), 5675–5681 (2016).
235. S. D. Jackson and T. A. King, "Theoretical modeling of Tm-doped silica fiber lasers," J. Light. Technol. 17(5), (1999).
236. H. Gebavi, D. Milanese, R. Balda, S. Chaussedent, M. Ferrari, J. Fernandez, and M. Ferraris, "Spectroscopy and optical characterization of thulium doped TZN glasses," J. Phys. Appl. Phys. 43(135104), (2010).
237. M. A. Taher, "Spectroscopy, modeling and investigation of thulium doped tellurite glass," Swansea University (2011).
238. H. Lin, K. Liu, L. Lin, Y. Hou, D. Yang, T. Ma, E. Y. B. Pun, Q. An, J. Yu, and S. Tanabe, "Optical parameters and upconversion fluorescence in Tm^{3+}/Yb^{3+}-doped alkali-barium-bismuth-tellurite glasses," Spectrochim. Acta - Part A 65(3–4), 702–707 (2006).
239. Thorlabs, "Thulium-doped single mode and large-mode-area optical fibers," .
240. X. Hu, T. Ning, L. Pei, Q. Chen, and J. Li, "Excellent initial guess functions for simple shooting method in Yb^{3+}-doped fiber lasers," Opt. Fiber Technol. 20(4), 358–364 (2014).
241. X. Hu, T. Ning, L. Pei, and W. Jian, "Novel shooting method with simple control strategy for fiber lasers," Optik 125(8), 1975–1979 (2014).
242. L. Shang, L. Qi, Y. Liao, and S. Zhang, "A combined algorithm for simulating fiber lasers based on the shooting and relaxation methods," Opt. Fiber Technol. 18(6), 502–508 (2012).

243. E. E. Okafor, J. M. Sompo, F. N. Igboamalu, and K. Ouahada, "Numerical approach for CW ring cavity fiber laser using shooting method," in *IEEE AFRICON Conference* (Institute of Electrical and Electronics Engineers Inc., 2021), 2021-September.
244. J. Liu, C. Zhao, S. Wen, D. Fan, and C. Shuai, "An improved shooting algorithm and its application to high-power fiber lasers," Opt. Commun. 283(19), 3764–3767 (2010).
245. Z. Lali-Dastjerdi, F. Kroushavi, and M. H. Rahmani, "An efficient shooting method for fiber amplifiers and lasers," Opt. Laser Technol. 40(8), 1041–1046 (2008).
246. S. Chowdhury, M. M. Al Furkan, and N. S. Ifat, *Numerical Solutions of Boundary Value Problems with So-Called Shooting Method* (Nova, 2021).
247. W. H. Press, S. A. Teukolsky, W. T. Vetterling, and B. P. Flannery, *Numerical Recipes: The Art of Scientific Computing* (Cambridge University Press, 2007).
248. M. A. Arefin, M. A. Nishu, M. N. Dhali, and M. H. Uddin, "Analysis of reliable solutions to the boundary value problems by using shooting method," Math. Probl. Eng. 2022(2895023), (2022).
249. M. R. Osborne, "On shooting methods for boundary value problems," J. Math. Anal. Appl. 27, 417–433 (1969).
250. O. Koch and E. B. Weinmüller, "The convergence of shooting methods for singular boundary value problems," Math. Comput. 72(241), (2001).
251. V. Akinsola, "Numerical methods: Euler and Runge-Kutta," in *Qualitative and Computational Aspects of Dynamical Systems* (IntechOpen, 2023).
252. S. V. Muravyev, E. A. Anashkina, A. V. Andrianov, V. V. Dorofeev, S. E. Motorin, M. Y. Koptev, and A. V. Kim, "Dual-band Tm^{3+}-doped tellurite fiber amplifier and laser at 1.9 μm and 2.3 μm," Sci. Rep. 8(1), (2018).
253. K. Miarabbas Kiani, "Thulium doped tellurium oxide amplifiers and lasers integrated on silicon and silicon nitride photonic platforms," McMaster University (2022).
254. B. L. Segat Frare, "GitHub repository: https://github.com/brunolsfrare/DBRLaserModels," (2024).
255. L. Xia, P. Shum, and T. H. Cheng, "Photonic generation of microwave signals using a dual-transmission-band FBG filter with controllable wavelength spacing," Appl. Phys. B 86(1), 61–64 (2006).
256. J. Chen, B. Liu, and H. Zhang, "Review of fiber Bragg grating sensor technology," Front. Optoelectron. China 4(2), 204–212 (2011).
257. X. Wang, W. Shi, R. Vafaei, N. A. F. Jaeger, and L. Chrostowski, "Uniform and Sampled Bragg Gratings in SOI Strip Waveguides with Sidewall Corrugations," IEEE Photonics Technol. Lett. 5678626 (2011).
258. Z. Du, C. Xiang, T. Fu, M. Chen, S. Yang, J. E. Bowers, and H. Chen, "Silicon nitride chirped spiral Bragg grating with large group delay," APL Photonics 5(10), 101302 (2020).
259. J. Hukriede, D. Runde, and D. Kip, "Fabrication and application of holographic Bragg gratings in lithium niobate channel waveguides," J. Phys. Appl. Phys. 36(3), R1–R16 (2003).
260. X. Wang, W. Shi, M. Hochberg, K. Adam, E. Schelew, J. F. Young, N. A. F. Jaeger, and L. Chrostowski, "Lithography simulation for the fabrication of silicon photonic devices with deep-ultraviolet lithography," in *The 9th International Conference on Group IV Photonics (GFP)* (2012), pp. 288–290.
261. C. M. Naraine, J. N. Westwood-Bachman, C. Horvath, M. Aktary, A. P. Knights, J. H. Schmid, P. Cheben, and J. D. B. Bradley, "Subwavelength Grating Metamaterial Waveguides and Ring Resonators on a Silicon Nitride Platform," Laser Photonics Rev. 17(2), 2200216 (2023).
262. C. G. H. Roeloffzen, M. Hoekman, E. J. Klein, L. S. Wevers, R. B. Timens, D. Marchenko, D. Geskus, R. Dekker, A. Alippi, R. Grootjans, A. Van Rees, R. M. Oldenbeuving, J. P. Epping, R. G. Heideman, K. Worhoff, A. Leinse, D. Geuzebroek, E. Schreuder, P. W. L. Van Dijk, I. Visscher, C. Taddei, Y. Fan, C. Taballione, Y. Liu, D. Marpaung, L. Zhuang, M. Benelajla, and K. J. Boller, "Low-loss Si3N4 triplex optical waveguides: technology and applications overview," IEEE J. Sel. Top. Quantum Electron. 24(4), (2018).
263. AGC Chemicals, "Cytop - technical brochure," (2023).
264. N. C. Anheier and H. A. Qiao, "A mid-infrared prism coupler for bulk and thin film optical analysis," in *Window and Dome Technologies and Materials XII* (SPIE, 2011), 8016, p. 80160E.

265. A. Bellemare, "Continuous-wave silica-based erbium-doped fibre lasers," Prog. Quantum Electron. 27(4), 211–266 (2003).
266. N. Zia, H. Tuorila, J. Viheriälä, S.-P. Ojanen, E. Koivusalo, J. Hilska, and M. Guina, "Hybrid silicon photonics DBR laser based on flip-chip integration of GaSb amplifiers and μm-scale SOI waveguides," Opt. Express 30(14), 24995 (2022).
267. N. N. Klimov, S. Mittal, M. Berger, and Z. Ahmed, "On-chip silicon waveguide Bragg grating photonic temperature sensor," Opt. Lett. 40(17), 3934 (2015).
268. R. Kaiser and B. Hüttl, "Monolithic 40-GHz mode-locked MQW DBR lasers for high-speed optical communication systems," IEEE J. Sel. Top. Quantum Electron. 13(1), 125–136 (2007).
269. L. Bastard, S. Blaize, and J.-E. Broquin, "Glass integrated optics ultranarrow linewidth distributed feedback laser matrix for dense wavelength division multiplexing applications," Opt. Eng. 42(10), 2800 (2003).
270. D. Bonneville, M. Albert, R. Arbi, M. Munir, B. L. Segat Frare, K. Miarabbas Kiani, H. C. Frankis, A. Knights, A. Turak, K. Sask, and J. D. B. Bradley, "Hybrid silicon-tellurium-dioxide DBR resonators coated in PMMA for biological sensing," Biomed. Opt. Express 14(4), 1545–1561 (2023).
271. S. Afzal, F. Schnabel, W. Scholz, J. P. Reithmaier, D. Gready, G. Eisenstein, P. Melanen, V. Vilokkinen, I. Montrosset, and M. Vallone, "1.3-μm two-section DBR lasers based on surface defined gratings for high-speed telecommunication," IEEE Photonics Technol. Lett. 23(7), 411–413 (2011).
272. M. Burla, L. R. Cortés, M. Li, X. Wang, L. Chrostowski, and J. Azaña, "Integrated waveguide Bragg gratings for microwave photonics signal processing," Opt. Express 21(21), 25120–25147 (2013).
273. N. Li, M. Xin, Z. Su, E. S. Magden, N. Singh, J. Notaros, E. Timurdogan, P. Purnawirman, J. D. B. Bradley, and M. R. Watts, "A silicon photonic data link with a monolithic erbium-doped laser," Sci. Rep. 10(1), 1–9 (2020).
274. X. Ji, J. K. Jang, U. D. Dave, M. Corato-Zanarella, C. Joshi, A. L. Gaeta, and M. Lipson, "Exploiting Ultralow Loss Multimode Waveguides for Broadband Frequency Combs," Laser Photonics Rev. 15(1), (2021).
275. Q. Wang, J. Geng, and S. Jiang, "2-μm fiber laser sources for sensing," Opt. Eng. 53(6), 061609 (2013).
276. P. Rice and B. K. Somani, "A Systematic Review of Thulium Fiber Laser: Applications and Advantages of Laser Technology in the Field of Urology," Res. Rep. Urol. Volume 13, 519–527 (2021).
277. O. Traxer and E. X. Keller, "Thulium fiber laser: the new player for kidney stone treatment? A comparison with Holmium:YAG laser," World J. Urol. 38(8), 1883–1894 (2020).
278. K. Scholle, S. Lamrini, P. Koopmann, and P. Fuhrberg, "2 μm Laser Sources and Their Possible Applications," in *Frontiers in Guided Wave Optics and Optoelectronics*, B. Pal, ed. (InTech, 2010).
279. A. Pal, S. Y. Chen, R. Sen, T. Sun, and K. T. V. Grattan, "A high- *Q* low threshold thulium-doped silica microsphere laser in the 2 μm wavelength region designed for gas sensing applications," Laser Phys. Lett. 10(8), 085101 (2013).
280. L. A. Hardy, C. R. Wilson, P. B. Irby, and N. M. Fried, "Thulium fiber laser lithotripsy in an *in vitro* ureter model," J. Biomed. Opt. 19(12), 128001 (2014).
281. A. Jha, B. Richards, G. Jose, T. Teddy-Fernandez, P. Joshi, X. Jiang, and J. Lousteau, "Rare-earth ion doped TeO_2 and GeO_2 glasses as laser materials," Prog. Mater. Sci. 57(8), 1426–1491 (2012).
282. M. Yu. Koptev, E. A. Anashkina, A. V. Andrianov, V. V. Dorofeev, A. F. Kosolapov, S. V. Muravyev, and A. V. Kim, "Widely tunable mid-infrared fiber laser source based on soliton self-frequency shift in microstructured tellurite fiber," Opt. Lett. 40(17), 4094 (2015).
283. G. Qin, M. Liao, T. Suzuki, A. Mori, and Y. Ohishi, "Widely tunable ring-cavity tellurite fiber Raman laser," Opt. Lett. 33(17), 2014 (2008).
284. J. S. Wang, E. M. Vogel, D. P. Machewirth, F. Wu, and E. Snitzer, "Neodymium-doped tellurite single-mode fiber laser," Opt. Lett. 19(18), 1448 (1994).
285. B. L. Segat Frare, P. Torab Ahmadi, B. Hashemi, D. B. Bonneville, H. M. Mbonde, H. C. Frankis, A. P. Knights, P. Mascher, and J. D. B. Bradley, "On-chip hybrid erbium-doped tellurium oxide–silicon nitride distributed Bragg reflector lasers," Appl. Phys. B 129(10), 158 (2023).

286. H. C. Frankis, D. Su, D. B. Bonneville, and J. D. B. Bradley, "A tellurium oxide microcavity resonator sensor integrated on-chip with a silicon waveguide," Sensors 18(11), 4061 (2018).
287. P. Primiani, S. Boust, J.-M. Fedeli, F. Duport, C. Gomez, J.-F. Paret, A. Garreau, K. Mekhazni, C. Fortin, and F. Van Dijk, "Silicon Nitride Bragg Grating With Joule Thermal Tuning for External Cavity Lasers," IEEE Photonics Technol. Lett. 31(12), 983–986 (2019).
288. G. Gao, D. Chen, S. Tao, Y. Zhang, S. Zhu, X. Xiao, and J. Xia, "Silicon nitride O-band (de)multiplexers with low thermal sensitivity," Opt. Express 25(11), 12260 (2017).
289. C. P. Ho, Z. Zhao, Q. Li, S. Takagi, and M. Takenaka, "Tunable Grating Coupler by Thermal Actuation and Thermo-Optic Effect," IEEE Photonics Technol. Lett. 30(17), 1503–1506 (2018).
290. S. Homampour, M. P. Bulk, P. E. Jessop, and A. P. Knights, "Thermal tuning of planar Bragg gratings in silicon-on-insulator rib waveguides," Phys. Status Solidi C 6(S1), (2009).
291. I. Kiyat, A. Aydinli, and N. Dagli, "Low-power thermooptical tuning of SOI resonator switch," IEEE Photonics Technol. Lett. 18(2), 364–366 (2006).
292. P. Edke, "Thermally tuned TeO_2-Si Microdisk Resonators," McMaster University (2022).
293. J. Liu, G. Huang, R. N. Wang, J. He, A. S. Raja, T. Liu, N. J. Engelsen, and T. J. Kippenberg, "High-yield, wafer-scale fabrication of ultralow-loss, dispersion-engineered silicon nitride photonic circuits," Nat. Commun. 12(1), 2236 (2021).

Appendix

I. Uniform grating and distributed Bragg reflector cavity coupled-mode theory solver Matlab code.

```
%Code that uses transfer matrices based on the couple-mode theory solutions
%to calculate uniform grating and DBR cavity responses. Refer to Chapter 2
%for more details.

%Uniform Bragg grating with gain/losses

%Central/Bragg wavelength (in m)
lambdaBragg = 1550E-9;
%Calculate transmission at lambdaBragg +- lambdaRange (in m)
lambdaRange= 1E-9;
%step size for spectrum calculation (in m)
stepsize = 0.001E-9;
%Creates lambda vector with the set range and step size
lambda = linspace(lambdaBragg-lambdaRange, lambdaBragg+lambdaRange,
1+lambdaRange*2/stepsize);
%Effective index of unperturbed waveguide - use simulated (RSoft) or
experimental data
neff = 2;
%Grating Period - can be replaced with fabricated/designed values (in m)
period = lambdaBragg/(2*neff);
%Propagation constant
Beta = 2*pi*neff./lambda;
%losses (if<0) or gain (if>0) in dB/cm
gammadB = 0;
%converts gamma to m^-1
gamma = (gammadB*100)/(10*log10(exp(1)));
%Phase mismatch: deviation from Bragg condition
deltaBeta = Beta-pi/period +1i*gamma;
%Grating length in m
gratingLength = 5E-3;

%Partial power inside the grating teeth, can be obtained with RSoft (between 0
and 1)
confinementFactor = 0.05;
%High refractive index material that makes up the grating (e.g. TeO2)
n_h = 2;
%Low refractive index material that makes up the grating (e.g. Si3N4)
n_l = 1.99;
DutyCycle = 0.5;
%coupling coefficient from Coupled-mode Theory in [1/m] - can be replaced with
kappa value, if known
kappa = confinementFactor*(n_h^2-n_l^2)*sin(pi*DutyCycle)/(lambdaBragg*neff);
%Defined to make writing easier – see Section 2.2.1
xi = sqrt(kappa^2-deltaBeta.^2);
```

```
%gratingLength=8/kappa; this can be used if you want to plot as a function
%of the grating strength, kL


%Bragg grating Transfer Matrix

% Build Bragg grating Transfer Matrix based on Coupled-Mode Theory results –
See Chapter 2
T11 = cosh(xi.*gratingLength) - 1i.*deltaBeta.*sinh(xi.*gratingLength)./xi;
T12 = 1i.*kappa.*sinh(xi.*gratingLength)./xi;
T21 = -1i.*kappa.*sinh(xi.*gratingLength)./xi;
T22 = cosh(xi.*gratingLength) + 1i.*deltaBeta.*sinh(xi.*gratingLength)./xi;

T_Bragg = [T11, T12; T21, T22];

%Calculate Reflectivity
R = (abs(-T21./T22)).^2;
%Calculate Transmissivity
T = (abs(1./T22)).^2;

%Plot reflected and transmitted spectra
Fig1=figure(1);
plot(lambda*1E9-1550, R,'LineWidth',1);
hold on;
ylim([0 1]);
plot(lambda*1E9-1550, T,':k','LineWidth',1);

x0=10;
y0=10;
width=15.29;
height=5;
Fig1.Units="centimeters";
Fig1.Position=[x0,y0,width,height];

ylabel('Relative Intensity','FontSize',12);
xlabel('Detuning from Bragg Wavelength (nm)','FontSize',12);


%% DBR with gain and losses
%Solves for symmetric and asymmetric DBR cavities (adjust grating lengths)

%Grating Matrices

%Parameters shared between the 2 sets of gratings
%Central/Bragg wavelength
lambdaBragg = 1550E-9;
%Calculate transmission at lambdaBragg +- lambdaRange
lambdaRange= 0.5E-9;
 %stepsize for spectrum calculation
stepsize = 0.0001E-9;
lambda = linspace(lambdaBragg-lambdaRange, lambdaBragg+lambdaRange,
1+lambdaRange*2/stepsize);
```

```
neff = 2;
period = lambdaBragg/(2*neff);
Beta = 2*pi*neff./lambda;
%losses (if<0) or gain (if>0) in dB/cm
gammadB = 0;
%converts gamma to m^-1
gamma = (gammadB*100)/(10*log10(exp(1)));
deltaBeta = Beta-pi/period +1i*gamma;
%Partial power inside the grating teeth, can be obtained with RSoft
confinementFactor = 0.025;
%High refractive index material that makes up the grating (e.g. TeO2)
n_h = 2;
%Low refractive index material that makes up the grating (e.g. Si3N4)
n_l = 1.99;
DutyCycle = 0.5;
%coupling coefficient from Coupled-mode Theory
kappa = confinementFactor*(n_h^2-n_l^2)*sin(pi*DutyCycle)/(lambdaBragg*neff);
xi = sqrt(kappa^2-deltaBeta.^2);

%Input grating transfer matrix

%Length in m (can be written in terms of kappa/grating strength)
gratingLength_g1 = 3E-3; %or 2/kappa, for instance;

%Matrix elements
T11_g1 = cosh(xi.*gratingLength_g1) -
1i.*deltaBeta.*sinh(xi.*gratingLength_g1)./xi;
T12_g1 = 1i.*kappa.*sinh(xi.*gratingLength_g1)./xi;
T21_g1 = -1i.*kappa.*sinh(xi.*gratingLength_g1)./xi;
T22_g1 = cosh(xi.*gratingLength_g1) +
1i.*deltaBeta.*sinh(xi.*gratingLength_g1)./xi;

%Build input grating matrix
T_Bragg_g1(1,1,:)=T11_g1;
T_Bragg_g1(1,2,:)=T12_g1;
T_Bragg_g1(2,1,:)=T21_g1;
T_Bragg_g1(2,2,:)=T22_g1;

%Output grating transfer matrix

%Length in m (can be written in terms of kappa/grating strength)
gratingLength_g2 = 3E-3; %or 2/kappa, for instance;

%Matrix elements
T11_g2 = cosh(xi.*gratingLength_g2) -
1i.*deltaBeta.*sinh(xi.*gratingLength_g2)./xi;
T12_g2 = 1i.*kappa.*sinh(xi.*gratingLength_g2)./xi;
T21_g2 = -1i.*kappa.*sinh(xi.*gratingLength_g2)./xi;
T22_g2 = cosh(xi.*gratingLength_g2) +
1i.*deltaBeta.*sinh(xi.*gratingLength_g2)./xi;
```

```
%Build output grating matrix
T_Bragg_g2(1,1,:)=T11_g2;
T_Bragg_g2(1,2,:)=T12_g2;
T_Bragg_g2(2,1,:)=T21_g2;
T_Bragg_g2(2,2,:)=T22_g2;

%Straight waveguide Transfer Matrix (for gap region between gratings)

%losses (if<0) or gain (if>0) in dB/cm
gamma_straightdB = 0;
%converts gamma_straight to m^-1
gamma_straight = (gamma_straightdB*100)/(10*log10(exp(1)));
%Length of straight section in m
length_straight = 5E-3;

%Matrix elements
T11_Straight = exp((-1i.*Beta + gamma_straight).*length_straight);
T12_Straight = zeros(1,length(T11_Straight));
T22_Straight =  exp((1i.*Beta - gamma_straight).*length_straight);
T21_Straight = T12_Straight;

%Build straight waveguide tranfer matrix
T_Straight(1,1,:)=T11_Straight;
T_Straight(1,2,:)=T12_Straight;
T_Straight(2,1,:)=T21_Straight;
T_Straight(2,2,:)=T22_Straight;

%DBR Transfer Matrix
T_DBR = 0.*T_Bragg_g1;
for n=1:length(T_Bragg_g1(1,1,:))
T_DBR(:,:,n) = T_Bragg_g2(:,:,n)*T_Straight(:,:,n)*T_Bragg_g1(:,:,n);
end

r = squeeze(T_DBR(2,1,:)./T_DBR(2,2,:));
t = squeeze(1./T_DBR(2,2,:));

%Reflected spectrum, DBR
R_DBR = (abs(r')).^2;
%Transmitted spectrum, DBR
Tr_DBR = (abs(t')).^2;

%Plot spectra
Fig2=figure(2);
plot((lambda-lambdaBragg).*1E9, R_DBR);
hold on;
plot((lambda-lambdaBragg).*1E9, Tr_DBR);

x0=10;
y0=10;
width=15.29/2;
height=5;
Fig2.Units="centimeters";
```

```
Fig2.Position=[x0,y0,width,height];
set(gca,'XTick',-0.5:0.25:0.5)
set(gca,'YTick',0:0.25:1)

ylim([0 1]);
ylabel('Relative Intensity','FontSize',12);
xlabel('Detuning from {\it\lambda}_B (nm)','FontSize',12);
```

II. Tm^{3+} STEADY STATE POPULATIONS SOLVER

```
% Code that solves Tm rate equations. To help with the fsolve convergence, I
wrote the equations in terms of the normalized populations (Ni/NT). Thanks to
% Arthur Mendez-Rosales for this suggestion.

%Pump wavelength in m
PumpWavelength = 1610e-9;
%Laser wavelength in m
LaserWavelength = 1875e-9;

%Loads physical constants

%Speed of light in m/s
c = physconst('LightSpeed');
%Planck's constant in m²kg/s
h = 6.62607015E-34;

%Pump and laser frequency calculation
PumpFreq = c/PumpWavelength;
LaserFreq = c/LaserWavelength;

%Photon energy
PumpPhotonEnergy = h*PumpFreq;
LaserPhotonEnergy = h*LaserFreq;

%Pump and laser powers in mW
PumpPower = 50e-3;
LaserPower = 10e-3;
%Tm concentration
NT = 4e26;

%Pump absorption and emission cross sections in m² (at 1610 nm)
PumpAbsCrossSection = 1.9e-25;
PumpEmCrossSection = 1.5e-26;
%Laser absorption and emission cross sections in m² (at 1875 nm)
LaserAbsCrossSection = 9.6e-26;
LaserEmCrossSection = 6.6e-25;
%Lifetime of excited state ³F4
tau1 = 0.3e-3;
%Lifetime of excited state ³H4
tau3 = 0.345e-3;
%Branching ratio
```

```
BranchingRatio = 0.082;
%Energy transfer upconversion and cross relaxation parameters
W_ETU = 5e-24;
W_RETU = 1.8E-22;
%Mode area (can be simulated with RSoft)
PumpArea = 1.24E-12;
LaserArea = 1.62E-12;
%Pump confinement factor in the gain medium
PumpNormIdist = 0.633;
%Laser confinement factor in the gain medium
LaserNormIdist = 0.573;

%Rates
R31 = (1-BranchingRatio)/tau3;
R01 =
(PumpPower.*PumpNormIdist.*PumpAbsCrossSection./PumpPhotonEnergy)./PumpArea +
(LaserPower.*LaserNormIdist.*LaserAbsCrossSection./LaserPhotonEnergy)./LaserAr
ea;
R10 =
(PumpPower.*PumpNormIdist.*PumpEmCrossSection./PumpPhotonEnergy)./PumpArea +
(LaserPower.*LaserNormIdist.*LaserEmCrossSection./LaserPhotonEnergy)./LaserAre
a + 1/tau1;
R32 = BranchingRatio/tau3;

%Solve steady state equations
F = @(x) [(R01.*x(1)-R10.*x(2)+R31.*x(3)+2.*(W_RETU.*x(1).*x(3).*NT-
W_ETU.*x(2).*x(2).*NT));
    -(1/tau3).*x(3)-(W_RETU.*x(1).*x(3).*NT-W_ETU.*x(2).*x(2).*NT);
    (x(1)+x(2)+x(3)-1)];

x=fsolve(F,[0.5 0.5 0.1])*NT;
```

III. SHOOTING-METHOD-BASED Er^{3+} DBR LASER MODEL MATLAB CODE

Auxiliar functions (implemented as separate files):

```
function [Areas,RefractiveIndex,PumpNormIdist,LaserNormIdist] =
GenerateMatrices(mesh,RefractiveIndex,PumpElectricFieldProfile,LaserElectricFi
eldProfile)
%Function that receives RSoft files and generate matrices for simulations

RefractiveIndex(:,1) = [];
LaserElectricFieldProfile(1,:) = [];
PumpElectricFieldProfile(1,:) = [];

%Mesh element area (in this case, 10 x 10 nm uniform mesh)
Areas=1E-16;
```

```
%Create intensity profiles from electric field profiles
PumpIntensityProfile=PumpElectricFieldProfile.^2;
LaserIntensityProfile=LaserElectricFieldProfile.^2;

%Create normalized intensity distributions
PumpNormIdist =
(PumpIntensityProfile.*Areas)./(sum(sum(PumpIntensityProfile.*Areas)));
LaserNormIdist =
(LaserIntensityProfile.*Areas)./(sum(sum(LaserIntensityProfile.*Areas)));

%Arrange distributions in the right orientation
RefractiveIndex=transpose(RefractiveIndex);
LaserNormIdist = transpose(LaserNormIdist);
PumpNormIdist = transpose(PumpNormIdist);

end
```

```
function [PumpAbsCrossSection, PumpEmCrossSection,LaserAbsCrossSection,
LaserEmCrossSection,PumpBGLoss,LaserBGLoss,c,h,PumpFreq,LaserFreq,PumpWaveleng
th, LaserWavelength,PumpPhotonEnergy,LaserPhotonEnergy, GratingLoss] =
LoadParameters(dopant,
PumpWavelength,LaserWavelength,PumpBGLossdB,LaserBGLossdB,GratingLossdB)
%Function that loads all simulation parameters to the main script

%Pump Absorption Cross Section
if dopant=='Er'
    if PumpWavelength==980
        %Not implemented
    else if PumpWavelength>=1460 && PumpWavelength<=1639
        %Loads Pump Abs Cross Section
        AbscsDat = 'TeO2_Abs_V1.dat';
        dat = importdata(AbscsDat);
        lambdaCS = dat(:,1); %(nm)
        sigma = dat(:,2); %(in cm^2)
            ind = find(lambdaCS > PumpWavelength, 1);
            lambdaA = lambdaCS(ind-1); lambdaB = lambdaCS(ind);
            sigmaA = sigma(ind-1); sigmaB = sigma(ind);
            PumpAbsCrossSection = sigmaA + (PumpWavelength - lambdaA) *
((sigmaB - sigmaA)/(lambdaB - lambdaA));

        %Loads Pump Em Cross Section
        EmcsDat = 'TeO2_EmASE_V1.dat';
        dat2 = importdata(EmcsDat);
        lambdaCS = dat2(:,1); %(nm)
        sigma = dat2(:,2); %(in cm^2)
            ind = find(lambdaCS > PumpWavelength, 1);
            lambdaA = lambdaCS(ind-1); lambdaB = lambdaCS(ind);
            sigmaA = sigma(ind-1); sigmaB = sigma(ind);
            PumpEmCrossSection = sigmaA + (PumpWavelength - lambdaA) *
((sigmaB - sigmaA)/(lambdaB - lambdaA));
```

```
    end
PumpAbsCrossSection = PumpAbsCrossSection*1E-4; %convert to m²
PumpEmCrossSection = PumpEmCrossSection*1E-4; %convert to m²
    end

        %Loads Laser Abs Cross Section
        AbscsDat = 'TeO2_Abs_V1.dat';
        dat = importdata(AbscsDat);
        lambdaCS = dat(:,1); %(nm)
        sigma = dat(:,2); %(in cm^2)
            ind = find(lambdaCS > LaserWavelength, 1);
            lambdaA = lambdaCS(ind-1); lambdaB = lambdaCS(ind);
            sigmaA = sigma(ind-1); sigmaB = sigma(ind);
            LaserAbsCrossSection = sigmaA + (LaserWavelength - lambdaA) *
((sigmaB - sigmaA)/(lambdaB - lambdaA));


        %Loads Laser Em Cross Section
        EmcsDat = 'TeO2_EmASE_V1.dat';
        dat2 = importdata(EmcsDat);
        lambdaCS = dat2(:,1); %(nm)
        sigma = dat2(:,2); %(in cm^2)
            ind = find(lambdaCS > LaserWavelength, 1);
            lambdaA = lambdaCS(ind-1); lambdaB = lambdaCS(ind);
            sigmaA = sigma(ind-1); sigmaB = sigma(ind);
            LaserEmCrossSection = sigmaA + (LaserWavelength - lambdaA) *
((sigmaB - sigmaA)/(lambdaB - lambdaA));

LaserAbsCrossSection = LaserAbsCrossSection*1E-4; %convert to m²
LaserEmCrossSection = LaserEmCrossSection*1E-4; %convert to m²
end

%Convert losses from dB/cm to linear and meters (m^-1)
% "100*" converts to dB/m and 10*log10(exp(0)) converts to m^-1
PumpBGLoss= 100*PumpBGLossdB/(10*log10(exp(1)));
LaserBGLoss=100*LaserBGLossdB/(10*log10(exp(1)));
GratingLoss = 100*GratingLossdB/(10*log10(exp(1)));

%Loads physical constants
c = physconst('LightSpeed'); %Speed of light in m/s
h = 6.62607015E-34; %Planck's constant in m²kg/s

%Convert wavelengths to m
PumpWavelength=PumpWavelength*1E-9;
LaserWavelength=LaserWavelength*1E-9;

%Pump and laser frequency calculation
PumpFreq = c/PumpWavelength;
LaserFreq = c/LaserWavelength;

%Photon energy
PumpPhotonEnergy = h*PumpFreq;
```

```
LaserPhotonEnergy = h*LaserFreq;
end
```

```
function
[FwdPumpPower,BwdPumpPower,FwdLaserPower,BwdLaserPower,N0,N1,N2,N0_active,N1_a
ctive,N2_active,N0_quench,N1_quench,N2_quench,Gain_coeff,Abs_coeff,gain_coeff,
abs_coeff,FwdLaserElectricField,BwdLaserElectricField] =
CreateIterativeParameters(RefractiveIndex,NumOfSteps,GainMediumRefractiveIndex
,NT,NActive,NQuench)
%Creates the variables that are updated at each step of the simulation

%Creates total, active, quenched populations, gain and abs coefficients
N0 =
zeros(NumOfSteps,numel(RefractiveIndex(:,1)),numel(RefractiveIndex(1,:)));
N1 =
zeros(NumOfSteps,numel(RefractiveIndex(:,1)),numel(RefractiveIndex(1,:)));
N2 =
zeros(NumOfSteps,numel(RefractiveIndex(:,1)),numel(RefractiveIndex(1,:)));
N0_active =
zeros(NumOfSteps,numel(RefractiveIndex(:,1)),numel(RefractiveIndex(1,:)));
N1_active =
zeros(NumOfSteps,numel(RefractiveIndex(:,1)),numel(RefractiveIndex(1,:)));
N2_active =
zeros(NumOfSteps,numel(RefractiveIndex(:,1)),numel(RefractiveIndex(1,:)));
N0_quench =
zeros(NumOfSteps,numel(RefractiveIndex(:,1)),numel(RefractiveIndex(1,:)));
N1_quench =
zeros(NumOfSteps,numel(RefractiveIndex(:,1)),numel(RefractiveIndex(1,:)));
N2_quench =
zeros(NumOfSteps,numel(RefractiveIndex(:,1)),numel(RefractiveIndex(1,:)));
gain_coeff =
zeros(NumOfSteps,numel(RefractiveIndex(:,1)),numel(RefractiveIndex(1,:)));
abs_coeff =
zeros(NumOfSteps,numel(RefractiveIndex(:,1)),numel(RefractiveIndex(1,:)));

%Initialize powers/field and average coeffieicnets as zero
FwdPumpPower = zeros(NumOfSteps,1).*1E-8;
BwdPumpPower = zeros(NumOfSteps,1).*1E-8;
FwdLaserPower = zeros(NumOfSteps,1).*1E-8;
BwdLaserPower = zeros(NumOfSteps,1).*1E-8;
Gain_coeff = zeros(NumOfSteps,1);
Abs_coeff = zeros(NumOfSteps,1);
FwdLaserElectricField = FwdLaserPower;
BwdLaserElectricField = BwdLaserPower;

%Initialize total, active, and quenched ion populations in the ground state
%in the mesh points that correspond to TeO2
for i=1:1:numel(N0(1,:,1))
    for j=1:1:numel(N0(1,1,:))
        if RefractiveIndex(i,j) == GainMediumRefractiveIndex
            N0(:,i,j) = NT;
            N0_active(:,i,j) = NActive;
```

```
            N0_quench(:,i,j) = NQuench;

        end
    end
end
end
```

```
function [N0,N1,N2] =
UpdatePouplations_Er1480pump(tau1,tau2,W_ETU,PumpPower,LaserPower,NT,PumpNormI
dist,PumpAbsCrossSection, PumpEmCrossSection,
PumpPhotonEnergy,LaserPhotonEnergy,LaserNormIdist,LaserAbsCrossSection,LaserEm
CrossSection,RefractiveIndex,GainMediumRefractiveIndex,Areas)
%Function used at each iteration to calculate the population in each energy
level
% Steady-state populations (from Edward Bernhardi's thesis)
% The input variables PumpPower and LaserPower are the sum of Fwd and Bwd
% powers

%Rates
R21 = 1/tau2;
R01 = (PumpPower.*PumpNormIdist.*PumpAbsCrossSection./PumpPhotonEnergy +
LaserPower.*LaserNormIdist.*LaserAbsCrossSection./LaserPhotonEnergy)./Areas;
%1E16 term is dividing by area...mesh element area???
R10 = (PumpPower.*PumpNormIdist.*PumpEmCrossSection./PumpPhotonEnergy +
LaserPower.*LaserNormIdist.*LaserEmCrossSection./LaserPhotonEnergy)./Areas +
1/tau1;

%Auxiliar variables
A = W_ETU*(1+R01./R21);
B = R01 + R10;
C = -R01.*NT;

%Steady-state populations
N1 = (sqrt(B.^2-4*A.*C)-B)./(2*A);
N2 = (W_ETU*N1.^2)./R21;
N0 = NT - (N1+N2);

%Mesh points that are not TeO2 are not doped
for i=1:1:numel(RefractiveIndex(:,1))
    for j=1:1:numel(RefractiveIndex(1,:))
        if RefractiveIndex(i,j) ~= GainMediumRefractiveIndex
            N1(i,j)=0;
            N2(i,j)=0;
            N0(i,j)=0;
        end
    end
end

end
```

Main code:

```
clear all;
mesh=readtable("T92Mesh.txt"); %convert to txt before importing (MSH file)
RefractiveIndex = importdata("T92RefractiveIndex.txt"); %convert to txt and
delete header before importing
PumpElectricFieldProfile = importdata("T92PumpProfile.txt"); %In RSoft, need
to go to Mode solver>output>change to amplitude. It has to be a uniform mesh
or RSoft will not save it with the same number of points as the other files
(Ex.m00). Don't make sim window too large to make the sim a bit faster
LaserElectricFieldProfile = importdata("T92LaserProfile.txt"); %it has to be a
uniform mesh or RSoft will not save it with the same number of points as the
other files (Ex.m00)
[Areas,RefractiveIndex,PumpNormIdist,LaserNormIdist] =
GenerateMatrices(mesh,RefractiveIndex,PumpElectricFieldProfile,LaserElectricFi
eldProfile);
LaserNormEdist = sqrt(LaserNormIdist)./sum(sum(sqrt(LaserNormIdist)));
%CHECK ALL UNITS: cross sections, wavelengths....make sure everything is in
%meters,W, and SI

%Load simulation parameters (cross sections, rate equations, ...)
dopant = 'Er'; %choose rare-earth: Er, Er-Yb, Tm, Yb,Pr,... Only Er
implemented so far
PumpWavelength = 1470; %choose pump wavelength. For Er, a value between 1460
and 1639. 980 has not been implemented.
LaserWavelength = 1550; %in nm. For Er, between 1460 and 1640

PumpBGLossdB = 0.5; %Pump background propagation loss in dB/cm
LaserBGLossdB = 0.5; %Laser wavelength background propagation loss in dB/cm
GratingLossdB = 0; %Grating loss in dB/cm
%c is speed of light, h is Planck's constant
[PumpAbsCrossSection, PumpEmCrossSection,LaserAbsCrossSection,
LaserEmCrossSection,PumpBGLoss,LaserBGLoss,c,h,PumpFreq,LaserFreq,
PumpWavelength, LaserWavelength,PumpPhotonEnergy,LaserPhotonEnergy,
GratingLoss] =
LoadParameters(dopant,PumpWavelength,LaserWavelength,PumpBGLossdB,LaserBGLossd
B,GratingLossdB);
tau1 = 0.62e-3; %Excited-state lifetime of active ion in seconds
tau1_QuenchedIons = 1e-6; %Excited-state lifetime of quenched ions in seconds
tau2 = 1e-6; %Lifetime of energy level E2 in seconds
W_ETU = 2.8E-18; %cm^3*s^-1, from Henry Frankis' thesis. Will be converted to
m³/s later
NT = 2.5E20; %Er concentration (cm-3). Will be converted to m-³ later
IncidentPumpPower_Fwd =[25, 50, 75, 100]*1E-3; %in W
IncidentPumpPower_Bwd = [0,0,0,0]*1E-3; %in W
Lin = 4E-3; %Input grating length in m
Lout = 0.85E-3; %Output grating length in m
Ltotal = 2E-2; %Total device length (removing edge couplers) in m

GainMediumRefractiveIndex = 2.05; %MUST match value used in RSoft
(RefractiveIndex matrix)
W_ETU = W_ETU*1E-6; %Converts to m³/s
```

```
NT = NT*1E6; %Converts to m-³
Quenching_fraction = 0.2;
NQuench = NT*Quenching_fraction;
NActive = NT-NQuench;
kappa = 1150; %Grating coupling coefficient in m^-1
dZ = 0.01E-2; %Stepsize of our sims along Z in m
NumOfSteps = int16(Ltotal/dZ+1); %Number of steps
Z = linspace(0,Ltotal,NumOfSteps); %converts steps to actual position along
device

%sets simulation to Bragg wavelength
dBeta = 0;
%Sets tolerance, max iterations, guess correction
MaxIteration = 3E3;
PumpPowerError =ones(MaxIteration,1);
correction = 1E-7; %usually 1E-8 or 1E-7
Tolerance = 1E-3;

%Initializes variables
LaserPowerError=ones(numel(IncidentPumpPower_Fwd),NumOfSteps).*0.1;
ResultFwdLaserOutput = zeros(numel(IncidentPumpPower_Fwd),1);
ResultBwdLaserOutput = zeros(numel(IncidentPumpPower_Fwd),1);
AvgN0 = zeros(numel(IncidentPumpPower_Fwd),NumOfSteps);
AvgN1 = AvgN0;
AvgN2 = AvgN1;

%Loop that runs pump power sweep
for P=1:1:numel(IncidentPumpPower_Fwd)

[FwdPumpPower,BwdPumpPower,FwdLaserPower,BwdLaserPower,N0,N1,N2,N0_active,N1_a
ctive,N2_active,N0_quench,N1_quench,N2_quench,Gain_coeff,Abs_coeff,gain_coeff,
abs_coeff,FwdLaserElectricField,BwdLaserElectricField] =
CreateIterativeParameters(RefractiveIndex,NumOfSteps,GainMediumRefractiveIndex
,NT,NActive,NQuench);
    %Initialize powers
    FwdPumpPower(1)=IncidentPumpPower_Fwd(P);
    BwdPumpPower(1)=IncidentPumpPower_Bwd(P)/10;
    BwdPumpPower(NumOfSteps)=IncidentPumpPower_Bwd(P);
    FwdLaserPower(1) = 0;
    FwdLaserElectricField(1)=sqrt(FwdLaserPower(1));

    %If previous pump power converged, use the result as initial guess
    if P >1 && ResultBwdLaserOutput(P-1)~=0
        BwdLaserPower(1)=ResultBwdLaserOutput(P-1);
    else
        %otherwise, choose initial guess (usually between 1E-8 and 5E-6)
        BwdLaserPower(1)=1E-6;
    end
        BwdLaserElectricField(1) = sqrt(BwdLaserPower(1));
    IterationN = 1;
```

```
    %Main loop that propagates all parameters along Z
    while (abs(LaserPowerError(P,IterationN))>Tolerance &&
IterationN<MaxIteration)

        %Update initial guess
        BwdLaserPower(1)=BwdLaserPower(1)+correction;
        BwdLaserElectricField(1) = sqrt(BwdLaserPower(1));


        %Start guesses
        for z=1:1:NumOfSteps
            %Calculate paramters at first point
            if z==1
                %Update populations
                [N0_active(z,:,:),N1_active(z,:,:),N2_active(z,:,:)] =
UpdatePouplations_Er1480pump(tau1,tau2,W_ETU,FwdPumpPower(z)+BwdPumpPower(z),F
wdLaserPower(z)+BwdLaserPower(z),NActive,PumpNormIdist,PumpAbsCrossSection,
PumpEmCrossSection,
PumpPhotonEnergy,LaserPhotonEnergy,LaserNormIdist,LaserAbsCrossSection,LaserEm
CrossSection,RefractiveIndex,GainMediumRefractiveIndex,Areas);
                [N0_quench(z,:,:),N1_quench(z,:,:),N2_quench(z,:,:)] =
UpdatePouplations_Er1480pump(tau1_QuenchedIons,tau2,W_ETU,FwdPumpPower(z)+BwdP
umpPower(z),FwdLaserPower(z)+BwdLaserPower(z),NQuench,PumpNormIdist,PumpAbsCro
ssSection, PumpEmCrossSection,
PumpPhotonEnergy,LaserPhotonEnergy,LaserNormIdist,LaserAbsCrossSection,LaserEm
CrossSection,RefractiveIndex,GainMediumRefractiveIndex,Areas);
                N0(z,:,:)=N0_active(z,:,:)+N0_quench(z,:,:);
                N1(z,:,:)=N1_active(z,:,:)+N1_quench(z,:,:);
                N2(z,:,:)=N2_active(z,:,:)+N2_quench(z,:,:);
                %Calculate gain and absorption coefficients for each mesh
point
                gain_coeff(z,:,:) = LaserEmCrossSection.*N1(z,:,:)-
LaserAbsCrossSection.*N0(z,:,:);
                abs_coeff(z,:,:) = PumpEmCrossSection.*N1(z,:,:)-
PumpAbsCrossSection.*N0(z,:,:);
                %Calculate total (average) gain an absorption coefficients
                Gain_coeff(z) =
sum(sum(LaserNormIdist.*squeeze(gain_coeff(z,:,:))));
                Abs_coeff(z) =
sum(sum(PumpNormIdist.*squeeze(abs_coeff(z,:,:))));

                BwdPumpPower(z) = BwdPumpPower(z+1)+(Abs_coeff(z)-
PumpBGLoss)*BwdPumpPower(z+1)*dZ;


            elseif z>1 && Z(z)<=Lin %calculate propagation within input
grating
                %Update populations
                [N0_active(z,:,:),N1_active(z,:,:),N2_active(z,:,:)] =
UpdatePouplations_Er1480pump(tau1,tau2,W_ETU,FwdPumpPower(z-1)+BwdPumpPower(z-
1),FwdLaserPower(z-1)+BwdLaserPower(z-
1),NActive,PumpNormIdist,PumpAbsCrossSection, PumpEmCrossSection,
```

```
PumpPhotonEnergy,LaserPhotonEnergy,LaserNormIdist,LaserAbsCrossSection,LaserEm
CrossSection,RefractiveIndex,GainMediumRefractiveIndex,Areas);
                [N0_quench(z,:,:),N1_quench(z,:,:),N2_quench(z,:,:)] =
UpdatePouplations_Er1480pump(tau1_QuenchedIons,tau2,W_ETU,FwdPumpPower(z-
1)+BwdPumpPower(z-1),FwdLaserPower(z-1)+BwdLaserPower(z-
1),NQuench,PumpNormIdist,PumpAbsCrossSection, PumpEmCrossSection,
PumpPhotonEnergy,LaserPhotonEnergy,LaserNormIdist,LaserAbsCrossSection,LaserEm
CrossSection,RefractiveIndex,GainMediumRefractiveIndex,Areas);
                N0(z,:,:)=N0_active(z,:,:)+N0_quench(z,:,:);
                N1(z,:,:)=N1_active(z,:,:)+N1_quench(z,:,:);
                N2(z,:,:)=N2_active(z,:,:)+N2_quench(z,:,:);
               %Calculate gain and absorption coefficients for each mesh point
                gain_coeff(z,:,:) = LaserEmCrossSection.*N1(z-1,:,:)-
LaserAbsCrossSection.*N0(z-1,:,:);
                abs_coeff(z,:,:) = PumpEmCrossSection.*N1(z-1,:,:)-
PumpAbsCrossSection.*N0(z-1,:,:);
                %Calculate total gain an absorption coefficients
                Gain_coeff(z) =
sum(sum(LaserNormIdist.*squeeze(gain_coeff(z,:,:))));
                Abs_coeff(z)
=sum(sum(PumpNormIdist.*squeeze(abs_coeff(z,:,:))));

                %Propagates fields
                FwdLaserElectricField(z) = FwdLaserElectricField(z-1)+((-
1i.*kappa*BwdLaserElectricField(z-1).*exp(+1i.*2.*dBeta.*dZ)) +
(Gain_coeff(z)-LaserBGLoss-GratingLoss)*FwdLaserElectricField(z-1)).*dZ;
                BwdLaserElectricField(z) = BwdLaserElectricField(z-
1)+((1i.*kappa*FwdLaserElectricField(z-1).*exp(-1i.*2.*dBeta.*dZ)) -
(Gain_coeff(z)-LaserBGLoss-GratingLoss)*BwdLaserElectricField(z-1)).*dZ;

                %Calculates powers
                FwdLaserPower(z) = abs(FwdLaserElectricField(z))^2;
                BwdLaserPower(z) = abs(BwdLaserElectricField(z))^2;
                FwdPumpPower(z) = FwdPumpPower(z-1) +(Abs_coeff(z)-
PumpBGLoss)*FwdPumpPower(z-1)*dZ;
                BwdPumpPower(z) = BwdPumpPower(z+1)+(Abs_coeff(z)-
PumpBGLoss)*BwdPumpPower(z+1)*dZ;

            %Propagates parameters in region between gratings
            elseif Z(z)<=Ltotal-Lout
                %Update populations
                [N0_active(z,:,:),N1_active(z,:,:),N2_active(z,:,:)] =
UpdatePouplations_Er1480pump(tau1,tau2,W_ETU,FwdPumpPower(z-1)+BwdPumpPower(z-
1),FwdLaserPower(z-1)+BwdLaserPower(z-
1),NActive,PumpNormIdist,PumpAbsCrossSection, PumpEmCrossSection,
PumpPhotonEnergy,LaserPhotonEnergy,LaserNormIdist,LaserAbsCrossSection,LaserEm
CrossSection,RefractiveIndex,GainMediumRefractiveIndex,Areas);
                [N0_quench(z,:,:),N1_quench(z,:,:),N2_quench(z,:,:)] =
UpdatePouplations_Er1480pump(tau1_QuenchedIons,tau2,W_ETU,FwdPumpPower(z-
1)+BwdPumpPower(z-1),FwdLaserPower(z-1)+BwdLaserPower(z-
1),NQuench,PumpNormIdist,PumpAbsCrossSection, PumpEmCrossSection,
```

```
PumpPhotonEnergy,LaserPhotonEnergy,LaserNormIdist,LaserAbsCrossSection,LaserEm
CrossSection,RefractiveIndex,GainMediumRefractiveIndex,Areas);
                N0(z,:,:)=N0_active(z,:,:)+N0_quench(z,:,:);
                N1(z,:,:)=N1_active(z,:,:)+N1_quench(z,:,:);
                N2(z,:,:)=N2_active(z,:,:)+N2_quench(z,:,:);
               %Calculate gain and absorption coefficients for each mesh point
                gain_coeff(z,:,:) = LaserEmCrossSection.*N1(z-1,:,:)-
LaserAbsCrossSection.*N0(z-1,:,:);
                abs_coeff(z,:,:) = PumpEmCrossSection.*N1(z-1,:,:)-
PumpAbsCrossSection.*N0(z-1,:,:);
                %Calculate total gain an absorption coefficients
                Gain_coeff(z) =
sum(sum(LaserNormIdist.*squeeze(gain_coeff(z,:,:))));
                Abs_coeff(z) =
sum(sum(PumpNormIdist.*squeeze(abs_coeff(z,:,:))));

                %Propagates fields
                FwdLaserElectricField(z) = FwdLaserElectricField(z-1) +
(Gain_coeff(z)-LaserBGLoss-GratingLoss)*FwdLaserElectricField(z-1).*dZ;
                BwdLaserElectricField(z) = BwdLaserElectricField(z-1) -
(Gain_coeff(z)-LaserBGLoss-GratingLoss)*BwdLaserElectricField(z-1).*dZ;

                %Calculate powers
                FwdPumpPower(z) = FwdPumpPower(z-1) +(Abs_coeff(z)-
PumpBGLoss)*FwdPumpPower(z-1)*dZ;
                BwdPumpPower(z) = BwdPumpPower(z+1)+(Abs_coeff(z)-
PumpBGLoss)*BwdPumpPower(z+1)*dZ;
                FwdLaserPower(z) = abs(FwdLaserElectricField(z))^2;
                BwdLaserPower(z) = abs(BwdLaserElectricField(z))^2;

               %Propagate parameters within output grating region
            elseif z<NumOfSteps
                [N0_active(z,:,:),N1_active(z,:,:),N2_active(z,:,:)] =
UpdatePouplations_Er1480pump(tau1,tau2,W_ETU,FwdPumpPower(z-1)+BwdPumpPower(z-
1),FwdLaserPower(z-1)+BwdLaserPower(z-
1),NActive,PumpNormIdist,PumpAbsCrossSection, PumpEmCrossSection,
PumpPhotonEnergy,LaserPhotonEnergy,LaserNormIdist,LaserAbsCrossSection,LaserEm
CrossSection,RefractiveIndex,GainMediumRefractiveIndex,Areas);
                [N0_quench(z,:,:),N1_quench(z,:,:),N2_quench(z,:,:)] =
UpdatePouplations_Er1480pump(tau1_QuenchedIons,tau2,W_ETU,FwdPumpPower(z-
1)+BwdPumpPower(z-1),FwdLaserPower(z-1)+BwdLaserPower(z-
1),NQuench,PumpNormIdist,PumpAbsCrossSection, PumpEmCrossSection,
PumpPhotonEnergy,LaserPhotonEnergy,LaserNormIdist,LaserAbsCrossSection,LaserEm
CrossSection,RefractiveIndex,GainMediumRefractiveIndex,Areas);
                N0(z,:,:)=N0_active(z,:,:)+N0_quench(z,:,:);
                N1(z,:,:)=N1_active(z,:,:)+N1_quench(z,:,:);
                N2(z,:,:)=N2_active(z,:,:)+N2_quench(z,:,:);
               %Calculate gain and absorption coefficients for each mesh point
                gain_coeff(z,:,:) = LaserEmCrossSection.*N1(z-1,:,:)-
LaserAbsCrossSection.*N0(z-1,:,:);
                abs_coeff(z,:,:) = PumpEmCrossSection.*N1(z-1,:,:)-
PumpAbsCrossSection.*N0(z-1,:,:);
```

```
                %Calculate total gain an absorption coefficients
                Gain_coeff(z) = 
sum(sum(LaserNormIdist.*squeeze(gain_coeff(z,:,:))));
                Abs_coeff(z) = 
sum(sum(PumpNormIdist.*squeeze(abs_coeff(z,:,:))));

                %Propagates fields
                FwdLaserElectricField(z) = FwdLaserElectricField(z-1)+((-
1i.*kappa*BwdLaserElectricField(z-1).*exp(+1i.*2.*dBeta.*(-dZ))) + 
(Gain_coeff(z)-LaserBGLoss-GratingLoss)*FwdLaserElectricField(z-1)).*(-dZ);
                BwdLaserElectricField(z) = BwdLaserElectricField(z-
1)+((1i.*kappa*FwdLaserElectricField(z-1).*exp(-1i.*2.*dBeta.*(-dZ))) - 
(Gain_coeff(z)-LaserBGLoss-GratingLoss)*BwdLaserElectricField(z-1)).*(-dZ);

                %Calculates powers
                FwdLaserPower(z) = abs(FwdLaserElectricField(z))^2;
                BwdLaserPower(z) = abs(BwdLaserElectricField(z))^2;
                FwdPumpPower(z) = FwdPumpPower(z-1) +(Abs_coeff(z)-
PumpBGLoss)*FwdPumpPower(z-1)*dZ;
                BwdPumpPower(z) = BwdPumpPower(z+1)+(Abs_coeff(z)-
PumpBGLoss)*BwdPumpPower(z+1)*dZ;

            %Calculate parameters in the last mesh point along Z
            else
                [N0_active(z,:,:),N1_active(z,:,:),N2_active(z,:,:)] = 
UpdatePouplations_Er1480pump(tau1,tau2,W_ETU,FwdPumpPower(z-1)+BwdPumpPower(z-
1),FwdLaserPower(z-1)+BwdLaserPower(z-
1),NActive,PumpNormIdist,PumpAbsCrossSection, PumpEmCrossSection, 
PumpPhotonEnergy,LaserPhotonEnergy,LaserNormIdist,LaserAbsCrossSection,LaserEm
CrossSection,RefractiveIndex,GainMediumRefractiveIndex,Areas);
                [N0_quench(z,:,:),N1_quench(z,:,:),N2_quench(z,:,:)] = 
UpdatePouplations_Er1480pump(tau1_QuenchedIons,tau2,W_ETU,FwdPumpPower(z-
1)+BwdPumpPower(z-1),FwdLaserPower(z-1)+BwdLaserPower(z-
1),NQuench,PumpNormIdist,PumpAbsCrossSection, PumpEmCrossSection, 
PumpPhotonEnergy,LaserPhotonEnergy,LaserNormIdist,LaserAbsCrossSection,LaserEm
CrossSection,RefractiveIndex,GainMediumRefractiveIndex,Areas);
                N0(z,:,:)=N0_active(z,:,:)+N0_quench(z,:,:);
                N1(z,:,:)=N1_active(z,:,:)+N1_quench(z,:,:);
                N2(z,:,:)=N2_active(z,:,:)+N2_quench(z,:,:);

               %Calculate gain and absorption coefficients for each mesh point
                gain_coeff(z,:,:) = LaserEmCrossSection.*N1(z-1,:,:)-
LaserAbsCrossSection.*N0(z-1,:,:);
                abs_coeff(z,:,:) = PumpEmCrossSection.*N1(z-1,:,:)-
PumpAbsCrossSection.*N0(z-1,:,:);
                %Calculate total gain an absorption coefficients
                Gain_coeff(z) = 
sum(sum(LaserNormIdist.*squeeze(gain_coeff(z,:,:))));
                Abs_coeff(z) = 
sum(sum(PumpNormIdist.*squeeze(abs_coeff(z,:,:))));
```

```
                %Propagates fields
                FwdLaserElectricField(z) = FwdLaserElectricField(z-1)+((-
1i.*kappa*BwdLaserElectricField(z-1).*exp(+1i.*2.*dBeta.*dZ)) +
(Gain_coeff(z)-LaserBGLoss-GratingLoss)*FwdLaserElectricField(z-1)).*dZ;
                BwdLaserElectricField(z) = BwdLaserElectricField(z-
1)+((1i.*kappa*FwdLaserElectricField(z-1).*exp(-1i.*2.*dBeta.*dZ)) -
(Gain_coeff(z)-LaserBGLoss-GratingLoss)*BwdLaserElectricField(z-1)).*dZ;

                %Calculates powers
                FwdLaserPower(z) = abs(FwdLaserElectricField(z))^2;
                BwdLaserPower(z) = abs(BwdLaserElectricField(z))^2;
                FwdPumpPower(z) = FwdPumpPower(z-1) +(Abs_coeff(z)-
PumpBGLoss)*FwdPumpPower(z-1)*dZ;
            end
        %Calculates average populations along Z
        AvgN0(P,z) = mean(nonzeros(N0(z,:,:)));
        AvgN1(P,z) = mean(nonzeros(N1(z,:,:)));
        AvgN2(P,z) = mean(nonzeros(N2(z,:,:)));
        end
    %Check boundary conditions and update values
    IterationN=IterationN+1;
    LaserPowerError(P,IterationN) =BwdLaserElectricField(NumOfSteps);

    %Displays the value of Bwd Laser Electric field at the last point after
    %each iteration. This value should be negative initially and then as it
    %reaches zero, the code will converge. If it shows positive values,
    %choose smaller guess and correction. If it's negative but it's taking
    %too long to converge, increase guess and correction values.If no matter
    %how low you choose your guess it always converges in the first
    %iteratction, the device does not lase with that pump power
    disp((BwdLaserElectricField(NumOfSteps)));

    %If the model did not converge, no lasing
    if IterationN==MaxIteration
        disp("MaxIteration reached, no convergence");
        FwdLaserPower(:)=0;
        BwdLaserPower(:)=0;
    end

    end
    %Laser output powers after converging
    ResultFwdLaserOutput(P)=FwdLaserPower(NumOfSteps);
    ResultBwdLaserOutput(P)=BwdLaserPower(1);

    fprintf("Finished %d",1000*IncidentPumpPower_Fwd(P));
end
a=linspace(1,IterationN,IterationN);

filename = sprintf("Test");
save(filename,"ResultFwdLaserOutput","ResultBwdLaserOutput","IncidentPumpPower
_Fwd","IncidentPumpPower_Bwd","AvgN0","AvgN1","AvgN2","Z","FwdLaserPower","Bwd
```

```
LaserPower","FwdPumpPower","BwdPumpPower","Gain_coeff","Abs_coeff","FwdLaserEl
ectricField","BwdLaserElectricField","LaserPowerError");
```

IV. Shooting-method-based Tm^{3+} DBR laser model Matlab code

Auxiliar functions (implemented as separate files):

```
function [PumpAbsCrossSection, PumpEmCrossSection,LaserAbsCrossSection,
LaserEmCrossSection,PumpBGLoss,LaserBGLoss,c,h,PumpFreq,LaserFreq,PumpWaveleng
th, LaserWavelength,PumpPhotonEnergy,LaserPhotonEnergy, GratingLoss] =
LoadParameters(dopant,
PumpWavelength,LaserWavelength,PumpBGLossdB,LaserBGLossdB,GratingLossdB)
%Function that loads all simulation parameters to the main script

%Pump Absorption Cross Section
if dopant== 'Tm'
    if PumpWavelength==790
        %Not implemented
    else if PumpWavelength>=1520 && PumpWavelength<=2100
        %Loads Pump Abs Cross Section
        AbscsDat = 'TmAbsCrossSection_TelluriteFiber.csv';
        dat = importdata(AbscsDat);
        lambdaCS = dat(:,1); %(nm)
        sigma = dat(:,2); %(in cm^2)
            ind = find(lambdaCS > PumpWavelength, 1);
            lambdaA = lambdaCS(ind-1); lambdaB = lambdaCS(ind);
            sigmaA = sigma(ind-1); sigmaB = sigma(ind);
            PumpAbsCrossSection = sigmaA + (PumpWavelength - lambdaA) *
((sigmaB - sigmaA)/(lambdaB - lambdaA));

        %Loads Pump Em Cross Section
        EmcsDat = 'TmEmCrossSection_TelluriteFiber.csv';
        dat2 = importdata(EmcsDat);
        lambdaCS = dat2(:,1); %(nm)
        sigma = dat2(:,2); %(in cm^2)
            ind = find(lambdaCS > PumpWavelength, 1);
            lambdaA = lambdaCS(ind-1); lambdaB = lambdaCS(ind);
            sigmaA = sigma(ind-1); sigmaB = sigma(ind);
            PumpEmCrossSection = sigmaA + (PumpWavelength - lambdaA) *
((sigmaB - sigmaA)/(lambdaB - lambdaA));
    end
PumpAbsCrossSection = PumpAbsCrossSection*1E-4; %convert to m²
PumpEmCrossSection = PumpEmCrossSection*1E-4; %convert to m²
    end

        %Loads Laser Abs Cross Section
        AbscsDat = 'TmAbsCrossSection_TelluriteFiber.csv';
        dat = importdata(AbscsDat);
        lambdaCS = dat(:,1); %(nm)
        sigma = dat(:,2); %(in cm^2)
```

```
            ind = find(lambdaCS > LaserWavelength, 1);
            lambdaA = lambdaCS(ind-1); lambdaB = lambdaCS(ind);
            sigmaA = sigma(ind-1); sigmaB = sigma(ind);
            LaserAbsCrossSection = sigmaA + (LaserWavelength - lambdaA) *
((sigmaB - sigmaA)/(lambdaB - lambdaA));

        %Loads Laser Em Cross Section
        EmcsDat = 'TmEmCrossSection_TelluriteFiber.csv';
        dat2 = importdata(EmcsDat);
        lambdaCS = dat2(:,1); %(nm)
        sigma = dat2(:,2); %(in cm^2)
            ind = find(lambdaCS > LaserWavelength, 1);
            lambdaA = lambdaCS(ind-1); lambdaB = lambdaCS(ind);
            sigmaA = sigma(ind-1); sigmaB = sigma(ind);
            LaserEmCrossSection = sigmaA + (LaserWavelength - lambdaA) *
((sigmaB - sigmaA)/(lambdaB - lambdaA));

LaserAbsCrossSection = LaserAbsCrossSection*1E-4; %convert to m²
LaserEmCrossSection = LaserEmCrossSection*1E-4; %convert to m²
end

%Convert losses from dB/cm to linear and meters (m^-1)
%"100*" converts to dB/m and 10*log10(exp(0)) converts to m^-1
PumpBGLoss= 100*PumpBGLossdB/(10*log10(exp(1)));
LaserBGLoss=100*LaserBGLossdB/(10*log10(exp(1)));
GratingLoss = 100*GratingLossdB/(10*log10(exp(1)));

%Loads physical constants
c = physconst('LightSpeed'); %Speed of light in m/s
h = 6.62607015E-34; %Planck's constant in m²kg/s

%Convert wavelengths to m
PumpWavelength=PumpWavelength*1E-9;
LaserWavelength=LaserWavelength*1E-9;

%Pump and laser frequency calculation
PumpFreq = c/PumpWavelength;
LaserFreq = c/LaserWavelength;

%Photon energy
PumpPhotonEnergy = h*PumpFreq;
LaserPhotonEnergy = h*LaserFreq;
```

```
function
[FwdPumpPower,BwdPumpPower,FwdLaserPower,BwdLaserPower,N0,N1,N2,Gain_coeff,Abs
_coeff,gain_coeff,abs_coeff,FwdLaserElectricField,BwdLaserElectricField] =
CreateIterativeParameters(NumOfSteps,NT)
```

```
%Creates the variables that are updated at each step of the simulation

N0 = ones(NumOfSteps,1)*NT;
N1 = zeros(NumOfSteps,1);
N2 = zeros(NumOfSteps,1);
gain_coeff = zeros(NumOfSteps,1);
abs_coeff = zeros(NumOfSteps,1);

FwdPumpPower = zeros(NumOfSteps,1).*1E-8;
BwdPumpPower = zeros(NumOfSteps,1).*1E-8;
FwdLaserPower = zeros(NumOfSteps,1).*1E-8;
BwdLaserPower = zeros(NumOfSteps,1).*1E-8;
Gain_coeff = zeros(NumOfSteps,1);
Abs_coeff = zeros(NumOfSteps,1);
FwdLaserElectricField = FwdLaserPower;
BwdLaserElectricField = BwdLaserPower;
```

```
function [N0,N1,N3] =
UpdatePouplations_Tm1610pump(tau1,tau3,W_ETU,PumpPower,LaserPower,NT,PumpAbsCr
ossSection, PumpEmCrossSection,
PumpPhotonEnergy,LaserPhotonEnergy,LaserAbsCrossSection,LaserEmCrossSection,Br
anchingRatio,W_RETU,ModeArea_pump,ModeArea_laser,OverlapTellurite_pump,Overlap
Tellurite_laser)
%Function used at each iteration to calculate the population in each energy
level steady-state populations (see Chapter 2)
%To help with the fsolve convergence, I wrote the equations in terms of the
normalized populations (Ni/NT). Thanks to Arthur Mendez-Rosales for this
suggestion.
% The input variables PumpPower and LaserPower are the sum of Fwd and Bwd
powers

%Rates
R31 = (1-BranchingRatio)/tau3;
R01 =
(PumpPower.*OverlapTellurite_pump.*PumpAbsCrossSection./PumpPhotonEnergy)/Mode
Area_pump +
(LaserPower.*OverlapTellurite_laser.*LaserAbsCrossSection./LaserPhotonEnergy).
/ModeArea_laser;
R10 =
(PumpPower.*OverlapTellurite_pump.*PumpEmCrossSection./PumpPhotonEnergy)/ModeA
rea_pump +
(LaserPower.*OverlapTellurite_laser.*LaserEmCrossSection./LaserPhotonEnergy)./
ModeArea_laser + 1/tau1;
R32 = BranchingRatio/tau3;
            options = optimset('Display','off');
            F = @(x) [(R01.*x(1)-
R10.*x(2)+R31.*x(3)+2.*(W_RETU.*x(1).*x(3).*NT-W_ETU.*x(2).*x(2).*NT));
                      -(1/tau3).*x(3)-(W_RETU.*x(1).*x(3).*NT-
W_ETU.*x(2).*x(2).*NT);
                       (x(1)+x(2)+x(3)-1)];
```

```
        %Solve rate equations
        x=fsolve(F,[0.5 0.5 0.1],options);
        N0 = x(1)*NT;
        N1 = x(2)*NT;
        N3 = x(3)*NT;

    end
```

Main code:

```
clear all;

%Mode areas and overlap with tellurite (from RSoft)
ModeArea_pump = 1.24551e-12;
ModeArea_laser = 1.61908e-12;
OverlapTellurite_pump = 0.633;
OverlapTellurite_laser = 0.573;

%Load simulation parameters (cross sections, rate equations, ...)
dopant = 'Tm'; %choose rare-earth: Er, Er-Yb, Tm, Yb,Pr,... Only Tm
implemented in this version
PumpWavelength = 1610; %choose pump power. For Tm, a value between 1510 and
2100.
LaserWavelength = 1875; %in nm. For Tm, between 1565 and 2200

PumpBGLossdB = 0.5;%Losses(Lsweep);%0.5; %Pump background propagation loss in
dB/cm
LaserBGLossdB = 0.5;% Losses(Lsweep);%0.5; %Laser wavelength background
propagation loss in dB/cm
GratingLossdB = 0; %Grating loss in dB/cm
%c is speed of light, h is Planck's constant
[PumpAbsCrossSection, PumpEmCrossSection,LaserAbsCrossSection,
LaserEmCrossSection,PumpBGLoss,LaserBGLoss,c,h,PumpFreq,LaserFreq,
PumpWavelength, LaserWavelength,PumpPhotonEnergy,LaserPhotonEnergy,
GratingLoss] =
LoadParameters(dopant,PumpWavelength,LaserWavelength,PumpBGLossdB,LaserBGLossd
B,GratingLossdB);
tau1 = 0.3e-3; %Lifetime in seconds
tau3 = 345e-6; %Lifetime in seconds
BranchingRatio = 0.082;
W_ETU = 5E-18; %cm^3*s^-1. Will be converted to m³/s later
W_RETU = 1.8E-22; %in  m³/s
NT = 4E20; %Er concentration (cm-3). Will be converted to m-³ later
IncidentPumpPower_Fwd =[25, 50, 75, 100]*1E-3; %in W
IncidentPumpPower_Bwd = [0,0,0,0]*1E-3; %in W
Lin = 4E-3; %Input grating length in m
Lout = 0.5E-3; %Output grating length in m
Ltotal =2E-2; %Total device length (removing edge couplers) in m
```

```
W_ETU = W_ETU*1E-6; %Converts to m³/s
NT = NT*1E6; %Converts to m-³
kappa = 1150; %Grating coupling coefficient in m^-1
dZ = 0.01E-2; %Step size along z in m
NumOfSteps = int16(Ltotal/dZ+1); %Number of steps
Z = linspace(0,Ltotal,NumOfSteps); %converts steps to actual position along
device

%Solve at the Bragg wavelength
dBeta = 0;
%Sets max iterations, correction, and tolerance
MaxIteration = 3E3;
PumpPowerError =ones(MaxIteration,1);
correction = 1E-7;
Tolerance = 1E-3;

%Initialize parameters
LaserPowerError=ones(numel(IncidentPumpPower_Fwd),NumOfSteps).*0.1;
ResultFwdLaserOutput = zeros(numel(IncidentPumpPower_Fwd),1);
ResultBwdLaserOutput = zeros(numel(IncidentPumpPower_Fwd),1);
AvgN0 = zeros(numel(IncidentPumpPower_Fwd),NumOfSteps);
AvgN1 = AvgN0;
AvgN3 = AvgN1;

%Loops that runs pump power sweep
for P=1:1:numel(IncidentPumpPower_Fwd)

[FwdPumpPower,BwdPumpPower,FwdLaserPower,BwdLaserPower,N0,N1,N3,Gain_coeff,Abs
_coeff,gain_coeff,abs_coeff,FwdLaserElectricField,BwdLaserElectricField] =
CreateIterativeParameters(NumOfSteps,NT);
    FwdPumpPower(1)=IncidentPumpPower_Fwd(P);
    BwdPumpPower(1)=IncidentPumpPower_Bwd(P)/10;
    BwdPumpPower(NumOfSteps)=IncidentPumpPower_Bwd(P);
    FwdLaserPower(1) = 0;
    FwdLaserElectricField(1)=sqrt(FwdLaserPower(1));

    %Choose initial guess
    if P >1
        BwdLaserPower(1)=ResultBwdLaserOutput(P-1);
    else
        BwdLaserPower(1)=1E-6;
    end
        BwdLaserElectricField(1) = sqrt(BwdLaserPower(1));
    IterationN = 1;

    %main loop that propagates parameters
    while (abs(LaserPowerError(P,IterationN))>Tolerance &&
IterationN<MaxIteration)

        BwdLaserPower(1)=BwdLaserPower(1)+correction;
        BwdLaserElectricField(1) = sqrt(BwdLaserPower(1));
```

```
        %Start guesses
        for z=1:1:NumOfSteps
            %Calculates parameters at z=0
            if z==1
                %Solve rate equations
                [N0(z),N1(z),N3(z)] = 
UpdatePouplations_Tm1610pump(tau1,tau3,W_ETU,FwdPumpPower(z)+BwdPumpPower(z),F
wdLaserPower(z)+BwdLaserPower(z),NT,PumpAbsCrossSection, PumpEmCrossSection, 
PumpPhotonEnergy,LaserPhotonEnergy,LaserAbsCrossSection,LaserEmCrossSection,Br
anchingRatio,W_RETU,ModeArea_pump,ModeArea_laser,OverlapTellurite_pump,Overlap
Tellurite_laser);
                %Calculate gain and absorption coefficients
                Gain_coeff(z) = (LaserEmCrossSection.*N1(z)-
LaserAbsCrossSection.*N0(z))*OverlapTellurite_laser;
                Abs_coeff(z) = (PumpEmCrossSection.*N1(z)-
PumpAbsCrossSection.*N0(z))*OverlapTellurite_pump;

                BwdPumpPower(z) = BwdPumpPower(z+1)+(Abs_coeff(z)-
PumpBGLoss)*BwdPumpPower(z+1)*dZ;

            elseif z>1 && Z(z)<=Lin %calculate parameters within input grating
                %Solve rate equations
                [N0(z),N1(z),N3(z)] = 
UpdatePouplations_Tm1610pump(tau1,tau3,W_ETU,FwdPumpPower(z-1)+BwdPumpPower(z-
1),FwdLaserPower(z-1)+BwdLaserPower(z-1),NT,PumpAbsCrossSection, 
PumpEmCrossSection, 
PumpPhotonEnergy,LaserPhotonEnergy,LaserAbsCrossSection,LaserEmCrossSection,Br
anchingRatio,W_RETU,ModeArea_pump,ModeArea_laser,OverlapTellurite_pump,Overlap
Tellurite_laser);
                %Calculate gain and absorption coefficients
                Gain_coeff(z) = (LaserEmCrossSection.*N1(z-1)-
LaserAbsCrossSection.*N0(z-1))*OverlapTellurite_laser;
                Abs_coeff(z) = (PumpEmCrossSection.*N1(z-1)-
PumpAbsCrossSection.*N0(z-1))*OverlapTellurite_pump;

                %Propagates fields
                FwdLaserElectricField(z) = FwdLaserElectricField(z-1)+((-
1i.*kappa*BwdLaserElectricField(z-1).*exp(+1i.*2.*dBeta.*dZ)) + (Gain_coeff(z-
1)-LaserBGLoss-GratingLoss)*FwdLaserElectricField(z-1)).*dZ;
                BwdLaserElectricField(z) = BwdLaserElectricField(z-
1)+((1i.*kappa*FwdLaserElectricField(z-1).*exp(-1i.*2.*dBeta.*dZ)) -
(Gain_coeff(z-1)-LaserBGLoss-GratingLoss)*BwdLaserElectricField(z-1)).*dZ;

                %Calculates powers
                FwdLaserPower(z) = abs(FwdLaserElectricField(z))^2;
                BwdLaserPower(z) = abs(BwdLaserElectricField(z))^2;
                FwdPumpPower(z) = FwdPumpPower(z-1) +(Abs_coeff(z)-
PumpBGLoss)*FwdPumpPower(z-1)*dZ;
                BwdPumpPower(z) = BwdPumpPower(z+1)+(Abs_coeff(z+1)-
PumpBGLoss)*BwdPumpPower(z+1)*dZ;
```

```
            elseif Z(z)<=Ltotal-Lout %calculate parameters in region between
gratings
                %Solve rate equations
                [N0(z),N1(z),N3(z)] =
UpdatePouplations_Tm1610pump(tau1,tau3,W_ETU,FwdPumpPower(z-1)+BwdPumpPower(z-
1),FwdLaserPower(z-1)+BwdLaserPower(z-1),NT,PumpAbsCrossSection,
PumpEmCrossSection,
PumpPhotonEnergy,LaserPhotonEnergy,LaserAbsCrossSection,LaserEmCrossSection,Br
anchingRatio,W_RETU,ModeArea_pump,ModeArea_laser,OverlapTellurite_pump,Overlap
Tellurite_laser);
                %Calculate gain and absorption coefficients
                Gain_coeff(z) = (LaserEmCrossSection.*N1(z-1)-
LaserAbsCrossSection.*N0(z-1))*OverlapTellurite_laser;
                Abs_coeff(z) = (PumpEmCrossSection.*N1(z-1)-
PumpAbsCrossSection.*N0(z-1))*OverlapTellurite_pump;

                %Propagates fields
                FwdLaserElectricField(z) = FwdLaserElectricField(z-1) +
(Gain_coeff(z)-LaserBGLoss-GratingLoss)*FwdLaserElectricField(z-1).*dZ;
                BwdLaserElectricField(z) = BwdLaserElectricField(z-1) -
(Gain_coeff(z)-LaserBGLoss-GratingLoss)*BwdLaserElectricField(z-1).*dZ;

                %Calculates powers
                FwdPumpPower(z) = FwdPumpPower(z-1) +(Abs_coeff(z)-
PumpBGLoss)*FwdPumpPower(z-1)*dZ;
                BwdPumpPower(z) = BwdPumpPower(z+1)+(Abs_coeff(z)-
PumpBGLoss)*BwdPumpPower(z+1)*dZ;
                FwdLaserPower(z) = abs(FwdLaserElectricField(z))^2;
                BwdLaserPower(z) = abs(BwdLaserElectricField(z))^2;


            elseif z<NumOfSteps %calculate parameters within output grating
                %Solve rate equations
                [N0(z),N1(z),N3(z)] =
UpdatePouplations_Tm1610pump(tau1,tau3,W_ETU,FwdPumpPower(z-1)+BwdPumpPower(z-
1),FwdLaserPower(z-1)+BwdLaserPower(z-1),NT,PumpAbsCrossSection,
PumpEmCrossSection,
PumpPhotonEnergy,LaserPhotonEnergy,LaserAbsCrossSection,LaserEmCrossSection,Br
anchingRatio,W_RETU,ModeArea_pump,ModeArea_laser,OverlapTellurite_pump,Overlap
Tellurite_laser);
                %Calculate gain and absorption coefficients for each mesh
point
                Gain_coeff(z) = (LaserEmCrossSection.*N1(z-1)-
LaserAbsCrossSection.*N0(z-1))*OverlapTellurite_laser;
                Abs_coeff(z) = (PumpEmCrossSection.*N1(z-1)-
PumpAbsCrossSection.*N0(z-1))*OverlapTellurite_pump;

                %Propagates fields
                FwdLaserElectricField(z) = FwdLaserElectricField(z-1)+((-
1i.*kappa*BwdLaserElectricField(z-1).*exp(+1i.*2.*dBeta.*(-dZ))) +
(Gain_coeff(z)-LaserBGLoss-GratingLoss)*FwdLaserElectricField(z-1)).*(-dZ);
```

```
                BwdLaserElectricField(z) = BwdLaserElectricField(z-
1)+((1i.*kappa*FwdLaserElectricField(z-1).*exp(-1i.*2.*dBeta.*(-dZ))) -
(Gain_coeff(z)-LaserBGLoss-GratingLoss)*BwdLaserElectricField(z-1)).*(-dZ);

                %Calculates powers
                FwdLaserPower(z) = abs(FwdLaserElectricField(z))^2;
                BwdLaserPower(z) = abs(BwdLaserElectricField(z))^2;
                FwdPumpPower(z) = FwdPumpPower(z-1) +(Abs_coeff(z)-
PumpBGLoss)*FwdPumpPower(z-1)*dZ;
                BwdPumpPower(z) = BwdPumpPower(z+1)+(Abs_coeff(z)-
PumpBGLoss)*BwdPumpPower(z+1)*dZ;


            else
                %Solve rate equations
                [N0(z),N1(z),N3(z)] =
UpdatePouplations_Tm1610pump(tau1,tau3,W_ETU,FwdPumpPower(z-1)+BwdPumpPower(z-
1),FwdLaserPower(z-1)+BwdLaserPower(z-1),NT,PumpAbsCrossSection,
PumpEmCrossSection,
PumpPhotonEnergy,LaserPhotonEnergy,LaserAbsCrossSection,LaserEmCrossSection,Br
anchingRatio,W_RETU,ModeArea_pump,ModeArea_laser,OverlapTellurite_pump,Overlap
Tellurite_laser);
                %Calculate gain and absorption coefficients for each mesh
point
                Gain_coeff(z) = (LaserEmCrossSection.*N1(z-1)-
LaserAbsCrossSection.*N0(z-1))*OverlapTellurite_laser;
                Abs_coeff(z) = (PumpEmCrossSection.*N1(z-1)-
PumpAbsCrossSection.*N0(z-1))*OverlapTellurite_pump;

                %Propagates fields
                FwdLaserElectricField(z) = FwdLaserElectricField(z-1)+((-
1i.*kappa*BwdLaserElectricField(z-1).*exp(+1i.*2.*dBeta.*dZ)) +
(Gain_coeff(z)-LaserBGLoss-GratingLoss)*FwdLaserElectricField(z-1)).*dZ;
                BwdLaserElectricField(z) = BwdLaserElectricField(z-
1)+((1i.*kappa*FwdLaserElectricField(z-1).*exp(-1i.*2.*dBeta.*dZ)) -
(Gain_coeff(z)-LaserBGLoss-GratingLoss)*BwdLaserElectricField(z-1)).*dZ;

                %Calculates powers
                FwdLaserPower(z) = abs(FwdLaserElectricField(z))^2;
                BwdLaserPower(z) = abs(BwdLaserElectricField(z))^2;
                FwdPumpPower(z) = FwdPumpPower(z-1) +(Abs_coeff(z)-
PumpBGLoss)*FwdPumpPower(z-1)*dZ;
            end

        end
    %Check boundary conditions and update values
    IterationN=IterationN+1;
    LaserPowerError(P,IterationN) =BwdLaserElectricField(NumOfSteps);

    disp((BwdLaserElectricField(NumOfSteps)));

    if IterationN==MaxIteration
```

```
        disp("MaxIteration reached, no convergence");
        FwdLaserPower(:)=0;
        BwdLaserPower(:)=0;
    end

    end
    ResultFwdLaserOutput(P)=FwdLaserPower(NumOfSteps);
    ResultBwdLaserOutput(P)=BwdLaserPower(1);

    fprintf("Finished %d",1000*IncidentPumpPower_Fwd(P));
end
a=linspace(1,IterationN,IterationN);

filename = sprintf("Test");
save(filename,"ResultFwdLaserOutput","ResultBwdLaserOutput","IncidentPumpPower
_Fwd","IncidentPumpPower_Bwd","AvgN0","AvgN1","AvgN3","Z","FwdLaserPower","Bwd
LaserPower","FwdPumpPower","BwdPumpPower","Gain_coeff","Abs_coeff","FwdLaserEl
ectricField","BwdLaserElectricField");
```